Dissertation
submitted to the
Combined Faculties of the Natural Sciences and Mathematics
of the Ruperto-Carola-University of Heidelberg, Germany
for the degree of
Doctor of Natural Sciences

Put forward by
Alberto Nardin
born in: Treviso, Italy
Oral examination: 17th April, 2015

On the Stäckel potential approximation in the extended solar neighbourhood

Referees:	apl. Prof. Dr. Andreas Just
	Prof. Dr. Hans-Walter Rix

Abstract:

The problem of the third integral of motion has been studied for decades. Its existence was determined at the beginning of numerical experiments with orbits in an axisymmetric potential and by observations of triaxiality in the velocity dispersion of nearby stars. In general it is not possible to derive an exact expression for a general axisymmetric potential analytically. One way to find an exact third integral of motion is to approximate the gravitational potential with a potential of the Stäckel form. In addition to the third integral of motion, another important property of the Stäckel potential is that it separates the Hamilton-Jacobi equation in confocal spheroidal coordinates. This results in an alignment of the velocity ellipsoid with the spheroidal coordinate system in the meridional plane. In this thesis we construct a Stäckel model, fixing the focal point of these coordinates based on recent observations of the velocity ellipsoid (Binney et al. 2014a).

The aim of this PhD thesis is to show how a universal Stäckel potential works. This Stäckel model is focused on the region of the extended solar neighbourhood, up to 2 kpc radius around the Sun. The free parameters are constrained with the observational values of the local volume and surface density. Studying the vertical structure we can predict the behaviour of the local vertical force and radial dependencies at 1.1 kpc far from the plane. The value of the focal point is very important, because for different values we obtain different profiles for the radial density, different values for the scale length and different behaviour for the vertical force at large heights. We derive again the orientation of the velocity ellipsoid in the meridional plane based on RAVE data. The result for the tilt angle is in agreement with Binney et al. (2014a), both for the complete sample of red clump giants and also for different metallicities. This result is a confirmation of the derived Stäckel model.

Zusammenfassung:

Das Problem des dritten Bewegungsintegrals wird schon jahrzehntelang studiert. Seine Existenz wurde mit dem Beginn numerischer Experimente mit Orbits in achsensymmetrischen Potentialen und durch die Beobachtung der Dreiachsialität in der Geschwindigkeitsdispersion nahegelegener Sterne bestätigt. Im Allgemeinen kann jedoch kein exakter Ausdruck eines generellen, achsensymmetrischen Potentials analytisch abgeleitet werden. Ein Weg, um ein exaktes drittes Bewegungsintegral zu bestimmen, ist die mathematische Näherung des Gravitationspotentials mittels eines Potentials in der Stäckel-Form. Des Weiteren besitzt das Stäckel-Potential die wichtige Eigenschaft, die Hamilton-Jacobi-Gleichung in konfokalen Kugel-Koordinaten zu separieren. Dadurch richtet sich das Geschwindigkeitsellipsoid in der meridionalen Ebene entlang des Koordinatensystems aus. In dieser Arbeit konstruieren wir ein Stäckel-Potential und legen dabei den Brennpunkt des Koordinatensystems mittels kürzlich gemachter Beobachtungen des Geschwindigkeitsellipsoids (Binney et al. 2014a) fest.

Das Ziel dieser Dissertation ist zu zeigen, wie ein universelles Stäckel-Potential funktioniert. Das Stäckel-Potential in dieser Arbeit befasst sich hauptsächlich mit der Region der erweiterten Sonnenumgebung in einem Radius von 2 kpc um die Sonne. Die freien Parameter werden mittels beobachteter Werte der lokalen Volumen- und Oberflächendichte festgelegt. Indem wir die vertikale Struktur untersuchen, ist es möglich, Vorhersagen über das Verhalten der lokalen vertikalen Kraft sowie über ihre radiale Abhängigkeit in einer Höhe von 1.1 kpc über der Ebene zu machen. Die Wichtigkeit der Lage des Brennpunkt zeigt sich dadurch, dass wir für verschiedene Brennpunkt-Werte verschiedene Profile der radialen Dichte erhalten sowie verschiedene Werte für die Skalenlänge und unterschiedliches Verhalten der vertikalen Kraft in größeren Entfernungen. Wir erhalten die Orientierung des Geschwindigkeitsellipsoids in der meridionalen Ebene mittels RAVE Daten. Das Ergebnis steht in Einklang mit den Resultaten von Binney et al. (2014a) – sowohl für die gesamten Daten zu Red Clump Stars sowie für unterschiedliche Metallizitäten. Dadurch wird das konstruierte Stäckel-Modell bestätigt.

Alla mia famiglia

Contents

1 Introduction **1**
- 1.1 Structure of the Milky Way . . . 4
- 1.2 Orbits in an axisymmetric potential . . . 7
  - 1.2.1 Epicycle approximation . . . 8
- 1.3 Collisionless systems . . . 9
- 1.4 Distribution function . . . 10
- 1.5 Collisionless Boltzmann Equation (CBE) . . . 10
  - 1.5.1 First Jeans equation . . . 11
  - 1.5.2 Second Jeans equation . . . 12
- 1.6 Integrals of motion and Jeans theorem . . . 13
  - 1.6.1 Problem of the third integral of motion . . . 14

2 Jeans equations **19**
- 2.1 Velocity ellipsoid . . . 19
  - 2.1.1 Equatorial velocity dispersions . . . 20
  - 2.1.2 Orientation of the velocity ellipsoid . . . 20
- 2.2 Jeans equations for axisymmetric system . . . 22
  - 2.2.1 Asymmetric Drift . . . 23
  - 2.2.2 Vertical force . . . 24
  - 2.2.3 Isopotential lines . . . 28

3 Stäckel potentials **35**
- 3.1 Coordinate system . . . 37
- 3.2 Analytic third integral of motion . . . 39
- 3.3 Velocity ellipsoid . . . 40
  - 3.3.1 Tilt of velocity ellipsoid . . . 41
- 3.4 Stäckel model . . . 42
  - 3.4.1 Focal point determination . . . 44
  - 3.4.2 Rotation Curve . . . 45
  - 3.4.3 Radial density . . . 46
  - 3.4.4 Radial scale length . . . 48
- 3.5 Logarithmic case . . . 49
  - 3.5.1 Local density . . . 49
  - 3.5.2 Radial profile . . . 50
- 3.6 Power-law case . . . 53
  - 3.6.1 Rotation curve . . . 53
  - 3.6.2 Local density . . . 55
  - 3.6.3 Radial profile . . . 56
- 3.7 Isopotential lines . . . 59
- 3.8 Vertical structure . . . 63

3.9 Discussion 68

4 **Tilt of the velocity ellipsoid based on RAVE data** **73**
4.1 RAVE sample 74
4.1.1 Red giants and cold dwarfs 76
4.1.2 Input data 77
4.2 Methods 79
4.3 Binning data 80
4.3.1 Overlapping bins 80
4.3.2 Uncorrelated bins 80
4.4 Velocity dispersion tensor 81
4.4.1 Shape of the velocity ellipsoid 83
4.4.2 Tilt of the velocity ellipsoid 84
4.5 Subpopulations 87
4.5.1 Velocity dispersions 88
4.5.2 Tilt of the velocity ellipsoid 88
4.6 Tilt close to the plane 90
4.7 Discussion 91

5 **Future work** **97**
5.1 Two-component model 97
5.1.1 Linear profile 98
5.1.2 Isothermal profile 98
5.1.3 Surface density at 1.1 kpc ($K_{1.1}(R)$) 99
5.2 Future work 100

A **Stäckel potential** **105**
A.1 De Zeeuw coordinate system 105
A.1.1 Transformations 106
A.2 Jacobian 107
A.3 Derivatives 109
A.3.1 Inverse transformation 109
A.3.2 First derivatives 109
A.3.3 Second derivatives 111
A.4 Derivatives of Stäckel potentials 112
A.4.1 u-derivatives 112
A.4.2 v-derivatives 114
A.5 Hamiltonian-Jacobi equation 115
A.6 Third integral of motion 117

B **Data analysis** **119**
B.1 Overlapping bins 120
B.2 Non-Axisymmetry effects 121

Bibliography **125**

Acknowledgements **129**

List of Tables

1.1 Values for three different objects: open clusters, globular clusters and elliptical galaxies. Using typical values for the number of stars belonging to these systems, their sizes and velocities, we obtain respective values for the relaxation and crossing times. 10

2.1 Values of z-derivative of the angle formed by the force field for different gravitational potentials. 33

3.1 Values for the parameter η in a range $0.60 \leq \eta \leq 1.00$, the corresponding tilt angle α_{tilt} of the velocity ellipsoid and the focal point Δ are given. 46

4.1 The first selection is listed in the first 3 rows: total number of RAVE data, number of stars with distance measurements and selections in proper motion errors. Two groups of stars are selected: red clump giants and cold dwarfs. The sample reduces when we consider the cylinder around the solar neighbourhood ($7 \leq R \leq 9$ kpc, $-2 \leq z \leq 2$ kpc). . 79

List of Figures

1.1 Sketch of the rotation curve of the Milky Way. The contribution given by the visible matter is not enough to explain the high speed of stars. The difference between the observed rotation curve and the contribution of the disc is the evidence for the dark matter halo. 2
1.2 Artistic picture of the Milky Way. Credit: NASA/Adler/U. Chicago/Wesleyan/JPL-Caltech. 5
1.3 Meridional plane (R, z) of a star orbiting in a Milky Way-like potential (Ollongren 1962). As we can see the orbit does not fill completely the area inside the isopotential line. . . . 8
1.4 This sketch represents the link between the kinematics, the density and the gravitational potential. Linking together these three quantities permits us to study the problem self-consistently. 11
1.5 Surface of sections using Henon-Heiles potential. We can recognize ordered figures which correspond to regular orbits and are immersed in a 'sea' of irregular orbits. 15

2.1 Orientation of the velocity ellipsoid with respect to the meridional plane. v_1 and v_2 are the velocities in the new rotated system (Yurin & Springel 2014). 21
2.2 Asymmetric drift relation assuming that the orientation of the velocity ellipsoid is aligned with the cylindrical $(\eta = 0)$ and the spherical $(\eta = 1)$ coordinate system. 25
2.3 Asymmetric drift relation assuming that the orientation of the velocity ellipsoid is aligned with the cylindrical $(\eta = 0)$ and the spherical $(\eta = 1)$ coordinate system, assuming a 10% error in the estimation of the radial scale length of the density and velocity dispersion. . . 25
2.4 Representation of the total volume density and surface density as a function of z (Kuijken & Gilmore 1989). 27
2.5 Vertical surface density assuming $\Sigma_0 = (56 \pm 6)$ $M_\odot/pc^2$ for the luminous and (76 ± 6) $M_\odot/pc^2$ including the dark matter found by Holmberg & Flynn (2004) with a scale height of 300 pc. Overplotted is the contribution given by the tilt of the velocity ellipsoid, which increases the value of the vertical surface density. 29
2.6 Vertical surface density assuming $\Sigma_0 = (56 \pm 6)$ $M_\odot/pc^2$ for the baryons and (76 ± 6) $M_\odot/pc^2$ including the dark matter found by Holmberg & Flynn (2004) with a scale height of 300 pc. Overplotted is the contribution given by the tilt of the velocity ellipsoid, which increases the value of the vertical surface density. The shadow regions correspond to assuming 100% error in the estimation of the local dark matter density ρ_{dm}. 30
2.7 The sketch shows the angle α corresponding to the inclination of the velocity ellipsoid with respect to the Galactic plane and the angle β corresponding to the angle between the vertical and radial force components. 31

3.1 Orbits in a logarithmic potential (full curves) can be constrained in the meridional plane approximately with a confocal spheroidal coordinate system (dotted lines) (Binney & Tremaine 2008). 36
3.2 Prolate spheroidal coordinate system. Surfaces of constant u are ellipses elongated along the z-axis and surfaces of constant v are hyperbolas. 38

3.3 Sketch of the alignment of the velocity ellipsoid with the spheroidal coordinate system. The ellipses represent the velocity ellipsoids. 42

3.4 Variation of the tilt of the velocity ellipsoid above and below the plane. The green line corresponds to the alignment of the velocity ellipsoid with the spherical coordinates; the black one assuming the Stäckel model with $\Delta = 0$ kpc; the red one is the value found by Binney et al. (2014a) and the blue one assumes the Stäckel model with $\Delta = 4$ kpc. 45

3.5 'Vertical' oscillation frequency for the logarithmic potential for values of the focal point between 1 and 10 kpc, with zero integration constant C_0 (blue points) and C_0 which normalises the 'radial' potential to a two-component model composed by a Bessel disc plus a cored isothermal halo (green points) with values given by (Golubov 2012). The red points correspond to the case of $\Delta = 4$ kpc for the two different integration constants. 50

3.6 'Vertical' oscillation frequency for the logarithmic potential for values of C_0 between $-v_0^2$ and v_0^2 for $\Delta = 4$ kpc. The red point corresponds to the case for $\Delta = 4$ kpc and $C_0 = 0$. 51

3.7 Radial density profile for the logarithmic potential for different values of Δ and with integration constant C_0 normalised to a value corresponding to the case of a two-component (Bessel disc plus cored isothermal halo) model. 51

3.8 Radial density profile for the logarithmic potential for different values of $C_0[-v_0^2 : v_0^2]$ for $\Delta = 4$ kpc. 52

3.9 Radial density profile for the logarithmic potential after the subtraction of the dark matter profile for different values of Δ and with integration constant C_0 normalised to a value corresponding to the case of a two-component (Bessel disc plus cored isothermal halo) model. The dashed line corresponds to an exponential profile for the case $\Delta = 4$ kpc with a radial scale length of $R_d = 2.55$ kpc. 53

3.10 Radial scale length for the logarithmic potential (after the subtraction of the dark matter) for different values of Δ and with integration constant C_0 normalised to a value corresponding to the case of two-component (Bessel disc plus cored isothermal halo) model. . 54

3.11 Radial scale length for the logarithmic potential (after the subtraction of the dark matter) for $\Delta = 4$ kpc and for different values of $C_0[-v_0^2 : v_0^2]$. 54

3.12 Variation of the Oort's parameters A and B with radius. 55

3.13 'Vertical' oscillation frequency for the power-law potential for values of the focal point between 1 and 10 kpc, with C_0 normalised to a value corresponding to the case of a two-component model (Bessel disc plus cored isothermal halo). The red point corresponds to the case for $\Delta = 4$ kpc. 56

3.14 Radial density profile for the power-law potential for different values of Δ with C_0 normalises to a value corresponding to a two-component model (Bessel disc plus cored isothermal halo). 57

3.15 'Vertical' oscillation frequency for the power-law potential for values of the focal point between 1 and 10 kpc. 58

3.16 Radial scale length for the power-law potential for different values of Δ with C_0 normalised to a case corresponding to the case of a two-component (Bessel disc plus cored isothermal halo) model. 58

3.17 Comparison between the radial density profile generated by a power-law potential with $\Delta = 4$ kpc and the exponential density profile with scale length $R_d = 2.6$ kpc. 59

3.18 Comparison between the radial density profile generated by a power-law potential with $\Delta = 8$ kpc and the exponential density profile with scale length $R_d = 4.3$ kpc. 60

3.19 Radial density profile for the power-law potential for Δ =4 kpc with different values of the power-law index α[-0.5:0.5]. The dashed line corresponds to the case of $\alpha = 0$ which corresponds to the logarithmic case. 60

3.20 Radial scale length for the power-law potential for $\Delta = 4$ kpc with different values of the power-law index α[-0.5:0.5]. The dashed line corresponds to the case of $\alpha = 0$ which corresponds to the logarithmic case. 61

3.21 The sketch shows the angle α corresponding to the inclination of the velocity ellipsoid with respect to the Galactic plane and the angle β corresponding to the angle between the vertical and radial force components. 62

3.22 Isopotential (red) lines of a three-component Plummer-Kuzmin potential (Just et al. 2009) with isocoordinate (green) lines for a spheroidal coordinate system with $\Delta = 4$ kpc. 62

3.23 Local K_z-force along the ν-coordinate using the approximation given by Kuijken & Gilmore (1989) for the 'vertical' potential $G(\nu)$ for different values of Δ. The observational constrain is given by Holmberg & Flynn (2004). 66

3.24 Local K_z-force using the approximation given by Kuijken & Gilmore (1989) for the 'vertical' function $G(\nu)$, adopting the complete formula 3.22, for different values of Δ. The observational constrain is given by Holmberg & Flynn (2004). 67

3.25 Radial surface density at 1.1 kpc using the approximation given by Kuijken & Gilmore (1989) for the 'vertical' function $G(\nu)$ for different values of Δ. The observational constrain is given by Holmberg & Flynn (2004). The dashed line corresponds to an exponential profile with scale length $R_d = 2.55$ kpc derived from the radial profile for the logarithmic case. 68

3.26 Dynamical estimation of the disc thickness using the approximation given by Kuijken & Gilmore (1989) for the 'vertical' function $G(\nu)$ for different values of Δ. 69

4.1 Tilt of velocity ellipsoid in literature: Siebert et al. (2008) (red point), Casetti-Dinescu et al. (2011) (green point) and Büdenbender et al. (2014) (magenta points). The black line corresponds to an orientation of the velocity ellipsoid with the spherical coordinates; the blue line corresponds to the result found by Binney et al. (2014a). 75

4.2 Colour-Magnitude Diagram (CMD) of all RAVE stars (red points) with overplotted the cold dwarfs with a gravity-temperature selection (blue points). 76

4.3 Location of the cold dwarfs in the meridional (R, z)-plane. 77

4.4 Colour-Magnitude Diagram of all RAVE stars (red points) with overplotted the cold dwarfs (blue point) adding a magnitude cut to the previous selection and the red clump giants (green points) selected by gravity-colour cut. 78

4.5 Locations of the red clump giants in the meridional (R, z)-plane in a height range $-2 \leq z \leq 2$ kpc. 78

4.6 Vertical velocity dispersion σ_z increasing with z for red clump giants using the biweight and the MCMC method. 82

4.7 Radial velocity dispersion σ_R increasing with z for red clump giants using the biweight and the MCMC method. 82

4.8 Fraction of halo stars in a height range $0 \leq z \leq 2$ kpc calculated using the MCMC simulation. 83

4.9 Ratio between the vertical and radial velocity dispersion for the red clump giants using the biweight and the MCMC method. 84

4.10 Covariant term of the velocity dispersion matrix (σ_{Rz}) decreasing with z for the red clump giants using the biweight and the MCMC method. 85

4.11 Tilt of velocity ellipsoid for the red clump giants using the biweight and the MCMC method. 86

4.12 Least-square fit of the tilt of velocity ellipsoid, assuming a zero tilt angle in the midplane, for the red clump giants using the biweight method. 86
4.13 Least-square fit of the tilt of velocity ellipsoid, assuming a zero tilt angle in the midplane, for the red clump giants using the MCMC method. 87
4.14 $[Fe/H]$ vs $[\alpha/Fe]$ abundances of red clump giants. 88
4.15 Radial velocity dispersion σ_R for three subpopulations ($[Fe/H] \leq -0.5$, $-0.5 < [Fe/H] \leq -0.2$, $[Fe/H] > -0.2$) of red clump giants. 89
4.16 Vertical velocity dispersion σ_z for three subpopulations ($[Fe/H] \leq -0.5$, $-0.5 < [Fe/H] \leq -0.2$, $[Fe/H] > -0.2$) of red clump giants. 89
4.17 Covariant term of the velocity ellipsoid (σ_{Rz}) for three subpopulations ($[Fe/H] \leq -0.5$, $-0.5 < [Fe/H] \leq -0.2$, $[Fe/H] > -0.2$) of red clump giants. 90
4.18 Tilt of the velocity dispersion for three subpopulations ($[Fe/H] \leq -0.5$, $-0.5 < [Fe/H] \leq -0.2$, $[Fe/H] > -0.2$) of red clump giants. 93
4.19 Tilt of the velocity ellipsoid for the red clump giant sample and the cold dwarf sample close to the plane ($-500 < z < 500$ kpc) using the biweight method. 94
4.20 Comparison of the tilt of velocity ellipsoid for red clump giants using the biweight method and Büdenbender et al. (2014). 95

5.1 Local vertical force for a two-component model for the potential function $G(v)$ using a linear profile for the dark matter halo with scale height $z_0 = 300$ pc, for different values of Δ. The observational constrain is given by Holmberg & Flynn (2004). 99
5.2 Local vertical force for a two-component model for the potential function $G(v)$ using a cored isothermal profile for the dark matter halo with scale height $z_0 = 300$ pc with a flattening $q = 1$, for different values of Δ. The observational constrain is given by Holmberg & Flynn (2004). 100
5.3 Radial surface density at $z = 1.1$ kpc for different values of Δ. The observational constrain is given by Holmberg & Flynn (2004). The dashed line corresponds to an exponential profile with scale length $R_d = 2.55$ kpc derived from the radial profile for the logarithmic case. 101
5.4 Dynamical estimation of the disc thickness using a two-component model for the potential function $G(v)$ for different values of Δ. 101

A.1 Stäckel coordinates using the mathematical description of de Zeuuw. It is possible to obtain the prolate and oblate coordinate system considering $a > c$ or $a < c$. The prolate coordinate system generates an oblate density distribution, whereas the oblate coordinate system a prolate density distribution. 107
A.2 Prolate spheroidal coordinate system generated with the 'de Zeeuw description'. 108
A.3 Prolate spheroidal coordinate system generated with the 'de Zeeuw description', assuming a value for the parameter $a = 1$ (red lines) and $a = 0$ (green lines). 108

B.1 Error distribution for the proper motion (pm rad and pm dec) for the PPMXL Catalogue. 119
B.2 Error distribution for the proper motions (pm rad and pm dec) for the UCAC Catalogue and the radial velocity distribution (vlos). 120
B.3 Error distribution for the proper motions (pm rad and pm dec) and the radial velocity distribution (vlos) using log plot. 120
B.4 Error distribution for the proper motion (pm rad and pm dec) and the radial velocity distribution (vlos) using log-log plot. The red line is a quadratic function which corresponds to a log-normal distribution in the normal plot. 121

B.5 Tilt of the velocity ellipsoid calculated using the MCMC method and using 1000 stars per bin for different overlaps. The overlaps are 200, 400, 600 and 800 stars between two following bins. The black line corresponds to an orientation of the velocity ellipsoid with the spherical coordinates and the blue line for the Stäckel model with $\Delta = 4$ kpc. 122
B.6 Mean radial velocity $\overline{v_R}$ for the red clump giants using the biweight method. 123
B.7 Mean vertical velocity $\overline{v_z}$ for the red clump giants using the biweight method. 123
B.8 Tilt of velocity ellipsoid for the red clump giants using the biweight method for the axisymmetric (red points) and non-axisymmetric case (green points). 124

1

Introduction

Dark matter (DM) plays a central role in the model of structure formation and galaxy evolution. From looking at anisotropies in the Cosmic Microwave Background (CMB) it is possible to measure its effect. The CMB can be assumed homogeneous and isotropic on large scales, but these assumptions are not valid on small scales. The temperature inhomogeneities in the CMB correspond to the seeds of the galaxies that we observe today. These seeds evolved during the cosmic time and became bigger following the Hubble flow. After that, the density of these structures reached a critical density ($\rho_{crit} \sim 200\,\rho_0$, where ρ_0 is the background density of the universe at a particular redshift), which leads to a collapse of the structures and the formation of galaxies. This process includes relaxation and phase-mixing and is called 'virialization'. The formation of these structures has to be driven by the dark matter only, because otherwise it would be impossible to form the present-day observed structures. The standard cosmological model is represented by Lambda Cold Dark Matter (ΛCDM): Cold because the velocities of these particles are much smaller than the speed of light c, in contrast to the Hot Dark Model with velocities comparable to c; and Dark because this matter interacts only gravitationally and not via electromagnetic waves. This standard model implies a hierarchical evolution of the galaxies, small systems collapsed earlier than large systems and small systems merged together to form bigger structures. The role of baryons was to follow the evolution of the dark matter structures and be converted by accretion and feedback processes into stars.

Dark matter was already postulated by Oort (1932) and Zwicky (1933). The first was studying the motion of stars in the solar neighbourhood, while the second found evidence of 'missing mass' in the orbital velocities of galaxies in clusters. Subsequently, other observations have indicated the presence of dark matter in the universe, including the rotational velocity curves in spiral galaxies, gravitational lensing of background objects by galaxy clusters and the temperature distribution of hot gas in galaxies and clusters of galaxies. The rotation curves (RCs) are expected to increase linearly with radius in the inner part of the disc galaxies rotating as a solid body. After having reached a maximum, RCs decrease with radius due to the Keplerian motion regulating the stellar orbits in the disc (Fig. 1.1). What has been observed instead are flat or increasing RCs as we depart from the centre, which is in contrast with the theoretical predictions. This behaviour can be explained by the presence of more mass than expected. All lines of evidence suggest that galaxies, clusters of galaxies, and the universe as a whole contain far more matter than that which interacts with electromagnetic radiation. Indeed, luminous matter represents only a small fraction (~4%) of the total matter, whereas the dark matter corresponds to ~22% and the remaining ~74% are due to the Dark Energy. Many studies on RCs have shown the presence of the dark

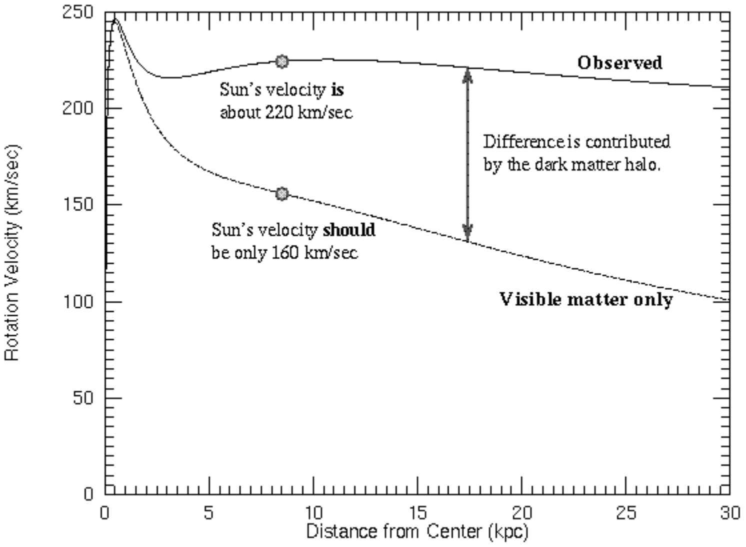

Figure 1.1: Sketch of the rotation curve of the Milky Way. The contribution given by the visible matter is not enough to explain the high speed of stars. The difference between the observed rotation curve and the contribution of the disc is the evidence for the dark matter halo.

matter, but uncertainty remains about its spatial distribution in the centre and its nature.

The Milky Way (MW) is a disc galaxy, one of many others in the Universe, and contains around 100 billion stars. Our MW is key to our understanding of the galaxy evolution as it is possible to study, in detail, many different aspects of astronomy: star formation, interstellar medium, stellar astrophysics, galaxy evolution, extragalactic astronomy and cosmology. It is possible to start from small scales studying star formation, its feedback and the interstellar medium in great details; we have access to resolutions high enough to study the faintest and oldest stars; we can obtain the six-dimensional information to study the stellar kinematics. We can study the fossil record, trying to understand the origin and evolution of the Milky Way and its neighbours, as well as the role and nature of dark matter. Understanding what happens in the Milky Way can help us in understanding the full picture of cosmic evolution.

The importance of these studies is evidenced by the large amount of surveys that have been developed for understanding the MW: SDSS/SEGUE, RAVE, APOGEE, LAMOST, finally culminating in the ESA's cornerstone mission Gaia which was launched in December 2013. This mission will produce a three dimensional map of the MW, detecting up to a billion stars reaching the limiting magnitude $G \sim 20$ during the span of five years. This mission will be revolutionary for Galactic Archeology, because it will increase the number of observations, from 10^5 to 10^9 stars, improving the accuracy in parallax and proper motions. This study is focused on a region called the 'solar neighbourhood', centred on the Sun at 8 kpc distance from the Galactic centre, and with a radius of few hundred parsecs. We can extend this region up to a radius of ~1-2 kpc distance from the Sun because the new surveys provide more extensive data. The new large amount of data that Gaia will provide, will probably change our understanding of the Milky Way. The Gaia mission will furnish six dimensional information which is very important to the study of the stellar kinematics in the solar neighbourhood. Assuming that galaxies are collisionless systems, the motion of stars in the phase-space is continuous. This means that by studying the kinematics of stars in the phase-space, we can understand their origin. The solar neighbourhood provides a fossil record of the formation history of the whole MW. The construction of dynamical models is important because of the connection between the phase-space distribution of stars with the gravitational potential. When we learn more about the distribution of stars in phase-space, we also learn more about the gravitational potential. Studying the stellar kinematics can address the question of what is the amount of dark matter in the solar neighbourhood. This value is very important for understanding the overall distribution of dark matter in the MW and is needed for direct dark matter search experiments.

The two approaches in the determination of the local dark matter density rely on the rotation curve and the gravitational force. The first method needs an assumption for the global and local shape of the dark matter halo (Garbari et al. 2011), otherwise it is not possible to separate the luminous contribution from the dark matter. The second method is based on the kinematics of stars in the solar neighbourhood, determining the vertical gravitational force K_z, which was studied for the first time by Oort (1932, 1960). The K_z-force for the tracer populations increases linearly with z and then flattens because there is no more luminous matter to contribute to the vertical force. At larger heights the dark matter becomes dominant and the K_z-force continues to increase linearly with a different slope. By separating the contribution of the dark matter from the luminous matter, it is possible to derive the local dark matter density in the solar neighbourhood. The value is expected to be small in this region because the density is contributed primarily by the disc. An estimate for the local dark matter density can be derived from the rotation curve assuming a spherical symmetry for the dark matter halo and a constant velocity ($\rho_{dm,RC} = 0.01$ $M_\odot/pc^3 = 0.38$ GeV/cm^3)[1] (Sofue et al. 2009). This value can be compared with the value derived from the estimation of the K_z-force (ρ_{dm,K_z}). By comparing these two values for the local dark matter density it is possible to derive the shape of the dark matter halo: if $\rho_{dm,K_z} < \rho_{dm,RC}$, the dark matter halo is prolate, whereas if $\rho_{dm,K_z} > \rho_{dm,RC}$, the dark matter halo is oblate; if the two values are the same it will confirm a spherical dark matter halo. After the work of Oort there were numerous studies to determine the local vertical gravitational force and the estimation of the local dark matter density (Kuijken & Gilmore 1989; Siebert et al. 2003; Garbari et al. 2011, 2012; Zhang et al. 2013; Piffl et al. 2014; Bienaymé et al. 2014).

If the number of conducted studies is so large, why yet another? The problem remains that the data can rule out neither the absence of, nor a high value of the dark matter. Studies of the last two years reanalysed the literature data, obtaining lower errors, therefore confirming the presence of dark matter and in the case of (Garbari et al. 2011) the amount of dark matter is as much as twice the typical value and the halo has to be flattened ($\rho_{dm} = 0.025^{+0.013}_{0.014}$ $M_\odot/pc^3$). Zhang et al. (2013) on the other hand found a lower estimate ($\rho_{dm} = 0.0065 \pm 0.0025$ $M_\odot/pc^3$), which is in agreement with Bovy & Tremaine (2012) ($\rho_{dm} = 0.008 \pm 0.003$ $M_\odot/pc^3$), and which they claim is the most robust direct measurement of the local dark matter to date. As method Bovy & Tremaine (2012) used the Jeans equations, which link spatial distribution, velocity dispersions and gravitational potential together. Until now, the study of the vertical force has implied the assumption for the Jeans equations: the radial and vertical motion is decoupled. The assumption that the velocity ellipsoid is aligned with the cylindrical coordinate system is not valid, a fact that has to be taken into account. The Jeans equations do not require knowledge of the phase-space distribution function, but the spatial binning of discrete data implies loss of information and is very sensitive to outliers. The other method to solve the problem is to construct a distribution function; in this case we have full phase-space information. However, assuming a false distribution function can lead to fatal errors. In principle, we do not have any idea how to construct this function; we know that it has to be a function of the six coordinates, position and velocities ($\vec{x}$,$\vec{v}$). Following the work of Eddington (1915) we can assume the 'ellipsoidal hypothesis': the distribution function has an exponential form, with the exponent having a quadratic expression for the velocities (de Zeeuw 1984). The Jeans theorem helps us in the construction of the distribution function: it claims that integrals of motion are necessary and that three of them are sufficient for describing regular orbits.

Here we come to the main assumption that our MW is in a steady-state, stationary equilibrium. Furthermore, the MW is phase-mixed because it rotated ~40 times around the Galactic Centre. A second important assumption is that the MW is axisymmetric. Deviations from the axisymmetry are ~5-10% (Rix & Bovy 2013). We can see these deviations by observing moving groups in the solar neighbourhood. If these two assumptions were true, we would observe a smooth velocity distribution, but this is not the case. There are concentrations corresponding to star streams – an observation made both for young and older populations of stars. Hence the two assumptions made above are not perfectly true because the MW contains a bar near the centre and spiral arms in the disc, and because the presence of streams in the halo are a clear signal that the MW is still evolving with time. The disc is close to axisymmetric (Jurić et al. 2008), since the gravitational potential does not depend strongly on the azimuthal coordinate and the assumption of equilibrium is necessary for studying the problem. Also in the case we would like to model these features, we should start first by seeking a dynamical equilibrium system and then perturbing it, but this method has been little used in galactic dynamics (Binney 2011). From the invariance of the gravitational potential over time the total energy of the system E is conserved. The absence of azimuthal force leads to the conservation of the vertical component of the angular momentum L_z. These two conserved quantities (E, L_z) are two classical integrals. But the determination of the third integral of motion is one of the big problems in Galactic astronomy.

---

[1] 1 GeV/cm^3 $\simeq$ 0.0263158 $M_\odot/pc^3$.

Numerical orbit simulations have shown its existence for most orbits but this is called a 'non-classical' integral of motion. Instead of focusing solely on a numerical approach, which surely is necessary, we should also keep in mind the idea of an analytical approach for the approximation of the real third integral, given the insights and generalizations it provides. Hence, our first aim is to find an approximation for it, which does not have to be exact but close enough to be reasonable and mathematically tractable. After many studies on the third integral of motion (Eddington 1915; Clark 1937; van Albada 1952; Kuzmin 1953; Hori 1962), each starting from different points of view, it became clear that the most useful analytic result involves the use of a special class of potentials, the so-called Stäckel potentials.

Another way is to use angle-action variables for the construction of an equilibrium distribution function for the local disc. These quantities are adiabatic invariants and can be assumed as integrals of motion. Binney & McMillan developed in recent years two techniques in the evaluation of the actions. The first method is the 'torus modelling' (Kaasalainen & Binney 1994; Binney & McMillan 2011) which derives observables from the actions. This method is numerically demanding and technically non-trivial (McMillan & Binney 2008). The second method is the 'adiabatic approximation' (Binney 2010; Binney & McMillan 2011) which delivers actions from the observables $(\vec{x}, \vec{v})$. This method is, however, limited to a region near the plane where it is possible to separate the radial motions of the stars from the vertical ones. Analytically the derivation of actions is possible only for special cases because they require the resolution of an integral in phase-space assuming separability in the potential. Binney (2012a,b) obtained approximate actions for a more general axisymmetric system assuming that the gravitational potential can be approximated by a Stäckel potential. This approximation with respect to the adiabatic one can be used to find more accurate actions.

Past research on dynamical modelling of the solar neighbourhood concluded that the Stäckel potential is one good way to find a reasonable analytic expression for the third integral of motion. The scope of this thesis is, after assuming that the gravitational potential of the extended solar neighbourhood can be approximated by a Stäckel potential, to investigate if this potential can reproduce the observables such as the rotation curve, the local matter density, and the local vertical force at $z = 1.1$ kpc for this region and how far it can go. But first, I want to give a short introduction to the different components of the MW, highlighting the behaviour of the stellar orbits in the disc. Furthermore I will introduce the basic concepts of galactic dynamics, such as the distribution function and the second order velocity distribution, important elements for the study of the Jeans equations.

1.1 Structure of the Milky Way

The Milky Way is a barred spiral galaxy and comprises three major components: bulge, halo and disc.

Understanding the structure of the different components of the MW is non-trivial, because of our location inside the disc. The bulge is the dominant component in the very inner part of the MW (< 1

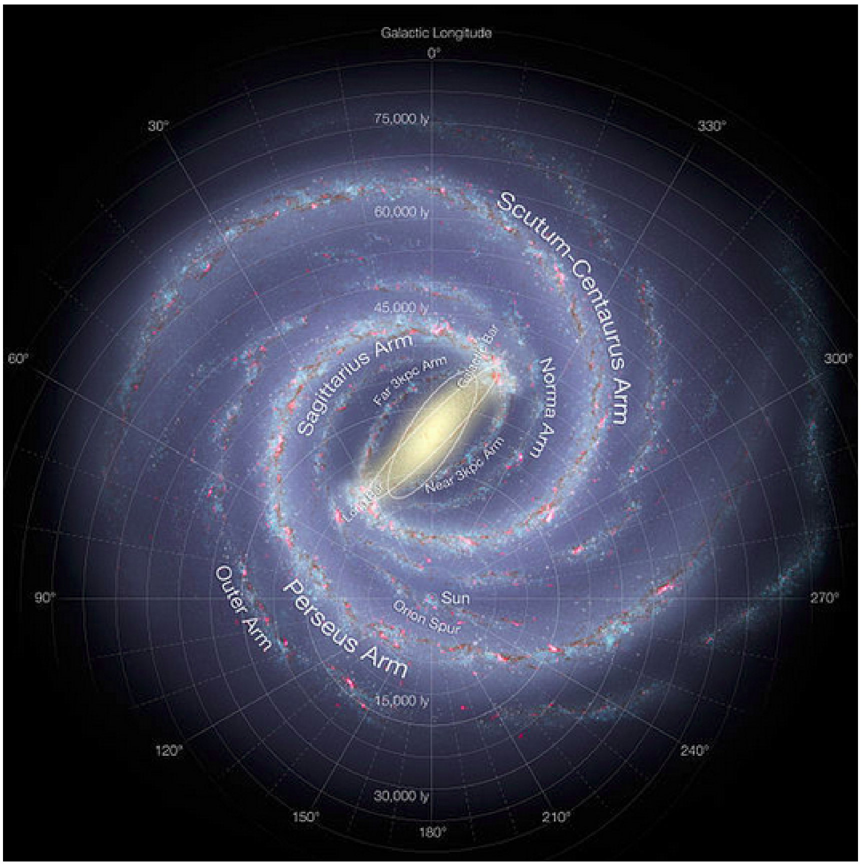

Figure 1.2: Artistic picture of the Milky Way. Credit: NASA/Adler/U. Chicago/Wesleyan/JPL-Caltech.

kpc). If we could see our Galaxy edge on, it would be possible to see that the bulge is thicker than the disc, contributing ~15% of the total luminosity (Binney & Tremaine 2008). The size of the bulge is related to the galaxy classification. Moving in the Hubble diagram from Sa to Sc spirals, the size of the bulge decreases and the ratio disc/bulge increases. The bulge of MW seems to be a small exponential bulge, rather than $r^{1/4}$ bulge. Such bulges are called 'pseudo-bulges', and have different properties than the 'classical bulges': their size/mass and profile, the inclusion of Population I stars and their formation mechanism. These small bulges seem to be driven by secular evolution, in contrast to classical bulges that are formed via mergers. A bar is present and is pointing towards our line of sight and the bulge can rotate (Beaulieu et al. 2000). The kinematics of stars in the bulge are dominated by high velocity dispersions, comparable to the circular velocity of the disc, and the system is called 'hot'. The α-enhancement indicates that star formation in this region proceeded rapidly, therefore these stars are old and supposed to have been formed more than 5 Gyrs ago (Clarkson et al. 2008). In the centre there is a super massive black hole (SMBH) with $M_{SMBH} = (4.3 \pm 0.20|_{stat} \pm 0.30|_{sys}) \times 10^6$ $M_\odot$ (Gillessen et al. 2009). In general the SMBH mass is related with the host bulge mass, which is a fundamental property between SMBH and their host galaxies (Ferrarese & Merritt 2000).

The globular clusters found in the halo mostly extend up to 30 kpc, but there are also a few cases found at larger distances. The stars in the stellar halo feel a spherical potential and move like rosettes, with larger eccentricity than disc stars. The stars are old (Population II) and very metal-poor with metallicity range $[Fe/H] \sim$ -1 to -5. These properties tell us that these stars have formed during the collapse in the early stage of Galaxy formation.

The most massive component of the MW is the dark matter halo with a mass of $(1 \div 1.5) \times 10^{12}$ $M_\odot$

(Xue et al. 2008; McMillan 2011; Golubov 2012). The presence of a halo is indicated by the flat rotation curve of the MW, a more extended distribution of mass than the density distribution of the disc only. In order to accommodate a flat RC, the density of the halo has to decline with R^{-2}. However, a radial density profile declining with $\propto R^{-3}$ at large radii is in agreement with observations (Binney & Tremaine 2008) and numerical simulations (Navarro et al. 1996). In the inner part, the profile is still matter of debate because from simulations the best profile seemed to be cuspy Navarro et al. (1996) whereas observations of dark-dominated systems (e.g. dwarfs spheroidal galaxies) show a core (Spano et al. 2008). This is the so-called 'cusp/core problem'. An alternative profile that is better in agreement with dark matter simulations is given by the Einasto profile. Whether the halo is spherical or triaxial is yet clear. The attempt to calculate the local dark matter density gives the possibility to derive additional information on the shape, size and mass of the halo. It is unclear what the halo is made of, but the most popular candidates as dark matter particles are non-baryonic weakly interacting massive particles (WIMPS) or axions.

Disc galaxies are highly flattened structures, where the disc component extends to 15 kpc radially and 1 kpc vertically. The Sun is located at 8 kpc from the Galactic centre and few pc above the Galactic plane. The local circular speed (v_0) is 220 km/s. The mass of the disc is $M \simeq 5 \times 10^{10}$ $M_\odot$ (Flynn et al. 2006; McMillan 2011; Rix & Bovy 2013). Observations of external galaxies suggest that the surface brightness has approximately an exponential profile (Binney & Tremaine 2008), with a radial scale length between 2 and 3 kpc. In the solar neighbourhood the velocity dispersions have values of $\sigma_R = 32.4 \pm 0.1$ km/s, $\sigma_\phi = 23.0 \pm 0.1$ km/s and $\sigma_z = 18.1 \pm 0.2$ km/s (Fuchs et al. 2009), approximately in the ratio 2: $\sqrt{2}$:1. These random motions are much smaller than the local circular speed, which is why we can define the disc as 'cool'. If there are no velocity dispersions, i.e. the stars rotate in a perfect circular orbit, the disc is called 'cold'.

The standard picture for the vertical profile given by Gilmore & Reid (1983) consists of two populations: a thin disc and a thick disc where the density is represented well by an exponential:

$$\rho(R, z)_{disc} = \rho_0 \exp\left(-\frac{R}{R_d} - \frac{|z|}{z_0}\right)$$

The thin disc has a scale height (z_0) of 300 pc and the thick disc a scale height of 900 pc (Jurić et al. 2008). The radial scale length R_d for the thin and thick disc are 2.6 and 3.6 kpc, respectively (Jurić et al. 2008). The density ratio between these two populations $f = \rho_{thick}/\rho_{thin}$ at the solar position is 0.12 (Jurić et al. 2008). This means that the contribution of stars with high-eccentricity orbits is $\sim$10%.

The differences in the two populations lie in the height that they can reach above the Galactic plane, in their age, kinematics and chemical composition (both $[Fe/H]$ and α-enrichment). After the most massive stars have finished burning, they explode in Supernovae (SN) type II, enriching the interstellar medium (ISM) with α-elements. The thick disc stars are formed in a very short time (less than 1 Gyr), therefore they are old, metal-poor and α-enriched. Only when explosions of SN type Ia occurred, was it possible to dilute the α-enrichment with iron elements. The thin disc stars are thus metal-rich and younger than the thick disc stars. These stars have a near circular motion around the MW due to the fact that the interstellar medium is confined next to the plane and they have lower velocity dispersions compared to the thick disc stars. The oldest stars were also possibly born in circular orbits, but they had time to experience dynamical heating, probably due to spiral arms and molecular clouds, which gradually increased their velocity dispersion. Another possible scenario for the formation of the thick disc is the accretion from satellites galaxies. In the disc between the star systems exists a thin layer of ISM, thinner than the stellar disc. The ISM, with a scale height of $\sim$100 pc, contributes to $\sim$25% of the total disc surface density.

1.2 Orbits in an axisymmetric potential

The Milky Way disc is close to axisymmetric. Therefore we show the disc stellar orbits using the cylindrical reference system (R, ϕ, z). Later on, we introduce spheroidal coordinates, which are a more general case than cylindrical. In kinematic study, stars of late spectroscopic types are involved, i.e. stars that live long enough to be phase-mixed and in dynamical equilibrium. The system is collisionless and the orbits are considered test particles in a smooth potential:

$$\ddot{\vec{r}} = -\vec{\nabla}\Phi(R, z) = -\frac{\partial \Phi}{\partial R}\hat{e}_R - \frac{\partial \Phi}{\partial z}\hat{e}_z$$

We can divide the gravitational potential on the sum of potentials of the components depending on R and z. If a star is in the equatorial plane, it will feel a central force and be confined to the plane. If $z \neq 0$, it is possible to have different components. The acceleration is:

$$\ddot{\vec{r}} = (\ddot{R} - R\dot{\phi})\hat{e}_R + (R\ddot{\phi} + 2\dot{R}\dot{\phi})\hat{e}_\phi + \ddot{z}\hat{e}_z$$

where the components represent the equations of motion. Since there is no dependence of Φ on the azimuthal coordinate, the azimuthal component of the acceleration is zero. This leads to the conservation of the z-component of the angular momentum (L_z), which represents the second integral of motion after the total energy E. The conservation of the angular momentum reduces the motion of stars to a two dimensional plane (R, z) which is non-uniformly rotating around the z-axis, with angular velocity $\dot{\phi} = L_z/R^2$. This is the 'meridional plane' which exists for every star.

The total energy is given by the Hamiltonian:

$$H = \frac{1}{2}(\dot{R}^2 + R^2\dot{\phi}^2 + z^2) + \Phi = \frac{1}{2}(\dot{R}^2 + \dot{z}^2) + \Phi_{eff}$$

where we can define the effective potential (Φ_{eff}):

$$\Phi_{eff} = \frac{L_z^2}{2R^2} + \Phi(R, z)$$

Then the equations of motion become:

$$-\frac{\partial \Phi_{eff}}{\partial R} = \ddot{R} \quad ; \quad -\frac{\partial \Phi_{eff}}{\partial z} = \ddot{z}$$

which are two harmonic oscillators in the limit of constant forces in the meridional plane.

The energy is always greater than the gravitational potential $(E \geq \Phi_{eff})$, and each orbit is restricted to a region defined by the isopotential lines. An orbit will touch the isopotential lines only when the velocity is zero. If there are no additional restrictions, i.e. no additional isolating integral of motion than the total energy, the stars explore all the region inside the isopotential lines and the orbits are called 'ergodic'. We look at the minimum of the effective potential:

$$\frac{\partial \Phi_{eff}}{\partial R} = 0 \Rightarrow \left(\frac{\partial \Phi}{\partial R}\right)_{(R_g, 0)} = R_g\dot{\phi}^2$$

$$\frac{\partial \Phi_{eff}}{\partial z} = 0 \Rightarrow \left(\frac{\partial \Phi}{\partial z}\right)_{(R_g, 0)} = 0$$

The point $(R_g, 0)$, where the effective potential has a minimum is the 'guiding radius'. If a star was located at this point, its motion would be perfectly circular. A star located in the equatorial plane $(R, 0)$ will have a rosette motion, feeling a central force, and if it is at a generic point in the meridional plane, the stars will move inside of a torus as an oscillator in R and z direction.

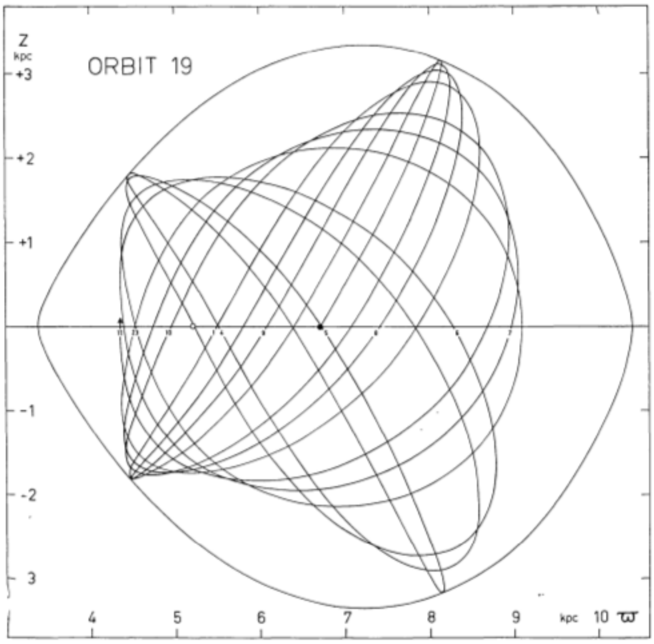

Figure 1.3: Meridional plane (R, z) of a star orbiting in a Milky Way-like potential (Ollongren 1962). As we can see the orbit does not fill completely the area inside the isopotential line.

1.2.1 Epicycle approximation

The equations of motion cannot be solved analytically unless the gravitational potential is of a special form. Orbits of many stars in disc galaxies are almost circular, and we can expand the effective potential in a Taylor expansion near its minimum:

$$\Phi_{eff} = \Phi_{eff}(R_g, 0) + \frac{1}{2}\left(\frac{\partial^2 \Phi_{eff}}{\partial R^2}\right)_{(R_g,0)} (R - R_0)^2 + \frac{1}{2}\left(\frac{\partial^2 \Phi_{eff}}{\partial z^2}\right)_{(R_g,0)} z^2 + (O^2) + const$$

where the mixed term is cancelled because of symmetry about $z = 0$, and terms higher than the second order are small enough to be negligible. We can define:

$$\left(\frac{\partial^2 \Phi_{eff}}{\partial R^2}\right)_{(R_g,0)} = \kappa^2$$

$$\left(\frac{\partial^2 \Phi_{eff}}{\partial z^2}\right)_{(R_g,0)} = \nu^2$$

as the radial and vertical frequencies.

$$\Phi_{eff} = \Phi_{eff}(R_g, 0) + \frac{1}{2}\kappa^2 (R - R_g)^2 + \frac{1}{2}\nu^2 z^2$$

When we know the expansion of the effective potential, the equations of motion are:

$$-\frac{\partial \Phi_{eff}}{\partial R} = -\kappa^2 (R - R_g) = \ddot{R}$$

$$-\frac{\partial \Phi_{eff}}{\partial z} = -\nu^2 z = \ddot{z}$$

finding two harmonic oscillators around the minimum of Φ_{eff}. Adding the azimuthal coordinate ϕ it is possible to show that the motion in the plane is composed of two terms; the first term corresponds to the circular motion at radius R_g whereas the second term is a sinusoidal correction. The angular velocity can slow down or increase depending on the sign of the sine-function. The motion is composed of an epicycle in the plane plus an vertical oscillation out of the plane with constant vertical oscillation frequency. The vertical reachable height depends on the value of the vertical energy.

Which is the region of validity of these equations? The vertical frequency is linked with the second derivative of the potential, then with the density ρ. This means they are valid close to the plane, i.e. for $z << 300$ pc at R_0 (Binney & Tremaine 2008). The vertical density remains constant only very near to the Galactic plane and then decreases exponentially at higher altitude. The epicycle approximation is a good approximation for stars in near-circular orbits that do not have large radial ($e << 1$, e=eccentricity) and vertical motions. Both oscillation frequencies are linked with the gravitational potential to the second order, and have to remain constant for the validity of this theory. An improvement is given by the work of Dekker (1976), taking a Taylor expansion with respect to $1/R$ instead of R resulting in a new approximation that is also valid for orbits which are deviating from a circular motion, up to $e = 0.5$.

1.3 Collisionless systems

Galaxies are a gravitational bound system which contain billions of stars. We are not able to solve the equations of motion for this large number of stars. What is usually done is to adopt a statistical treatment for the stellar dynamics, assuming the stars as a continuous fluid and solve the equation of kinematics in the six-dimensional phase-space. If we want to use fluid dynamics in the galaxies, we need to determine if the collisions between stars are important or not. Let us consider a star with some specific radius $\mathrm{R}_\star$ and velocity v. In an interval of time t the star sweeps out a cylinder of base $\pi R_\star^2$ and height vt. Given the number density of stars n, we can calculate the number of stars in the cylinder which can collide:

$$N = \pi R_\star^2 vtn$$

The typical time for having a geometrical collision is obtained when $N = 1$:

$$t = \frac{1}{\pi R_\star^2 vn} \sim 10^{19} yrs$$

assuming the typical value for the radius of a star $R_\star \sim 10^8$ cm and the numerical density in the solar neighbourhood $n = 0.1/\mathrm{pc}^3$, the time between collision is $t >> t_{universe}$.

Even though a pure geometrical collision between two stars does not happen, we have to consider the small deviations which the star is subjected to. The mean value of this deviation can be zero, but this does not mean that the star is not subjected to deflection and the bigger the angle, the more deflected is the star.

From statistics of two-body encounter it is possible to derive the relaxation time:

$$T_R \sim \frac{v^3}{8\pi G^2 m^2 n \ln N}$$

We can look at the ratio between the relaxation time and the crossing time, $2R/v$, which is the time for a star to cross the galaxy. Then we can find the number of crossings needed to cause the deviation:

$$n_c = \frac{T_R}{T_c} \sim 0.1 \frac{N}{\ln N}$$

where N is the number of objects. The force from these collisions depends on how much time is needed for a crossing as well on the dimension of the system. If the relaxation time is greater than the age of the

Universe, the system can be considered as collisionless. In Table 1.1 the relaxation times for different objects – open cluster, globular cluster and elliptical galaxies – are shown. Elliptical galaxies similar to our Galaxy have a relaxation time greater than the age of the Universe and can thus be considered collisionless systems, but this is not true for smaller systems like open and globular clusters.

	N	R [pc]	v $(=\sigma)$ [km/s]	T_R [yr]	T_c [yr]	n_c
Open Cluster	10^2	1	2	4×10^6	2×10^6	2
Globular Cluster	10^5	10	10	2×10^9	2×10^6	700
Elliptical Galaxies	10^{11}	3000	200	10^{16}	3×10^7	3×10^8

Table 1.1: Values for three different objects: open clusters, globular clusters and elliptical galaxies. Using typical values for the number of stars belonging to these systems, their sizes and velocities, we obtain respective values for the relaxation and crossing times.

1.4 Distribution function

It is not worthwhile to follow orbits of billions of stars in galaxies. Since we can neglect collisions in galaxies, we can consider them as an incompressible fluid in phase-space $(\vec{r},\vec{v})$, i.e. the phase-space density along the orbits is constant. For modelling collisionless galaxies it is better to define a distribution function (DF) f: in the galaxy there is a potential $\Phi(\vec{x},t)$ generated by the mass of stars, which are considered as a fluid uniformly distributed over the surface of the galaxy with a density that is not necessarily constant. We are looking for the number of stars and the velocity at every time t. Then we construct a function as $f(\vec{x},\vec{v},t)d^3\vec{x}d^3\vec{v}$, which is the number of stars located in a small volume $d^3\vec{x}$ centred in $\vec{x}$ with a velocity in a small volume $d^3\vec{v}$ centred in $\vec{v}$.

It is not possible to measure directly the distribution function at each six-dimensional point and if we take sufficiently small volumes, the distribution function can cease to be a well-behaved function. An observer can rather measure the number of stars in finite volume elements. This is called a coarse-grained distribution function. We will use the description for the DF as density distribution for the system. As the DF evolves, probability must be conserved, in the same way that mass is conserved in a fluid flow (Binney & Tremaine 2008).

1.5 Collisionless Boltzmann Equation (CBE)

In the phase-space the position is defined as $\vec{w}=(\vec{x},\vec{v})$ and the velocity as $\dot{\vec{w}}=(\dot{\vec{x}},\dot{\vec{v}})=(\vec{v},-\vec{\nabla}\Phi)$. The motion of the stars is defined by $\vec{w}$ and $\dot{\vec{w}}$. We can write the continuity equation for a collisionless system in the phase-space as:

$$\frac{\partial f}{\partial t}+\sum_{i=1}^{6}\frac{\partial(f\dot{w}_i)}{\partial w_i}=0$$

Assuming that the velocity does not depend on the position and the acceleration does not depend on the velocity, we can write this equation in the ordinary space:

$$\frac{\partial f}{\partial t}+\vec{v}\cdot\vec{\nabla}f-\frac{\partial f}{\partial\vec{v}}\cdot\vec{\nabla}\Phi=0 \tag{1.1}$$

This is the collisionless Boltzmann equation, the fundamental equation for Galactic Dynamics. Using this equation we can derive f from the knowledge of the gravitational potential Φ or vice versa, but this equation needs to be solved for seven independent variables. In case of collisions the term on the right side is not zero and we have to use the Fokker-Planck equation. We can see the equivalence with the one-dimensional Liouville's equation:

$$\frac{D}{Dt}f = 0$$

where D/Dt is the convective derivative in the six-dimensional space including the time t. This proves that the distribution function is constant along any trajectory in phase space and the fluid incompressible.

Since the distribution function is the number density of stars in the phase-space, we can integrate over the velocities and obtain the spatial density:

$$\nu = \int f d^3\vec{v}$$

where ν is the number density per unit volume of the tracers. In the next two section we calculate the zeroth, first and second order velocity moments of the collisionless Boltzmann equation and we will see their meaning and how these quantities are related to the gravitational potential:

$$\int (CBE) v^n d^3\vec{v}$$

where $n = 0, 1, 2$.

The Poisson equation links together the gravitational potential and the total density ρ:

$$\nabla^2\Phi = 4\pi G\rho$$

We would like to link together these three quantities, kinematics (given by f), density and gravitational potential. This problem remains unresolved, unless we impose initial conditions on the potential. The mass is concentrated in the stars, but we are not considering the dark matter, which must be enclosed in the Poisson equation. When the potential is generated by the mass of the tracers, and only that, the problem is self-consistent, but the result is not a realistic representation of the galaxies.

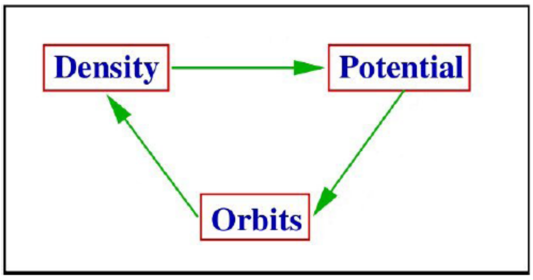

Figure 1.4: This sketch represents the link between the kinematics, the density and the gravitational potential. Linking together these three quantities permits us to study the problem self-consistently.

1.5.1 First Jeans equation

We can integrate the collisionless Boltzmann equation over the velocity space, with the summation convention on the indices, and find some moments for the phase-space distribution function:

$$\int \frac{\partial f}{\partial t} d^3\vec{v} + \int \frac{\partial f}{\partial x_i} v_i d^3\vec{v} - \int \frac{\partial f}{\partial v_i}\frac{\partial \Phi}{\partial x_i} d^3\vec{v} = 0$$

By introducing the zeroth-order moment of $f(\vec{x}, \vec{v}, t)$ which is the number density:

$$\nu(\vec{x}, t) = \int f(\vec{x}, \vec{v}, t) d^3\vec{v}$$

and considering that the first moments are the mean velocities:

$$\overline{v}_i = \frac{\int f v_i d^3\vec{v}}{\int f d^3\vec{v}} = \frac{1}{\nu} \int f v_i d^3\vec{v}$$

we obtain the first Jeans equation:

$$\frac{\partial \nu}{\partial t} + \frac{\partial}{\partial x_i}(\nu \overline{v}_i) = 0 \tag{1.2}$$

This equation is equivalent to the continuity equation, with density ρ and velocity $\vec{v}$:

$$\frac{\partial \rho}{\partial t} + \vec{\nabla} \cdot (\rho \vec{v}) = 0$$

The first Jeans equation can be referred to the continuity equation for Galactic dynamics. The density is conserved and the trajectory is continuous.

1.5.2 Second Jeans equation

By multiplying the CBE by v_j, it is possible to derive the first order of the CBE (Eq. 1.1):

$$\frac{\partial}{\partial t} \int f v_j d^3\vec{v} + \frac{\partial}{\partial x_i} \int v_i v_j f d^3\vec{v} - \frac{\partial \Phi}{\partial x_i} \int v_j \frac{\partial f}{\partial v_i} d^3\vec{v} = 0$$

We obtain:

$$\frac{\partial (\nu \overline{v}_j)}{\partial t} + \frac{\partial}{\partial x_i}(\nu \overline{v_i v_j}) + \frac{\partial \Phi}{\partial x_j} \nu = 0 \tag{1.3}$$

We multiply Eq. 1.2 by $\overline{v}_j$ and we subtract it from Eq. 1.3:

$$\nu \frac{\partial \overline{v}_i}{\partial t} + \frac{\partial}{\partial x_i}[\nu \underbrace{(\overline{v_i v_j} - \overline{v}_i \overline{v}_j)}_{\sigma^2_{ij}}] + \frac{\partial \Phi}{\partial x_j} \nu + \overline{v}_i \nu \frac{\partial \overline{v}_j}{\partial x_i} = 0$$

where we define the new parameter as:

$$\sigma^2_{ij} = \overline{v_i v_j} - \overline{v}_i \overline{v}_j = \frac{\int f (v_i - \overline{v}_i)(v_j - \overline{v}_j) d^3\vec{v}}{\int f d^3\vec{v}}$$

This is the second order moment of the distribution function f and it is defined as stress tensor, which coincides with the velocity ellipsoid. The tensor is symmetric and is always possible to find a reference system where the only non zero elements are on the diagonal, i.e.: $\sigma^2_{ij} = \sigma^2_{ji}$ and $\sigma^2_{ii} = \delta_{ij}\sigma^2_{ij}$.

We can write the final form for the first order of the CBE:

$$\nu \frac{\partial \overline{v}_j}{\partial t} + \overline{v}_j \nu \frac{\partial \overline{v}_i}{\partial x_i} = -\frac{\partial \Phi}{\partial x_j} \nu - \frac{\partial}{\partial x_i}(\nu \sigma^2_{ij})$$

This equation is very similar to the Euler equation:

$$\rho \frac{d\vec{v}}{dt} + (\vec{v} \cdot \vec{\nabla})\vec{v} = -\rho \vec{\nabla} \Phi - \vec{\nabla} P$$

The four terms are the acceleration, the convection, the external potential force and the pressure, respectively. Therefore the term ($\nu\sigma^2_{ij}$), which appears in the second Jeans equation, can be assigned to the fluid pressure, and the velocity dispersion corresponds to a temperature tensor.

The elements in the diagonal (variances) give an idea of the degree of the random motions and can be assigned to the semi-axis of the velocity ellipsoid after diagonalization. The off-diagonal terms (covariances) express the coupling between the velocity distributions and show the deviation of the ellipsoid from the adopted reference system. In a disc galaxy these random motions are much smaller than the ordered motion of disc stars rotating around the Milky Way. In this case we can define the disc as 'cool'. If the velocity dispersions are zero, the stars rotate in a perfect circular orbit, the disc is called 'cold' and the perfect ellipsoid becomes a point. There are however other galaxies, ellipticals, which are supported by pressure instead of rotation. In this case velocity dispersions are higher than the ordered motions and the system is called 'hot'.

1.6 Integrals of motion and Jeans theorem

We want to define the concept of integrals of motion and their importance in the Galactic dynamics. A constant of motion is any function of the phase-space and time that remains constant during the orbit of a star:

$$C(\vec{x}, \vec{v}, t) = const$$

Moreover, an integral of motion is a function that depends only on the phase-space coordinates:

$$I(\vec{x}, \vec{v}) = const$$

and is invariant both during an orbit of a star and over time:

$$\frac{d}{dt} I(\vec{x}, \vec{v}) = 0 \tag{1.4}$$

Integrals of motion are also constants of motion but the contrary is not true. Any orbit has six independent constants of motion but they can posses from zero to five integrals of motion. Integrals of motion are classified as non-isolating and isolating. Each isolating integral restricts the orbit of a star to a $2n - 1$ surface, whereas the non-isolating integrals do not affect the phase-space distribution of an orbit. For this reason, the latter are not important in Galactic dynamics.

From Eq. 1.4:

$$\frac{dI}{dt} = \frac{\partial I}{\partial \vec{x}} \frac{\partial \vec{x}}{\partial t} + \frac{\partial I}{\partial \vec{v}} \frac{\partial \vec{v}}{\partial t} = 0$$

Remembering the equation for the CBE:

$$\frac{\partial f}{\partial t} + \vec{v} \cdot \vec{\nabla} f - \frac{\partial f}{\partial \vec{v}} \cdot \vec{\nabla} \Phi = 0$$

We can see that the condition for a function $I(\vec{x}, \vec{v})$ to be an integral is identical to the condition that satisfies the CBE. This brings us to the Jeans theorem: *Any steady-state solution of the collisionless Boltzmann equation depends on the phase-space coordinates only through integrals of motion in the given potential, and any function of the integrals yields a steady-state solution of the collisionless Boltzmann equation* (Binney & Tremaine 2008). This theorem claims that if a distribution function is a function of integrals of motion ($f(I_i)$), it fulfils the CBE.

The strong Jeans theorem provides us also with the number of integrals that we need. If an orbit has the same number of integrals as dimensions this orbit is called regular. If the number of integrals is less than the dimensions this orbit is called irregular or chaotic. Since it has been observed that in the solar neighbourhood the ratio between regular and chaotic orbits is high, we are expecting three integrals of motion. The Jeans theorem is telling us not only how to construct the DF (as function of integrals of motion) in order to fulfil equation of kinematics, but also how many integrals do we need. Once we know these three integrals, it will be possible to construct a phase-space distribution function which describes three dimensional regular orbits.

However, the reality is more complicated, and it is not so easy to write down the integrals of motions analytically. Sometimes it is possible to find them but a few assumptions are required: if the gravitational potential is in steady-state, it does not vary with the time and the first integral is the total energy of the system. If the galaxy is spherical, another integral of motion is the total angular momentum. In this case all three components of the angular momentum are conserved and the system has four integrals of motion. This means that the integrals of motion restrict the orbits of the stars to two dimensional motion. If the galaxy is axisymmetric, only the vertical component of the angular momentum L_z is conserved but not the other two. From assuming a steady-state and axisymmetric system, we recover already two integrals of motion. However the third integral of motion is non-classical and its determination is one of the big challenges that many scientists have undertaken since the last century.

1.6.1 Problem of the third integral of motion

If we construct a phase-space distribution function that depends only on two integrals of motion as representative of an axisymmetric galaxy, we see already that there is a problem. A distribution function depending only on energy $f(E)$ has terms in the velocity that enter in a quadratic way and make no distinction among these velocities. This means that the three variances of the velocity dispersion have to be the same ($\sigma_R^2 = \sigma_\phi^2 = \sigma_z^2$) and the covariances vanish. As result the velocity ellipsoid is a sphere. If we introduce also the second integral of motion, the vertical component of the angular momentum L_z, we can break the degeneracy between the radial and the azimuthal velocity dispersion ($\sigma_R^2 \neq \sigma_\phi^2$). However the radial and vertical velocity dispersions have to be the same and all the covariances, including the coupling between the radial and vertical velocities, vanish. This is inconsistent with the observations, since the radial velocity dispersion is approximately twice the vertical one (Fuchs et al. 2009), producing an anisotropy in the meridional plane. Furthermore, if we look at the isopotential lines in the meridional plane, there are some additional restrictions in the stellar orbits. Since the energy E is always greater than the gravitational potential:

$$E = \frac{1}{2}(v_R^2 + v_z^2) + \Phi(R, z) \geq \Phi(R, z)$$

all the volume inside the isopotential lines can be filled with the orbits of a star. Adding the second integral L_z brings a restriction that limits the orbital motion radially and the orbits no longer completely fill the isopotential lines.

From numerical simulations another restriction emerges, including vertical boundaries. Ollongren (1962) already discovered that stellar orbits do not fill completely the volume defined by the isopotential lines; all the orbits in the Milky Way-potential did not fill completely the region inside the isopotential lines. It was thought that maybe this occurred because of some special property of his model, but Henon & Heiles (1964) showed the presence of a third integral of motion using the Poincaré surfaces of section (SoS) and a very simple potential. If the same result can be found with a simple analytic potential, the existence of such an integral can be expected. We are interested in the motion in the meridional plane and thus have to deal with a four-dimensional motion of stars (R, z, v_R, v_z). Since the Hamiltonian is constant, the motion is reduced to three dimensions. Morevore, considering only orbits that cross the plane at $z = 0$, we reduce the problem to two dimensions. These plots are called 'Poincaré surface of sections'. In the SoS the radius versus the radial velocity (R, v_R) are plotted, every time the orbit crosses the midplane. Henon & Heiles (1964) noticed that the orbits did not fill the region inside the isopotential lines but plotting the SoS they obtained ordered figures. The presence of these features are another evidence for the existence of the third integral of motion. Another result they found was that the orbits become chaotic with increasing value of energy, showing that these features are destroyed and the region inside the isopotential lines become completely filled. This means that increasing the value of the energy, the third integral will be no longer isolating. The orbits become chaotic, destroying the ordered figures in the surface of sections. In Fig. 1.5 we have a plot of SoS using the Henon-Heiles potential. It shows that the circles correspond to regular orbits, which are like islands in a 'sea' of chaotic orbits. Following the understanding that a third integral of motion exists, many scientists tried to derive analytically its expression. Only in this way we can describe completely the three dimensional motion of regular orbits and construct a DF that describes the system.

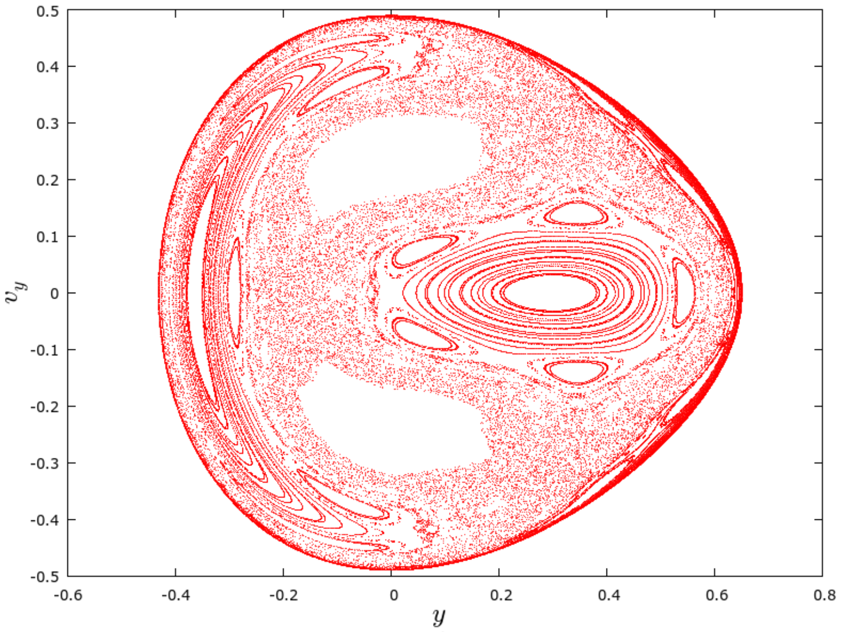

Figure 1.5: Surface of sections using Henon-Heiles potential. We can recognize ordered figures which correspond to regular orbits and are immersed in a 'sea' of irregular orbits.

One result is that given by the Oort-Lindblad approximation, which assumes a separability in the radial and vertical motion:

$$\Phi(R, z) = \Phi(R) + \Phi(z)$$

where the vertical energy is an approximation of the third integral of motion, and used by Schwarzschild (Binney & Tremaine 2008) to reproduce the observables of the solar neighbourhood:

$$I_3 = E_z = \frac{1}{2}v_z^2 + \Phi(z)$$

It reproduces the velocity dispersion anisotropy in the meridional plane but not the tilt of the velocity ellipsoid. This approximation is valid only locally since the vertical energy does not remain constant when we extend further away from the guiding radius and the separability in the gravitational potential is no longer true.

Later studies done by Contopoulos (1960) represented the potential in the solar neighbourhood by power series. He was able to write down an analytic expression for the third integral as asymptotic series, but he was never able to show their convergence. Although these series deviate only slightly from the exact third integral, Manabe (1979) showed that even the best approximations for stellar orbits in the solar neighbourhood deviate significantly from the true ones with large departures of 2-3 kpc (Kent & de Zeeuw 1991).

Another idea is to use angle-action variables, quantities that remain constant during the orbit of a star and over the time. This idea has received more attention recently and consists in the conversion of phase-space coordinates in a new coordinate system represented by actions and angles. The actions are invariable quantities, where the angles increase linearly over time. If we can find these three invariants, it would be possible – using the Jeans theorem – to construct a distribution function as function of these three new variables. We need, however, to know the generating function that is the bridge between the coordinate systems and therefore must perform an integral:

$$J = \frac{1}{2\pi} \int \vec{v} d\vec{x}$$

To solve this integral we need to impose some conditions on the gravitational potential Φ. Assuming the case of the epicycle approximation, where the radial motion is decoupled from the vertical one, it is possible to solve the integral and to find the actions. The azimuthal action is the vertical component of the angular momentum as before ($J_\phi = L_z$); the radial and vertical actions are the radial and vertical energy divided by the radial and vertical oscillation frequencies, respectively:

$$J_R = E_R/\kappa \qquad ; \qquad J_\phi = L_z \qquad ; \qquad J_z = E_z/\nu$$

The epicycle approximation, however, is valid only for regions close to the plane and for small eccentricity. Far from the plane the results are not very accurate (Binney 2012b). For this reason Binney (2012b) introduced a more accurate approximation for calculating action-angle variables for each orbits in potentials which are close to Stäckel form. This special potential was already studied long time ago as it leads to an analytic expression of the third integral of motion, which can recover the vertical energy for stars in the solar neighbourhood and the total angular momentum for stars far away from the midplane.

The scope of this thesis is, after approximating the gravitational potential of the extended solar neighbourhood by a Stäckel potential, to investigate if this potential can reproduce the observables such as the rotation curve, the local matter density and the local vertical force, as well as make predictions on the radial surface density at $z = 1.1$ kpc.

In Chapter 2 we will describe the velocity ellipsoid, its shape and orientation in the meridional plane. After that we give an introduction to the Jeans equations, which are the first order equations of the CBE. These equations link the spatial stellar distribution to their kinematics and the gravitational potential. From the radial and vertical Jeans equations it is possible to study the asymmetric drift and the vertical force. The asymmetric drift is still a matter of debate, since Binney (2010) and Schönrich et al. (2010) reviewed the value of the local standard of rest, increasing its value of ~7 km/s, with respect to the classic one. The vertical force, instead, is determined 1.1 kpc away from the plane, where the contribution of the stars should separate from that of the dark matter. Several studies on it were conducted, mainly due to the large uncertainties about the determination of the dark matter density, whose existence can neither be proofed nor be discarded. Here is also studied the link between the velocity ellipsoid and the gravitational potential.

In Chapter 3 we will describe the tools necessary to study the Stäckel potential, namely the confocal spheroidal coordinates and the velocity dispersion matrix in the new reference system. Afterwards, we will construct a model for the extended solar neighbourhood, determining the radial density profile and the vertical surface density based on observational constrains. The derivation of the radial density leads to the determination of the radial scale length, with an immediate check on the selected value for the focal point. The vertical behaviour of the Stäckel potential is not an easy task, because far away from the Galactic plane the vertical force is sensible to the curvilinear coordinate system. After we fix all the free parameters for our model, it will be possible to make predictions on the radial surface density at 1.1 kpc and to compare the results to recent observations.

In Chapter 4 we will study the stellar kinematic properties through the velocity ellipsoid. We will determine the variance and the covariance terms in the meridional plane (R, z) based on RAVE data. Our research focuses on red clump giants, so that we can derive the orientation of the velocity ellipsoid far away from the plane. We will use two methods: a Markov Chain Monte Carlo (MCMC) discrete likelihood fitting developed by Alex Büdenbender at MPIA, Heidelberg (see Büdenbender et al. (2014)) and a method calculating the 'standard' statistical moments using robust statistics. Furthermore, we split the sample of red clump giants in three different metallicity bins and determine the velocity dispersion components and its orientation in the meridional plane for the different subpopulations. This is a way to proof the consistency of our model and to verify the value determined for the focal point.

In Chapter 5 we will discuss a more realistic model of the vertical structure of the Stäckel potential. We will construct a two component model, including the stellar disc and the dark matter halo, in the derivation of the vertical force using the Stäckel potential. At the end of the thesis we will discuss the future work that it is required to construct a realistic dynamical model for the extended solar neighbourhood.

2

Jeans equations

2.1 Velocity ellipsoid

The collisionless Boltzmann equation (Eq. 1.1) describes the kinematics of the stars by linking the phase-space distribution function with the gravitational potential. The velocity ellipsoid is the realization in velocity space of the second order moment of the distribution function. By integrating the first-order CBE over the velocity space, we obtain the Jeans equations which link the gravitational potential through the velocity dispersions σ_{ij}^2. These dispersions are assigned to pressure terms and balance the radial and vertical force.

The distribution of space velocities of the local stars was described in the past with the so-called ellipsoidal distribution. Fitting three Gaussians for the velocity distribution, based on Schwarzschild's classical assumption, generates an ellipsoidal figure in velocity space, because of the analogy of the Gaussian form used for the fit and the equation for an ellipsoid. In general, dropping the assumption that the velocity distribution is Gaussian, the velocity dispersion tensor describes an ellipsoid, which is a measure of the kinetic energy distribution. The velocity dispersion tensor is expressed by a symmetric matrix T_{σ^2} consisting of nine elements:

$$T_{\sigma^2} = \begin{pmatrix} \sigma_R^2 & \sigma_{R\phi}^2 & \sigma_{Rz}^2 \\ \sigma_{R\phi}^2 & \sigma_\phi^2 & \sigma_{\phi z}^2 \\ \sigma_{Rz}^2 & \sigma_{\phi z}^2 & \sigma_z^2 \end{pmatrix} \tag{2.1}$$

It is always possible to diagonalize this symmetric matrix, i.e. to find eigenvectors which are aligned to a specific coordinate system, leaving only the diagonal terms which correspond to the axis of the velocity ellipsoid in the new coordinate system. In the case of axisymmetric systems, the terms $\sigma_{R\phi}^2$ and $\sigma_{\phi z}^2$ should be zero but not the mixed term σ_{Rz}^2, which is crucial in the understanding of the stellar kinematics. However, it has been observed that the axis of the velocity ellipsoid in the plane ($\sigma_{R\phi}^2$) does not point exactly in the direction of the Galactic centre. This is called the 'vertex deviation', which originates from the fact that the Milky Way is not perfectly axisymmetric. The deviation from axisymmetry is around 5-10% (Rix & Bovy 2013), possibly due to the presence of spiral arms and a Galactic bar. This non-axisymmetry results in a deviation of an angle of ~20°. In the present work this is neglected.

In the case of isotropic systems, the distribution function depends only on the energy, which means that the velocities enter in a quadratic way, there is no preferential motion and the three velocity dispersions are equal. If we have a DF describing an axisymmetric system that depends not only on the energy, but also on the vertical component of angular momentum, L_z, the azimuthal velocity dispersion differs from the radial and vertical one. With only two integrals of motion, we still have equality between the radial and vertical velocity dispersion, and the tilt of the velocity ellipsoid cannot be reproduced. This is because only even terms enter in the energy and thus it is impossible to obtain an anisotropic velocity dispersion in the meridional plane in this way. These two results are not observed. The difference between the two velocity dispersions in the meridional plane is of a factor of two (Fuchs et al. 2009). From theoretical expectations (Binney & McMillan 2011) and from observations it has been shown that one of the eigenvectors of the velocity ellipsoid in the meridional plane is pointing approximately to the Galactic centre (Siebert et al. 2008; Carollo et al. 2010; Casetti-Dinescu et al. 2011; Smith et al. 2012; Binney et al. 2014a; Büdenbender et al. 2014). Furthermore the three velocity dispersions are all different from each other. Therefore, we are looking for a DF depending on three integrals of motion, which can reflect the triaxiality and the observed inclination of the velocity ellipsoid. The existence of the third integral does not imply necessarily that the ratio of the vertical to radial velocity dispersions has to be anisotropic. However, if only two integrals of motion exist, the meridional velocity dispersions would have to be isotropic and the orientation of the velocity ellipsoid undetermined because the radial and vertical axis would be equal. The consequence is that the covariance term σ_{Rz} is zero and the radial and vertical motion is decoupled.

2.1.1 Equatorial velocity dispersions

The equatorial velocity ellipsoid can be determined by using the epicycle theory and the rotation curve. 'Equatorial' describes the behaviour of the velocity ellipsoid in the equatorial plane $R\phi$. The ratio between the azimuthal and radial velocity dispersion $(\sigma_\phi^2/\sigma_R^2)$ gives the shape of the velocity ellipsoid in the plane. Considering orbits near the plane, we can determine this ratio using the epicycle approximation and find a dependence on the Oort's parameters A and B only:

$$\frac{\sigma_\phi^2}{\sigma_R^2} = \frac{B}{B-A}$$

It is possible to handle this calculation by writing it in terms of the circular velocity and its derivative:

$$\frac{\sigma_\phi^2}{\sigma_R^2} = \frac{1}{2}\frac{R}{v_c}\left(\frac{dv_c}{dR} - \frac{v_c}{R}\right) + 1$$

If we assume a power-law behaviour for the rotation curve $v_c \propto R^\alpha$:

$$\frac{\sigma_\phi^2}{\sigma_R^2} = \frac{\alpha+1}{2}$$

this ratio depends only on the slope α of the rotation curve. We obtain the value 0.5 for a flat rotation curve ($\alpha \sim 0$), in agreement with other observations (Fuchs et al. 2009; Golubov et al. 2013).

2.1.2 Orientation of the velocity ellipsoid

The orientation of the velocity ellipsoid in the Rz-plane is a crucial point. This term is included in the Jeans equations and is usually eliminated, assuming that the velocity ellipsoid is aligned with the cylindrical coordinate system. This assumption is no longer true and thus we have to take into account the 'tilt' of the velocity ellipsoid. The tilt of the velocity ellipsoid is the orientation of the velocity ellipsoid in the meridional plane, its inclination with respect to the cylindrical coordinate (R, z) forming

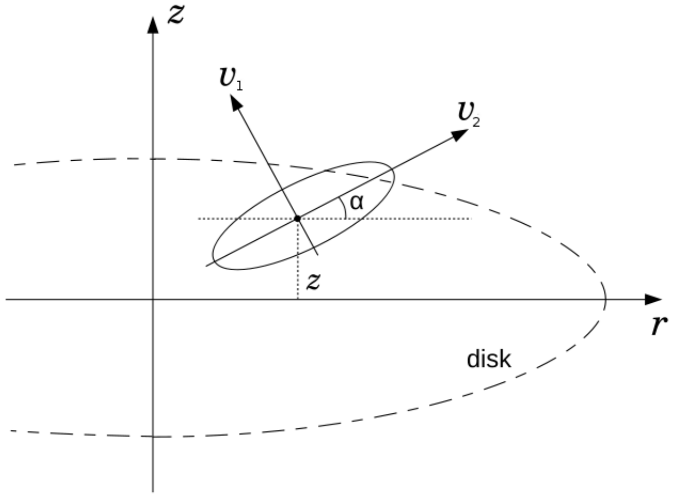

Figure 2.1: Orientation of the velocity ellipsoid with respect to the meridional plane. v_1 and v_2 are the velocities in the new rotated system (Yurin & Springel 2014).

an angle α_{tilt} between the longer axis of the velocity ellipsoid (σ_1) and the plane parallel to the equatorial plane (Fig. 2.1).

From Eq. 2.1 we can find the eigenvalues rotating the matrix of the dispersion tensor:

$$A_{rot} \cdot T_\sigma^2 \cdot A_{rot}^{-1} = \begin{pmatrix} \sigma_1 & 0 & 0 \\ 0 & \sigma_2 & 0 \\ 0 & 0 & \sigma_3 \end{pmatrix}$$

where A_{rot} is the 3D rotation matrix around the unit vector $\hat{e}_\phi$, with the assumption that the mixed terms are zero ($\sigma_{R\phi} = \sigma_{\phi z} = 0$):

$$A_{rot} = \begin{pmatrix} \cos\alpha & 0 & -\sin\alpha \\ 0 & 1 & 0 \\ \sin\alpha & 0 & \cos\alpha \end{pmatrix}$$

where α is the tilt angle. Applying a rotation in front of the velocity dispersion matrix and an inverse matrix after it (A_{rot}^{-1}), it is possible to diagonalize the matrix:

$$A_{rot} \cdot T_\sigma^2 \cdot A_{rot}^{-1} = \begin{pmatrix} \cos\alpha & 0 & \sin\alpha \\ 0 & 1 & 0 \\ -\sin\alpha & 0 & \cos\alpha \end{pmatrix} \begin{pmatrix} \sigma_R^2 & 0 & \sigma_{Rz}^2 \\ 0 & \sigma_\phi^2 & 0 \\ \sigma_{Rz}^2 & 0 & \sigma_z^2 \end{pmatrix} \begin{pmatrix} \cos\alpha & 0 & -\sin\alpha \\ 0 & 1 & 0 \\ \sin\alpha & 0 & \cos\alpha \end{pmatrix}$$

The eigenvalues, which are the new velocity dispersion terms in the new rotated system, read:

$$\sigma_1 = (\sigma_R^2 \cos^2\alpha + \sigma_{Rz}^2 \sin\alpha\cos\alpha + \sigma_{Rz}^2 \sin\alpha\cos\alpha + \sigma_z^2 \sin^2\alpha)$$

$$\sigma_3 = (\sigma_R^2 \sin^2\alpha - \sigma_{Rz}^2 \sin\alpha\cos\alpha - \sigma_{Rz}^2 \sin\alpha\cos\alpha + \sigma_z^2 \cos^2\alpha)$$

These are the velocity dispersions in a reference system rotated through an angle $-\alpha$ with respect to the cylindrical coordinates. The mixed term:

$$\sigma_{13} = (-\sigma_R^2 \cos\alpha\sin\alpha - \sigma_{Rz}^2 \sin^2\alpha + \sigma_{Rz}^2 \cos^2\alpha + \sigma_z^2 \sin\alpha\cos\alpha) = 0$$

will be zero because of the matrix diagonalization, under the condition that the tilt angle is linked to the velocity dispersion terms in the following way (Binney & Merrifield 1998):

$$\tan(2\alpha) = \frac{2\sigma_{Rz}^2}{\sigma_R^2 - \sigma_z^2} \tag{2.2}$$

The covariant term $\sigma_{Rz}^2 = \overline{v_R v_z} - \overline{v_R} \cdot \overline{v_z}$ represents the coupling between the radial and the vertical motion. If σ_{Rz}^2 was zero, the tilt angle would also be zero and the velocity ellipsoid would be aligned with the cylindrical coordinate system. Hence we expect that σ_{Rz}^2 and the tilt angle are negative ($\alpha_{tilt} < 0$) at $z > 0$.

2.2 Jeans equations for axisymmetric system

We use cylindrical coordinates (R, ϕ, z) for the Galaxy assuming that it is a steady-state and axisymmetric equilibrium system. With these assumptions we can eliminate derivatives with respect to the time t and azimuthal component ϕ and derive the CBE for axisymmetric systems (Amendt & Cuddeford 1991):

$$v_R \frac{\partial f}{\partial R} + v_z \frac{\partial f}{\partial z} - \left(\frac{\partial \Phi}{\partial R} - \frac{v_\phi^2}{R} \right) \frac{\partial f}{\partial v_R} - \frac{v_R v_\phi}{R} \frac{\partial f}{\partial v_\phi} - \frac{\partial \Phi}{\partial z} \frac{\partial f}{\partial v_z} = 0$$

Multiplying this equation by v_R and integrating over the velocities, we obtain:

$$\frac{\partial(\nu \overline{v_R^2})}{\partial R} + \frac{\partial(\nu \overline{v_R v_z})}{\partial z} + \nu \left(\frac{\overline{v_R^2} - \overline{v_\phi^2}}{R} \right) + \nu \frac{\partial \Phi}{\partial R} = 0 \tag{2.3}$$

Multiplying by v_ϕ and v_z leads to the other equations:

$$\frac{\partial(\nu \overline{v_R v_\phi})}{\partial R} + \frac{\partial(\nu \overline{v_\phi v_z})}{\partial z} + 2\nu \left(\frac{\overline{v_R v_\phi}}{R} \right) = 0 \tag{2.4}$$

$$\frac{\partial(\nu \overline{v_R v_z})}{\partial R} + \frac{\partial(\nu \overline{v_z^2})}{\partial z} + \nu \left(\frac{\overline{v_R v_z}}{R} \right) + \nu \frac{\partial \Phi}{\partial z} = 0 \tag{2.5}$$

These three equations are called the Jeans equations. We have in general ten unknowns – namely the density, the three velocities and the six velocity dispersion terms – for only four equations – three Jeans equations and the continuity equation. One idea would be to go to higher orders, multiplying the CBE by $v_i v_j$ and then integrating over the velocity space. In this way we could have more equations, but we could also obtain more unknowns. The higher the order we go to, the bigger will be the difference between unknowns and equations. This is the so-called *closure problem*. The study at higher order was pursued by Cuddeford in his PhD thesis. He assumed that the disc is 'cool' because the random motions are much smaller than the rotation speed and proceeded to expand all the kinematic quantities in terms of a small parameter represented by the ratio between the random motion and rotation velocity. He took into account only terms in leading order and assumed that the velocity distribution is quasi-isothermal. Finally he came to describe the derivative of the covariant term in the plane:

$$\frac{\partial \sigma_{Rz}^2}{\partial z}(R, 0) = \eta(R) \left(\frac{\sigma_R^2 - \sigma_z^2}{R} \right)(R, 0)$$

with

$$\eta(R, 0) = \left(\frac{R^2 \partial_{Rzz}^3 \Phi}{3\partial_R \Phi + R\partial_{RR}^2 \Phi - 4R\partial_{zz}^2 \Phi} \right)(R, z = 0)$$

where ∂_R, ∂^2_{RR}, ∂^2_{zz}, ∂^3_{Rzz} are the first, second and third derivative applied to the potential Φ. The parameter $\eta(R)$ assumes a value between 0, for an ellipsoid aligned with the cylindrical coordinate system, and 1 for an alignment with the spherical coordinates. Cuddeford came to close the problem and found a correlation between the tilt of the velocity ellipsoid and the gravitational potential calculated in the plane. This correlates intrinsically with the third integral of motion. Knowing the potential Φ, we could derive its derivatives and calculate the values in the plane, find the orientation for the velocity ellipsoid and constrain the third integral of motion. Cuddeford also showed that this relation is exact in the case of Stäckel potentials (Amendt & Cuddeford 1991). This is the only known analytic expression which links the gravitational potential and the tilt of the velocity ellipsoid, but the problem caused by going to higher orders is that we cannot compare the results with observables.

In the past, scientists tended to avoid going to higher orders. They usually used the Jeans equations imposing some assumptions and relations between the velocity dispersions. The azimuthal Jeans equation (Eq. 2.4) does not give information on the kinematics. Interesting to study are the radial Jeans equation (Eq. 2.3), which gives information about the asymmetric drift, and the vertical Jeans equation (Eq. 2.5), which – in turn – results in the equation of the vertical gravitational force. The tilt of the velocity ellipsoid enters in both relations and we seek to quantify the impact that this term has on the equations.

2.2.1 Asymmetric Drift

The asymmetric drift is defined as the difference between the circular speed and the mean rotational velocity. The circular speed at the solar radius is called the Local Standard of Rest (LSR). Its determination corresponds to measuring the peculiar motion ($U_\odot, V_\odot, W_\odot$), where $U_\odot$ is the velocity of the Sun in the direction of the Galactic centre, $V_\odot$ along the Galactic rotation and $W_\odot$ perpendicular to the plane.

The standard method to derive the asymmetric drift is based on the radial Jeans equation applied by Dehnen & Binney (1998) to the Hipparcos data. They found that the asymmetric drift depends linearly on the square of the radial velocity dispersion; a linear extrapolation to zero velocity dispersion led to the estimation of the LSR. They found that the velocity of the Sun with respect to the Local Standard of Rest is $S_\odot = (10.0; 5.2; 7.17)$ km/s. The most complicated measurement is $V_\odot$ because it requires a correction for the asymmetric drift. These values held true for a long time and were confirmed by Aumer & Binney (2009), where a similar approach was used resulting in the same value for $V_\odot$ but with a smaller error. In contrast, Schönrich et al. (2010) applied a non-linear fit to the Hipparcos data and compared it with the predictions of their chemodynamical model of the Galaxy. The result was a slight update of the values for $U_\odot$ and $W_\odot$ but a significant increase in the value for the velocity along the Galactic rotation: $V_\odot = 12.24$ km/s. Two recent studies favour the increase of the old value of $V_\odot$ of $\sim$6 km/s. Binney (2010) constructed a dynamical model using distribution functions and found satisfactory fits using this new value. The second study dealt with observations of maser sources in star formation regions (Reid et al. 2009). Bovy et al. (2012b) found a value still larger for the asymmetric drift based on APOGEE data ($V_\odot = 24$ km/s).

The disagreement between these results put this value into question and Golubov et al. (2013) derived again the asymmetric drift relation from the Jeans equation. They derived the asymmetric drift for three different metallicities, including a radial alignment of the velocity ellipsoid ($\eta = 1$). The result is linearly dependent on the square of the radial velocity dispersion, as in Dehnen & Binney (1998). Golubov et al. (2013) extrapolated linearly the three asymmetric drift relations to zero radial velocity dispersion leading to the value for $V_\odot = (3.06 \pm 0.68)$ km/s. They found a value even smaller than the old value of Dehnen & Binney (1998).

For the derivation of the asymmetric drift relation we have to start from Eq. 2.3 and consider the case near the plane ($z \sim 0$). One assumption is that the vertical density is approximately constant next to the plane ($\partial \nu/\partial z = 0$). Then we replace $\overline{v_\phi^2}$ with the azimuthal velocity dispersion using $\sigma_\phi^2 = \overline{v_\phi^2} - \overline{v_\phi}^2$ and $\overline{v_R^2}$ with σ_R^2, where $\overline{v_R} = 0$ because of the axisymmetry. Remembering that the circular velocity is given by equating the centripetal force and the gravitational force ($R\partial\Phi/\partial R = v_c^2$) we obtain:

$$v_a = \frac{\sigma_R^2}{2v_c}\left[\frac{\sigma_\phi^2}{\sigma_R^2} - 1 - \frac{R}{\nu\sigma_R^2}\frac{\partial}{\partial R}(\nu\sigma_R^2) - \frac{R}{\sigma_R^2}\frac{\partial}{\partial z}(\overline{v_R v_z})\right]$$

The terms in parenthesis depend on the shape of the velocity ellipsoid in the equatorial plane, the radial gradient term including density and radial velocity dispersion and the variation of the tilt of the velocity ellipsoid. Following the work of Golubov et al. (2013) and holding the same definitions, we can parametrize the radial gradient term by the local radial scale length R_E as $R_E^{-1} = -\partial \ln(\nu\sigma_R^2)/\partial R$. This term is a composition of the radial scale length R_d of the tracer density ν and the radial scale length R_σ of the radial velocity dispersion σ_R^2 related by $R_E^{-1} = R_d^{-1} + R_\sigma^{-1}$.

The inclination of the velocity ellipsoid is usually unknown but we can write it as (Amendt & Cuddeford 1991; Binney & Tremaine 2008):

$$\sigma_{Rz}^2 = \eta\frac{z}{R}(\sigma_R^2 - \sigma_z^2) \tag{2.6}$$

where η is a value between 0 and 1. $\eta = 0$ means that the velocity ellipsoid is aligned with the cylindrical coordinate system whereas $\eta = 1$ means an alignment with the spherical coordinates. The final expression for the asymmetric drift reads:

$$v_a = \frac{\sigma_R^2}{2v_c}\left[\frac{\sigma_\phi^2}{\sigma_R^2} - 1 + \frac{R_0}{R_E} - \eta\left(1 - \frac{\sigma_z^2}{\sigma_R^2}\right)\right]$$

We assume a shape for the velocity ellipsoid where the ratio between the azimuthal and radial velocity dispersion is 0.5, the value of the circular velocity is 220 km/s, and the radial scale length for the density and the velocity dispersion are the same ($R_d = R_\sigma$). The last condition leads to a constant thickness for the disc where the tilt angle is zero. The terms in parenthesis result in a number and then the dependence of the asymmetric drift is linear with σ_R^2. We consider both the cases, when the velocity ellipsoid is oriented with the cylindrical and spherical coordinate system and they are plotted in (Fig. 2.2). All possible orientations in between are constrained by these two lines and the value assumed for the LSR is $V_\odot = 3.06$ km/s (Golubov et al. 2013). If we assume a larger value for R_σ, as observed by Bovy & Tremaine (2012), the asymmetric drift decreases. The same result occurs if the radial scale length of the density R_d increases. The more inclined the velocity ellipsoid is with respect to the midplane, the lower the value for the asymmetric drift results.

Uncertainties in the asymmetric drift calculation are the tilt of the velocity ellipsoid, where many observations are converging now to the result of an alignment with the spherical coordinate system, and the scale length for the density and velocity dispersion which can be summarized in the parameter R_E. If we take into account an error of 10% in the determination of the scale length for the density R_d and the velocity dispersion R_σ, we see that we can no longer recognize which slope of the asymmetric drift relation is related to which inclination of the velocity ellipsoid (Fig. 2.3). The term R_0/R_E dominates the asymmetric drift and the parameter η cannot be measured from this relation. If we wish to identify the tilt of the velocity ellipsoid from the asymmetric drift relation we need a value for the scale length with an error smaller than 10%.

2.2.2 Vertical force

There are two methods for deriving the vertical force: using the distribution function or the vertical Jeans equation. The first method assumes that the distribution function is of the form:

$$f(R, z, v_R, v_\phi, v_z) = f(R, v_R, v_\phi) \times f(z, v_z)$$

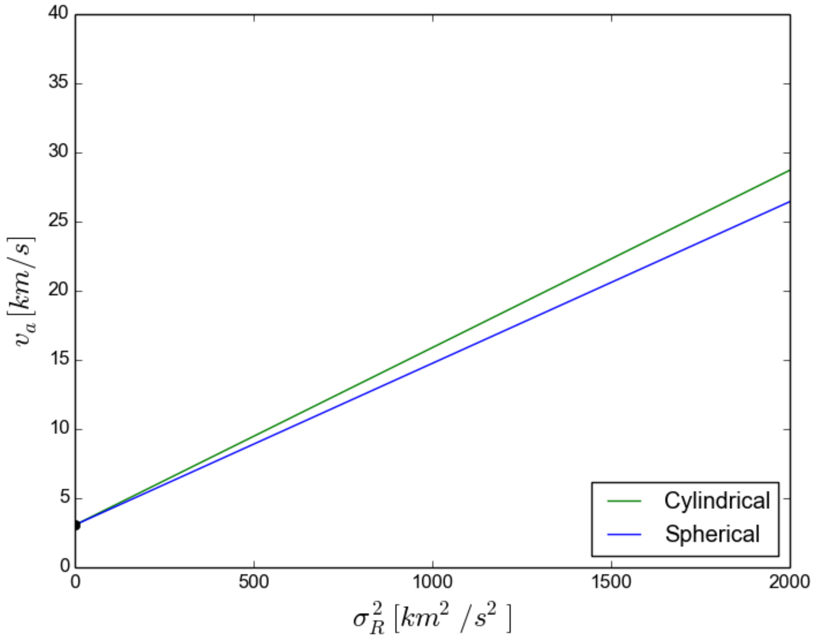

Figure 2.2: Asymmetric drift relation assuming that the orientation of the velocity ellipsoid is aligned with the cylindrical ($\eta = 0$) and the spherical ($\eta = 1$) coordinate system.

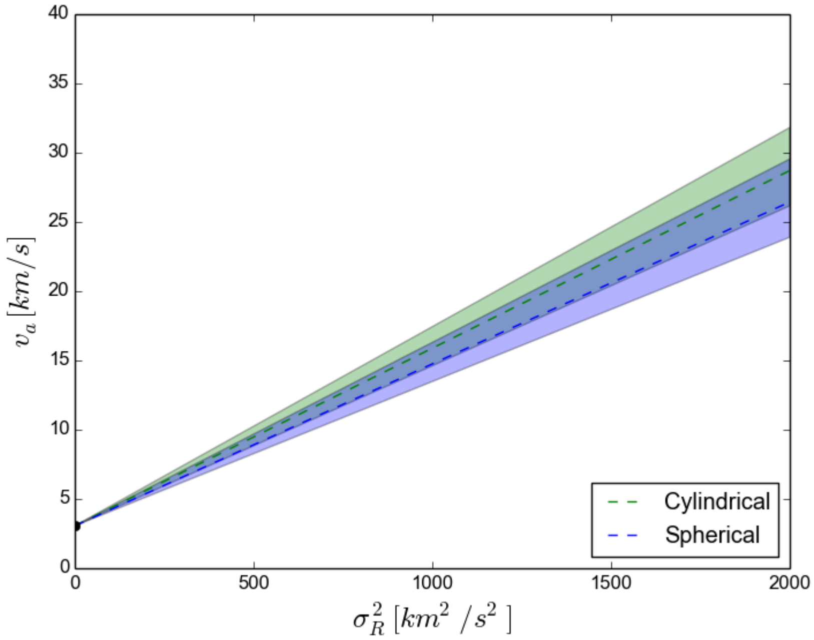

Figure 2.3: Asymmetric drift relation assuming that the orientation of the velocity ellipsoid is aligned with the cylindrical ($\eta = 0$) and the spherical ($\eta = 1$) coordinate system, assuming a 10% error in the estimation of the radial scale length of the density and velocity dispersion.

Thus, it separates the planar distribution function from the vertical one. In this way we consider the one-dimensional motion with z without any radial dependence. From separability in the distribution function there follows a separability in the radial and vertical motion,

$$\Phi(R, z) = \Phi(R) + \Phi(z)$$

but not vice versa. If the motion is separable, but the distribution function is not, one can still derive the vertical Jeans equation without the tilt term (Statler 1989).

Holmberg & Flynn (2000, 2004) integrated the vertical distribution function

$$\nu(z) = \int_{-\infty}^{\infty} f(z, v_z) dv_z$$

In this way it is possible to predict the behaviour of the vertical density of the tracers. The advantage of this method is that we assume the whole phase-space information, but if the assumption about the separability of the distribution function is wrong, the result is biased.

Kuijken & Gilmore (1989) used the same method but worked in a different way. Since the vertical density of the tracers $\nu(z)$ is known better than the distribution function, they inverted the integral applying the Abel transformation:

$$f_z(E_z) = \frac{1}{\pi} \int_{E_z}^{\infty} \frac{-d\nu/d\Phi}{\sqrt{2(\Phi - E_z)}} d\Phi$$

so there is a unique relation between the vertical density and the distribution function: $f_z(E_z)$ depends on the density only at points where the gravitational potential exceeds the vertical energy ($\Phi > E_z$). This means that we can estimate the gravitational force from data at large distances only. On the other hand, it is possible to find high-energy stars at all heights, and estimations of the gravitational potential at low z require the knowledge of the tail of the distribution function. Therefore, to measure the gravitational potential we need to know either the high energy tail of the distribution function at low z, or the density and gravitational potential at high z. We know only the density from observation and Kuijken & Gilmore (1989) gave an ansatz for the gravitational potential:

$$\Phi(z) = K(\sqrt{z^2 + D^2} - D) + Fz^2 \tag{2.7}$$

where D is the scale height, K is the total disc surface density and F is proportional to the dark matter density. The total density is due to the disc at low z, whereas at large height the contribution of the halo becomes dominant. The surface density increases linearly due to the contribution of the disc component. When the vertical density $\rho(z)$ falls, the surface density $\Sigma(z)$ tends to flatten to an height where there is no further contribution from the luminous component. At larger heights the surface density continues to increase linearly, but with a different slope due to the contribution of the dark matter component (Kuijken & Gilmore 1989), as we can see in Fig. 2.4.

The second method considers the vertical Jeans equation:

$$\frac{1}{R}\frac{\partial}{\partial R}(R\nu\sigma_{Rz}^2) + \frac{\partial}{\partial z}(\nu\sigma_z^2) + \nu\frac{\partial\Phi}{\partial z} = 0 \tag{2.8}$$

The advantage in this method is that we do not have to use the distribution function, but in this way we throw away information. Usually it is assumed that the velocity ellipsoid is parallel to the cylindrical coordinates and the Jeans equation is reduced to that for a one dimensional slab. However, we know that the velocity ellipsoid is approximately oriented with the spherical coordinates. It has been shown that this term is small, approximately 1% of the second term when the vertical scale height is much smaller than the radial scale height (Binney & Tremaine 2008; Garbari et al. 2011, 2012; Zhang et al. 2013).

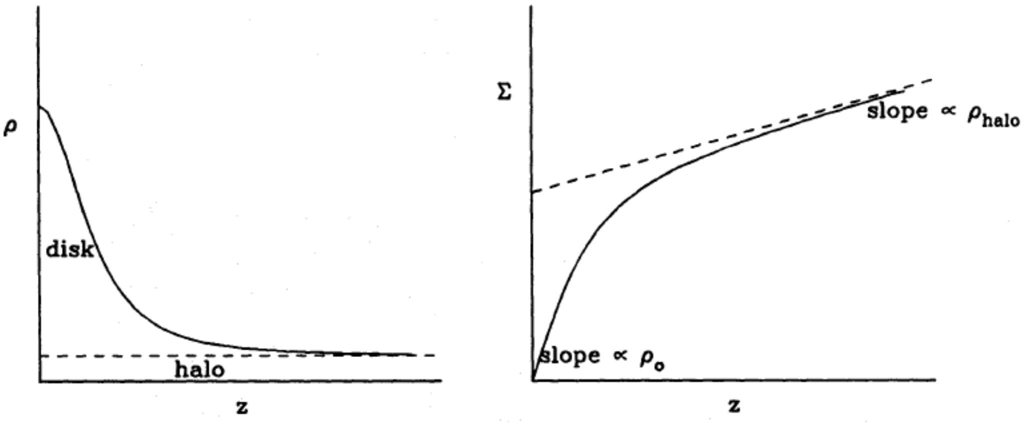

Figure 2.4: Representation of the total volume density and surface density as a function of z (Kuijken & Gilmore 1989).

The Jeans equation links the gravitational potential with the density and the velocity dispersion of the tracers. If we want to consider the relation between the potential and the total density we require the Poisson equation:

$$\frac{\nabla^2\Phi}{4\pi G} = \rho_{tot} = \rho_s + \rho_{dm}$$

where ρ_s and ρ_{dm} are the luminous and dark matter density, respectively. We can assume a vertical exponential density profile for the tracers and a constant density for the dark matter:

$$\rho_{tot} = \rho_0 \exp(-|z|/z_0) + \rho_{dm}$$

z_0 is the scale height, ρ_0 and ρ_{dm} are the local density for the tracers and the dark matter. The dark matter density can be assumed to be constant over the range of z, if the disc scale height is much smaller than the dark matter halo scale length (Garbari et al. 2011, 2012; Zhang et al. 2013). By integrating the density over z, it is possible to obtain the vertical surface density which expresses a measure for the vertical force:

$$\Sigma(z) = \frac{|K_z|}{2\pi G} = \Sigma_0(1 - \exp(-|z|/z_0)) + 2\rho_{dm}z$$

where $\Sigma_0 = 2\rho_0 z_0$ is the luminous dynamical surface density of the disc at infinite, which is approximately $\Sigma(1.1\ \text{kpc})$. Knowing Σ_0 and ρ_0 it is possible to calculate directly the scale height of the disc. Another assumption that was made for this result is that the rotation curve is approximately constant, so that the radial contribution resulting from the Poisson equation due to the Oort's parameter can be neglected. We use the values of Holmberg & Flynn (2004) for the vertical surface density, $\Sigma_0 = (56 \pm 6)$ $M_\odot/pc^2$ for the baryons and (76 ± 6) $M_\odot/pc^2$ including also the contribution of the dark matter, with a value for the scale height of 300 pc and local dark matter density ~10% ($\rho_{0,dm} = 0.008$ $M_\odot/pc^2$) of the total volume density.

This force could be measured by an application of the 'no-tilt' Jeans equation. We now want to calculate the impact of the orientation of the velocity ellipsoid on the vertical force, considering the extra force term in the vertical Jeans equation (Eq. 2.8):

$$\Sigma_{tilt} = \frac{|K_{z,tilt}|}{2\pi G} = -\frac{1}{R\nu}\frac{\partial}{\partial R}(R\nu\sigma^2_{Rz})$$

where we call its contribution to the vertical force $K_{z,tilt}$, and the corresponding vertical surface density Σ_{tilt}. It was always assumed that this term either is zero because the velocity ellipsoid is oriented with the cylindrical coordinate system or it is small. However, it was previously claimed that the uncertainty in the tilt is the largest source of errors in the vertical Jeans equation and leads to a 10-20% variation in the estimate of the mass density (Kuijken & Gilmore 1989; Kent & de Zeeuw 1991), and for this reason we want to estimate this value.

We assume that the radial density of the tracers is exponentially declining with radial scale length R_d ($\nu \propto \exp(-R/R_d)$), the radial and vertical velocity dispersions are also exponentially declining with the radius but with radial scale length R_σ ($\sigma_R^2 \propto \sigma_z^2 \propto \exp(-R/R_\sigma)$), and the covariant term of the velocity ellipsoid is given by Eq. 2.6. The result is:

$$\Sigma_{tilt} = \frac{1}{2\pi G}\eta\frac{z}{R}(\sigma_R^2 - \sigma_z^2)\left(\frac{1}{R_d} + \frac{2}{R_\sigma}\right)$$

We can rewrite the same expression, assuming that $\gamma = \sigma_R/\sigma_z$ gives the anisotropy of the velocity dispersion in the meridional plane, as:

$$\Sigma_{tilt} = \frac{1}{2\pi G}\eta\frac{z}{R}\sigma_z^2(\gamma^2 - 1)\left(\frac{1}{R_d} + \frac{2}{R_\sigma}\right)$$

We assume that the radial velocity dispersion is twice the vertical one locally ($\gamma = 2$). We take the same value for the radial scale length for the density and the velocity dispersion $R_d = R_\sigma = 2.6$ kpc, constraint required for a constant disc thickness in the case of $\eta = 0$. This could however not be true for a different orientation of the velocity ellipsoid. In Fig. 2.5 the vertical force is plotted, in the case of a velocity ellipsoid parallel to the midplane ($\eta = 0$) and with an orientation parallel to the spherical coordinates ($\eta = 1$). All the possible orientations of the velocity ellipsoid between an orientation with the cylindrical and spherical coordinate are constrained to be between these two lines. The contribution of the tilt of the velocity ellipsoid increases the vertical force K_z. Hence if K_z increases, the volume density has to increase as well, independent of the disc thickness. The contribution given by the tilt of the velocity ellipsoid to the gravitational force is indeed small (~4%) at 1.1 kpc and up to 3 kpc above the plane it is always less than 10%. If we take a larger radial scale length for the velocity dispersion ($R_\sigma = 3.5$ as in Bovy & Tremaine (2012)), $\Sigma(z)$ becomes smaller. In general, increasing either the radial scale length R_d, R_σ or the vertical scale height z_0 will reduce slightly the contribution of $\Sigma(z)$. If the anisotropy of the meridional velocity dispersion (γ) becomes smaller, the $\Sigma(z)$ term decreases and when it approaches $\gamma = 1$, Σ_{tilt} tends to zero and the vertical force is the same as in the case of being oriented with the cylindrical coordinates. The explanation is that the radial and vertical axis of the velocity dispersion are equal and we can no longer recognize the orientation of the velocity ellipsoid because it has become a circle in the meridional plane. Taking into account errors of 10% in the radial scale lengths R_d, R_σ, vertical scale height z_0 and in the estimation of the local dark matter density ρ_{dm}, the result changes slightly (~3%). The case of an uncertainty of 100% in the determination of the local dark matter density is shown in Fig. 2.6. With this large uncertainty we can neither proof nor discard the presence of the dark matter. The range of the local dark matter density values extend from zero up to twice the most probable value.

2.2.3 Isopotential lines

We know from the Jeans equations that the velocity ellipsoid is related to the gravitational potential. Smith et al. (2009), studying halo stars, found that the velocity ellipsoid is aligned with the spherical coordinate system and implied that the gravitational potential of the halo is spherical. It has been observed approximately the same tilt angle for disc stars but the potential near the disc is flattened. We want to understand the relation between the velocity ellipsoid and gravitational potential, if one of the eigenvectors of the velocity ellipsoid in the meridional plane is aligned with the gravitational force vector, i.e. perpendicular to the isopotential lines of the gravitational potential.

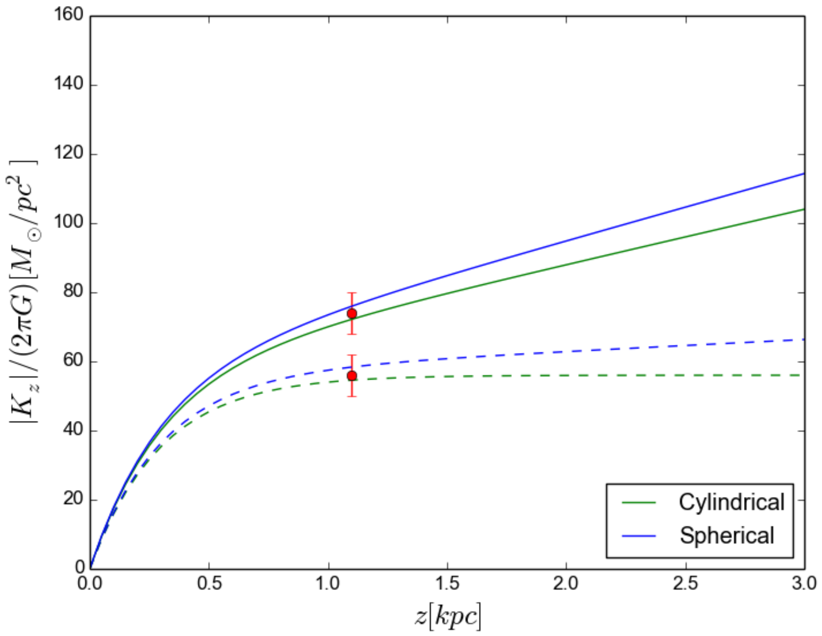

Figure 2.5: Vertical surface density assuming $\Sigma_0 = (56 \pm 6)\ \mathrm{M}_\odot/\mathrm{pc}^2$ for the luminous and $(76 \pm 6)\ \mathrm{M}_\odot/\mathrm{pc}^2$ including the dark matter found by Holmberg & Flynn (2004) with a scale height of 300 pc. Overplotted is the contribution given by the tilt of the velocity ellipsoid, which increases the value of the vertical surface density.

The velocity ellipsoid is oriented with the cylindrical coordinates in the plane, but its behaviour can be different at different heights above the plane. We want to derive its dependence as to the vertical coordinate z. First, we have to transform $\tan(2\alpha)$ to the tangent of the simple tilt angle α:

$$s = \tan(2\alpha) = \frac{2\tan(\alpha)}{1 - \tan^2(\alpha)}$$

$$\tan\alpha = \frac{s}{1 + \sqrt{1 + s^2}}$$

We calculate its z-derivative and use the subscript 0 for the value in the plane ($z = 0$):

$$\left[\frac{\partial \tan\alpha}{\partial z}\right]_0 = \frac{\partial}{\partial z}\left[\frac{s}{1 + \sqrt{1 + s^2}}\right]_0 = \frac{1}{2}\left[\frac{\partial s}{\partial z}\right]_0$$

where $s(z = 0) = s_0 = 0$ and

$$\left[\frac{\partial s}{\partial z}\right]_0 = \left[\frac{\partial}{\partial z}\frac{2\sigma_{Rz}^2}{\sigma_R^2 - \sigma_z^2}\right]_0 = \frac{2}{\sigma_R^2 - \sigma_z^2}\left[\frac{\partial \sigma_{Rz}^2}{\partial z}\right]_0$$

assuming that σ_R and σ_z are constant with height (Bovy et al. 2012a; Büdenbender et al. 2014). Then the vertical gradient of the angle between the two eigenvectors of the velocity ellipsoid in the meridional plane is related to the vertical gradient of the mixed term of the velocity dispersion matrix (σ_{Rz}^2):

$$\left[\frac{\partial \tan\alpha}{\partial z}\right]_0 = \frac{1}{\sigma_R^2 - \sigma_z^2} \cdot \left[\frac{\partial \sigma_{Rz}^2}{\partial z}\right]_0$$

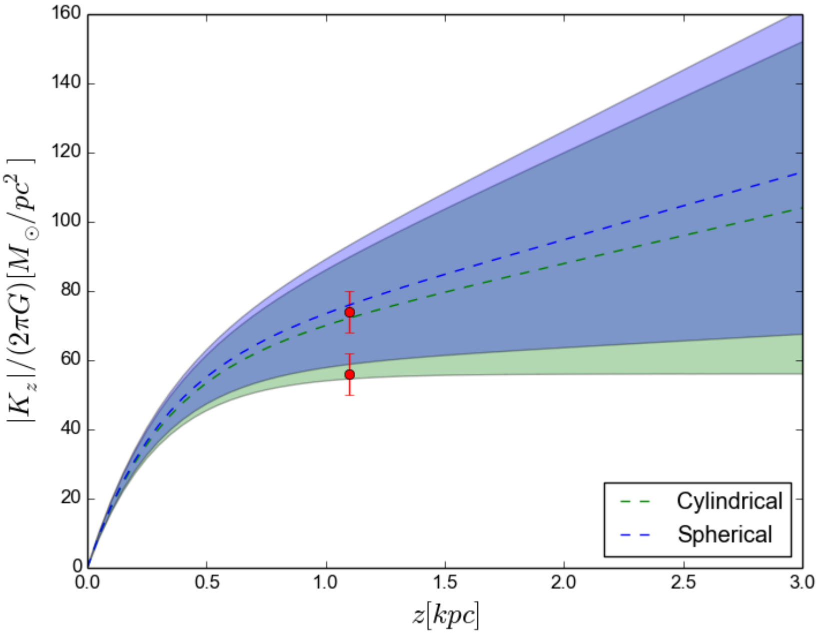

Figure 2.6: Vertical surface density assuming $\Sigma_0 = (56 \pm 6)$ $\mathrm{M}_\odot/\mathrm{pc}^2$ for the baryons and (76 ± 6) $\mathrm{M}_\odot/\mathrm{pc}^2$ including the dark matter found by Holmberg & Flynn (2004) with a scale height of 300 pc. Overplotted is the contribution given by the tilt of the velocity ellipsoid, which increases the value of the vertical surface density. The shadow regions correspond to assuming 100% error in the estimation of the local dark matter density ρ_{dm}.

From the expression for the covariance term σ^2_{Rz} (Eq. 2.6):

$$\left[\frac{\partial \tan\alpha}{\partial z}\right]_0 = \frac{\eta}{R}$$

The velocity ellipsoid is oriented with the cylindrical coordinate system in the plane and the z-derivative of the tilt angle can vary from zero (parallel to the cylindrical coordinate system) to $1/R$, i.e. pointing towards the Galactic centre.

We want to compare the tilt angle α with the angle formed by the gravitational force lines, which we call β. This angle β is given by the ratio between the vertical force and the radial force component (see Fig. 2.7):

$$\tan\beta = \frac{\partial\Phi/\partial z}{\partial\Phi/\partial R}$$

and we determine it using the radial and vertical Jeans equations:

$$\frac{\partial\Phi}{\partial R} = -\frac{1}{\nu}\frac{\partial}{\partial R}(\nu\sigma^2_R) - \frac{1}{\nu}\frac{\partial}{\partial z}(\nu\sigma^2_{Rz}) - \left(\frac{\sigma^2_R - \overline{v^2_\phi}}{R}\right) \tag{2.9}$$

$$\frac{\partial\Phi}{\partial z} = -\frac{1}{\nu}\frac{\partial}{\partial z}(\nu\sigma^2_z) - \frac{1}{\nu}\frac{\partial}{\partial R}(\nu\sigma^2_{Rz}) - \left(\frac{\sigma^2_{Rz}}{R}\right) \tag{2.10}$$

From the assumptions that the vertical dispersion σ_z is isothermal with z, the vertical density is constant close to the plane, and that the tilt of the velocity ellipsoid is zero in the midplane ($\sigma^2_{Rz} = 0$), we obtain

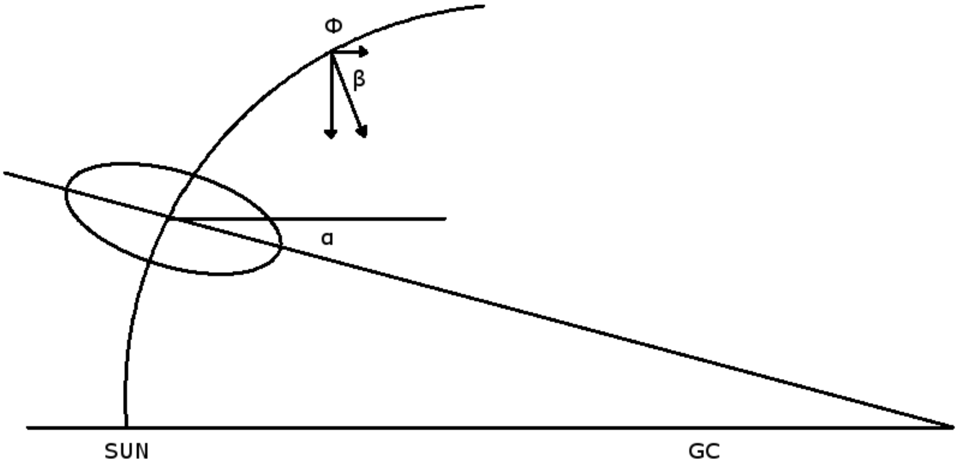

Figure 2.7: The sketch shows the angle α corresponding to the inclination of the velocity ellipsoid with respect to the Galactic plane and the angle β corresponding to the angle between the vertical and radial force components.

that the vertical force is zero at $z = 0$:

$$\left[\frac{\partial\Phi}{\partial z}\right]_0 = 0$$

and consequently that also the angle β is zero. Therefore, the two angles are the same and equal zero in the plane ($\tan\alpha|_0 = \tan\beta|_0 = 0$). Now we want to compare their variation above the plane.

The z-derivative for the angle β is:

$$\frac{\partial}{\partial z}\tan\beta = \frac{\partial}{\partial z}\left[\frac{\partial\Phi/\partial z}{\partial\Phi/\partial R}\right] = \frac{\partial^2\Phi/\partial z^2}{\partial\Phi/\partial R} - \frac{(\partial^2\Phi/\partial z\partial R)\partial\Phi/\partial z}{(\partial\Phi/\partial R)^2} \tag{2.11}$$

Looking in the midplane the second term disappears because the vertical force is zero in the plane. Assuming that the gravitational potential does not depend on the coordinate ϕ, the total Laplacian in cylindrical coordinates reads:

$$\nabla^2\Phi = \frac{1}{R}\frac{\partial}{\partial R}\left(R\frac{\partial\Phi}{\partial R}\right) + \frac{\partial^2\Phi}{\partial z^2} = 4\pi G\rho \tag{2.12}$$

We can write the radial term in terms of the Oort's parameters as:

$$\nabla^2\Phi(z = 0) = -2(A - B)(A + B) + \left(\frac{\partial^2\Phi}{\partial z^2}\right)_0$$

where the term $(A-B)$ corresponds to the angular velocity and the term $(A+B)$ is the slope of the rotation curve, which is small for a flat rotation curve.

$$\nabla^2\Phi(z = 0) = 2\frac{v_c}{R}\frac{dv_c}{dR} + \left(\frac{\partial^2\Phi}{\partial z^2}\right)_0 = 4\pi G\rho_0$$

The second term is dominant compared to the first one. This implies that the vertical variation of the potential at a given radius R depends only on the density distribution at that radius (Binney & Tremaine 2008):

$$\left(\frac{\partial^2\Phi}{\partial z^2}\right)_0 = 4\pi G\rho_0 \tag{2.13}$$

The z-derivative of the tangent of β then reads:

$$\left[\frac{\partial}{\partial z}\frac{\partial\Phi/\partial z}{\partial\Phi/\partial R}\right]_0 = \frac{4\pi G\rho_0 R}{v_c^2} = \frac{1}{R}\frac{4\pi G\rho_0}{\Omega^2} \tag{2.14}$$

where Ω is the angular velocity. In the axisymmetric case the local density is proportional to the square of the local vertical oscillation frequency, which is derived from the density and dominant compared to the radial part:

$$\rho_0 = \frac{v_{z,0}^2}{4\pi G}$$

Holmberg & Flynn (2000) derived an estimate of the local dynamical mass density of (0.102 ± 0.010) $M_\odot/pc^3$, which may be compared with an estimate of 0.095 $M_\odot/pc^3$ in visible disc matter. The value corresponding to the vertical oscillation frequency is 76 km/s/kpc. By introducing a typical value for the angular velocity $\Omega_0 = 27.5$ km/s/kpc in the solar neighbourhood ($R = R_0$):

$$\left(\frac{\partial\tan\beta}{\partial z}\right)_0 = \frac{1}{R_0}\left(\frac{v_{z,0}}{\Omega_0}\right)^2 = \frac{7.6}{R}$$

we can see that the two angles are different by a factor ~8:

$$\left(\frac{\partial\tan\alpha}{\partial z}\right)_0 \neq \left(\frac{\partial\tan\beta}{\partial z}\right)_0$$

The longer axis of the velocity ellipsoid is not aligned with the gravitational force vector because the potential is flattened. If the gravitational potential were spherical, these two angles would be the same, however this would be a special case. From the velocity ellipsoid we can guess some information about the gravitational potential, but we cannot understand its nature directly.

Error determination in $\partial\tan\beta/\partial z$

We can take into account errors in the last calculation, assuming ~20% error in the values for the local density and 10% for the solar position and the circular speed:

$$\rho_0 = (0.102 \pm 0.2) M_\odot/pc^3$$

$$R = (8 \pm 0.5)\cdot 10^3 pc$$

$$v_c = (220 \pm 20) km/s$$

From error propagation theory:

$$\Delta x = \sqrt{\left(\frac{\partial x}{\partial\rho_0}\right)^2 (\Delta\rho_0)^2 + \left(\frac{\partial x}{\partial R}\right)^2 (\Delta R)^2 + \left(\frac{\partial x}{\partial v_c}\right)^2 (\Delta v_c)^2}$$

where $x = \partial\tan\beta/\partial z = \rho_0 R/v_c^2$. Then:

$$\frac{\Delta x}{x} = \sqrt{\left(\frac{\Delta\rho_0}{\rho_0}\right)^2 + \left(\frac{\Delta R}{R}\right)^2 + 4\left(\frac{\Delta v_c}{v_c}\right)^2} = 0.28$$

Assuming 20% errors for the local density and 10% for the solar position and circular speed, the error in determination of $\partial \tan\beta/\partial z$ is approximately 30%:

$$R_0 \partial_z \tan\beta|_0 = 7.6 \pm 2.2|_{6.4}^{9.8}$$

This means that the two angles cannot be equal and we cannot infer the shape of the gravitation potential directly from the orientation of the velocity ellipsoid. In Table 2.1 the values of the angle β for different potentials are listed. The two angles, α and β, are the same for the case of Plummer and isochrone potential, but differ in all other cases.

Φ	v_c^2	$\rho\ (R >>)$	$\partial_z \tan\beta$
Observables	const	$\exp(-R/R_d)$	$\frac{1}{R}\frac{v_z^2}{\Omega^2}$
Plummer	$\frac{GMR^2}{(R^2+b^2)^{3/2}}$	R^{-5}	$\frac{1}{R}$
Isochrone	$\frac{GMR^2}{(b+\sqrt{b^2+r^2})^2\sqrt{b^2+R^2}}$	R^{-4}	$\frac{1}{R}$
Logarithmic	$\frac{v_0^2R^2}{R_c^2+R^2}$	R^{-2}	$\frac{1}{q^2R}$
Kuzmin	$\frac{GMR^2}{(R^2+a^2)^{3/2}}$	R^{-3}	$\frac{1}{R}(a+\frac{R^2-2a^2}{R^2+a^2})$
Miyamoto-Nagai	$\frac{GMR^2}{(R^2+(a+b)^2)^{3/2}}$	R^{-3}	$\frac{a+b}{bR} = \frac{a}{b}\frac{1+b/a}{R}$

Table 2.1: Values of z-derivative of the angle formed by the force field for different gravitational potentials.

3

Stäckel potentials

To solve the equation of stellar kinematics we need to construct a phase-space distribution function depending on the three integrals of motion. Then we can describe our dynamical system completely. From the third integral of motion the three dimensional orbits can be obtained and the anisotropy of the velocity ellipsoid with its inclination in the meridional plane can be derived. The problem is that the third integral of motion is not known analytically for a general gravitational potential. For this reason models with Stäckel potentials became popular. This very special class of potentials has the useful property that the Hamilton-Jacobi equation (Goldstein et al. 2001) is separable for systems with such a potential, and it is this feature which enables us to obtain an analytic expression for the third integral I_3 (de Zeeuw 1985).

Stäckel potentials are called 'Stäckel potentials' because they were first systematically studied by Paul Stäckel in 1890. Stäckel showed that the only coordinate system in which the Hamilton-Jacobi equation separates is the confocal spheroidal coordinate system. The usual Cartesian, spherical and cylindrical coordinate systems are limiting cases of these coordinates. Stäckel potentials were introduced in galactic dynamics by Eddington in 1915, who showed that the velocity dispersion tensor is diagonal in the coordinate system in which the potential is separable. Hence, the principal axes of the velocity ellipsoid everywhere line up with the local coordinate system. Later investigations were made by Weinacht (1924), Clark (1936) and Lynden-Bell (1962). It is this property related to the velocity ellipsoid, plus the fact that three isolating integrals of motion can be written explicitly, that makes Stäckel potentials most useful.

In his PhD thesis de Zeeuw (1984) applied Stäckel potentials to elliptical galaxies, being able to describe very well the orbits of the stars in those systems. In the triaxial case studied by de Zeeuw, it can be shown that stellar orbits can be classified in four families, namely box, inner long axis, outer long axis and short axis tube orbits. He discussed the relevance of mass models with Stäckel potentials for the construction of self-consistent models of elliptical galaxies. The axisymmetric case was only a special case of his description and only recently some scientists like van de Ven et al. (2003), Binney (2012a) and Bienaymé et al. (2014) started to look again at Stäckel potentials for describing the orbits and the phase-space also for disc galaxies. In axisymmetric potentials only one family of orbits exists as a set of stable orbits, namely the short axis orbits. These orbits have a toroidal shape with ellipsoidal and hyperboloidal outer boundaries and a fixed sense of rotation around the z-axis.

If the Hamilton-Jacobi equation can be separated for a potential in a particular coordinate system, the motion of stars will be constrained by the coordinate system itself. For example, if we have two harmonic oscillations along the Cartesian coordinates *x* and *y* the orbits will be constrained in a rectangular shape. If the potential is spherical, the orbits will be constrained by curves along the spherical coordinates. It is possible to see that real orbits are bound by constant spheroidal coordinates, and the boundaries of the orbits reflect the symmetry of the potential (Binney & Tremaine 2008). We can see in Fig. 3.1 how two integrated orbits for a logarithmic potential are constrained by the spheroidal coordinates in the meridional plane. This means that this potential is a reasonable approximation to real potentials.

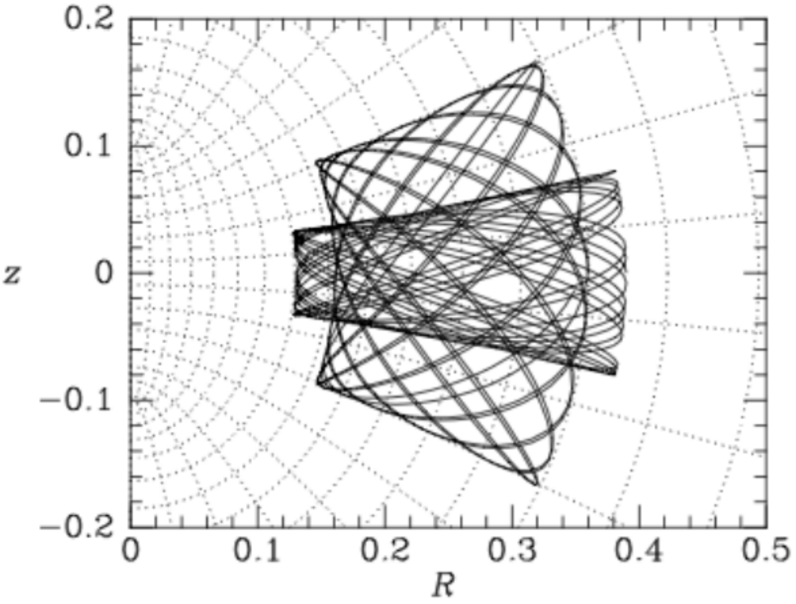

Figure 3.1: Orbits in a logarithmic potential (full curves) can be constrained in the meridional plane approximately with a confocal spheroidal coordinate system (dotted lines) (Binney & Tremaine 2008).

It was known for a long time that it is not possible to fit a Stäckel potential globally, because of the condition that it fulfils: a function of two variables has to be written as the sum of two functions depending on one variable (Binney & Tremaine 2008). Dejonghe & de Zeeuw (1988) described a method for fitting an axisymmetric potential with a Stäckel potential from the study of stars in the Galactic halo. They produced global fits for the Bahcall-Schmidt-Soneira Galaxy model (Bahcall et al. 1982) with errors nowhere exceeding 3% (Dejonghe & de Zeeuw 1988). The fit in the central regions of the Galaxy does not work very good because of the Galactic bulge since the potential is no further axisymmetric. Kent & de Zeeuw (1991) outlined three different methods for fitting an axisymmetric potential with one of the Stäckel form: a local fit expanding in power series the potential near circular orbits; the least-square fit involves the fit of the spheroidal coordinate system to the specific orbits; a conformal fitting method can be applied for potentials where the Stäckel approximation breaks down. De Bruyne et al. (2000) investigated the third integral of motion, I_3, for axisymmetric potentials. They fitted these potentials locally using a set of Stäckel potentials. When applied to a Miyamoto-Nagai potential, I_3 was found to vary by approximately 10% along an orbit (De Bruyne et al. 2000). Sanders (2012) applied the technique used by Dejonghe & de Zeeuw (1988) for fitting locally a Stäckel potential to a general axisymmetric potential. A local fit near the disc can be done with higher accuracy than a global fit.

We want to study the possibility to reproduce the observables in the extended solar neighbourhood of our Galaxy – like the velocity ellipsoid, the rotation curve, the gravitational force, the local density, the radial density and the radial scale length – by using one Stäckel potential. Further, we will assess, how far the potential is valid. Further details about the description used by de Zeeuw and the mathematical derivations can be found in Appendix A.

3.1 Coordinate system

The first point is to define a spheroidal coordinates system. We can have four different transformations to convert spheroidal to cylindrical coordinates:

1. $R = \Delta \sinh u \sin v$, $z = \Delta \cosh u \cos v$
2. $R = \Delta \sinh u \cos v$, $z = \Delta \cosh u \sin v$
3. $R = \Delta \cosh u \sin v$, $z = \Delta \sinh u \cos v$
4. $R = \Delta \cosh u \cos v$, $z = \Delta \sinh u \sin v$

The first two cases correspond to the prolate coordinate system, i.e. the ellipses are elongated along the z-axis, whereas in the last two the ellipses are elongated along the R-axis. We consider prolate coordinates, because they are used to fit the boundaries of orbits in oblate potentials (Eddington 1915; de Zeeuw 1985) and they reproduce oblate density distribution (de Zeeuw 1985). We will use only the first description because it defines the zero point for the z-axis and we want that the spheroidal coordinates become spherical when we go far away from the centre, where the halo contribution dominates. Therefore the transformation we are interested in is:

$$R = \Delta \sinh u \sin v \quad ; \quad z = \Delta \cosh u \cos v \tag{3.1}$$

For the inverse transformation, i.e. how the coordinates u and v depend on R and z, we start from the equations for ellipses:

$$\frac{R^2}{\Delta^2 \sinh^2 u} + \frac{z^2}{\Delta^2 \cosh^2 u} = 1$$

and hyperbolas:

$$\frac{R^2}{\Delta^2 \sin^2 u} - \frac{z^2}{\Delta^2 \cos^2 u} = -1$$

where the relations $\cosh^2 u - \sinh^2 u = 1$ and $\cos^2 v + \sin^2 v = 1$ are valid. We can define two variables τ_1 and τ_2 as:

$$\tau_1 = \Delta^2 \cosh^2 u \qquad ; \qquad \tau_2 = \Delta^2 \cos^2 v \tag{3.2}$$

and inserting them in the equations for ellipses:

$$\frac{R^2}{\Delta^2 \sinh^2 u} + \frac{z^2}{\Delta^2 \cosh^2 u} = \frac{R^2}{\tau_1 - \Delta^2} + \frac{z^2}{\tau_1} = 1$$

and hyperbolas:

$$\frac{R^2}{\Delta^2 \sin^2 u} - \frac{z^2}{\Delta^2 \cos^2 u} = \frac{R^2}{\Delta^2 - \tau_2} - \frac{z^2}{\tau_2} = -1$$

we can unify the two equations in a generic one:

$$\frac{R^2}{\tau_{1,2} - \Delta^2} + \frac{z^2}{\tau_{1,2}} = 1 \tag{3.3}$$

We have an equation of the second order and we can find the roots for τ:

$$\tau_{1,2} = \frac{(R^2 + z^2 + \Delta^2)}{2} \pm \frac{1}{2}\sqrt{(R^2 + z^2 + \Delta^2)^2 - 4\Delta^2 z^2}$$

Using back Eq. 3.2 it is possible to find the real solutions:

$$u = acosh\left[\sqrt{\frac{1}{2\Delta^2}[(R^2 + z^2 + \Delta^2) + \sqrt{(R^2 + z^2 + \Delta^2)^2 - 4\Delta^2 z^2}]}\right]$$

$$v = acos\left[\sqrt{\frac{1}{2\Delta^2}[(R^2 + z^2 + \Delta^2) - \sqrt{(R^2 + z^2 + \Delta^2)^2 - 4\Delta^2 z^2}]}\right]$$

We define a confocal spheroidal coordinate system (u, v, ϕ) and plot in Fig. 3.2 the meridional plane (u, v). Surfaces of constant u are prolate ellipses, and surfaces of constant v are hyperbolas. The third coordinate corresponds to the usual ϕ-coordinate which is responsible for the rotation along the z-axis.

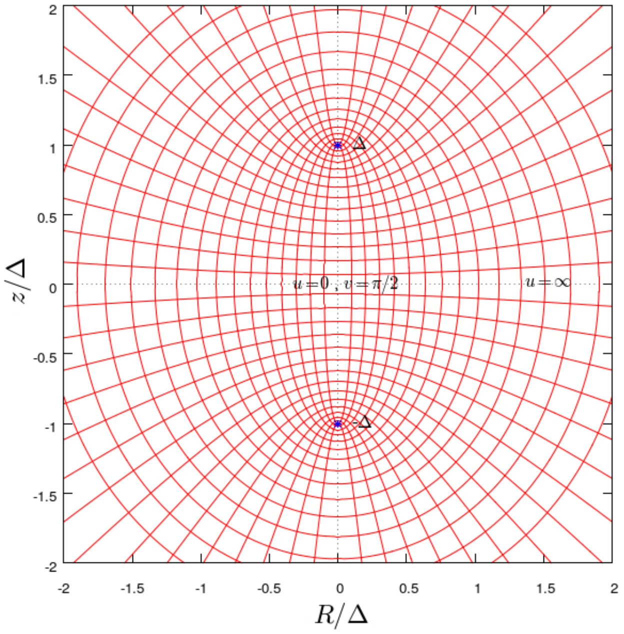

Figure 3.2: Prolate spheroidal coordinate system. Surfaces of constant u are ellipses elongated along the z-axis and surfaces of constant v are hyperbolas.

There is one free parameter in this description, which defines the value of the focal points ($\pm\Delta$) on the z-axis. The description used by de Zeeuw[1] is different from using these trigonometric and hyperbolic functions. He used a mathematical description, which avoids the use of these functions and introduced instead two free parameters for the determination of the focal points. The difference between the description used by de Zeeuw and our description is that with our description we need only one free parameter for the determination of the focal points of the coordinate system, instead of two. Furthermore, we do not have problems at the origin of the coordinate system, avoiding singularities. Once the value of focal points is fixed, the coordinate system is fixed. With the de Zeeuw description it is possible to change the two free parameters modifying the slope and producing a shift of the coordinate system. We could modify the orientation of the velocity ellipsoid changing these two parameters. This modification is not allowed in our description. Once we fix the focal point, we fix the coordinate system and we fix the orientation of the velocity ellipsoid.

---

[1] see Appendix for the description used by de Zeeuw for the confocal spheroidal coordinates and the comparison with the adopted one.

The line element $ds^2 = dx^2 + dy^2 + dz^2$ of this curvilinear coordinate system is equal to $ds^2 = P^2du^2 + P^2dv^2 + R^2d\phi^2$ with metric coefficients:

$$P^2 = \Delta^2(\sinh^2 u + \sin^2 v) \quad ; \quad R^2 = \Delta^2 \sinh^2 u \sin^2 v$$

where R is the usual cylindrical coordinate.

In small regions around the Sun's position in the Galactic plane, u is approximately equivalent to R and v to z. For larger ranges their curvilinear nature becomes more evident: the ellipsoidal coordinates become nearly spherical and the hyperboloidal ones are almost indistinguishable from their asymptotic surfaces which are cones around the z-axis (de Zeeuw 1985).

On the z-axis between the focal points ($[-\Delta, \Delta]$) we have that the coordinate u is zero and v varies from zero to π, assuming a value of $\pi/2$ in the midplane. We adopt this convention so that v can be assigned to the polar angle far away from the origin of the coordinate system. Outside the focal points ($]-\infty, -\Delta]$ and $[\Delta, \infty[$), v is fixed, and u varies from 0 to infinity. If the value of Δ decreases the coordinate system becomes more spherical, whereas if Δ increases it becomes more cylindrical.

3.2 Analytic third integral of motion

The choice to study these special potentials is because it is possible to separate the Hamilton-Jacobi equation[2] in spheroidal coordinates and to obtain an analytic expression for the third integral of motion. The Hamilton-Jacobi equation is the partial differential equation that satisfies the canonical transformation and gives the new Hamiltonian equal to zero. The system can be integrated and the motion is separable along the coordinate system. The integrals are in involution at each point of the coordinate system and we obtain the foliation by tori.

This means that the Hamilton-Jacobi equation is just the Hamiltonian in the new coordinate system equals to the energy E, assuming that the Hamiltonian has no explicit dependence on time and that the generating function is separable:

$$H = \frac{1}{2}\frac{p_u^2 + p_v^2}{\Delta^2(\sinh^2 u + \sin^2 v)} + \frac{1}{2}\frac{p_\phi^2}{R} + \Phi(u, v) = E$$

If we want to separate the Hamilton-Jacobi equation we need a gravitational potential of the form:

$$\Phi_s(u, v) = \frac{U(u) - V(v)}{\sinh^2 u + \sin^2 v}$$

where $U(u)$ and $V(v)$ are two functions, each depending on one curvilinear coordinate, ellipses u and hyperbolas v, respectively. Introducing this special form for the gravitational potential we can obtain now the expression:

$$2\Delta^2[E \sinh^2 u - U(u)] - p_u^2 - \frac{L_z^2}{\sinh^2 u} = \frac{L_z^2}{\sin^2 v} + p_v^2 - 2\Delta^2[E \sin^2 v + V(v)]$$

the left side of the equation does not depend on v, and the right side does not depend on u, so both sides must equal some constant, say $2\Delta^2 I_3$ (Binney & Tremaine 2008). The resulting expression for the third integral of motion I_3 reads:

---

[2] For a complete demonstration see Appendix A.5.

$$I_3 = \frac{1}{\sinh^2 u + \sin^2 v}\left[\sinh^2 u\left(\frac{p_v^2}{2\Delta^2} - V(v)\right) - \sin^2 v\left(\frac{p_u^2}{2\Delta^2} + U(u)\right)\right] + \\ + \frac{p_\phi^2}{2\Delta^2}\left(\frac{1}{\sin^2 v} - \frac{1}{\sinh^2 u}\right) \tag{3.4}$$

Therefore for the determination of the third integral of motion I_3 we have three free parameters: the focal point Δ, the 'radial' potential $U(u)$ and the 'vertical' potential $V(v)$. The labels 'radial' and 'vertical' are used because in the solar neighbourhood the coordinate u is approximately equivalent to R and v to z but leaving this region they show their curvilinear nature.

3.3 Velocity ellipsoid

The special form of the Stäckel potential leads to the separation of the Hamilton-Jacobi equation (Stäckel 1890; Lynden-Bell 1962; Goldstein et al. 2001). The orbits have three isolating integrals of motion, which are quadratic in the velocities (de Zeeuw 1985) and do not possess irregular orbits. The Jeans theorem claims that we can construct a distribution function depending on these three integrals of motion. The three dimensional orbits are a composition of three one-dimensional motions, that can be a rotation or an oscillation along the coordinates. For elliptical galaxies four families of orbits were found using Stäckel potential, whereas for axisymmetric galaxies only one type of orbit exists. These toroidal orbits are composed by one rotation along the ϕ-coordinate and two oscillations along the u and v coordinates.

If the motion is separable along the coordinate system, the axes of the velocity ellipsoid are perpendicular to the coordinate surfaces (van de Ven et al. 2003). Eddington (1915) showed that the velocity ellipsoid lines up with the spheroidal coordinate system if the velocity distribution is a trivariate Gaussian. This result turned out to be more general, not following from the Gaussian property of the velocity distribution but from both assuming that the distribution function is separable and from symmetry properties. We need a separable distribution function if we want to separate the motion along the spheroidal coordinates. If we construct a separable distribution function depending on the three integrals of motion, it is possible to determine that $\overline{v}_u = \overline{v}_v = 0$ and $\overline{v}_\phi \neq 0$. The integrals for $\overline{v}_u$ and $\overline{v}_v$ vanish because the integrands are odd functions of v_u and v_v, respectively. The integral for $\overline{v}_\phi$ does not vanish because it is not an even function of L_z. The mixed terms of the second velocity moment are zero and the velocity dispersion tensor is diagonal ($\sigma_{u\phi} = \sigma_{v\phi} = \sigma_{uv} = 0$).

The tilt of the velocity dispersion with respect to the cylindrical coordinates is shown by the mixed term σ_{uv}:

$$\sigma_{uv}^2 = \frac{1}{\nu}\int dv_u v_u \int dv_v v_v \int dv_\phi f[E(v_u^2, v_v^2, v_\phi^2), L_z(v_\phi), I_3(v_u^2, v_v^2, v_\phi^2)]$$

that can be expressed as an integral of the DF multiplied by $v_u v_v$. We know that the energy integral is proportional to the velocities at the second order whereas the vertical component of the angular moment is not quadratic. The third integral has to be independent on the other two integrals and we have found that it is quadratic in the velocities. For this reason σ_{uv}^2 becomes zero.

We can also explain this by symmetry properties. The expressions for the integrals can be considered to be simultaneous equations for the velocity components v_u, v_v, v_ϕ. Looking at the meridional plane without considering the azimuthal motion, the velocity components appear in the equations to its second power only. The solutions are in pairs $\pm v_u, \pm v_v$, so that at a given point there are four possible values of the velocity vector. If all four solutions occur, then it is easy to see that cancellation of positive and negative values will make the net contribution zero for all off-diagonal second moments, so that the principal axes do indeed lie along the coordinate lines. It is like the case of the epicycle approximation with two oscillations along R and z where we cannot reproduce the observed inclination of the velocity ellipsoid, the radial motion is decoupled from the vertical motion and the mixed term of the velocity dispersion σ_{Rz} equals zero. For the case of spheroidal coordinates we have two oscillations in the u-v plane, the stars oscillate along the u and v coordinates, and the motion is decoupled because of the Hamilton-Jacobi theory.

3.3.1 Tilt of velocity ellipsoid

The generating function of the canonical transformation between the cylindrical and spheroidal coordinates is:

$$S(p_R, p_z, u, v) = p_R R(u, v) + p_z z(u, v)$$

This function depends on the new coordinates and the old momenta and we assume that it is separable. From $p_u = \partial S/\partial u$ we obtain:

$$p_u = \Delta(p_R \cosh u \sin v + p_z \sinh u \cos v)$$

$$p_v = \Delta(p_R \sinh u \cos v - p_z \cosh u \sin v)$$

We also know the relationships between the momenta, velocities and derivatives of the coordinates:

$$p_u = P v_u = P^2 \dot{u} \quad ; \quad p_v = P v_v = P^2 \dot{v}$$

where $P = \Delta \sqrt{\sinh^2 + \sin^2 v}$ is the scale factor of the coordinate transformation. The new velocities are:

$$v_u = \frac{\Delta}{P} \cosh u \sin v v_R + \frac{\Delta}{P} \sinh u \cos v v_z$$

$$v_v = \frac{\Delta}{P} \sinh u \cos v v_R - \frac{\Delta}{P} \cosh u \sin v v_z$$

where $v_u \sim v_R$ and $v_v \sim -v_z$ in the solar neighbourhood ($v = \pi/2$ and $P = \Delta \cosh u$). Now it is possible to calculate the mixed term σ^2_{uv}:

$$\sigma^2_{uv} = \frac{\Delta^2}{P^2}[\cosh u \sinh u \cos v \sin v(\sigma^2_R - \sigma^2_z) - \sigma^2_{Rz}(\cosh^2 u \sin^2 v - \sinh^2 u \cos^2 v)]$$

From the knowledge that the velocity ellipsoid is aligned with the spheroidal coordinate system, the term σ_{uv} is zero:

$$\sigma^2_{Rz} = \frac{\cosh u \sinh u \cos v \sin v(\sigma^2_R - \sigma^2_z)}{\cosh^2 u \sin^2 v - \sinh^2 u \cos^2 v}$$

which results in cylindrical coordinates:

$$\sigma^2_{Rz} = -\frac{Rz}{R^2 - z^2 + \Delta^2}(\sigma^2_R - \sigma^2_z)$$

which results in a negative value at $z > 0$ in our description. We know that the observed angle of the velocity ellipsoid is linked to the velocity moments (Binney & Merrifield 1998) in the following way:

$$\tan(2\alpha) = \frac{2\sigma^2_{Rz}}{\sigma^2_R - \sigma^2_z} = -\frac{2Rz}{R^2 - z^2 + \Delta^2} \tag{3.5}$$

that gives us the orientation of the velocity ellipsoid for a Stäckel potential. If we consider small heights from the plane, we can do a Taylor expansion of the tilt angle and the tangent of the angle is approximately the angle itself:

$$\alpha \simeq -\frac{Rz}{R^2 - z^2 + \Delta^2}$$

We calculate the z-derivative looking at the result in the plane, and we can derive the behaviour of the velocity ellipsoid when we move away from the plane.

$$\partial_z \alpha|_{z=0} = -\frac{1}{R}\frac{R^2}{R^2+\Delta^2} \tag{3.6}$$

if R is much greater than the focal point Δ, we can recover spherical coordinates and obtain:

$$\partial_z \alpha|_{z=0} = -\frac{1}{R}$$

which means that one axis in the meridional plane points in the direction of the Galactic centre; if the value of the focal point is very large, we can recover cylindrical coordinates:

$$\partial_z \alpha|_{z=0} = 0$$

which defines a velocity ellipsoid always parallel to the plane.

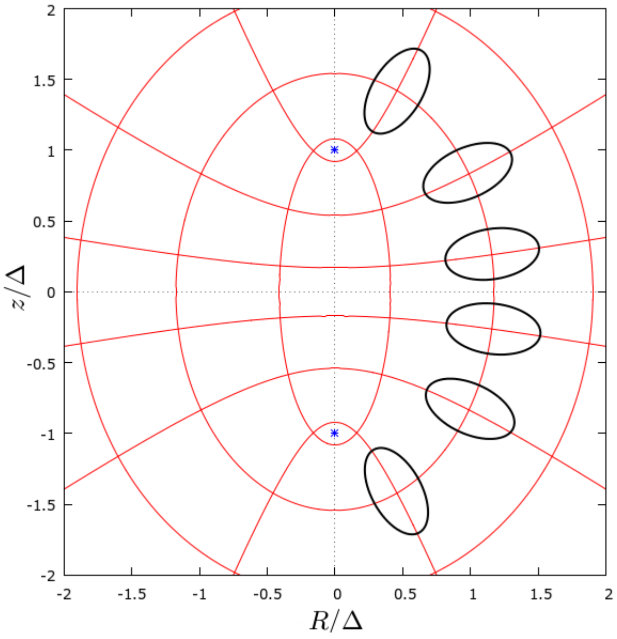

Figure 3.3: Sketch of the alignment of the velocity ellipsoid with the spheroidal coordinate system. The ellipses represent the velocity ellipsoids.

3.4 Stäckel model

We want to find the best Stäckel potential for the local gravitational potential, which reproduces the observables in the extended solar neighbourhood. We require that the potential is of the separable form:

$$\Phi_s(u,v) = \frac{U(u)-V(v)}{\sinh^2 u + \sin^2 v} \tag{3.7}$$

The denominator corresponds to P^2/Δ^2, which is the scale factor of the coordinate transformation squared divided by the square of the focal point. $U(u)$ and $V(v)$ are two functions, that we can choose independently and that depend only on one variable. If we want to have a smooth potential everywhere, it has to be smooth in the plane at $v = \pi/2$ (Statler 1989).

The denominator vanishes at the focal points when $u = 0$, $v = 0$. However, we may avoid a singularity in the potential at the focal points by choosing $U(u)$ and $V(v)$ such that $U(0) = V(0) = 0$. If we do not choose this criteria we will have a singularity at these points. Since we do not want to reproduce the all Galaxy with our Stäckel potential and we are interested in studying only the extended solar neighbourhood, we do not need the assumption that the potential $U(u)$ and $V(v)$ are zero at $(0, \pm\Delta)$.

The best local approximation for the Stäckel potential can be derived in four steps from four pieces of information:

1. we derive the focal point (Δ) of the spheroidal coordinate system from the result found by Binney et al. (2014a) about the orientation of the velocity ellipsoid based on RAVE data;

2. from the rotation curve we can derive the derivative of the 'radial' potential function $F'(u)$, and with an integration we can recover $F(u)$;

3. then it is possible to derive the second derivative of the 'vertical' potential in the plane $G''(v = \pi/2)$ from the local mass density and the radial scale length from the 'radial' potential;

4. at the end we can derive the 'vertical' potential $G(v)$ up to the second order using the K_z-force at 1.1 kpc far from the plane.

The work of Kent & de Zeeuw (1991) suggested that it is convenient to write the two potentials in the following way:

$$U(u) = \cosh^2 u F(u) \quad ; \quad V(v) = (\sinh^2 u_0 + \sin^2 v) G(v)$$

u_0 is the value of the coordinate u at the solar neighbourhood ($u_0 = (R_0, 0)$), while $F(u)$ and $G(v)$ can be assigned to the radial and vertical functions. These two functions are everywhere finite, because the potential in the midplane is given simply by $\Phi(u, v = \pi/2) = F(u)$ (Statler 1989). This requires that the function $G(v)$ goes to zero when we go to the midplane and moreover that the first derivative $G'(v)$ goes to zero as well to avoid a cusp in the potential. This choice for the potential $U(u)$ and $V(v)$ is due to the fact that the motion in the midplane ($v = \pi/2$) is determined by the potential $F(u)$ and the vertical motion approximately by $G(v)$ at the solar position.

We consider the Stäckel potential as the total potential and we do not combine different potentials to obtain the total one. Adding several Stäckel potentials we obtain again a Stäckel potential, but we would have different values of the focal point for the different components, which correspond to different stellar populations. There are several works in the literature done by Dejonghe and his collaborators, like Batsleer & Dejonghe (1994) and Famaey & Dejonghe (2003), where they combined two or three different Stäckel potentials to reproduce the local observables of the Milky Way, like the rotation curve. They added different components, a thin and a thick disc and a halo. Each component is described by a Kuzmin-Kutuzov Stäckel potential, which is a flattened potential with all the mass concentrated in the plane. They used the 'de Zeeuw description' for the spheroidal coordinates and they obtain the same focal point for all the components. Two free parameters are necessary for the determination of the focal point. Changing these two parameters, it is possible to obtain the same focal point for the different components, but it leads to different coordinate representations. The coordinates can be shifted and the hyperbolas change their curvature, with a following variation for the tilt of the velocity ellipsoid. The difference with their work is that our description does not allow to generate different coordinate systems. Once the focal point is fixed we have always the same coordinate system. Therefore we are considering only one Stäckel potential as the total potential. This is also what we would require for the construction of the distribution function.

3.4.1 Focal point determination

The first step to generate our model is to choose the value of the focal point Δ. Once we choose this parameter we generate a spheroidal coordinate system and obtain an orientation for the velocity ellipsoid because of its alignment with the coordinate system.

We consider the last result found by Binney et al. (2014a) based on RAVE data. They found that the velocity ellipsoid does not point exactly towards the Galactic centre as first found by Siebert et al. (2008), although with large errorbars, but less inclined with an angle of $\alpha_{tilt} \simeq -0.8 \arctan(z/R)$. The sign has been changed to be in agreement with our convention. We recall the tilt angle of the velocity ellipsoid for the Stäckel potential (Eq. 3.5):

$$\tan(2\alpha) = -\frac{2Rz}{R^2 - z^2 + \Delta^2}$$

We can determine the value of the focal point Δ equating these two results, after a Taylor expansion for small angles:

$$\frac{R^2}{R^2 + \Delta^2}\frac{z}{R} = 0.8\frac{z}{R}$$

We find that the value for the focal point is 4 kpc and we can fix the prolate spheroidal coordinate system. The value found for Δ is half of the solar position ($\Delta = R_0/2$). It can be consider something in between the spherical coordinate system ($\Delta \rightarrow 0$) and the cylindrical case ($\Delta \rightarrow \infty$), for the study of the solar neighbourhood. In this region the u coordinate surfaces are neither as curved as in the first case nor perfect vertical lines with respect to the midplane at all z as in the second one. They start to curve when we are interested in regions far from the plane and the variation has to be taken into account. Once we fix the coordinate system, we have the orientation of the velocity ellipsoid. The velocity ellipsoid is pointing towards the Galactic centre for the case $\Delta \rightarrow 0$ and is parallel to the Galactic plane for large values of Δ.

In Fig. 3.4 the inclination of the velocity ellipsoid is plotted with respect to the Galactic plane as a function of the height z above and below the plane. The green line corresponds to the alignment of the velocity ellipsoid with the spherical coordinates pointing in the direction of the Galactic centre, which is exactly overplotted by the black one assuming the Stäckel model with $\Delta = 0$ kpc; the red line is the value found by Binney et al. (2014a) and the blue one is assuming the Stäckel model with $\Delta = 4$ kpc. The difference between the last two lines is minimal and the value $\Delta = 4$ kpc is the best case for our Stäckel model.

There are not many values for the focal point Δ in literature. Small values were used, like $\Delta = 0.1$ kpc (Statler 1989) and 0.88 kpc (Dejonghe & de Zeeuw 1988), for studies finalized to the halo component. These results are understandable because halo stars undergo the influence of a more spherical gravitational potential and small values of Δ are expected. Sommer-Larsen & Zhen (1990) build a two component model for disc and halo using a value of $\Delta = 4$ kpc. More recent works that focused on stellar orbits in a disc potential remain close to the values $\Delta = 3.5$ kpc (Binney 2012a) and $\Delta = 0.45 \cdot R_0$ kpc (Bovy & Rix 2013), which is almost in agreement with what we have found. Bienaymé (1999) estimated a value for $\Delta = (5.7 \pm 1.4)$ kpc from Hipparcos data using a three-dimensional distribution function depending on three integrals of motion. This value leads to $\eta = 0.69$, but uncertainties on the scale length lead to a value of $\eta = 0.83$, more similar to the result found by Binney et al. (2014a). Bienaymé et al. (2014) used a value of $\Delta = 2$ kpc corresponding to a tilt pointing towards the Galactic centre in deriving the vertical force up to $z = 2$ kpc. Sanders & Binney (2014) used the axisymmetric 'Stäckel fudge' together with the torus code showed as in McMillan & Binney (2008) and derived a value for the focal point $\Delta = 4.4$ kpc.

Amendt & Cuddeford (1991) found an expression, which links the tilt of the velocity ellipsoid to the mass gradient in the galactic plane. Bienaymé (1999) derived a relation between the tilt angle and the radial scale length assuming an exponential disc inside a spheroidal halo with a flat rotation curve

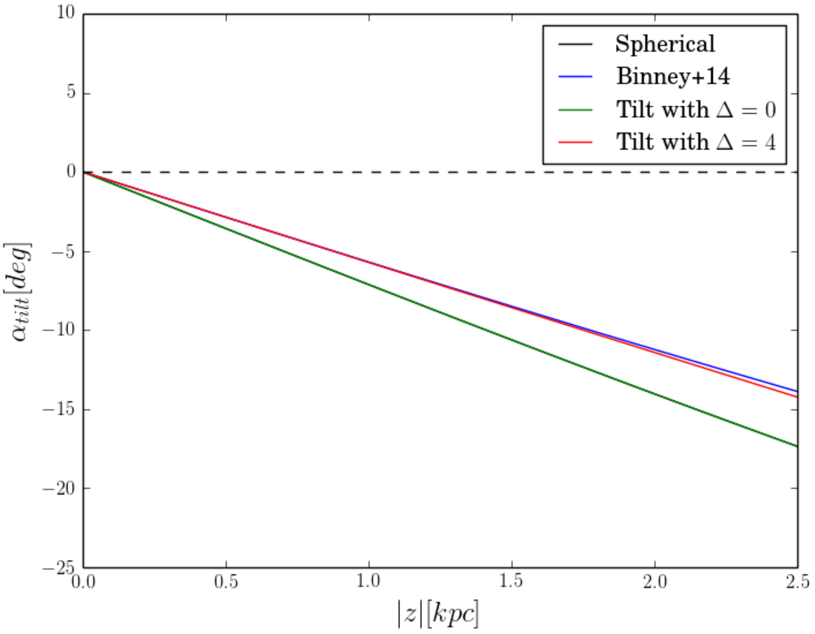

Figure 3.4: Variation of the tilt of the velocity ellipsoid above and below the plane. The green line corresponds to the alignment of the velocity ellipsoid with the spherical coordinates; the black one assuming the Stäckel model with $\Delta = 0$ kpc; the red one is the value found by Binney et al. (2014a) and the blue one assumes the Stäckel model with $\Delta = 4$ kpc.

($\eta = R/(4R_d)$). If we assume the solar position and a value for $\eta = 0.8$, we can derive a scale length $R_d = 2.5$. As we will see this result is in perfect agreement with what we found and with the observations. Uncertainties of 10% in R_d lead to an uncertainty in η of 0.04. This corresponds to a variation of the tilt angle of ~0.3°/kpc, with a following variation in Δ of 0.5 kpc. The first result found by Siebert et al. (2008) in the determination of the tilt of the velocity ellipsoid had an errorbar of 1.8°. As we can see in Table 3.1 large errorbars in the tilt angle can lead to large uncertainty in the determination of the focal point.

3.4.2 Rotation Curve

We can use the rotation curve to determine the 'radial' potential function $F'(u)$, and then derive $F(u)$ through an integration. The rotation curve is given by the equilibrium between the centripetal force and the gravitational force, i.e. it is the velocity that a star would have if it was in a circular orbit, calculated in the plane. The rotation curve in spheroidal coordinates reads, using the chain derivatives:

$$v_c^2 = R\frac{\partial \Phi}{\partial R} = R\left[\frac{\partial u}{\partial R}\frac{\partial \Phi_s}{\partial u} + \frac{\partial v}{\partial R}\frac{\partial \Phi_s}{\partial v}\right]$$

Since we are looking in the plane ($z = 0$ or $v = \pi/2$), we can immediately cancel the second term because both the v-derivative of the Stäckel potential ($\partial\Phi/\partial v|_{v=\pi/2} = 0$) and the radial derivative of the coordinate v are zero in the plane ($\partial v/\partial R|_{v=\pi/2} = 0$)[3]. Then it remains:

$$v_c^2 = R\left(\frac{\partial u}{\partial R}\frac{\partial \Phi_s}{\partial u}\right)_{z=0}$$

---

[3] see Appendix A.3 and A.4 for mathematical derivatives of the spheroidal coordinates and of the Stäckel potential.

η	$\lvert\alpha_{tilt}/z\rvert[deg/kpc]$	$\Delta[kpc]$
0.60	4.275	6.50
0.64	4.56	6.00
0.68	4.845	5.50
0.72	5.13	5.00
0.76	5.415	4.50
0.80	**5.70**	**4.00**
0.84	5.985	3.50
0.88	6.27	3.00
0.92	6.555	2.50
0.96	6.84	2.00
1.00	7.125	1.50

Table 3.1: Values for the parameter η in a range $0.60 \leq \eta \leq 1.00$, the corresponding tilt angle α_{tilt} of the velocity ellipsoid and the focal point Δ are given.

where

$$\left(\frac{\partial\Phi_s}{\partial u}\right)_{z=0} = F'(u)\Big|_{z=0} + 2\left(\frac{\sinh u}{\cosh^3 u}\right)_{z=0} V_0$$

We can assume that the 'vertical' potential is zero in the plane ($V_0 = G_0 = 0$) and the first u-derivative of the Stäckel potential $\Phi_s(u, v)$ is the first derivative $F'(u)$ in the plane. This assumption implies a direct relation between $F'(u)$ and the rotation curve:

$$F'(u)\Big|_{z=0} = \left(\frac{\cosh u}{\sinh u}\right)_{z=0} v_c^2 \tag{3.8}$$

From the rotation curve we can determine the first derivative of the 'radial' potential $F'(u)$ and after an integration we obtain the 'radial' profile of the Stäckel potential $F(u)$ with an integration constant C_0.

3.4.3 Radial density

In the construction of a density model of the Milky Way we have to consider the local density. We want to check if using a Stäckel potential is possible to reproduce observables like the local density and the radial scale length. The reproducibility of an exponential radial density profile means that the radial scale length will be constant with radius. Since we are studying the Stäckel potential as the total one, we derive the radial density starting from the Laplacian $\nabla^2\Phi$. The form of the Laplacian for a generic coordinate system is given by:

$$\nabla^2\Phi = \frac{1}{h_1h_2h_3}\left[\frac{\partial}{\partial q_1}\left(\frac{h_2h_3}{h_1}\frac{\partial\Phi}{\partial q_1}\right) + \frac{\partial}{\partial q_2}\left(\frac{h_3h_1}{h_2}\frac{\partial\Phi}{\partial q_2}\right) + \frac{\partial}{\partial q_3}\left(\frac{h_1h_2}{h_3}\frac{\partial\Phi}{\partial q_3}\right)\right] \tag{3.9}$$

(Binney & Tremaine 2008, appendix B3), where h_1, h_2, h_3 are the scale factors and q_1, q_2, q_3 are the coordinates. If we assume $q_1 = R$, $q_2 = \phi$ and $q_3 = z$, we obtain the Laplacian in cylindrical coordinates (Eq. 2.12). Since we are dealing with a spheroidal coordinate system (u, v, ϕ), we substitute the coordinates $q_1 = u$, $q_2 = v$, $q_3 = \phi$ and the scale factors $h_1 = h_2 = P = \Delta\sqrt{\sinh^2 u + \sin^2 v}$, $h_3 = R$ into Eq. 3.9:

$$\nabla^2\Phi_s = \frac{1}{P^2R}\left[\frac{\partial}{\partial u}\left(R\frac{\partial\Phi_s}{\partial u}\right) + \frac{\partial}{\partial v}\left(R\frac{\partial\Phi_s}{\partial v}\right)\right] \tag{3.10}$$

There is no dependence of the gravitational potential on the azimuthal coordinate ϕ, as for the cylindrical case, and its derivative along ϕ has been eliminated. Dividing the Laplacian by $(4\pi G)$ we obtain the Poisson equation, which links the total density with the gravitational potential. Studying the case in the plane ($z = 0$) we can obtain the total radial density. Using cylindrical coordinates the term corresponding to the second vertical derivative of the gravitational potential dominates in a disc galaxy because it is much greater than the radial contribution. Using spheroidal coordinates we are not certain that the second term dominates with respect to the first one. This is why we want to study the contribution of each term:

$$\nabla^2\Phi_s = \frac{1}{P^2R}\left[\frac{\partial R}{\partial u}\frac{\partial \Phi_s}{\partial u} + R\frac{\partial^2\Phi_s}{\partial u^2} + \frac{\partial R}{\partial v}\frac{\partial \Phi_s}{\partial v} + R\frac{\partial^2\Phi_s}{\partial v^2}\right]$$

All the following calculations about the radial density will be calculated in the plane ($z = 0$ or $v = \pi/2$). The v-derivative of the radial coordinate R is zero in the plane and consequently the third term of the Laplacian vanishes ($\partial R/\partial v|_{v=\pi/2}$). In the first two terms enter the first and second derivatives of the 'radial' potential ($F'(u)$ and $F''(u)$) and the coordinates u, with the assumption that the 'vertical' potential V is zero in the plane ($G_0 = 0$):

$$\left(\frac{\partial^2\Phi_s}{\partial u^2}\right)_{z=0} = F''(u)\big|_{z=0}$$

The interesting result is that the first and the second derivative of the Stäckel potential in the plane with respect to u are the first and second u-derivatives of the 'radial' $F(u)$ function. Hence, the choice for $U(u) = \cosh^2 uF(u)$ is very convenient in the study of the radial part. After the substitution of the radial derivatives in the Laplacian, the density reads:

$$\rho(u,\pi/2) = \frac{1}{4\pi G}\left[\frac{v_c^2}{\Delta^2\sinh^2 u} + \frac{F''(u)}{\Delta^2\cosh^2 u} + \frac{1}{\Delta^2\cosh^2 u}\left(\frac{\partial^2\Phi_s}{\partial v^2}\right)\right]_{z=0} \tag{3.11}$$

It is possible to convert back the second u-derivative $F''(u)$ in cylindrical coordinates and obtain:

$$\frac{1}{(R^2+\Delta^2)}\left(\frac{\partial^2\Phi_s}{\partial u}\right)_{z=0} = \frac{1}{(R^2+\Delta^2)}\left(\frac{\partial^2 F(u)}{\partial u^2}\right)_{z=0} = 2\frac{v_c}{R}\frac{dv_c}{dR} - \frac{v_c^2}{R^2} + \frac{v_c^2}{R^2+\Delta^2} \tag{3.12}$$

The first term on the right side can be represented by the Oort's parameters, the second term get eliminated by the first term in Eq. 3.11 and the third term, which is not present for the cylindrical case, comes from the curvature of the coordinate system.

The 'vertical' part of the Laplacian can be converted in the cylindrical coordinates as:

$$\frac{1}{R^2+\Delta^2}\left(\frac{\partial^2\Phi_s}{\partial v^2}\right)_{z=0} = -\frac{v_c^2}{R^2+\Delta^2} + \left(\frac{\partial^2\Phi_s}{\partial z^2}\right)_{z=0}$$

The first term on the right side can be eliminated with the last term of Eq. 3.12. We are able to recover the cylindrical case, where the main term is the second z-derivative of the potential.

We can derive the last term of the Laplacian in Eq. 3.11 in terms of the spheroidal coordinates u and v:

$$\left(\frac{\partial^2\Phi_s}{\partial v^2}\right)_{z=0} = \left(-G''\frac{\cosh^2 u_0}{\cosh^2 u} + \frac{2}{\cosh^2 u}(F(u)+C_0)\right)_{z=0}$$

where $G''(v = \pi/2) = G_0''$ is the second derivative of the 'vertical' potential in the plane and C_0 is the integration constant. From Eq. 3.11 the general result for the radial density after the conversion in cylindrical coordinates reads:

$$\rho(R) = \frac{1}{4\pi G}\left[\frac{v_c^2}{R^2+\Delta^2} + 2\frac{v_c}{R}\frac{dv_c}{dR} - \frac{R_0^2+\Delta^2}{(R^2+\Delta^2)^2}G_0'' + \frac{2\Delta^2}{(R^2+\Delta^2)^2}(F(R)+C_0)\right] \tag{3.13}$$

The potential $G(v)$ and its first derivative $G'(v)$ of the 'vertical' potential are zero in the plane, but the second derivative G''_0 is not zero and we can derive it from the total local mass density at $R = R_0$:

$$\nu^2_{z,s} = -\frac{1}{(R_0^2 + \Delta^2)} G''_0 = \left[\nu^2_{z,0} - \frac{v_c^2}{R_0^2 + \Delta^2} - 2\frac{v_c}{R_0}\frac{dv_c}{dR}\bigg|_{R=R_0} - \frac{2\Delta^2}{(R_0^2 + \Delta^2)^2}(F(R_0) + C_0) \right] \tag{3.14}$$

where $4\pi G\rho_0 = \nu^2_{z,0}$ is the vertical oscillation frequency squared in the thin disc approximation, which corresponds to the second z-derivative of the potential at $z = 0$ in the solar neighbourhood. The second derivative of $G(v)$ in the plane (G''_0) divided by $(R_0^2 + \Delta^2)$, which is the value of the scale factor P^2, is a measure for the oscillation frequency squared. We call $\nu_{z,s}$ the new 'vertical' oscillation frequency for the Stäckel potential. It is an oscillation frequency for the motion along the v-coordinate. It has to be negative to obtain a positive value for the density and it does not depend on the coordinate u because it enters only in the 'vertical' function $G(v)$. It differs slightly from the vertical oscillation frequency $\nu_{z,0}$ having always lower values. The amount of how much this new frequency differs from the vertical oscillation frequency $\nu_{z,0}$ is determined by the first and the last term in Eq. 3.13. These terms are proportional to the angular velocity Ω^2, but they depend on the value of Δ. The greater the value Δ is, the lower the contribution of these terms. This means that for greater Δ the second v-derivative of the potential tends to the value of $\nu_{z,0}$ and the coordinate system becomes more cylindrical.

To evaluate the radial density we have to choose a 'radial' potential $F(u)$ and we will consider two cases, a logarithmic and a power-law potential. In the first example we can assume that the rotation curve is exactly flat in the vicinity of the Sun, whereas in the second case we consider a more general case leaving open the possibility that the rotation curve has some slope.

3.4.4 Radial scale length

After we have chosen a potential $F(u)$ and obtained the radial density profiles for different Δ, we want to calculate the radial scale length. The density derived by the Laplacian corresponds to the total density, i.e. the density given by the tracers and the dark matter. It is not possible to separate from the rotation curve the contribution of the disc and the halo. This is the so-called 'disc-halo' degeneracy. Different combinations of disc and halo profiles can lead to the same rotation curve.

We can assume a cored isothermal profile for the dark matter ($\rho = \rho_{0,dm}R_c^2/(R^2 + R_c^2)$), where R_c is the core radius and $\rho_{0,dm}$ is the corresponding centred dark matter density. We can subtract the dark halo profile from the total density to obtain the contribution of the tracers only.

We need only the density produced by the tracers to compare it with the observations; the same is valid for the radial scale length. First, we examine whether the radial scale length is constant with radius, so that the generated Stäckel potential can reproduce an exponential density profile. Next, we examine if the observed radial scale lengths ($2 < R_d < 3$ kpc) are consistent with the initial choice of Δ.

We derive the radial density (Eq. 3.13) with respect to R:

$$\begin{aligned} \frac{d\rho}{dR} = \frac{1}{4\pi G}\Bigg[& -\frac{2Rv_c^2}{(R^2 + \Delta^2)^2} - 2\frac{v_c}{R^2}\frac{dv_c}{dR} + 2\frac{v_c}{R}\frac{d^2v_c}{dR^2} \\ & -4R\frac{(R_0^2 + \Delta^2)}{(R^2 + \Delta^2)^3}G''_0 - 2RF(R)\frac{\Delta^2}{(R^2 + \Delta^2)^3} + 2\frac{\Delta^2}{(R^2 + \Delta^2)^2}F'(R)\Bigg] \end{aligned} \tag{3.15}$$

Then we can calculate the radial scale length dividing the radial density by its radial derivative:

$$R_d = -\left(\frac{\rho(R)}{d\rho(R)/dR}\right) \tag{3.16}$$

It is possible to see immediately that if the radial profile is exponential, we can obtain a constant scale length with radius. We will use this formula for the derivation of the radial scale length for both cases (logarithmic and power-law) after having subtracted the cored isothermal profile due to the dark matter because we want to compare the results with the observations.

3.5 Logarithmic case

For the derivation of the radial density we need the rotation curve and the 'radial' potential function $F(u)$. First, we consider the case of a constant rotation curve with a circular velocity v_0 constant with radius. From Eq. 3.8 we obtain the first derivative of the 'radial' potential:

$$F'(u) = \frac{\cosh u}{\sinh u} v_0^2 \tag{3.17}$$

and integrating we obtain the 'radial' function:

$$F(u) = v_0^2 \log(\sinh u) + C_0 = v_0^2 \log\left(\frac{R}{\Delta}\right) + C_0 \tag{3.18}$$

where C_0 is the integration constant and the last relation is valid in the plane. We choose $R_0 = 8$ kpc as solar radius and $v_0 = 220$ km/s for the circular velocity at the solar position. The slope of the rotation curve is equal to zero at R_0 and does not change for different values of Δ.

3.5.1 Local density

We want to calculate the radial density for the logarithmic potential. We need to insert the 'radial' potential function $F(u)$ and its first derivative $F'(u)$. Substituting these terms in the Eq. 3.13 we obtain for the radial density:

$$\rho(R) = \frac{1}{4\pi G}\left[\frac{v_0^2}{R^2+\Delta^2} - G_0'' \frac{R_0^2+\Delta^2}{(R^2+\Delta^2)^2} + 2\frac{\Delta^2}{(R^2+\Delta^2)^2}\left(v_0^2 \log\left(\frac{R}{\Delta}\right) + C_0\right)\right] \tag{3.19}$$

The Oort's parameters do not enter in the density equation for the logarithmic potential because the rotation curve is exactly flat and its radial derivative is zero ($dv_c/dR = 0$).

We have two free parameters, G_0'' and C_0 which we want to quantify at the solar neighbourhood. We can substitute in Eq. 3.19 the value $R = R_0$ and the expression for the local density results in:

$$\nu_{z,s}^2 = -G_0'' \frac{1}{(R_0^2+\Delta^2)} = \left(4\pi G\rho_0 - \frac{v_0^2}{R_0^2+\Delta^2} - 2\frac{\Delta^2}{(R_0^2+\Delta^2)^2}\left(v_0^2 \log\left(\frac{R_0}{\Delta}\right) + C_0\right)\right]$$

We want to reproduce the value of the local density found by Holmberg & Flynn (2000) ($\rho_0 = 0.102$ $M_\odot/pc^3$), from which we can derive the value for the vertical oscillation frequency $\nu_{z,0} = 76$ km/s/kpc.

We can obtain the value for the new frequency $\nu_{z,s}$ by changing the values of the focal point Δ and thus setting the integration constant C_0 to zero (blue points in Fig. 3.5). We find a value of ~71 km/s/kpc for $\Delta = 4$ kpc, which is ~7% lower than the vertical oscillation frequency $\nu_{z,0}$. This difference comes principally from the first term $\sim \Omega^2$ due to the curvature of the coordinate system.

The integration constant has to be zero if we want a global fit for the gravitational potential when we go to infinity. Since we are interested in a local fit we can set this constant also to a different value. We calculate the new frequency also in the case that the integration constant normalises the local gravitational potential to a corresponding value for a two-component model composed by a Bessel disc plus a cored isothermal halo, with values given by Golubov (2012). The result for this case is slightly greater: $\nu_{z,s} =$ 72 km/s/kpc for $\Delta = 4$ kpc (green points in Fig. 3.5). The result for $\Delta = 8$ kpc is approximately the same for both cases. This is because the potential at the solar position is zero for this value of Δ. We will see that this case is interesting because it will generate an exponential density profile in the plane. The value for the new frequency increases with Δ and tends to $\nu_{z,0}$ for larger values of Δ. This new value of the frequency remains constant with the radius because it enters in the $V(v)$ function, and not in the $U(u)$.

We can also change the value C_0 from $-v_0^2$ to v_0^2 holding fix the value for the focal point $\Delta = 4$ kpc (Fig. 3.6). The value of the new frequency decreases for larger values of the constant C_0.

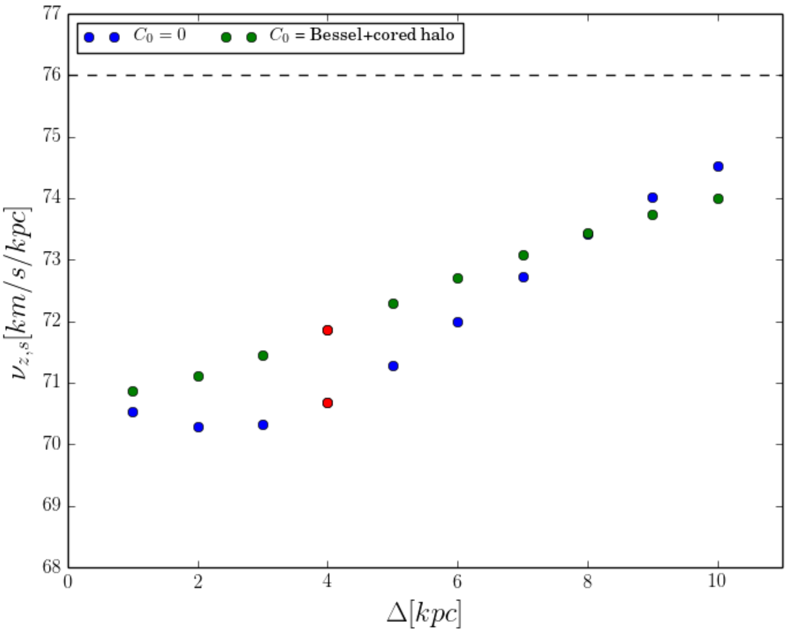

Figure 3.5: 'Vertical' oscillation frequency for the logarithmic potential for values of the focal point between 1 and 10 kpc, with zero integration constant C_0 (blue points) and C_0 which normalises the 'radial' potential to a two-component model composed by a Bessel disc plus a cored isothermal halo (green points) with values given by (Golubov 2012). The red points correspond to the case of $\Delta = 4$ kpc for the two different integration constants.

3.5.2 Radial profile

We consider the region of the extended solar neighbourhood, a region of 2 kpc around the Sun, corresponding to a distance from the Galactic centre between 6 and 10 kpc. We plot in Fig. 3.7 the total radial profile for the logarithmic case, assuming the integration constant corresponding to a two-component model (Bessel disc plus cored isothermal halo). For smaller values of Δ we obtain larger values of the density at small galactocentric radii ($6 \leq R \leq 8$ kpc) and lower values at large radii ($8 \leq R \leq 10$ kpc). The greater Δ is, the lower becomes the density in the inner part of the Galaxy and the greater in the outer part (Fig. 3.7). We calculate the total radial density profiles also for different values of C_0 holding fix $\Delta = 4$ kpc (Fig. 3.8). In this case there is no change in the slope of the radial profile.

It is possible to subtract the contribution of the dark matter using a cored isothermal profile ($\rho(R) = \rho_{0,dm}R_c^2/(R^2+R_c^2)$), where R_c is the core radius and $\rho_{0,dm}$ is the corresponding centred dark matter density. We can choose that the local dark matter density is approximately 10% of the total density and a value $R_c = 3.5$ kpc for the core radius. This value is required for a cored isothermal profile in order to produce a flat rotation curve at R_0, together with a Bessel disc, as in the Golubov-Just model (Golubov 2012).

After that we subtract the dark matter density profile from the total density, we can compare the

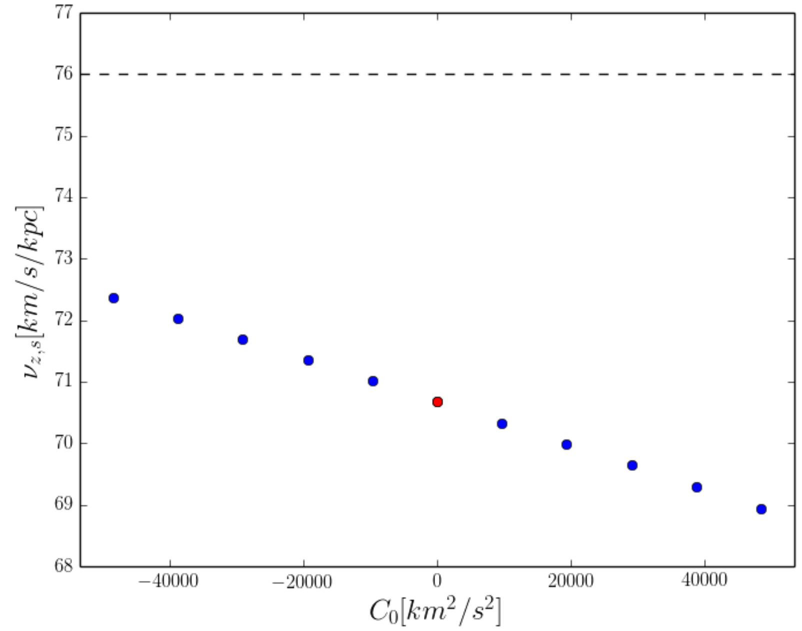

Figure 3.6: ’Vertical’ oscillation frequency for the logarithmic potential for values of C_0 between $-v_0^2$ and v_0^2 for $\Delta = 4$ kpc. The red point corresponds to the case for $\Delta = 4$ kpc and $C_0 = 0$.

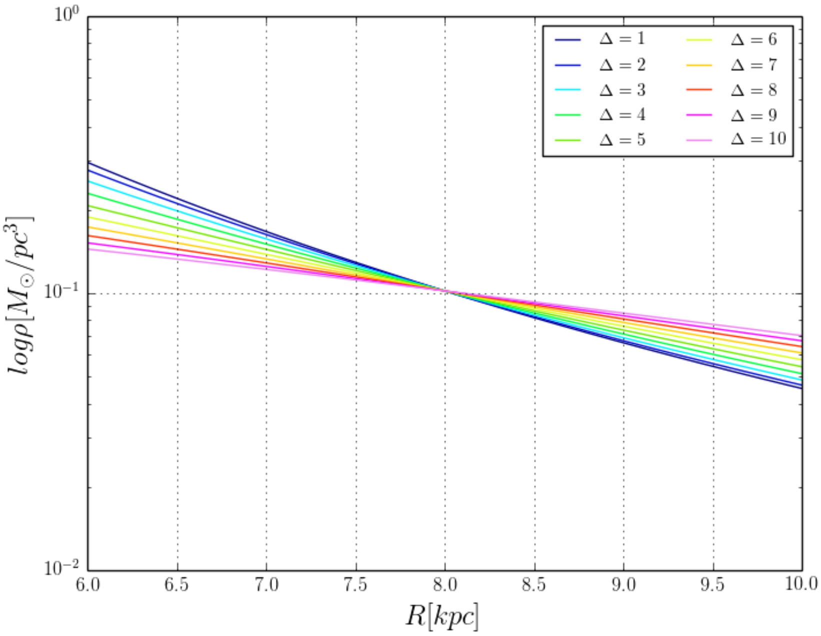

Figure 3.7: Radial density profile for the logarithmic potential for different values of Δ and with integration constant C_0 normalised to a value corresponding to the case of a two-component (Bessel disc plus cored isothermal halo) model.

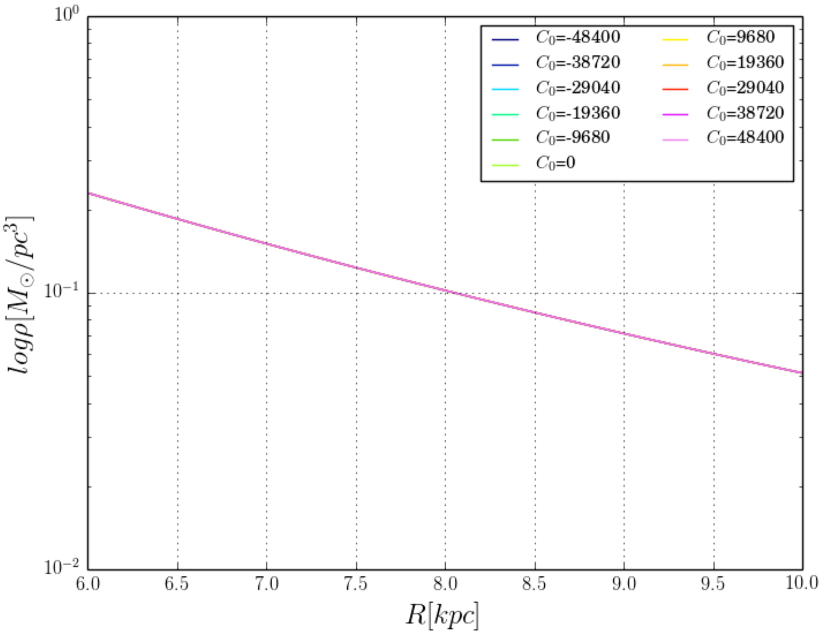

Figure 3.8: Radial density profile for the logarithmic potential for different values of $C_0[-v_0^2 : v_0^2]$ for $\Delta = 4$ kpc.

results with an exponential radial density profile for the case of $\Delta = 4$ kpc and with a radial scale length $R_d = 2.55$ kpc (Fig. 3.9). The difference of the density profile for $\Delta = 4$ kpc with respect to an exponential profile is less than 10%. The difference is small and inside the observational errors. Taking 10% error in the radial scale length the radial density for $\Delta = 4$ kpc is in agreement with an exponential profile. With this observational error, however, also the radial profiles for $\Delta = 3$ and 5 kpc are in agreement. For this reason we need a smaller error for the scale length to be able to distinguish between the possible profiles and to confirm if $\Delta = 4$ kpc is the correct choice for the selected spheroidal coordinate system. The radial profiles change from $R^{-3.8}$ for $\Delta = 1$ kpc to $R^{(-1.2\div-1.7)}$ for $\Delta = 10$ kpc.

We can derive the radial density (Eq. 3.19) with respect to R:

$$\frac{\partial\rho}{\partial R} = \frac{1}{4\pi G}\left[-v_0^2\frac{2R}{(R^2+\Delta^2)^2} - 4R\frac{(R_0^2+\Delta^2)}{(R^2+\Delta^2)^3}G_0'' + 2\frac{\Delta^2}{(R^2+\Delta^2)^2}\frac{v_0^2}{R} - \frac{8R\Delta^2}{(R^2+\Delta^2)^3}\left(v_0^2\log\left(\frac{R}{\Delta}\right)+C_0\right)\right]$$

and together with Eq. 3.16 we can obtain the radial scale length for the logarithmic potential.

We find a correlation between the radial scale length and the value of the focal point Δ. The scale length is small for smaller values of Δ and increases for greater values of Δ (Fig. 3.10). The values at R_0 change from $R_d = 2$ kpc for $\Delta = 1$ kpc increasing up to $R_d = 5.2$ kpc for $\Delta = 10$ kpc. The observational values for the scale length are between 2 and 3 kpc, thus we can exclude values for Δ greater than 5 kpc. We can also change the value C_0 holding fix the value for $\Delta = 4$ kpc but the radial scale length does not change (Fig. 3.11). It is not possible to change the slope of the radial profile and the scale length changing the integration constant.

The result for $\Delta = 4$ kpc is a radial scale length of 2.55 kpc at R_0, changing from a value of 2.2 kpc at 6 kpc and increasing up to 3 kpc at 10 kpc, corresponding to a ~13% variation in the extended solar neighbourhood.

We can notice that the radial scale length is constant for a value of $\Delta = 8$ kpc (Fig. 3.10). The profile generated by the Stäckel potential for $\Delta = 8$ kpc and an exponential profile with scale length $R_d = 4.23$

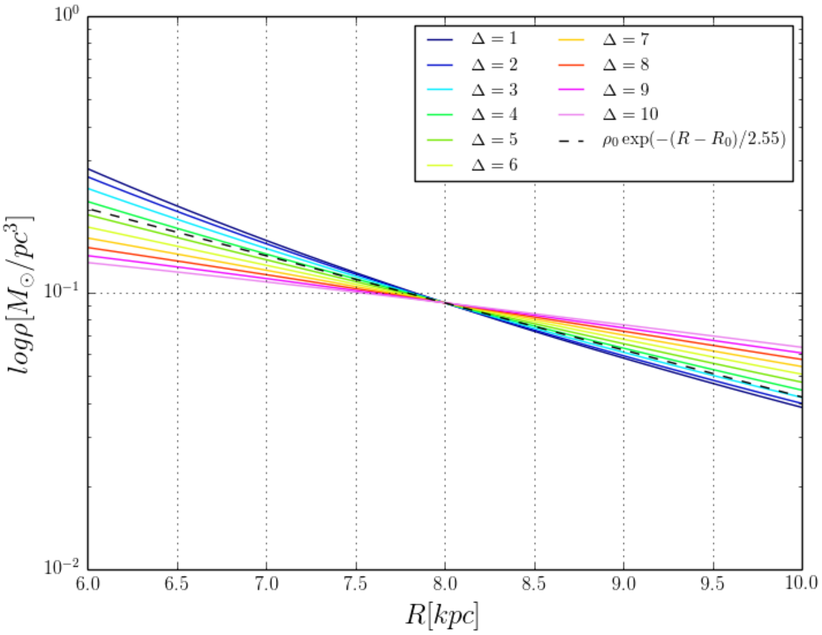

Figure 3.9: Radial density profile for the logarithmic potential after the subtraction of the dark matter profile for different values of Δ and with integration constant C_0 normalised to a value corresponding to the case of a two-component (Bessel disc plus cored isothermal halo) model. The dashed line corresponds to an exponential profile for the case $\Delta = 4$ kpc with a radial scale length of $R_d = 2.55$ kpc.

kpc match perfectly. However, this value for R_d is neither in agreement with the observations nor with the value derived from the observed tilt of the velocity ellipsoid.

3.6 Power-law case

3.6.1 Rotation curve

The second case of interest is a more general case, assuming a power law behaviour for the rotation curve:

$$v_c = v_0 \left(\frac{\Delta \sinh u}{\Delta \sinh u_0} \right)^{\alpha} = v_0 \left(\frac{R}{R_0} \right)^{\alpha}$$

where v_0 and u_0 are the values of the circular velocity and the coordinate u at the solar neighbourhood. The parameter α is the slope of the rotation curve. The last relation is considered in the plane after the conversion to cylindrical coordinates. The first derivative $F'(u)$ can be determined from Eq. 3.8:

$$F'(u) = v_0^2 \left(\frac{\Delta \sinh u}{\Delta \sinh u_0} \right)^{2\alpha} \frac{\cosh u}{\sinh u}$$

After the integration of the last expression, the resulting gravitational potential is a power-law as well:

$$F(u) = \frac{v_0^2}{2\alpha} \left(\frac{\Delta \sinh u}{\Delta \sinh u_0} \right)^{2\alpha} + C_0$$

We consider the case of a power-law potential with a slope $\alpha = 0.1$.

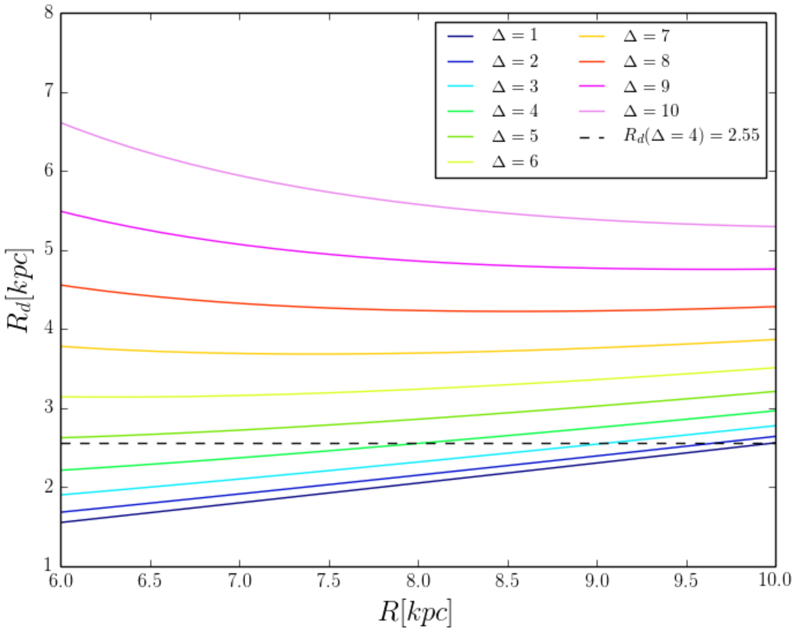

Figure 3.10: Radial scale length for the logarithmic potential (after the subtraction of the dark matter) for different values of Δ and with integration constant C_0 normalised to a value corresponding to the case of two-component (Bessel disc plus cored isothermal halo) model.

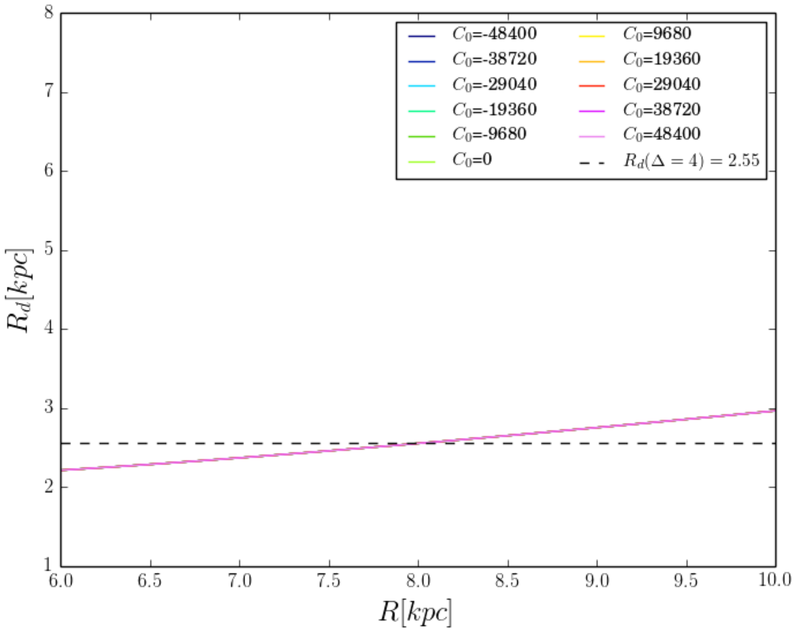

Figure 3.11: Radial scale length for the logarithmic potential (after the subtraction of the dark matter) for $\Delta = 4$ kpc and for different values of $C_0[-v_0^2 : v_0^2]$.

3.6.2 Local density

We focus on the first two terms of the Laplacian, which express the 'radial' dependence. Inserting the 'radial' potential $F(u)$ and its first derivative $F'(u)$ in Eq. 3.13, we obtain the radial density, and transforming it back in cylindrical coordinates we find:

$$\rho(R) = \frac{1}{4\pi G}\left[v_0^2\left(\frac{R}{R_0}\right)^{2\alpha}\left(\frac{2\alpha}{R^2}+\frac{1}{R^2+\Delta^2}\right) - G_0''\frac{R_0^2+\Delta^2}{(R^2+\Delta^2)^2} + \frac{2\Delta^2}{(R^2+\Delta^2)^2}(F(R)+C_0)\right] \quad (3.20)$$

From the radial part in the Laplacian two terms result: one is proportional to the angular velocity ($\propto \Omega^2$), as for the logarithmic case, while the second term is related to the Oort's parameters. The Oort's parameters for the rotation curve with a slope $\alpha = 0.1$ at the solar neighbourhood are: $A = 12.375$ km/s/kpc and $B = -15.125$ km/s/kpc (Fig. 3.12). The second term is much smaller than the oscillation frequency term and can be neglected for a nearly flat rotation curve.

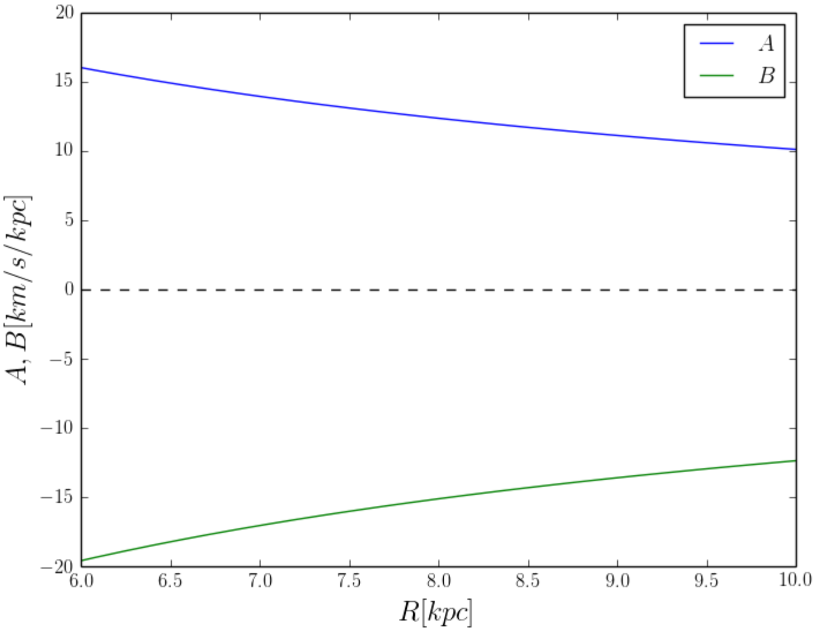

Figure 3.12: Variation of the Oort's parameters A and B with radius.

We can substitute in Eq. 3.20 the value $R = R_0$. Thus the expression for the local density is:

$$v_{z,s}^2 = -G_0''\frac{1}{(R_0^2+\Delta^2)} = \left(4\pi G\rho_0 - v_0^2\left(\frac{2\alpha}{R_0^2}+\frac{1}{R_0^2+\Delta^2}\right) - 2\frac{\Delta^2}{(R_0^2+\Delta^2)^2}\left(v_0^2+C\right)\right)$$

We want to reproduce the value of the local density found by Holmberg & Flynn (2000) ($\rho_0 = 0.102$ $M_\odot/pc^3$), and we can derive from it the value for the vertical oscillation frequency $v_{z,0} = 76$ km/s/kpc. Then we obtain different values of $v_{z,s}$ for different values of the focal point Δ (Fig. 3.13). We set the integration constant C_0 in a way that the power-law potential has at R_0 the same value as a two-components model (Bessel disc plus cored isothermal halo). In this way we can compare the results of the two cases. For a global fit the constant C_0 should be set to zero, but it can assume also other values for a local fit. We find a value of ~71 km/s/kpc for $\Delta = 4$ kpc, which is ~8% lower than the vertical oscillation frequency $v_{z,0}$. This difference comes from the first term, which is due to the curvature of the coordinate system, and the last term. The value for the new frequency increases with Δ and tends to $\nu_{z,0}$ for large values of Δ. If we use the value for the vertical oscillation frequency corresponding to the

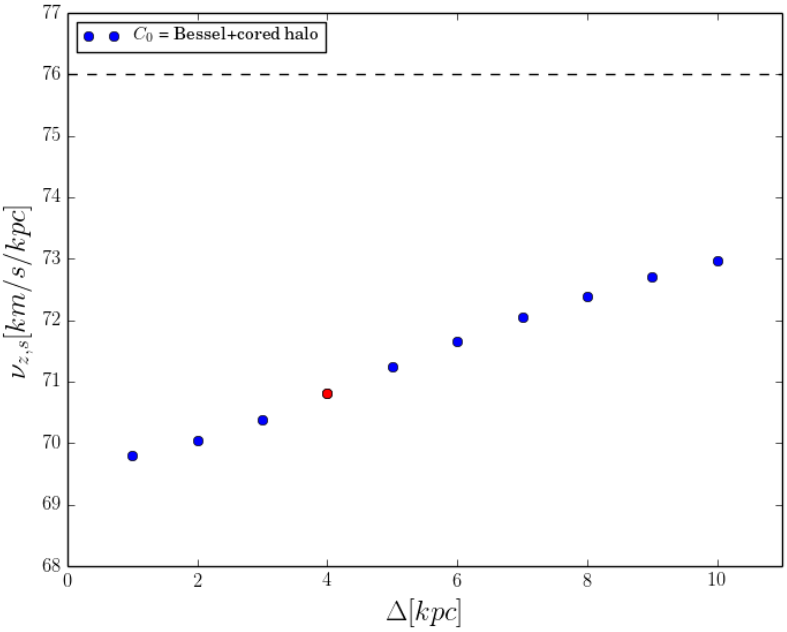

Figure 3.13: 'Vertical' oscillation frequency for the power-law potential for values of the focal point between 1 and 10 kpc, with C_0 normalised to a value corresponding to the case of a two-component model (Bessel disc plus cored isothermal halo). The red point corresponds to the case for Δ = 4 kpc.

cylindrical case, the value for the local density will be ~5% greater than what was found by Holmberg & Flynn (2000).

3.6.3 Radial profile

Now, we consider the region of the extended solar neighbourhood, corresponding to a region of 2 kpc radius around the solar position. We plot lines for the radial density profiles changing the value of Δ from 1 to 10 kpc (Fig. 3.14). For smaller values of Δ the density is larger at smaller radii and lower at larger radii. The greater Δ is, the lower is the density at smaller radii and the greater at larger radii. The larger the value of Δ is, the more cylindrical and the less spherical becomes the coordinate system.

We can subtract the contribution of the dark matter and obtain the radial density profile for the tracers only (Fig. 3.15), so that we can compare the result with the observations. We assume a cored isothermal profile for the dark matter with a value for the local dark matter density of 10% of the total mass density ρ_0. The value for the core radius is 3.5 kpc as in Golubov (2012). The radial density profile for the tracers is almost in agreement with the logarithmic case, they would match perfectly in the case of the coefficient α, which regulates the slope of the rotation curve, being zero. The radial density profiles change from $R^{-3.8}$ for Δ = 1 kpc to $R^{(-1.2\div-1.7)}$ for Δ = 10 kpc. For the case Δ = 10 kpc the radial density profile is proportional to $R^{-1.2}$ at smaller radii and to $R^{-1.7}$ at larger radii.

The overplotted dashed line in Fig. 3.15 corresponds to an exponential profile for the case Δ = 4 kpc with scale length of R_d = 2.6 kpc. The difference of the density profile for Δ = 4 kpc with respect to an exponential profile is less than 10% and thus is small and inside the observational errors. Taking 10% error in the radial scale length, the radial density for Δ = 4 kpc is in agreement with an exponential

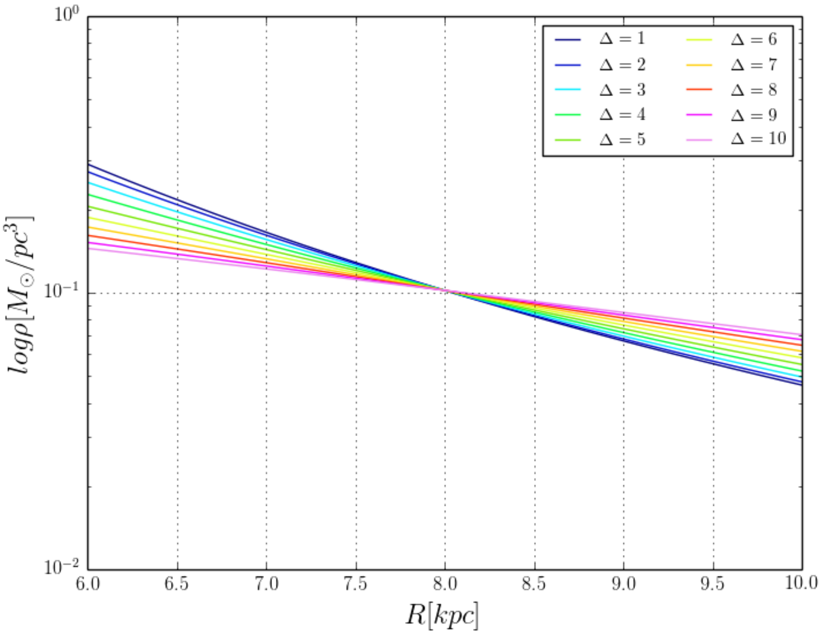

Figure 3.14: Radial density profile for the power-law potential for different values of Δ with C_0 normalises to a value corresponding to a two-component model (Bessel disc plus cored isothermal halo).

profile. With this observational error, however, also the radial profiles for $\Delta = 3$ and 5 kpc are in agreement. We need a smaller error than 10% for the scale length to be able to distinguish between the possible radial profiles and to confirm if $\Delta = 4$ is the correct choice for the selected spheroidal coordinate system.

We can derive the radial density (Eq. 3.20) with respect to R:

$$\frac{\partial\rho}{\partial R} = \frac{1}{4\pi G}\left[v_0^2\left(\frac{R}{R_0}\right)^{2\alpha}\left(-\frac{4\alpha}{R^3} - 2R\frac{1}{(R^2+\Delta^2)^2}\right) + 2\alpha\frac{v_0^2}{R}\left(\frac{R}{R_0}\right)^{2\alpha}\left(\frac{2\alpha}{R^2} + \frac{1}{R^2+\Delta^2}\right)\right.$$
$$\left. -4R\frac{R_0^2+\Delta^2}{(R^2+\Delta^2)^3}G_0'' - 2\frac{4R\Delta^2}{(R^2+\Delta^2)^3}F(R) + \frac{2\Delta^2}{(R^2+\Delta^2)^2}\frac{v_c^2}{R}\right]$$

and together with the Eq. 3.16 we can obtain the radial scale length for the power-law potential.

We find small scale lengths for smaller values of Δ and the values increase for greater values of Δ. Values for the observed radial scale length are between 2 and 3 kpc and the results exclude large values for Δ between 6 and 10 kpc (Fig. 3.16).

The value for the scale length for $\Delta = 4$ kpc at the solar neighbourhood is $R_d = 2.6$ kpc, less than 2% different from the logarithmic case. We can use this value in an exponential density profile and compare it to the radial density profile found for $\Delta = 4$ kpc (Fig. 3.17). The difference between the radial density profile for $\Delta = 4$ kpc and an exponential profile with the corresponding scale length $R_d = 2.6$ kpc is less than 10% . This result is in agreement with observations, because there is approximately a 10% error in the scale length and we do not know if the density is really exponential or not.

We can notice that the radial scale length is constant for a value of $\Delta = 8$ kpc (Fig. 3.16). The profile generated by the Stäckel potential for $\Delta = 8$ kpc and an exponential profile with scale length $R_d = 4.3$ kpc match perfectly (Fig. 3.18). However, this value for R_d is not in agreement with the observations. Furthermore, the value of Δ is not in agreement with the values derived from the observed tilt of the

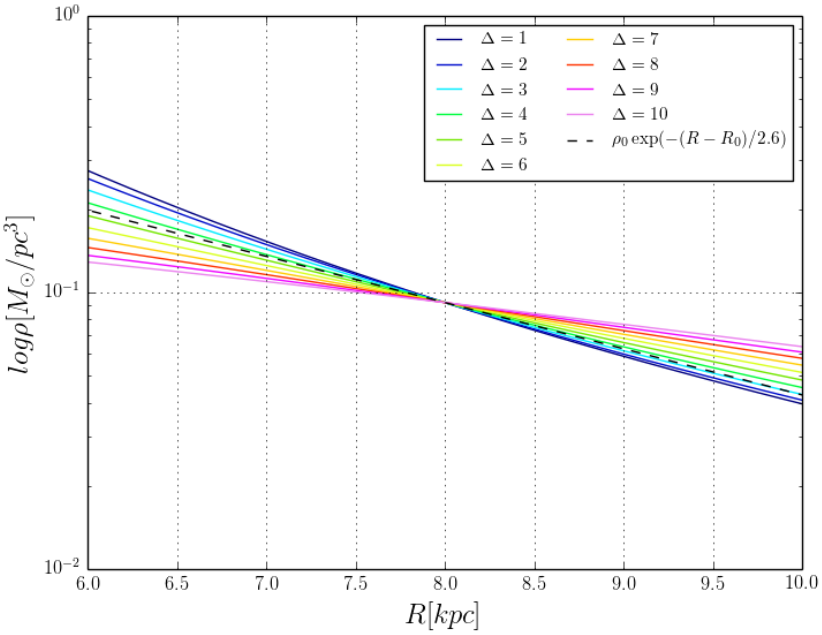

Figure 3.15: ’Vertical’ oscillation frequency for the power-law potential for values of the focal point between 1 and 10 kpc.

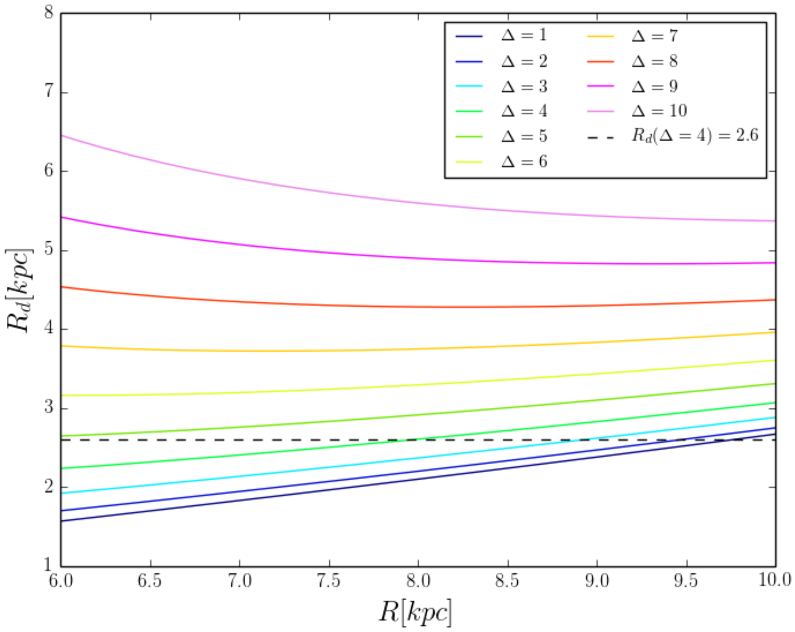

Figure 3.16: Radial scale length for the power-law potential for different values of Δ with C_0 normalised to a case corresponding to the case of a two-component (Bessel disc plus cored isothermal halo) model.

velocity ellipsoid. For this case the tilt angle would be ~4.1° at 1 kpc away from the plane (see Table 3.1). Even when assuming the largest errorbar of 1.8° (Siebert et al. 2008), this value is significantly smaller than the observations in the recent years. Assuming a power-law potential with a slope of $\alpha = 0.1$, it increases slightly the values for the radial scale lengths for all values of Δ with respect to the logarithmic case.

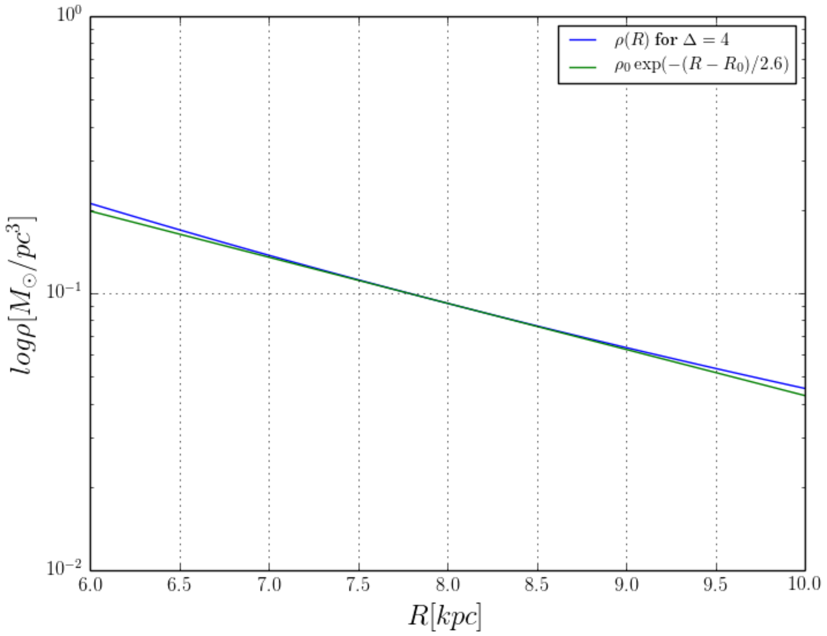

Figure 3.17: Comparison between the radial density profile generated by a power-law potential with $\Delta = 4$ kpc and the exponential density profile with scale length $R_d = 2.6$ kpc.

If the rotation curve is exactly flat ($\alpha = 0$) we obtain the logarithmic case. We can also look what happens when holding fix the value of $\Delta = 4$ kpc and changing the slope of the rotation curve, i.e. changing the value of α from -0.5 to 0.5 (Fig. 3.19). For smaller values of α we have greater values for the radial density at smaller radii and lower at larger radii. However, the density changes only slightly for different values of α. The radial scale length never remains constant and can reach large excursions between 6 and 10 kpc in radius for great and positive values of α (Fig. 3.20). The case for $\alpha = 0$ is shown by the dashed line and the scale length changes between 2.2 and 3 kpc in the extended solar neighbourhood. The largest excursion is for the slope $\alpha = 0.5$ where the scale length changes from 2.4 to 3.8 kpc, with a variation of $\sim 40\%$ in the region of the extended solar neighbourhood.

3.7 Isopotential lines

An old idea was that the velocity ellipsoid is aligned with the gravitational force lines in the case of Stäckel potential. We want to understand if there is some correlation between the orientation of the velocity ellipsoid and the gravitational potential by looking at the isopotential lines. We define α as the angle between the axis of the velocity ellipsoid in the meridional plane pointing towards the Galactic centre and a plane parallel to the midplane, and β as the angle shaped by the gravitational force lines between the vertical and radial force components (see Fig. 3.21).

We know that these two angles are equal in the midplane, but their behaviour above the plane is unknown and can be different. We want to calculate the first z-derivatives in the plane, so that we can have an idea how these two quantities behave near the plane and which is the link between the two. If the

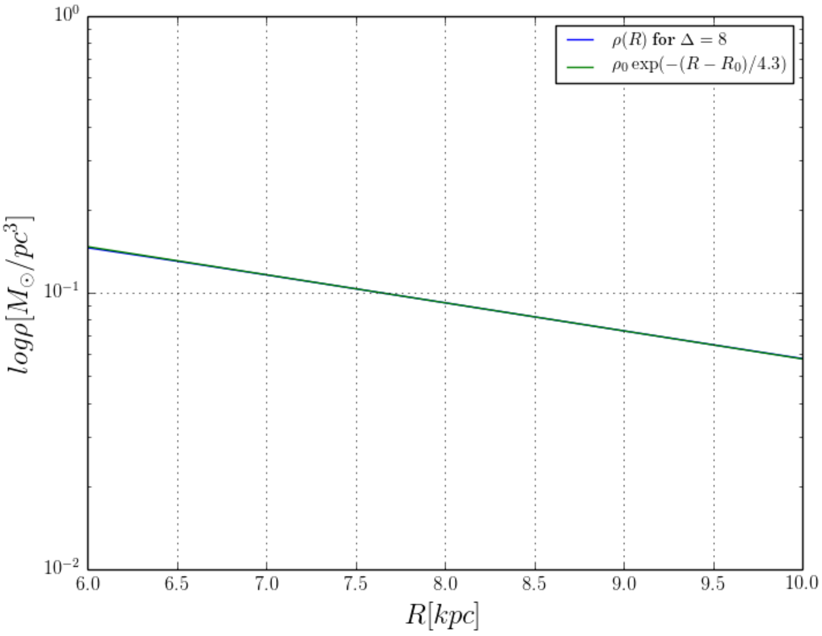

Figure 3.18: Comparison between the radial density profile generated by a power-law potential with Δ = 8 kpc and the exponential density profile with scale length R_d = 4.3 kpc.

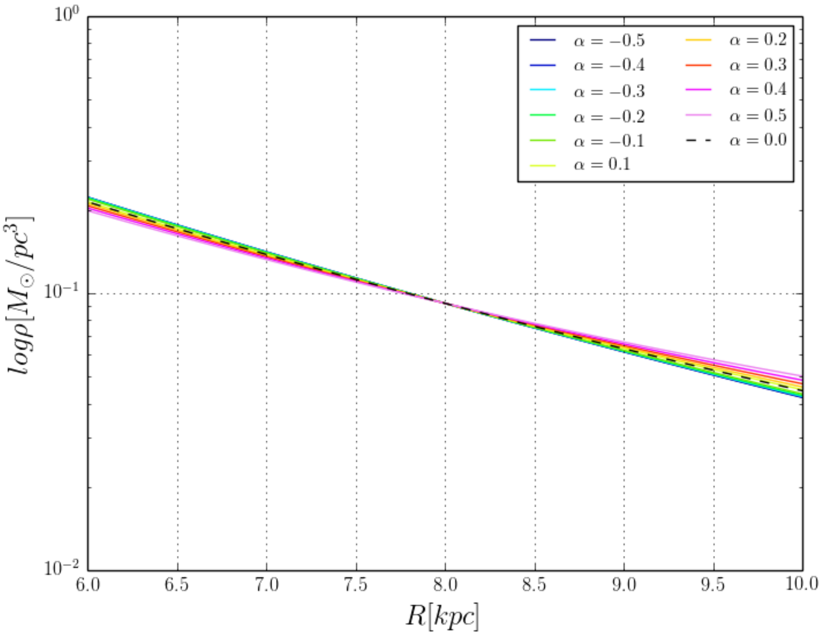

Figure 3.19: Radial density profile for the power-law potential for Δ =4 kpc with different values of the power-law index α[-0.5:0.5]. The dashed line corresponds to the case of α = 0 which corresponds to the logarithmic case.

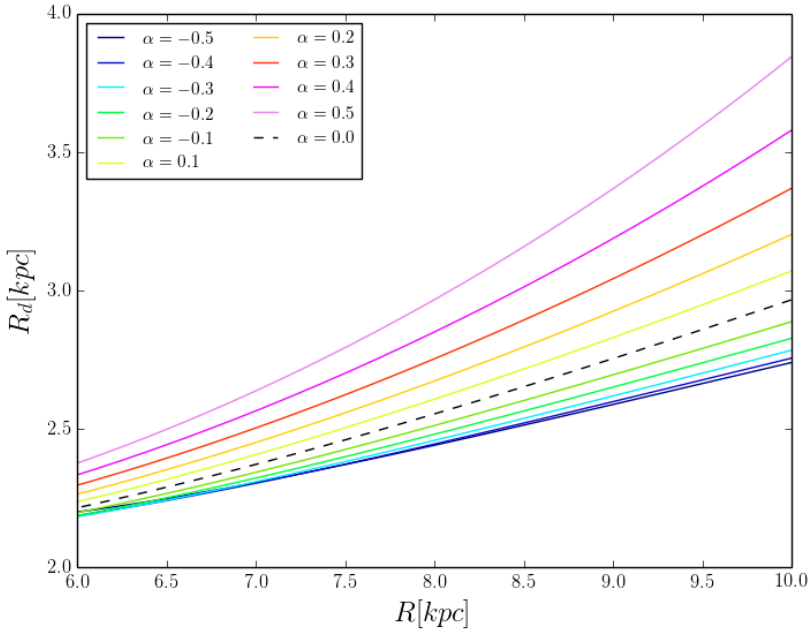

Figure 3.20: Radial scale length for the power-law potential for $\Delta = 4$ kpc with different values of the power-law index α[-0.5:0.5]. The dashed line corresponds to the case of $\alpha = 0$ which corresponds to the logarithmic case.

two z-derivatives are equal, it means that the velocity ellipsoid is aligned perpendicular to the isopotential lines close to the plane.

We have already considered the cylindrical case in Chapter 2, where we compared the inclination of the velocity ellipsoid (angle α) with the angle β derived from the Jeans equation. Now, we consider the case for the spheroidal coordinates where the orientations of the velocity ellipsoid and the angle β are given by the Stäckel model. We are not using the Jeans equation directly, because it would require the knowledge about the Jeans equations in spheroidal coordinates. We convert the derivatives from cylindrical to spheroidal coordinates and compare the result with the one of Chapter 2.

At first, we examine if these two angles are the same. Therefore, we look at the isopotential lines of a gravitational potential, like the three-component Plummer-Kuzmin potential used by Just et al. (2009) and Ernst et al. (2011) to describe the Milky Way, as well as the isocoordinate lines of the generated spheroidal coordinate system. It is immediately possible to see that these two angles cannot be the same, because the lines are not orthogonal to each other (see Fig. 3.22).

We transform the calculation done for $\partial_z \tan\beta$ in Chapter 2 in spheroidal coordinates and we calculate the result for $z = 0$:

$$\partial_z \tan\beta = \partial_z \frac{\partial\Phi/\partial z}{\partial\Phi/\partial R} = \frac{\partial^2\Phi/\partial z^2}{\partial\Phi/\partial R} - \frac{\partial\Phi/\partial z \partial^2\Phi/\partial R\partial z}{(\partial\Phi/\partial R)^2} \tag{3.21}$$

Remember that the first derivative transforms as:

$$\frac{\partial}{\partial z} = \frac{\partial}{\partial u}\frac{\partial u}{\partial z} + \frac{\partial}{\partial v}\frac{\partial v}{\partial z}$$

and the second derivative as:

$$\frac{\partial^2}{\partial z^2} = \left(\frac{\partial}{\partial u}\frac{\partial u}{\partial z} + \frac{\partial}{\partial v}\frac{\partial v}{\partial z}\right)^2$$

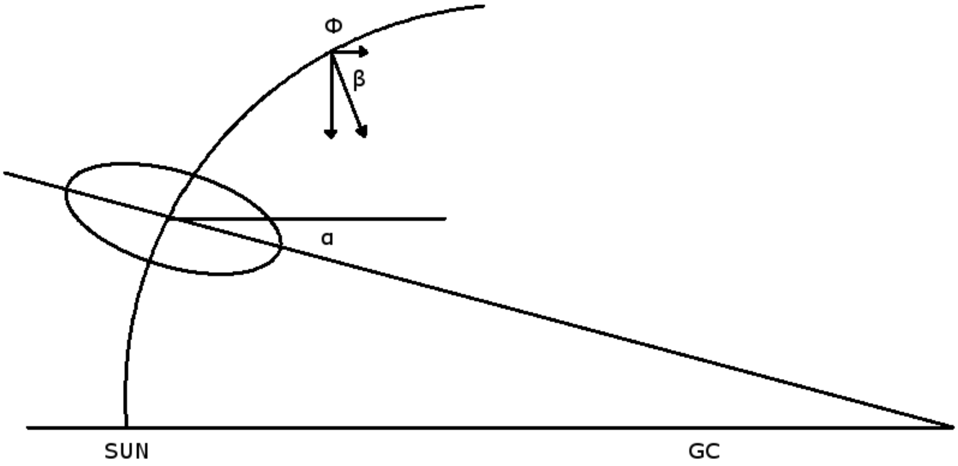

Figure 3.21: The sketch shows the angle α corresponding to the inclination of the velocity ellipsoid with respect to the Galactic plane and the angle β corresponding to the angle between the vertical and radial force components.

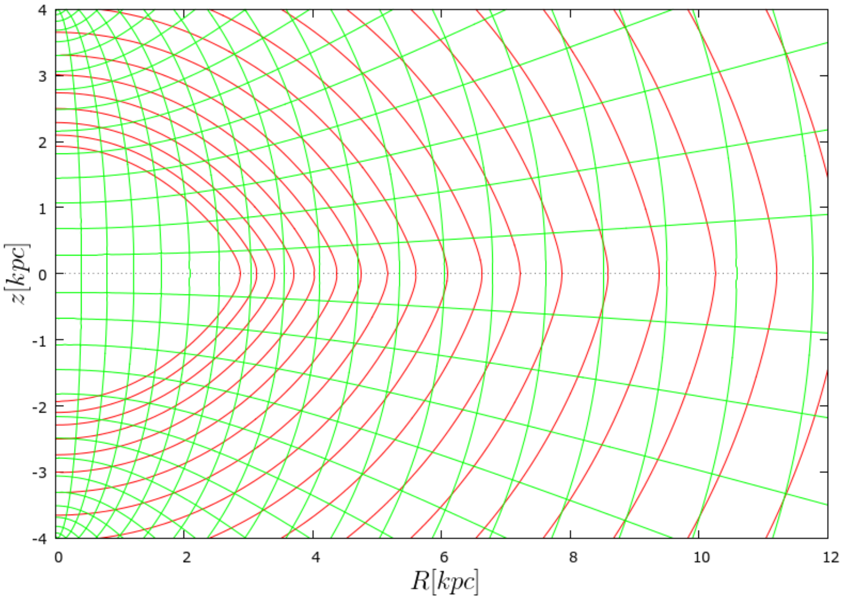

Figure 3.22: Isopotential (red) lines of a three-component Plummer-Kuzmin potential (Just et al. 2009) with isocoordinate (green) lines for a spheroidal coordinate system with Δ = 4 kpc.

Then the second term of Eq. 3.21 equals zero because the *u* coordinates fall perpendicular to the Galactic plane ($\partial u/\partial z|_{v=\pi/2} = 0$) and the v-derivative of the Stäckel potential is zero because we want to avoid a cusp in the potential in the plane ($\partial\Phi/\partial v|_{v=\pi/2} = 0$).

It remains only the first term that can be expressed in the new coordinates as:

$$\frac{\partial^2\Phi}{\partial z^2} = \frac{\partial^2\Phi}{\partial u^2}\left(\frac{\partial u}{\partial z}\right)^2 + \frac{\partial\Phi}{\partial u}\frac{\partial^2 u}{\partial z^2} + \frac{\partial^2\Phi}{\partial v^2}\left(\frac{\partial v}{\partial z}\right)^2 + \frac{\partial\Phi}{\partial v}\frac{\partial^2 v}{\partial z^2} + 2\frac{\partial^2\Phi}{\partial u\partial v}\frac{\partial u}{\partial z}\frac{\partial v}{\partial z}$$

For the reasons mentioned above and for the fact that the second mixed derivative of the potential ($\partial^2\Phi/\partial u\partial v$) is zero everywhere, only the second and the third terms remain in the plane. Then, it remains:

$$\partial_z \tan\beta|_{z=0} = \left[\frac{\partial^2 u/\partial z^2}{\partial u/\partial R} + \frac{\partial^2\Phi/\partial v^2}{\partial\Phi/\partial u}\frac{(\partial v/\partial z)^2}{\partial u/\partial R}\right]_{v=\pi/2}$$

The first term results in:

$$\left[\frac{\partial^2 u/\partial z^2}{\partial u/\partial R}\right]_{v=\pi/2} = \frac{1}{R}\frac{R^2}{R^2+\Delta^2} = \partial_z \tan\alpha|_{z=0}$$

which is $\partial_z \tan\alpha|_{z=0}$ as we have already found in Eq. 3.6.

The term including the derivatives of the Stäckel potential reads:

$$\left[\frac{\partial^2\Phi/\partial v^2}{\partial\Phi/\partial u}\right]_{v=\pi/2} = \frac{-G_0'' + 2F(u)/\cosh^2 u}{v_0^2 \cosh u/\sinh u} = \frac{v_{z,0}^2(R^2+\Delta^2) - v_0^2}{v_0^2\sqrt{R^2+\Delta^2}/R}$$

where the last relation is the conversion in cylindrical coordinates. The complete second term is:

$$\left[\frac{\partial^2\Phi/\partial v^2}{\partial\Phi/\partial u}\frac{(\partial v/\partial z)^2}{\partial u/\partial R}\right]_{v=\pi/2} = \frac{v_{z,0}^2}{v_0^2/R} - \frac{R}{R^2+\Delta^2}$$

Putting together the first and second term, we obtain:

$$\partial_z \tan\beta|_{z=0} = \frac{1}{R}\left(\frac{v_{z,0}^2}{\Omega^2}\right) \sim \frac{7.6}{R}$$

We are able to obtain the same result as in Chapter 2 which was that the velocity ellipsoid is not aligned with the gravitational force lines both for the cylindrical case and for the case of Stäckel potentials. The difference between the derivatives of the two angles is approximately a factor of 8. This value is large because the potential is flattened. The two angles are aligned only in special cases like the spherical potential, but there is no direct link between the two quantities. From the knowledge of the orientation of the ellipsoid we cannot derive directly the shape of the gravitational potential.

3.8 Vertical structure

We have derived the radial profile from the rotation curve and the second 'vertical' derivative of the potential in the plane from the local density.

Now, we want to determine the vertical structure for the Stäckel potential. From an Ansatz for the 'vertical' potential $G(v)$, we can calculate the vertical gravitational force K_z. Then, by dividing the vertical force by ($2\pi G$), we obtain a measure for the vertical surface density $\Sigma(z)$. The vertical surface density is usually determined at a distance of 1.1 kpc away from the midplane. Above this distance there is no further contribution from the luminous matter and an increase in the vertical surface density is due to the dark matter only. Values found for the K_z-force are between 70 − 80 $M_\odot/\mathrm{pc}^2$ at 1.1 kpc above the plane (Kuijken & Gilmore 1989; Siebert et al. 2003; Holmberg & Flynn 2004), while the baryonic matter contributes around 50−60 $M_\odot/pc^2$ (Holmberg & Flynn 2004; Bovy et al. 2012a; Bovy & Tremaine 2012). These values include both stellar and gas component, with a value of 13 $M_\odot/pc^2$ for the last one (Just & Jahreiß 2010).

We want to reproduce the observational values for the surface density found by Holmberg & Flynn (2004), where $K_z = (76 \pm 6)\ M_\odot/pc^2$ at 1.1 kpc above the plane with a contribution of $(56 \pm 6)\ M_\odot/pc^2$ given by the baryonic matter.

We are looking for a 'vertical' function for $G(v)$ that is as simple as possible, and from which we can derive the K_z-force and the second derivative up to the second order. The value of the second order derivative of the $G(v)$ in the plane has to match with what we found from the value of the local density. From Eqs. 3.1 we can find that at fixed radius ($R = R_0$), the coordinate z results:

$$z|_{R=R_0} = \sqrt{R_0^2 + \Delta^2 \sin^2 v}\frac{\cos v}{\sin v}$$

When we study the situation at larger distance from the plane, the v coordinate becomes smaller ($v \to 0$). This means that we move along the ellipses, towards the focal point Δ and the coordinate z reaches a divergence. Hence, there should be no z^2 term in $G(v)$, i.e. no linear term of z in the K_z-force arising from $V(v)$.

We have to take this into account when we write down a form for the 'vertical' potential. The function $G(v)$ can depend on the coordinate v only, and not on u. This is the way how Stäckel potentials are defined (Eq. 3.7). If we want to reproduce, for example, a potential linearly dependent on the coordinate z, the function $G(v)$ cannot be written as:

$$G(u, v) = \Delta \cosh u \cos v$$

because the function $G(v)$ would depend on both curvilinear coordinates u and v, or as

$$G(v) = \sqrt{R_0^2 + \Delta^2 \sin^2 v}\frac{\cos v}{\sin v}$$

The second relation is the conversion of the coordinate u to v at fixed radius R_0. The best way is to write $\cosh u$ as a constant, $\cosh u_0$, where u_0 is the value assumed from the coordinate u in the plane $(R_0, 0)$. Therefore the $G(v)$ potential is a function of $\cos v$ only.

We want to use the approximation given by Kuijken & Gilmore (1989) to describe the vertical structure (Eq. 2.7), that can be transformed in spheroidal coordinates as:

$$G(v) = -2\pi G\Sigma_0 \left(\sqrt{z_0^2 + \Delta^2 \cosh^2 u_0 \cos^2 v} - z_0 \right) - 2\pi G\rho_{0,dm}\Delta^2 \cosh^2 u_0 \cos^2 v$$

The first derivative of the 'vertical' potential function is:

$$G'(v) = 2\pi G\Sigma_0 \frac{\Delta^2 \cosh^2 u_0 \cos v \sin v}{\sqrt{z_0^2 + \Delta^2 \cosh^2 u_0 \cos^2 v}} + 4\pi G\rho_{0,dm}\Delta^2 \cosh^2 u_0 \cos v \sin v$$

and the second derivative in the plane is:

$$G''(v = \pi/2) = -2\pi G\Sigma_0 \frac{\Delta^2 \cosh^2 u_0}{z_0} - 4\pi G\rho_{0,dm}\Delta^2 \cosh^2 u_0$$

We know that the radial density is proportional to the second derivative of the Stäckel potential with respect to v:

$$\rho(R) \sim -\frac{1}{4\pi G}\frac{1}{R_0^2 + \Delta^2}\left(\frac{\partial^2 \Phi_s}{\partial v^2}\right)_{v=\pi/2} \sim -\frac{1}{4\pi G}\frac{G''(v = \pi/2)}{R_0^2 + \Delta^2}$$

$$= \frac{\Sigma_0}{2z_0} + \rho_{0,dm} = \rho_0$$

where $\Delta^2 \cosh^2 u_0 = (R_0^2 + \Delta^2)$ is the value in the plane and the values $\Sigma_0/(2z_0)$ and $\rho_{0,dm}$ correspond to the local volume density given by the baryonic and dark matter. This supports more the idea to construct $G(v)$ using $\Delta \cosh u_0$ as a constant value at the solar position $(R_0, 0)$ and depending only on $\cos v$ or $\cos^2 v$.

The expression for the gravitational force in the spheroidal coordinates reads:

$$K_z = -\frac{\partial \Phi}{\partial z} = -\left(\frac{\partial \Phi}{\partial v}\frac{\partial v}{\partial z} + \frac{\partial \Phi}{\partial u}\frac{\partial u}{\partial z}\right) \tag{3.22}$$

If the coordinates u fall perpendicular to the plane and are approximately invariant with height, the vertical force is given only by the first term:

$$K_z = -\frac{\partial \Phi_s}{\partial v}\frac{\partial v}{\partial z} = -\left[-\frac{V'(v)}{\sinh^2 u + \sin^2 v} - \frac{(U(u) - V(v))2\sin v \cos v}{(\sinh^2 u + \sin^2 v)^2}\right]\frac{\partial v}{\partial z} \tag{3.23}$$

where

$$V' = (\sinh^2 u_0 + \sin^2 v)G'(v) + 2G(v)\sin v \cos v \tag{3.24}$$

Substituting Eq. 3.23 and Eq. 3.24 in Eq. 3.22 we obtain four terms in the calculation:

$$\begin{aligned} K_z(z) = \Bigg[&-\frac{\sinh^2 u_0 + \sin^2 v}{\sinh^2 u + \sin^2 v}G'(v) - \frac{2G(v)\sin v \cos v}{\sinh^2 u + \sin^2 v} - \frac{2\cosh^2 u F(u) \sin v \cos v}{(\sinh^2 u + \sin^2 v)^2} \\ &+ \frac{2G(v)\sin v \cos v(\sinh^2 u_0 + \sin^2 v)}{(\sinh^2 u + \sin^2 v)^2}\Bigg]\frac{\partial v}{\partial z} \end{aligned} \tag{3.25}$$

We can rewrite it in this way:

$$K_z = \left[-sn(u,v)G'(v) - \frac{2G(v)\sin v \cos v}{\sinh^2 u + \sin^2 v}(1 - sn(u,v)) - \frac{2\cosh^2 u F(u)\sin v \cos v}{(\sinh^2 u + \sin^2 v)^2}\right]\frac{\partial v}{\partial z} \tag{3.26}$$

where

$$sn(u,v) = \frac{\sinh^2 u_0 + \sin^2 v}{\sinh^2 u + \sin^2 v}$$

is a function to take into account when we move away from the solar neighbourhood because this term is exactly equal to 1 at $u = u_0$. This is the force along the line of constant u. The farther we go from the plane and the larger the value of the focal point Δ is, the smaller are the variations of the coordinate u with z. For large values of Δ the K_z-force can be calculated using only the first term, because the force along the line of constant u corresponds to force along z.

However, if Δ tends to smaller values, we have to take into account also the second term in Eq. 3.22, i.e. the variation of the coordinate u with respect to z.

$$\frac{\partial \Phi_s}{\partial u}\frac{\partial u}{\partial z} = \left\{\frac{\cosh^2 u}{\sinh^2 u + \sin^2 v}F'(u) + \frac{2\sinh u \cosh u}{\sinh^2 u + \sin^2 v}\left[F(u)\left(1 - \frac{\cosh^2 u}{\sinh^2 u + \sin^2 v}\right) + sn(u,v)G(v)\right]\right\}\frac{\partial u}{\partial z} \tag{3.27}$$

The spheroidal coordinates lead to have many terms when we study the situation away from the plane. However, we have to consider all the terms if we want the correct variation of the vertical force with the coordinate z. Therefore, the vertical force is not only the first derivative $G'(v)$. This would be only a simplification because we already know that a radial term is coming from the v-derivative of the Stäckel potential. We consider the logarithmic case for the 'radial' profile.

Now, we have to fix two parameters to calculate the vertical force: the local volume density due to the baryonic $\rho_{0,b}$ and dark matter $\rho_{0,dm}$ contribution. The first parameter depends on the vertical surface density Σ_0 and the vertical scale height z_0. We want to reproduce the observational value of (76 ± 6) $M_\odot/pc^2$ for the local gravitational force ($R = R_0$) at 1.1 kpc away from the plane (Holmberg & Flynn 2004). By changing the vertical scale height, only the turning points of the curves derived for the K_z-force change. We need to change only Σ_0 and $\rho_{0,dm}$, and we use z_0 to make these value consistent with the value of the local volume density derived by Holmberg & Flynn (2000).

The vertical force along the coordinates ν is plotted in Fig. 3.23. The value for the vertical surface density Σ_0 is 55 $M_\odot/pc^2$ and for the local dark matter density 0.007 $M_\odot/pc^2$. These values together with the scale height $z_0 = 320$ pc give the same result for $G''(\nu = \pi/2)$ as in the logarithmic case for $\Delta = 4$ kpc, which reproduces the value of the local volume density. For different values of Δ, the value derived for the local volume density ρ_0 would be slightly different but inside the observational errors. If this is the gravitational force along the ν-coordinate, this means that we move along the ellipses and the gravitational force has to turn back to zero at larger distances from the plane.

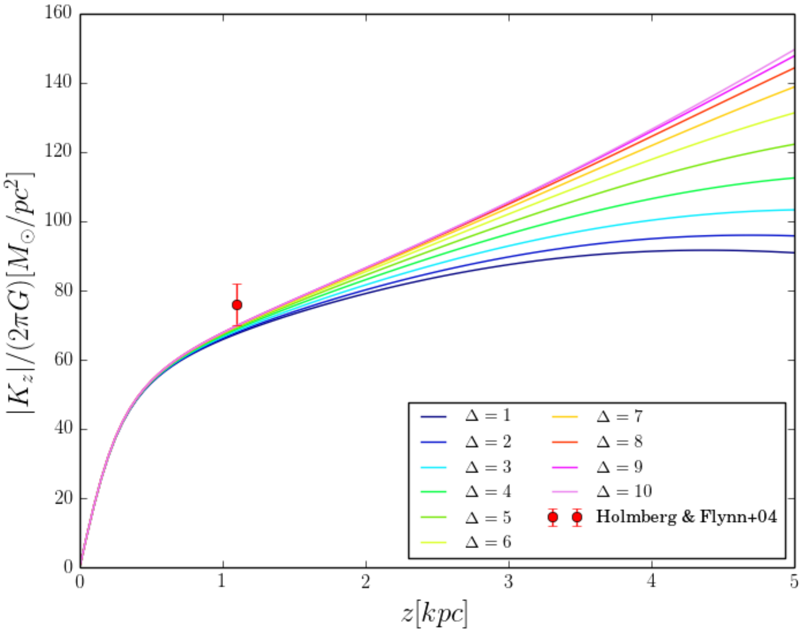

Figure 3.23: Local K_z-force along the ν-coordinate using the approximation given by Kuijken & Gilmore (1989) for the 'vertical' potential $G(\nu)$ for different values of Δ. The observational constrain is given by Holmberg & Flynn (2004).

We could change these parameters, so that we can fit the observational values. We need to increase either the local surface density or the local dark matter density. However, the selected values are given by using the complete formula for the conversion of the vertical force in spheroidal coordinates. The results can be seen in Fig. 3.24. With these parameters we can fit the value of 76 $M_\odot/pc^2$ for the local vertical force at 1.1 kpc. The complete formula gives the local vertical force and its dependence on the z-coordinate. It takes into account the variation of the coordinate u with respect to z. The smaller the value of Δ is, the greater is the variation of u with respect to z. The coordinates become more spherical and the value of the derivative du/dz becomes larger. We can see this effect, where the curves of the K_z for small values of Δ are rounder than for large values of Δ. At 1.1 kpc the K_z-force for small values of Δ is larger than that for large values of Δ, but it becomes smaller at large heights. The vertical force for large values of Δ corresponds to cylindrical case. It increases linearly, then it turns to a second linear increase with different slope, due to the contribution of the dark matter. The vertical force lines for different values of Δ start to separate at small distance from the plane. This is because the local dark matter density changes in the meridional plane. It would be interesting to derive the local dark matter density values for each value of Δ to obtain one line only corresponding to the vertical force.

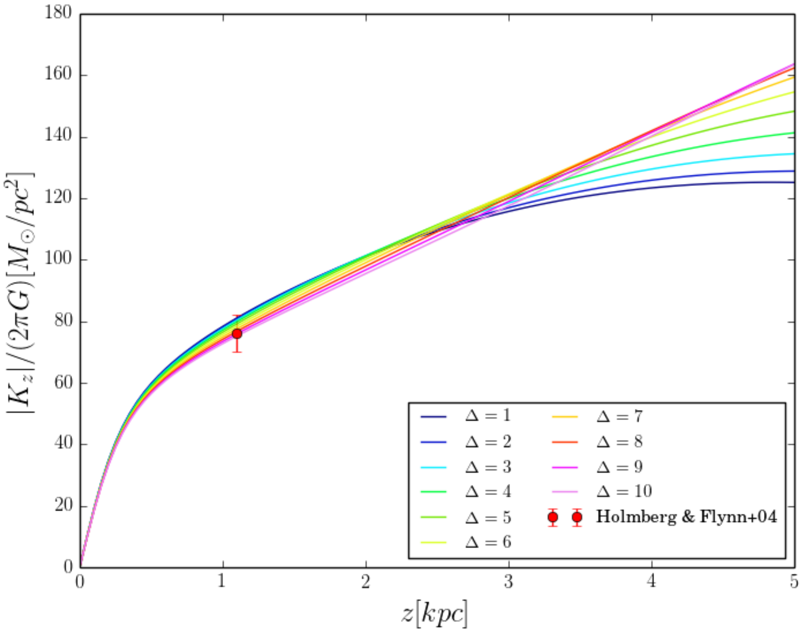

Figure 3.24: Local K_z-force using the approximation given by Kuijken & Gilmore (1989) for the 'vertical' function $G(v)$, adopting the complete formula 3.22, for different values of Δ. The observational constrain is given by Holmberg & Flynn (2004).

After we have fixed the two parameters, we do not have any further free parameter. We can make predictions on the radial surface density at 1.1 kpc away from the plane. We want to compare this result with observations. For this reason we need to subtract the contribution of the dark matter to the local gravitational force. We adopt a cored isothermal profile as we used in the radial structure. The result is shown in Fig. 3.25. We obtain larger results at smaller radii for smaller values of Δ. The larger Δ is, the smaller is the surface density at small radii. At large radii the surface density at 1.1 kpc is greater for larger values of Δ, but the difference between the results for different values of Δ is very small. It has been found by Rix & Bovy (2013) that the radial surface density at 1.1 kpc can be well fitted by an exponential in a radial range between 4 and 9 kpc:

$$\frac{|K_z(R,1.1)|}{2\pi G} = \frac{|K_z(R_0,1.1)|}{2\pi G}\exp(-(R-R_0)/R_d)$$

where $K_z(R_0)$ is the value of the local vertical force at 1.1 kpc. The dashed line in Fig. 3.25 corresponds to the exponential profile with R_d determined for the case $\Delta = 4$ kpc at R_0. The difference between the two profiles is ∼15% at small galactocentric radii. With the parameters that we have fixed, we are able to reproduce the observational value given by Holmberg & Flynn (2000) only for values of Δ between 1 and 6 kpc. For larger values of Δ, the radial surface density results in lower values. Another prediction is the dynamical derivation of the disc thickness. The thickness is given by the ratio between the radial

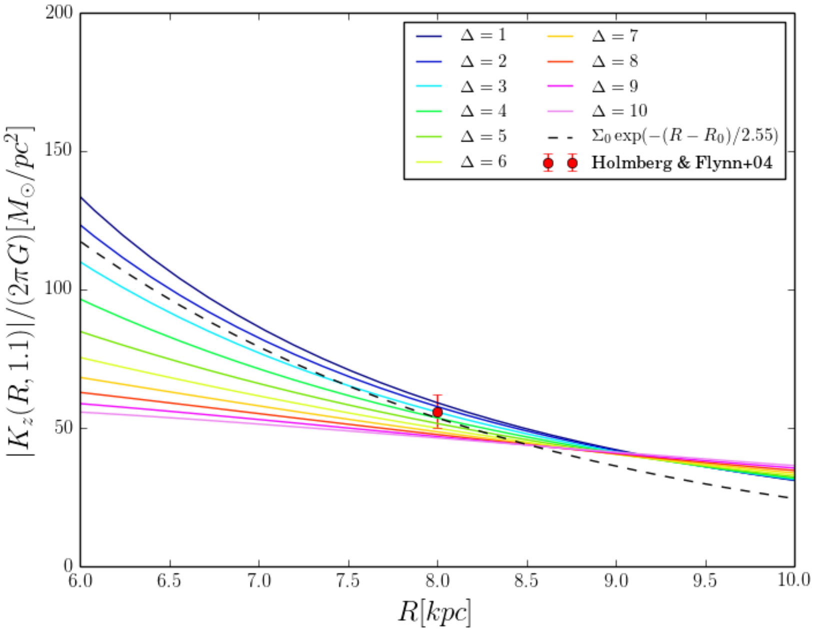

Figure 3.25: Radial surface density at 1.1 kpc using the approximation given by Kuijken & Gilmore (1989) for the 'vertical' function $G(v)$ for different values of Δ. The observational constrain is given by Holmberg & Flynn (2004). The dashed line corresponds to an exponential profile with scale length $R_d = 2.55$ kpc derived from the radial profile for the logarithmic case.

surface density at 1.1 kpc and the radial density in the plane:

$$h_z(R) = \frac{\Sigma_{1.1}(R)}{2\rho(R)}$$

We can see the results in Fig. 3.26. We obtain a value of the thickness increasing with radius for all values of Δ. This increase is between 25% and 35% in the extended solar neighbourhood, where the smallest variation corresponds to large values of Δ while the largest increase to small values of Δ.

3.9 Discussion

In this Chapter, we have studied the Stäckel potential and its properties. This potential separates the Hamilton-Jacobi equation in the spheroidal coordinate system and therefore we can obtain an analytic expression for the third integral of motion. The knowledge of the third integral of motion is necessary for the construction of a three-dimensional phase-space distribution function, which describes completely regular orbits. Another important result is that for a potential of the Stäckel form, the velocity ellipsoid lines up with the spheroidal coordinate system.

The required form for this potential, due to the separability in spheroidal coordinates, can be written as the sum of the potential functions $U(u)$ and $V(v)$, each depending on one coordinate only:

$$\Phi(u, v) = \frac{U(u) - V(v)}{\sinh^2 u + \sin^2 v} = \frac{\cosh^2 u F(u) - (\sinh^2 u_0 + \sin^2 v)G(v)}{\sinh^2 u + \sin^2 v}$$

We have constructed a very accurate Stäckel potential approximation for the extended solar neighbourhood. We are not limiting our research to a few hundred parsec around the Sun. We have constructed our

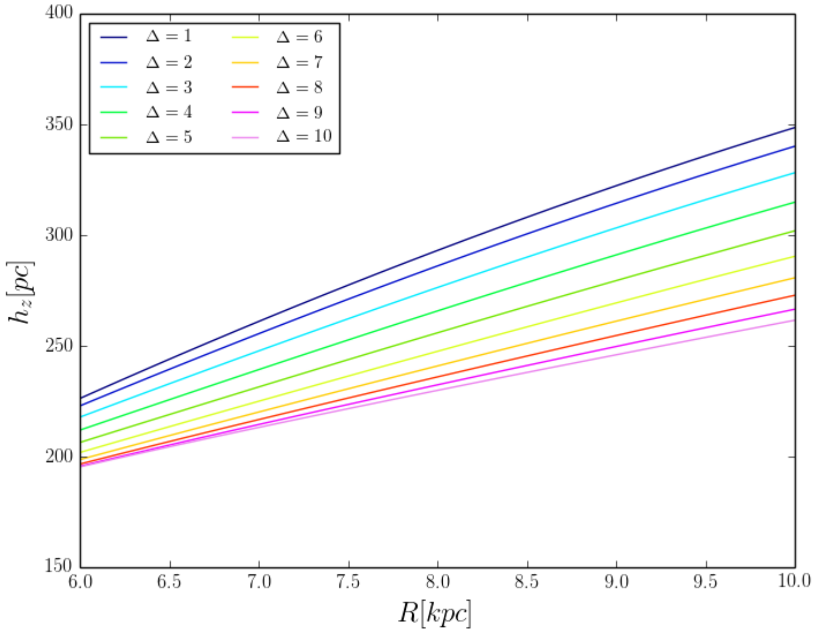

Figure 3.26: Dynamical estimation of the disc thickness using the approximation given by Kuijken & Gilmore (1989) for the 'vertical' function $G(v)$ for different values of Δ.

model for a region which covers 2 kpc radius around the Sun so that our results can be compared with data given by surveys like SDSS/SEGUE, RAVE and Gaia in the near future.

The idea is that we can approximate the local gravitational potential with a potential of the Stäckel form. For the construction of this Stäckel model, we have first determined the focal point Δ of the spheroidal coordinate system from observations of the velocity ellipsoid in the meridional plane based on RAVE data found by Binney et al. (2014a). We found that the best value for Δ is 4 kpc. Once we determined this value, we fixed the spheroidal coordinate system. This value is approximately in agreement with what was found by Binney (2012a) and Bovy & Rix (2013) assuming that $R_0 = 8$ kpc.

To fix the two potential functions $F(u)$ and $G(v)$ we used the observational constrains given by the rotation curve and by the vertical K_z-force, together with the local mass density. We can choose whatever 'radial' function $F(u)$ we want from the knowledge of the rotation curve. The rotation curve is directly linked to the first derivative of the 'radial' potential $F'(u)$. The only assumption is that the 'vertical' potential $G(v)$ is zero in the plane. This assumption avoids additional terms in the derivatives of the Stäckel potential with respect to the coordinate u and leads to the simple result: the first and second derivatives of the total Stäckel potential with respect to u in the plane are $F'(u)$ and $F''(u)$.

We looked at two cases for the radial profile in the plane, namely the logarithmic and the power-law potential. The first case reproduces a constant rotation curve with radius, while in the second case we can choose a slope for the rotation curve. It is possible to obtain $F'(u)$ from the rotation curve and through an integration we obtain the 'radial' potential function $F(u)$.

After we chose the value for the circular speed as $v_0 = 220$ km/s, we derived the second derivative of the 'vertical' potential $G''_0(v = \pi/2)$ from the total local mass density, for which we have assumed the value of $0.102\ \mathrm{M}_\odot/\mathrm{pc}^3$ (Holmberg & Flynn 2000). This local density corresponds to a vertical oscillation frequency ($\nu_{z,0}$) of 76 km/s/kpc. The value that we found for the new frequency is ~10% less than $\nu_{z,0}$.

The best way to derive the radial density profile would be to use the Jeans equations in spheroidal coordinates. These equations express the link between the gravitational potential, the density and the kinematics of the tracers. Since the Hamilton-Jacobi separates along the spheroidal coordinates, the velocity dispersion matrix would be diagonalized and composed of three terms only. The Jeans equations form a closed system and solutions were pursued by van de Ven et al. (2003). We wanted however to derive some properties of the density of tracer populations without using the Jeans equations. In our model we can derive the radial density from three free parameters: Δ, $F'(u)$, $G''(v = \pi/2)$.

After we set the two parameters v_c and $G''(v = \pi/2)$, we can determine the total radial density profile in the extended solar neighbourhood, in a radial range between $6 \leq R \leq 10$ kpc. From the total density we subtracted the contribution of the dark matter profile and we could derive the radial density given by the tracers. We found that we are not able to reproduce an exponential density profile for $\Delta = 4$ kpc. This is valid for all values of Δ except the case of $\Delta = 8$ kpc. In this case we were able to reproduce an exponential radial profile for the tracer population. However, this value is twice the best value we have found for the focal point based on the observation of the velocity ellipsoid. The effect of an exponential radial profile is that the scale length is constant with radius. This large value of Δ produces a radial scale length, which resides outside the observational range ($R_d = 4.3$ kpc). The result for $\Delta = 4$ kpc is in agreement with the exponential profile assuming an observational error of 10% for the radial scale length. The disagreement of the radial density profile from an exponential means that we do not reproduce a constant radial scale length with radius and this can have an impact on the Jeans analysis. The value of the scale length found is approximately 2.6 kpc at the solar position, for a constant rotation curve and a rotation curve with a slope $\alpha = 0.1$, which is in perfect agreement with the observations ($2 < R_d < 3$ kpc).

There is a fourth free parameter for the Stäckel potential, the 'vertical' potential $G(v)$, which we use to describe the vertical structure. We can derive this function from the K_z-force at 1.1 kpc. We used the observational constrain of (76 ± 6) $M_\odot/pc^2$ for the vertical force at 1.1 kpc, where the contribution from the baryonic component is (56 ± 6) $M_\odot/pc^2$ (Holmberg & Flynn 2004). We used as Ansatz the approximation given by Kuijken & Gilmore (1989) for the 'vertical' function $G(v)$. This approximation requires to fix three parameters: the scale height z_0, the surface density given by the baryonic matter Σ_0 and the local volume density given by dark matter $\rho_{0,dm}$. To fit the observational values for the local gravitational force given by the tracers and including also the contribution of the dark matter, we needed a small amount of dark matter $\rho_{0,dm} = 0.007$ $M_\odot/pc^2$.

After we have fixed all the free parameters it is possible to make a prediction about the K_z-force at different galactocentric radii. We cannot reproduce the vertical force at 1.1 kpc at different radii with an exponential profile as found by Bovy & Rix (2013). This result is valid for all values of Δ, also for $\Delta = 8$ kpc, where we were able to reproduce an exponential density profile. Values of Δ larger than 7 kpc produce smaller results for the radial surface density than the observational constrains given by Holmberg & Flynn (2004). A direct conclusion from this analysis is that we cannot reproduce a constant disc thickness with radius but always an increasing thickness, for all values of Δ. This is because we are trying to fit three functions using two parameters: the rotation curve and the shape of the gravitational potential. It is not possible to constrain a constant thickness from constrains of the rotation curve and vertical K_z-force only. As we have seen, it is possible to find a particular value for Δ, for which we can reproduce an exponential radial density profile (for $\Delta = 8$ kpc). However, if we are not able to obtain an exponential radial surface density for this special value, we cannot reproduce a constant thickness for the disc.

The Stäckel potential is limited to local approximations for the extended solar neighbourhood, and thus cannot reproduce the gravitational potential of the whole Milky Way. Since we obtain three isolating integrals of motion, with this potential we can study the three-dimensional motion of regular orbits. Most of the orbits are regular but there are also irregular families, which have a small angular momentum and reside next to resonances (Valera et al. 1994). For these orbits the third integral of motion is no further isolating and the orbits are chaotic. That is why the Stäckel potential cannot reproduce irregular orbits.

Binney (2012a) developed a method to derive the actions using the Stäckel potential approximation ('Stäckel fudge'). We have seen that the choice of the focal point is crucial. Different values of Δ lead to different spheroidal coordinate systems. For smaller values of Δ the v coordinates tend asymptotically to lines pointing towards the centre of the coordinate system, while for larger Δ they become more cylindrical. The values are linked to different kinematic properties, like the tilt of the velocity ellipsoid, the radial density profile, the scale length and the vertical force. The velocity ellipsoid aligns with the coordinates, and changing the coordinate system changes the tilt of the velocity ellipsoid. Moreover, the choice of the focal point changes the radial density profiles, which is an important ingredient for the construction of a mass model. The choice of Δ is thus not only a value that can be given by the 'Stäckel fudge' approximation, but it is a value which determines all kinematic properties in the extended solar neighbourhood. Nevertheless, the choice for Δ is also related with the accuracy for the derived actions (Sanders & Binney 2014).

From this, we can make the prediction that − since the tilt of the velocity ellipsoid is given by our chosen focal point Δ − the different stellar populations have the same orientation of the velocity ellipsoid and thus undergo the same gravitational potential. In the next Chapter, we will look at RAVE data for different subpopulations to see whether our prediction holds true.

4

Tilt of the velocity ellipsoid based on RAVE data

In the last Chapter we have constructed a model for the extended solar neighbourhood, approximating the local gravitational potential with that of the Stäckel form. Since this potential can be separated along the spheroidal coordinate system, the velocity ellipsoid shows a determined orientation, once we fix the focal points of the coordinate system. In this Chapter we want to analysed RAVE data and derive the orientation of the velocity ellipsoid with respect to the cylindrical coordinates, where the tilt angle α_{tilt} is defined as the angle between the longer axis in the meridional plane and the Galactic plane. If we determine the same tilt angle that Binney et al. (2014a) derived, we can confirm the validity of our model.

We have already introduced the tilt of the velocity ellipsoid, which is related to the second order velocity moments in the following way:

$$\tan(2\alpha_{tilt}) = \frac{2\sigma_{Rz}^2}{\sigma_R^2 - \sigma_z^2}$$

and we can find the tilt angle as

$$\alpha_{tilt} = \frac{1}{2} atan\left(\frac{2\sigma_{Rz}^2}{\sigma_R^2 - \sigma_z^2}\right) \sim \frac{\sigma_{Rz}^2}{\sigma_R^2 - \sigma_z^2}$$

where the last approximation is valid for small angles ($\alpha_{tilt} < 10^\circ$). In the case that the gravitational potential is axisymmetric and of the Stäckel form, the velocity ellipsoid is aligned with the spheroidal coordinate system and the tilt is expressed in cylindrical coordinates as:

$$\tan(2\alpha_{tilt}) = -\frac{2Rz}{R^2 - z^2 + \Delta^2}$$

where Δ is the focal point of the spheroidal coordinate system.

For an axisymmetric system the two covariance terms $\sigma_{R\phi}$ and $\sigma_{\phi z}$ should be zero but the mixed term σ_{Rz} should not. This term vanishes in the plane due to symmetry arguments but it can adopt different values at larger heights. σ_{Rz} expresses the inclination of the velocity ellipsoid in the meridional plane. If only two integrals of motion existed, σ_{Rz} would be zero and orientation of the velocity ellipsoid would result undetermined because the radial and vertical axis would be equal. The tilt reflects the projection of the third integral of motion in the meridional plane (Pasetto et al. (2012b)).

This term is important because it is included directly in the radial and vertical Jeans equations in the derivation of the vertical gravitational force (Kuijken & Gilmore 1989) and the asymmetric drift (Dehnen & Binney 1998). For the vertical gravitational force K_z this term can be neglected because it is small, at least in the first kpc (Binney & Tremaine 2008; Garbari et al. 2011; Zhang et al. 2013). In the asymmetric drift relation we look in the plane and the vertical variation of this term enters in the equation. To derive this equation and then the value for the velocity of the local standard of rest (LSR) we need to know the vertical gradient of σ_{Rz}. Another impact on the orientation of the velocity ellipsoid is related to the mass distribution of the Galaxy and to the flattening of the halo (Siebert et al. 2008).

In the last years many authors tried to derive the tilt of the velocity ellipsoid. Siebert et al. (2008) applied for the first time RAVE data (Data Release 2) to calculate the tilt of the velocity ellipsoid. They used 580 red clump stars below the Galactic plane between $0.5 \leq |z|/[kpc] \leq 1.5$ and found a tilt angle of $(7.3 \pm 1.8)^\circ$, showing for the first time that the velocity ellipsoid is pointing approximately to the Galactic centre. Casetti-Dinescu et al. (2011) combined the same second RAVE data release for 1450 red clumps with the Southern Proper Motion Program (SPMP) and after considering the sign flip for the vertical velocity they obtained a tilt angle of $(8.6 \pm 1.8)^\circ$ for heights $0.7 \leq |z|/[kpc] \leq 2$. Smith et al. (2012) used a restricted sample from the SDSS DR7, Stripes 82, and measured the tilt angle in four different bins in the height range $0.5 \leq |z|/[kpc] \leq 1.7$ for stars with metallicity $[Fe/H] < -0.5$ and $-0.8 \leq [Fe/H] \leq -0.5$. Smith et al. (2012) claimed that, despite the large error bars, the results are in agreement with the findings of Siebert et al. (2008). Binney et al. (2014a) applied to RAVE data an analytic fit for the variation of the velocity ellipsoid within the meridional plane by a technique that avoids binning data. Their result was that the tilt angle is less inclined than the earlier measurements suggested ($\alpha_{tilt} = -0.8 \arctan(z/R)$, where the minus is introduced to be consistent with our definition), without giving any value for the error unfortunately. The last measurement was carried out by Büdenbender et al. (2014) who applyed a Markov Chain Monte Carlo (MCMC) fitting to 16000 G-dwarfs from the SDSS/SEGUE survey, studying first 7 different subpopulations and then the full sample of stars, arriving to find that the orientation of the velocity ellipsoid is consistent with Siebert et al. (2008) with errors for the tilt less than 4° ($\alpha_{tilt} = (-0.78 \pm 0.2) \arctan(|z|/R_\odot)$). We can see these measurements in Fig. 4.1.

4.1 RAVE sample

RAVE (RAdial Velocity Experiment) is a multi-fibre spectroscopic survey of stars in the Milky Way carried out by the 1.2 metre Schmidt Telescope of the Anglo-Australian Observatory (AAO) located in Siding Spring, Australia.

During the last 10 years of operation (2003-2013) RAVE collected almost 500000 stars with high resolution ($\Delta\lambda/\lambda \sim 7500$), scanning a wavelength region near the infrared ionized Calcium triplet CaII ($\Delta\lambda = 8410 - 8794$ Å). This region is similar to the wavelength range chosen for Gaia's Radial Velocity Spectrometer (Cropper & Katz 2011; Kordopatis & RAVE collaboration 2014). It is a complementary mission to Sloan Extension for Galactic Understanding and Exploration (SDSS/SEGUE). From one side SEGUE covers the northern hemisphere and observes stars fainter than magnitude 14, whereas on the other side RAVE covers the southern hemisphere and observes stars within magnitude between 9 and 13.

In total, 425561 stars have been observed, collecting 482430 spectra (Data Release 4), with the primary goal to derive the radial velocity of stars from the observed spectra. The high resolution enables us to measure line-of-sight velocities with a median precision better than 1.5 km/s (Kordopatis et al. 2013). From RAVE spectra we can also obtain stellar parameters, such as effective temperature, surface gravity and metallicity.

In absence of direct measurements of stellar parallaxes there were several works to obtain distance determinations for RAVE stars (Breddels et al. 2010; Zwitter et al. 2010; Burnett et al. 2011; Binney et al. 2014b). Until the third Data Release (DR3) all the distance measurements were published, whereas

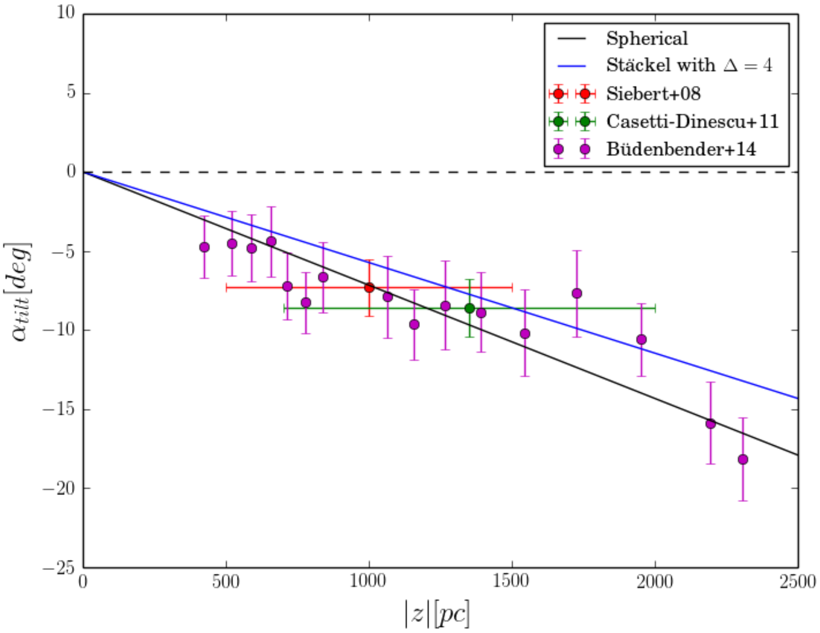

Figure 4.1: Tilt of velocity ellipsoid in literature: Siebert et al. (2008) (red point), Casetti-Dinescu et al. (2011) (green point) and Büdenbender et al. (2014) (magenta points). The black line corresponds to an orientation of the velocity ellipsoid with the spherical coordinates; the blue line corresponds to the result found by Binney et al. (2014a).

in the last Release (DR4) only the two latest works. Distances usually are obtained by projecting the atmospheric parameters on a set of theoretical isochrones, to find the most likely absolute magnitude. We choose distance measurements based on Burnett et al. (2011)'s method which gives us values of distances for 387105 stars.

In the RAVE catalogue the proper motions are also included and it is possible to choose between different possibilities: Tycho-2, UCAC2, UCAC3, UCAC4 (Zacharias et al. 2010, 2013), PPMX, PPMXL (Roeser et al. 2010), and SPM4 (Girard et al. 2011).

The choice for the proper motion catalogue is left to the user, because the errors are estimated in different ways and it is not said that the catalogue with the smallest error is also the one with the most accurate values (Kordopatis et al. 2013). We choose UCAC4 catalogue for two reasons: first, the errors in UCAC4 are 60% smaller than in the PPMXL. Second, the proper motion error distribution in PPMXL is not log-normal, but there are systematics showing some bumps in the error distribution (Fig. B.1 and B.2). For these reasons we focus only on the UCAC4 catalogue for proper motions to avoid any complications. Otherwise we could have to take care of these systematics, cleaning accurately the sample in the PPMXL catalogue.

We consider only data with errors in the proper motion values that are smaller than $\Delta pm \leq 8$ mas/yr, as in Binney et al. (2014a). The data left show an error in the line-of-sight velocity $\Delta v_r \leq 7$ km/s and a signal-to-noise ratio greater than 20 (as requirement for the Burnett et al. (2011) distances), which are good constraints for the following analysis. This cut leaves us 385080 stars.

Combining the proper motions with the photometric distances, we obtain the transverse velocities of the stars. By adding the measurements of the radial velocities we obtain the full phase-space (6D) information.

4.1.1 Red giants and cold dwarfs

In the RAVE catalogue is also included a cross-correlation with 2MASS for the photometry, therefore we have luminosity values for the stars in J, H and K magnitude. The Colour-Magnitude Diagram (CMD) for all stars of the RAVE Catalogue is shown in Fig. 4.2 (red points), plotting the absolute magnitude in K-band (M_K) relative to the colour ($J-K$). The absolute magnitude can be derived from the knowledge of the K-magnitude and the distance by using the distance modulus.

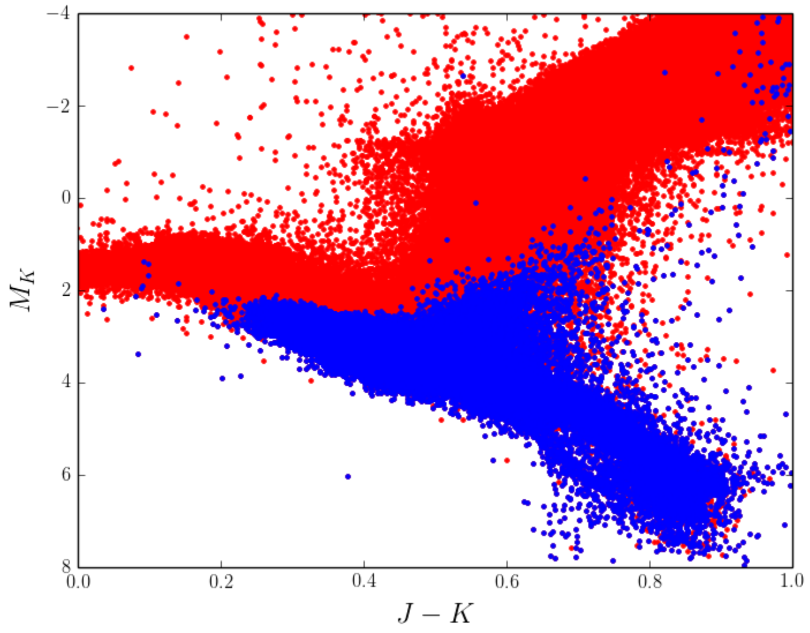

Figure 4.2: Colour-Magnitude Diagram (CMD) of all RAVE stars (red points) with overplotted the cold dwarfs with a gravity-temperature selection (blue points).

We want to study the kinematics in the extended solar neighbourhood for which 'cold' dwarf stars − G-K type stars with low surface temperature ($T \sim 4000-6000$ K, for this reason the name 'cold') and a mass similar to that of the Sun ($M \sim 0.6-1.2$ $M_\odot$) − are usually suited best. They build a good sample because they are old enough to be in dynamical equilibrium. Since the collisions between stars are negligible we can use this kind of stars for kinematical studies in six dimensional phase-space. They can also reach large distances from the plane, so that it is possible to use them to study disc surface mass density and the local mass density of dark matter (Zhang et al. 2013). Using SEGUE data they can be used to study the velocity ellipsoid of nearby stars and thereby to determine their tilt at heights between 0.5 and 2.5 kpc (Büdenbender et al. 2014).

The 'hot' dwarfs are not taken into account because they are young stars that can be disturbed by spiral structure. This means that they are not in dynamical equilibrium, which would be in contradiction to our hypothesis.

Dwarf stars are located on the main sequence because they are still burning hydrogen in the core. We select them by a gravity constraint ($\log g \geq 4$). We can divide the sample in cold dwarfs with a temperature of $T < 6000$ K and hot dwarfs with $T > 6000$ K. We are interested in cold dwarfs (blue points in Fig. 4.2) and with these two cuts (gravity and temperature) we obtain 50936 stars, but subgiants are also in the sample. We carry out a third cut in magnitude as in Golubov et al. (2013):

$$0.75(J-K) \leq M_K \leq 2.75(J-K)$$

and the number of cold dwarfs reduces to 45852.

These stars are faint and because RAVE observes in a range between 9 and 13 magnitudes we can only observe them in the first 400 pc of the plane (Fig. 4.3). Next to the plane we can apply the epicycle approximation ($z << 300$ pc), which assumes that the radial and vertical velocity dispersion is decoupled. This means that the tilt of the velocity ellipsoid should be zero and oriented with the cylindrical coordinate system. Thus, we can use these stars to understand how the velocity ellipsoid behaves next to the plane.

For studying the kinematics at greater heights we need to consider another sample, the red clump giants, which can extend up to 2 kpc. Red clump giants are stars that have already evolved from the main sequence after they stopped to burn hydrogen in the core, moving up to the red giant branch and set eventually on the horizontal branch, resulting in a clump in the colour-magnitude diagram. They occupy a well defined region in the CMD diagram (green points in Fig. 4.4), the metal-rich part of the horizontal branch. These stars are very bright with a mean absolute magnitude $M_K = -1.6$ with a dispersion of 0.22 magnitudes (Alves 2000; Kordopatis et al. 2013), more luminous than main sequence stars at the same surface temperature. They can be observed at large distances from the Galactic plane and are considered to be good standard candles. Therefore red clump giants can be used for kinematical studies far away from the plane. We select these stars by gravity ($1.7 \leq \log g < 2.4$) and by colour ($0.55 < (J - K) < 0.8$) as in Binney et al. (2014a). After this selection 46486 stars remain, the stars at negative z are more numerous and reach larger distances from the plane compared to stars at positive z (Fig. 4.5).

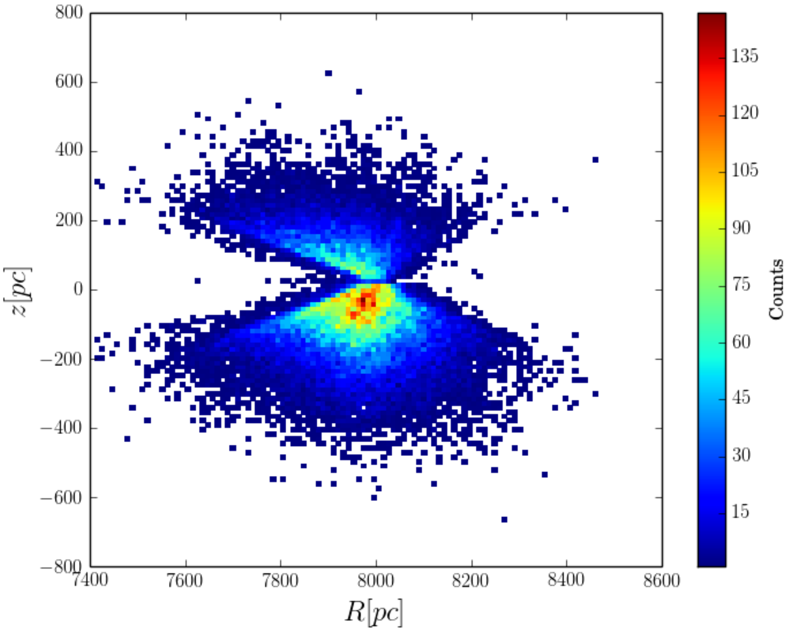

Figure 4.3: Location of the cold dwarfs in the meridional (R, z)-plane.

4.1.2 Input data

At first, we have to convert the line-of-sight velocity and proper motions in a cylindrical reference system (R, ϕ, z), using the transformation of Johnson & Soderblom (1987), corrected to $J2000$. This is the reference system for studies of the stellar kinematics in the Milky Way.

We use the values $R_0 = 8$ kpc and $z_0 = 27$ pc to describe the distance of the Sun from the Galactic

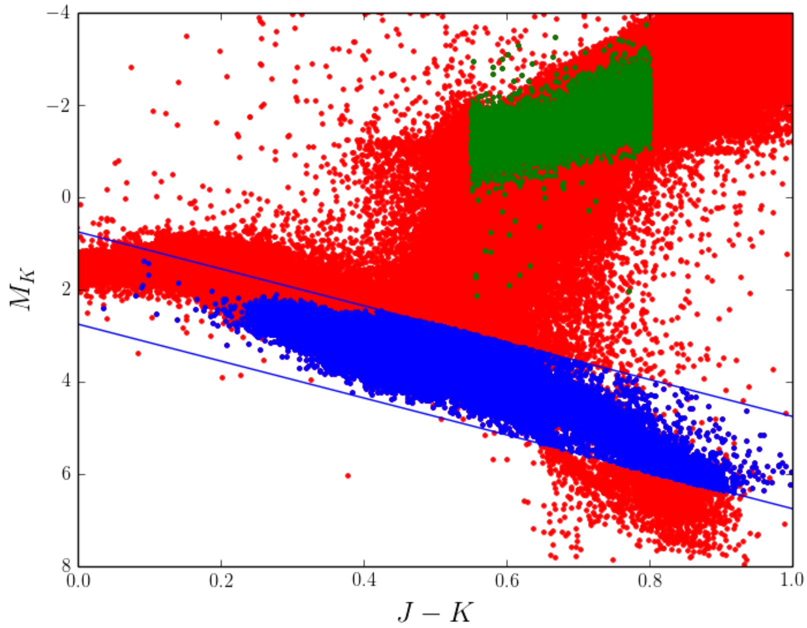

Figure 4.4: Colour-Magnitude Diagram of all RAVE stars (red points) with overplotted the cold dwarfs (blue point) adding a magnitude cut to the previous selection and the red clump giants (green points) selected by gravity-colour cut.

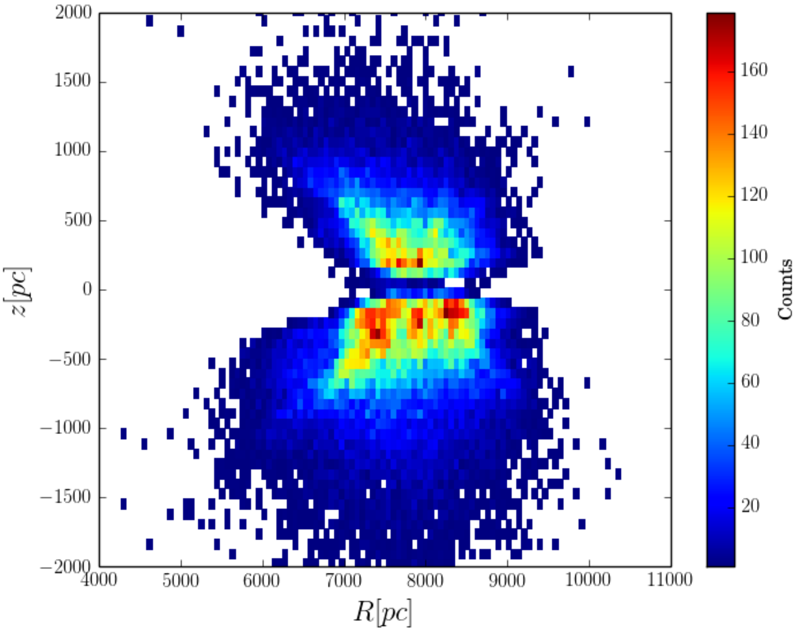

Figure 4.5: Locations of the red clump giants in the meridional (R, z)-plane in a height range $-2 \leq z \leq 2$ kpc.

centre and its height with respect to the Galactic plane, and $v_c(R_0) = 220$ km/s for the local circular velocity. As the velocity of the Sun with respect to the local standard of rest (LSR) we use the values $(U_\odot, V_\odot, W_\odot) = (11.1, 5.25, 7.25)$ km/s, where $U_\odot$ is the velocity in the direction of the Galactic centre, $V_\odot$ along the Galactic rotation and $W_\odot$ pointing to the North Galactic pole. We choose $U_\odot$ and $W_\odot$ from the updated results found by Schönrich et al. (2010) and the value for $V_\odot$ from Aumer & Binney (2009). We consider the old value for $V_\odot$ because it is in agreement with the determination of the asymmetric drift derived by Golubov et al. (2013).

We want to study the tilt of the velocity ellipsoid in a cylinder around the Sun with a radius of 1 kpc ($7 \leq R \leq 9$ kpc) up to an height of 2 kpc ($-2 \leq z \leq 2$ kpc), considering stars with absolute values for the radial and vertical velocities less than 150 km/s to avoid contamination by halo stars. Taking into account the errors in line-of-sight velocities, proper motions and distances the uncertainties for the radial (v_R) and for the vertical velocities (v_z) are 14% and 10%, respectively.

Our assumption is that the Milky Way is a steady-state, axisymmetric galaxy. This means that neither the gravitational potential ($\partial\Phi/\partial\phi = 0$) nor the phase-space distribution function ($\partial f/\partial\phi$) depend on the azimuthal component. Therefore we neglect the ϕ-dependence on the kinematics and focus on studying the variation of the velocity ellipsoid in the two dimensional meridional plane (R, z).

We consider stars above and below the plane in the cylinder, which are ~85% of the selected Red Clumps sample. Because of the symmetry with respect to the Galactic plane, the sign of the vertical velocity v_z for stars below the plane is flipped (Casetti-Dinescu et al. 2011; Büdenbender et al. 2014). The result will be a negative angle for the tilt of the velocity ellipsoid ($\alpha_{tilt} < 0$) (see Chapter 2). In Table 4.1 all the selections are listed as well as how the samples were reduced. The new chemical pipelines developed by Boeche et al. (2011) give chemical abundances for 270105 stars. Assuming stars with metallicities reduces the sample by 11% for red clump giants and by 29% for cold dwarfs.

Selections	no. stars w/o [Fe/H]	with [Fe/H]
RAVE DR4	482430	482430
Distances	387105	387105
PM errors	385080	385080
RC giants	54565	48087
RC giants (Cylinder)	46486	41510
Cold Dwarfs	45852	32527
Cold Dwarfs (Cylinder)	45774	32507

Table 4.1: The first selection is listed in the first 3 rows: total number of RAVE data, number of stars with distance measurements and selections in proper motion errors. Two groups of stars are selected: red clump giants and cold dwarfs. The sample reduces when we consider the cylinder around the solar neighbourhood ($7 \leq R \leq 9$ kpc, $-2 \leq z \leq 2$ kpc).

4.2 Methods

The methods used for the derivation of the tilt of the velocity ellipsoid are two: a Markov Chain Monte Carlo method and the 'biweight' method.

The first method is a MCMC discrete likelihood fitting developed by Alex Büdenbender at MPIA, Heidelberg (see Büdenbender et al. (2014)). With this method we aim to know the likelihood that a star came from the disc distribution assuming that the distribution in radial and vertical velocities is a bivariate Gaussian with a tilt. In addition it is also considered a background model which takes into account the contamination by halo stars. It is assumed that the tilt velocity ellipsoid for the halo stars is zero, with a dispersion matrix having zero covariant terms and values for the diagonal terms measured by Schönrich et al. (2011) ($\sigma_R = 157 \pm 10$ km/s and $\sigma_z = 75 \pm 8$ km/s). The assumption about the tilt of these stars is valid because the fraction of halo stars is very small. The best model is the one which maximises the likelihood (Büdenbender et al. 2014). This means that if we have some non-Gaussian distribution of our data, the tail will be fit for the halo stars and the core for the disc stars. From that we can derive the second order moments of velocity dispersion (σ_R, σ_z and $\overline{v_R v_z}$) and the fraction ϵ of halo stars. Further, it is assumed that the bulk motions are zero ($\overline{v_R} = \overline{v_z} = 0$) because the Galaxy is axisymmetric and deviations from it are very small (Fig. B.6 and B.7).

The second method consists in the calculation of the 'standard' statistical moments using the biweight function. The biweight function, which is an abbreviation for 'bisquared weight function', is one of the M-estimators, first introduced by Beaton and Tukey in 1974. The biweight iteratively reweight measures of central tendency, instead of using the mean, and is highly resistant to local misbehaviour caused by outlier data. Data farther than the cut-off radius receive a weight equal to zero. This function is used in robust statistics and combines the properties of resistance and high efficiency. This means that changes in a small part of data do not cause large changes in the estimate and that it is efficient also for not log-normally distributed data. If we have a skewed distribution this method will cut-off the tail and fit a Gaussian to the core.

4.3 Binning data

4.3.1 Overlapping bins

Since we are not constructing a dynamical model using a distribution function, we have to bin the data for our analysis. First, we study the red clump giants in detail, because they can be observed up to large distances from the plane using RAVE data. Later, in Section 4.6 we will compare the results for the red clump giants with the cold dwarfs close to the plane.

The first step was to choose overlapped bins assuming the same number of stars for each bin. The idea was to overlap the bins more and more and eventually obtain a result showing a continuum tilt of the velocity ellipsoid. This idea was misleading, overlapping bins introduce some correlations between the data resulting in artificial features of the second order moments (Fig. B.5). For this reason is better to use no-overlapping bins.

4.3.2 Uncorrelated bins

Büdenbender et al. (2014) applied the MCMC fitting to SEGUE data determining the tilt of the velocity ellipsoid and binning the same number of stars in each interval. In this way it is possible to obtain the same error for each bin. However, SEGUE observes at magnitudes fainter than 14, and the data cover a large magnitude range and are well distributed in a height range between 0.5 and 2.5 kpc. RAVE, instead, observes at lower magnitudes (greater brightnesses) and most of the data are close to the Galactic plane. For this reason we selected red clump giants for our analysis. They are very numerous close to the plane but they can extend up to large distances from the plane. However, their number decreases very fast with height after 0.8 kpc. If we want to bin data using the same number of stars per bin we can have two possible cases:

- we choose a low number of stars per bin: we obtain very small bins next to the Galactic plane (< 100 pc). After 0.8 kpc the number of stars decreases very fast. If we choose 500 stars for example, we will have only a few bins above 0.8 kpc and then the last bin is very big in comparison to the others, covering all the remaining height. The bins next to the plane are too small and the results are statistically fluctuating without showing a stable result for the tilt;

- we choose a large number of stars per bin (~3000 stars for example): we have larger bins close to the plane but only two bins above 0.8 kpc.

If we want to study the behaviour of the velocity ellipsoid up to large distances from the Galactic plane we need bins with a size of at least >100 pc for minimizing any statistical fluctuations. The best idea is to divide the bins in equal heights for studying in more detail what happens over the whole distance range. This means that we do not have the same number of stars per each bin, but we will have a larger number of stars next to the plane and a lower number at greater heights.

4.4 Velocity dispersion tensor

We want to study the second order moments of the phase-distribution function, i.e. the velocity dispersion tensor σ_{ij}. The velocity dispersion tensor is a symmetric matrix, with only six independent non-zero elements, the three diagonal terms σ_R, σ_ϕ, σ_z and the three covariances $\sigma_{R\phi}$, σ_{Rz}, $\sigma_{\phi z}$. The covariances correspond to any possible misalignment with the cylindrical coordinate system and after a rotation of the matrix the new terms in the diagonal correspond to the three axis of the velocity ellipsoid.

The mixed term $\sigma_{R\phi}$ and $\sigma_{\phi z}$ should be zero because the Galaxy is axisymmetric. Although the motion in R and ϕ and z and ϕ direction is coupled, the distribution function separates and the two mixed terms are zero. This means that the axis of the velocity ellipsoid corresponding to the azimuthal velocity dispersion (σ_ϕ^2) remains oriented with the cylindrical coordinate ϕ. This is certainly true for $\sigma_{\phi z}$, but it has been found that $\sigma_{R\phi}$ is not exactly zero, producing a deviation for the longer axis of the velocity ellipsoid of an angle of ~20° in the midplane. This so-called 'vertex' deviation $\sigma_{R\phi}$ expresses the fact that the gravitational potential is not axisymmetric due to resonances from the Galactic bar or spiral arms (Smith et al. 2012).

We are interested in the behaviour of the velocity dispersion in the two dimensional plane (R, z), then we want to calculate the two diagonal terms σ_R, σ_z and the covariant term $\overline{v_R v_z}$, neglecting σ_ϕ. These are the parameters which enters in the determination of the tilt of the velocity ellipsoid (Eq. 2.2). The trend of the radial and vertical velocity dispersion is not very well known because of the location within the Galactic disc and the dust absorption (Pasetto et al. 2012b). With RAVE survey it is possible to study it due to the large number of stars and to an extended radial range.

The result for the vertical velocity dispersion σ_z is consistent for both methods. It starts with a value of ~15 km/s in the plane, then increases up to ~26 km/s at 1 kpc and reaches a value of ~36 km/s at 2 kpc (Fig. 4.6). The vertical velocity dispersion increases linearly with height, reaching eventually a saturation at 1.5 kpc.

The two methods, however, produce two different results for the radial velocity dispersion σ_R and this difference appears above 1 kpc. The behaviour is the same at the beginning, σ_R increases with z starting from a value of ~26 km/s in the plane up to ~41 km/s at 1 kpc. Above this height, the MCMC fitting produces a lower result than the biweight function. In the first case σ_R increases up to 50 km/s at $z = 2$ kpc while in the second case it increases up to 61 km/s (Fig. 4.7).

A reason for the difference between the two results can be a contamination by halo stars. However, we find that the fraction of halo stars is constrained between 2% and 5% in a height range between 1 and 2 kpc (Fig. 4.8). Another point is that the spatial distribution in the meridional plane of the red clump giants is not symmetric. There is a predominant stream towards the inner part of the MW and this stream can modify the result about the radial velocity dispersion (see Fig. 4.5).

For the determination of the errors in the case of the biweight method we apply a bootstrap method,

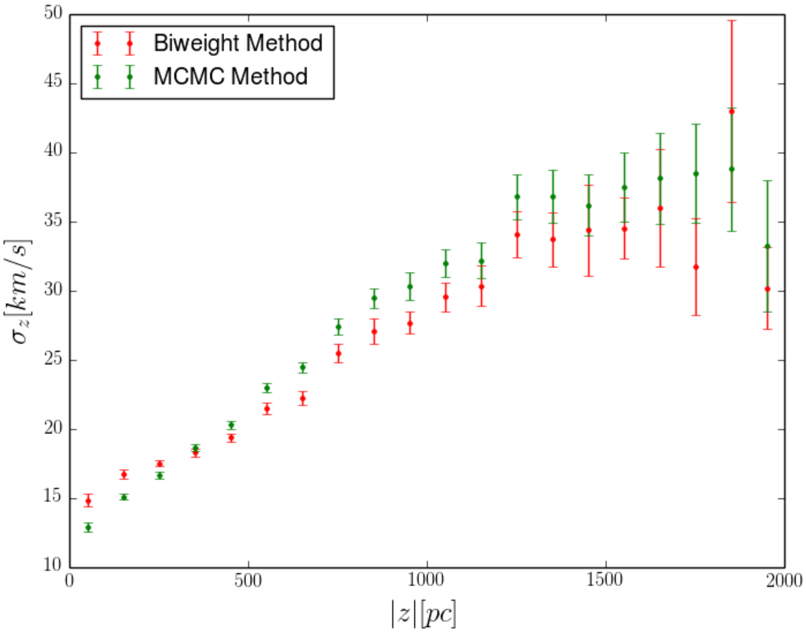

Figure 4.6: Vertical velocity dispersion σ_z increasing with z for red clump giants using the biweight and the MCMC method.

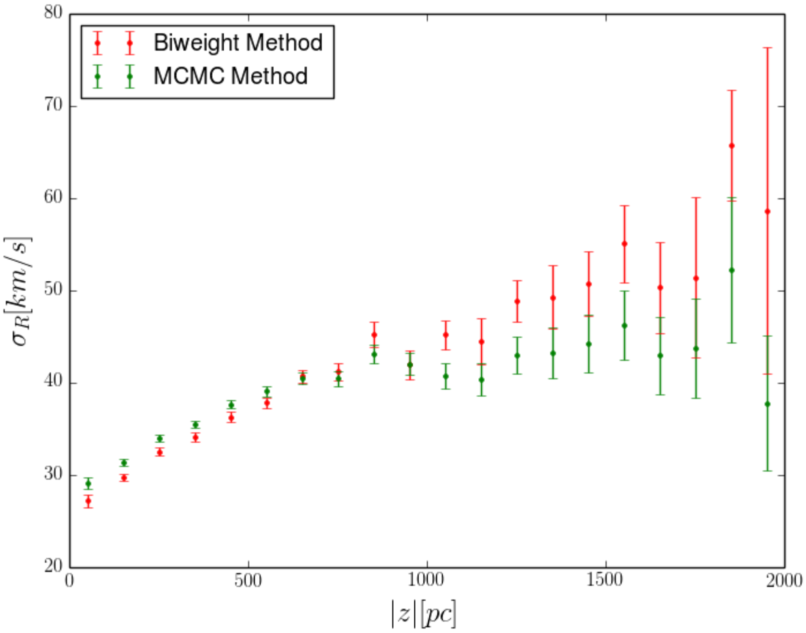

Figure 4.7: Radial velocity dispersion σ_R increasing with z for red clump giants using the biweight and the MCMC method.

which relies on random sampling with replacement. This technique allows assigning measures of accuracy to sample estimate methods. The bootstrapping is performed 100 times.

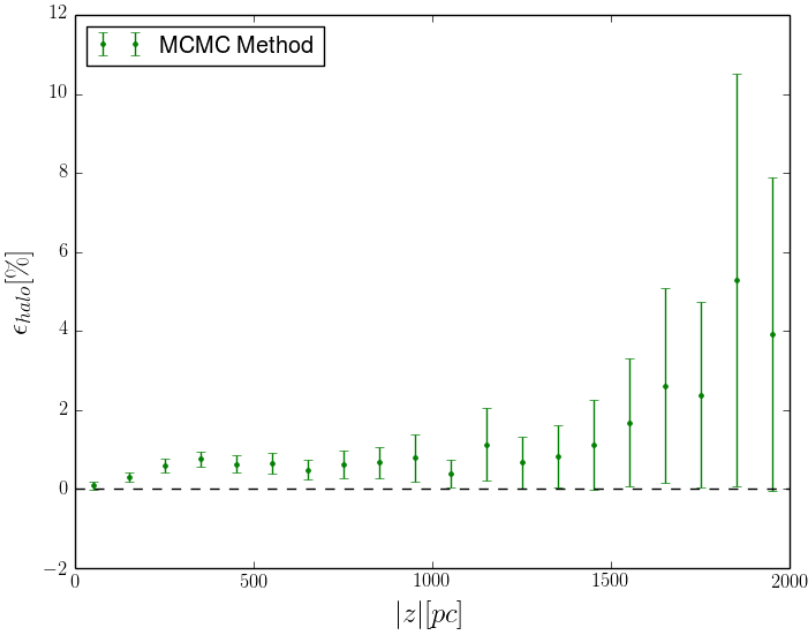

Figure 4.8: Fraction of halo stars in a height range $0 \leq z \leq 2$ kpc calculated using the MCMC simulation.

4.4.1 Shape of the velocity ellipsoid

The ratio between the azimuthal and radial axes of the velocity ellipsoid is determined by the epicycle approximation (Binney & Tremaine 2008) and it results in $\sigma_\phi^2/\sigma_R^2 \sim 0.5$ for a flat rotation curve.

We can define the ratio between the vertical and radial velocity dispersions as the anisotropy of the velocity ellipsoid in the meridional plane (σ_z/σ_R). If this ratio tends to unity, the two velocity dispersions are the same. This ratio tells us how the shape of the velocity dispersion changes in the meridional plane. The anisotropy does not change with radius, if we assume that the radial and vertical velocity dispersions can be described in the plane with an exponential profile:

$$\sigma_R^2 \propto \sigma_z^2 \propto \exp\left(-\frac{R-R_0}{R_\sigma}\right)$$

where R_σ is the radial scale length for the velocity dispersion.

The ratio between the vertical and radial velocity dispersion changes with z as we see in Fig. 4.9. This expresses how the shape of the velocity ellipsoid changes at larger distances from the Galactic plane, starting from a value of ~0.55 at $z = 0$ and increasing up to ~0.7 at $z = 2$ kpc for the biweight method. The MCMC method produces results rising from ~0.45 in the plane up to ~0.9 at $z = 2$ kpc. These greater values for the MCMC method are a reflection of the non-converging results for the radial velocity dispersion. The radial velocity dispersion is twice the vertical one at the solar position in the plane, confirming past observations in the solar neighbourhood (Wielen 1977; Dehnen & Binney 1998). The radial and vertical velocity dispersions are not equal ($\sigma_z/\sigma_R < 1$) and this is a confirmation about the existence of the third integral of motion. If only two integrals would exist, the two axis of the velocity ellipsoid are the same and this ratio equals 1.

The velocity dispersions are the results of what happened during the cosmic time, when stars could have experienced scattering due to spiral arms, molecular clouds (Binney & Tremaine 2008) or external processes like accretion of satellites onto the Milky Way (Villalobos & Helmi 2008). The ratio between

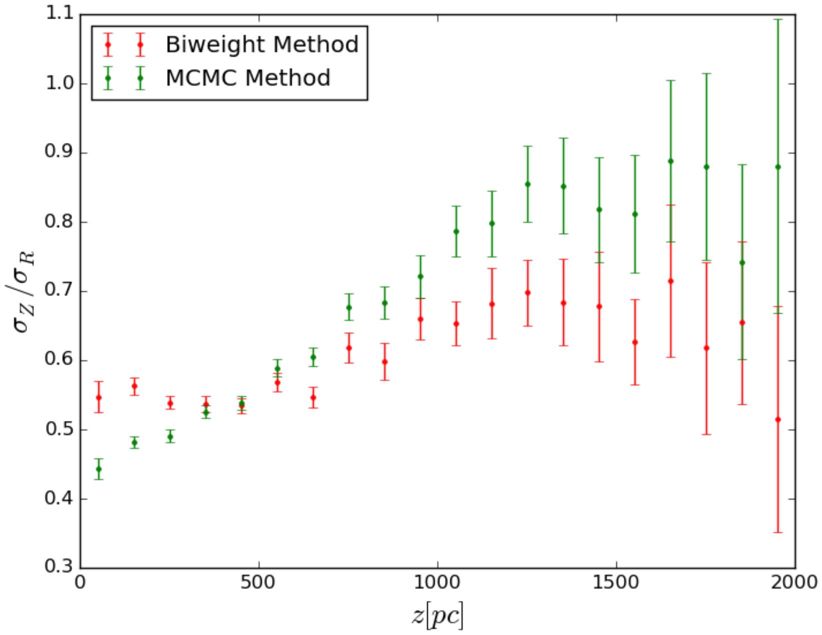

Figure 4.9: Ratio between the vertical and radial velocity dispersion for the red clump giants using the biweight and the MCMC method.

the vertical and radial velocity dispersion may provide a relic, which mechanism was able to heat the stellar disc.

The values in favour for the case of spiral arms and molecular clouds are in a range between 0.4 and 0.8 (Jenkins 1992) whereas for the case of the accretion disc they are between 0.4 and 0.9 (Villalobos & Helmi 2008). Our results cannot exclude any of the two mechanisms, but we can constrain the parameters for the models.

4.4.2 Tilt of the velocity ellipsoid

We want now to calculate the tilt of the velocity ellipsoid using the same MCMC fitting method used by Büdenbender et al. (2014) and the biweight method, and compare the two results with each other as well as with the results in the literature.

The last term that we need to calculate is the covariant term $\overline{v_R v_z}$ (Fig. 4.10). This parameter represents the correlation between the radial and vertical motion and shows the behaviour for the inclination of the velocity ellipsoid with respect to the Galactic plane. The result that we obtain is around zero near the plane, then it follows a declining monotonic trend. The results for both the methods are consistent with each other.

Fig. 4.11 shows the results for the tilt of the velocity ellipsoid. The black line corresponds to an orientation of the velocity ellipsoid with the spherical coordinate system and the blue line with the spheroidal coordinates for the case of Stäckel potential with $\Delta = 4$ kpc. The red points are the results found by using the biweight method whereas the green points found by using the MCMC fitting. At small distances from the midplane it is difficult to estimate the value for the tilt because the angle is very small (<5°). At larger z the MCMC method produces results per bin deviating from the biweight method. We obtain a value for the inclination of the velocity ellipsoid steeper than the case of alignment with spherical coordinates. The problem is that there are few stars at larger heights and the MCMC method requires a bigger number

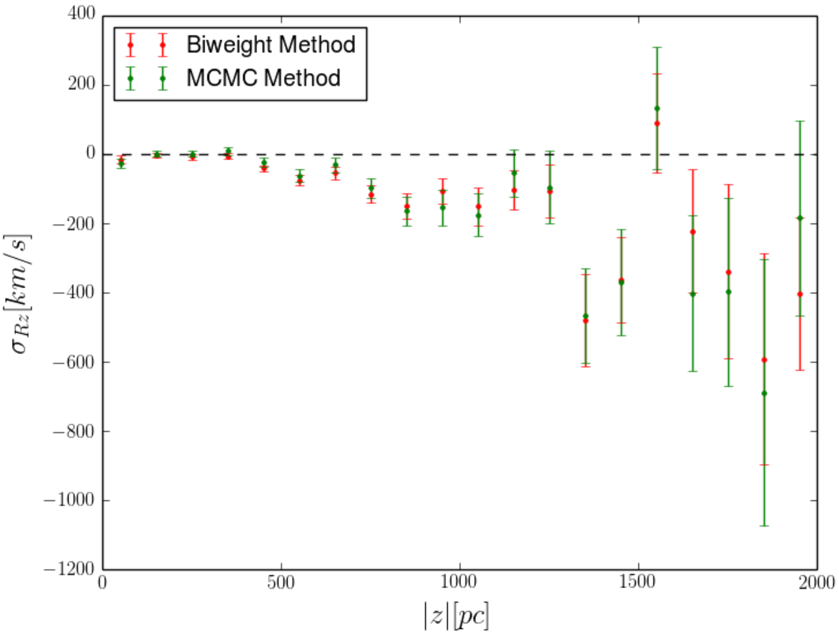

Figure 4.10: Covariant term of the velocity dispersion matrix (σ_{Rz}) decreasing with z for the red clump giants using the biweight and the MCMC method.

of stars to produce good results. Another problem is that the radial and vertical velocity distributions in the bins deviate from gaussianity, which is the assumption for the construction of the MCMC fitting. This result for the tilt is the reflection of the different results for the radial velocity dispersion between the two methods, because the vertical velocity dispersion and the covariant term $\overline{v_R v_z}$ are consistent. The halo contribution for the MCMC method is around ∼1% in bins up to 1 kpc and then rises up to 5% at 2 kpc.

If we apply a linear fit to the data while assuming $\alpha = 0$ at $z = 0$ and not considering bins at large distances, which tend to produce great errors due to the small number of stars, we obtain for the biweight method (see Fig. 4.12):

$$\alpha_{tilt} = (-0.75 \pm 0.09) \arctan(|z|/R_0)$$

whereas for the MCMC sampling (Fig. 4.13)

$$\alpha_{tilt} = (-0.58 \pm 0.18) \arctan(|z|/R_0)$$

Both methods are in agreement with each other but produce lower results than the recent derivations of the tilt of the velocity ellipsoid. The MCMC method produces a lower result but the errorbar is large.

We remind that the total gravitational potential can be separated in the radial and vertical contribution close to the plane (epicycle approximation). Then, we consider an horizontal orientation of the velocity ellipsoid up to 300 pc height and we fit the data for larger distances. With this double fit we obtain a larger value of the tilt angle, which is better in agreement with the observations of the last years. The result for the biweight method is:

$$\alpha_{tilt} = (-0.79 \pm 0.10) \arctan(|z|/R_0)$$

For the MCMC sampling we obtain:

$$\alpha_{tilt} = (-0.66 \pm 0.19) \arctan(|z|/R_0)$$

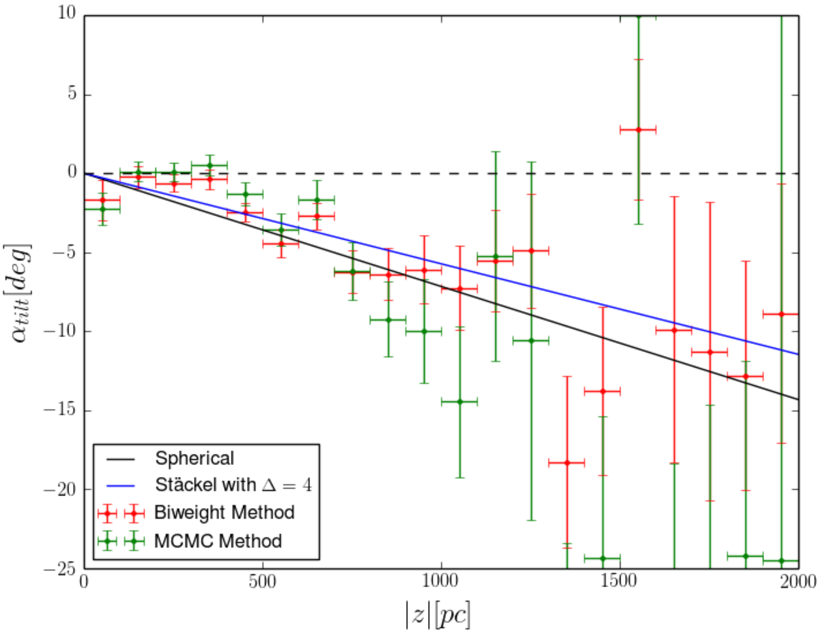

Figure 4.11: Tilt of velocity ellipsoid for the red clump giants using the biweight and the MCMC method.

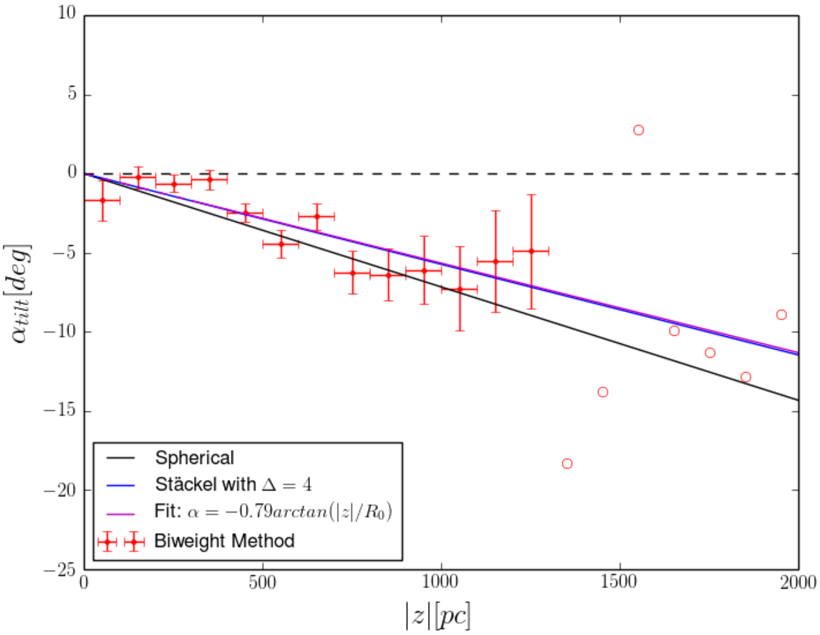

Figure 4.12: Least-square fit of the tilt of velocity ellipsoid, assuming a zero tilt angle in the midplane, for the red clump giants using the biweight method.

This result does not change neither if we change the position of the Sun by locating it in the Galactic

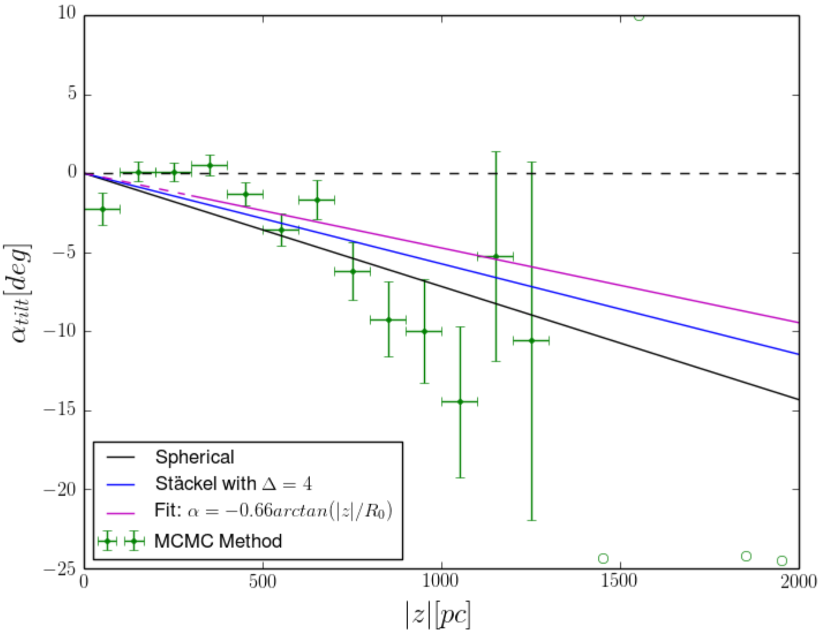

Figure 4.13: Least-square fit of the tilt of velocity ellipsoid, assuming a zero tilt angle in the midplane, for the red clump giants using the MCMC method.

plane ($z_0 = 0$) or assuming a different distance from the Galactic centre ($R_0 = 8.3$ kpc) nor if we assume an overestimation for the distances of ∼20%.

4.5 Subpopulations

After looking at all stars together, we divide now the sample in three subpopulations of different metallicity and study the orientation of the tilt of the velocity ellipsoid for each subpopulation using the biweight method only. For the case of Stäckel potential, after we fix the value for the focal point of the spheroidal coordinate system Δ, the velocity ellipsoid lines up with the coordinate system. If we split the sample in different subpopulations, the different tracers should not have different tilts of the velocity ellipsoid, because the total gravitational potential that each subpopulation undergoes is the same.

We have to consider stars with chemical abundances and the sample is smaller than before. With our selection for red clump giants we remain with a sample of 41510 stars, 15192 stars at $z > 0$ and 26318 stars at $z < 0$. The plot with values of $[Fe/H]$ versus $[\alpha/Fe]$ for the complete sample is shown in Fig. 4.14.

We divide the sample (of 41510 stars) in three subpopulations assuming the following ranges of metallicities:

- Metal-poor subpopulation: $[Fe/H] \leq -0.5$ with 10121 stars
- Middle subpopulation: $-0.5 < [Fe/H] \leq -0.2$ with 19756 stars
- Metal-rich subpopulation: $[Fe/H] > -0.2$ with 11633 stars

The metal-poor subpopulation contains a wide range in metallicity but the least number of stars (10121 stars). If we cut at $[Fe/H] > -1$ to be sure that the selection includes only disc stars, the result

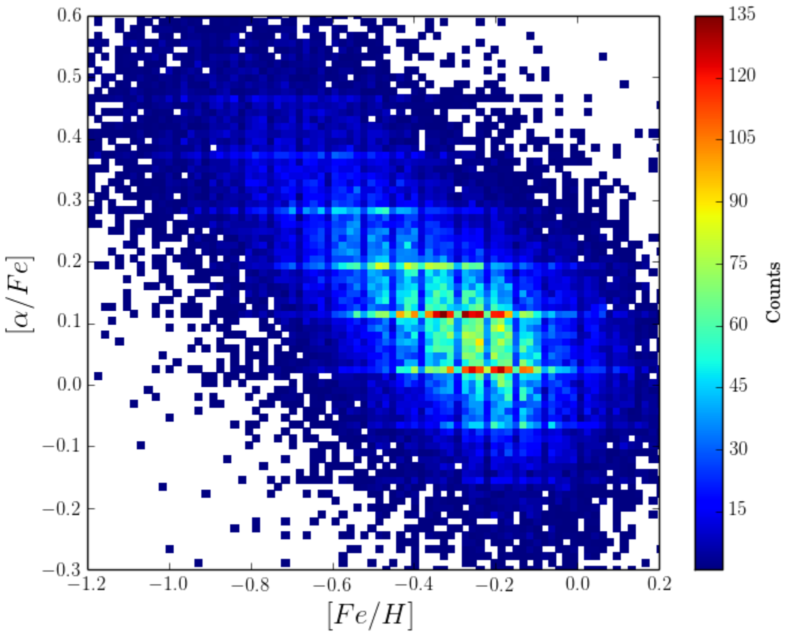

Figure 4.14: $[Fe/H]$ vs $[\alpha/Fe]$ abundances of red clump giants.

does not change. The middle subpopulation contains the largest number of stars (19756 stars). The metal-rich population does not extend at $[Fe/H]$ greater than 0.2 and contains 11633 stars.

4.5.1 Velocity dispersions

We can calculate the velocity dispersions, σ_R and σ_z, for the three subgroups and show the results in Fig. 4.15 and 4.16.

The radial and vertical velocity dispersions increase with the height. The less metals the subpopulation contains, the greater is the value for the velocity dispersion. One reason could be because the metallicity is a proxy of age, where more metal-poor stars correspond to older populations. The radial and vertical velocity dispersions are larger for older populations because these stars had more time to be affected by dynamical heating mechanisms. The most metal-poor subpopulation shows the largest values for the velocity dispersions (both for radial and vertical) with respect to the other two subpopulations whereas the difference between the other two subpopulations is less enhanced. The vertical velocity dispersion shows a stronger dependence in metallicity with respect to the radial velocity dispersion. More metal-poor subpopulations can reach larger distances above the midplane, whereas more metal-rich subpopulations lie at lower heights. Stars with different metallicities have different spatial distribution and kinematics due to their difference in ages and origin (Smith et al. 2012).

4.5.2 Tilt of the velocity ellipsoid

To derive the tilt of the velocity ellipsoid we need the covariance term $\overline{v_R v_z}$ whose trend is consistent for the three subpopulations (Fig. 4.17). The radial and vertical velocity dispersions together with the covariant term $\overline{v_R v_z}$ combine to determine the orientation of the velocity ellipsoid (Fig. 4.18). The best least square fit for the three subpopulations produces the following results for the tilt, assuming that the velocity ellipsoid is horizontal in the plane ($\sigma_{Rz} = 0$ at $z = 0$):

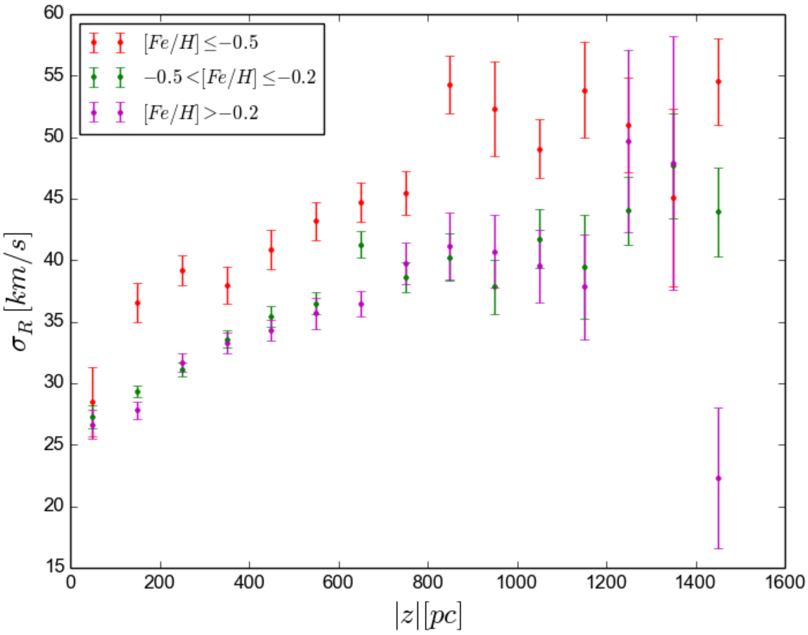

Figure 4.15: Radial velocity dispersion σ_R for three subpopulations ($[Fe/H] \leq -0.5$, $-0.5 < [Fe/H] \leq -0.2$, $[Fe/H] > -0.2$) of red clump giants.

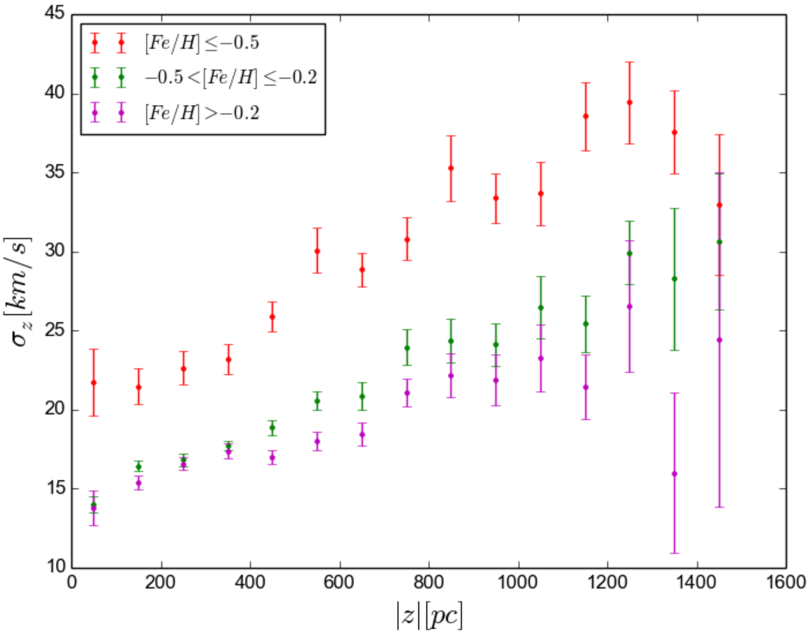

Figure 4.16: Vertical velocity dispersion σ_z for three subpopulations ($[Fe/H] \leq -0.5$, $-0.5 < [Fe/H] \leq -0.2$, $[Fe/H] > -0.2$) of red clump giants.

- Metal-poor subpopulation: $\alpha_{tilt} = (-0.56 \pm 0.23) \arctan(|z|/R_0)$

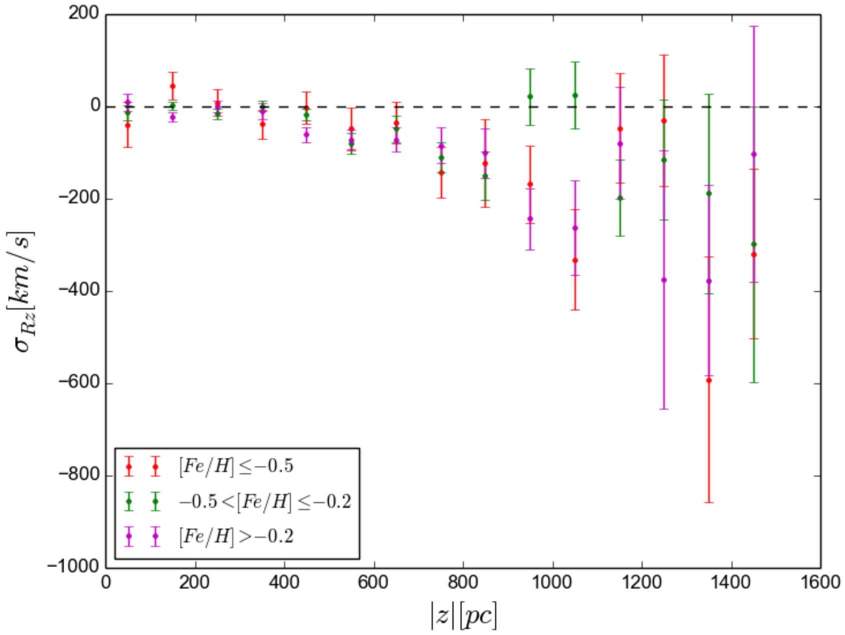

Figure 4.17: Covariant term of the velocity ellipsoid (σ_{Rz}) for three subpopulations ($[Fe/H] \leq -0.5$, $-0.5 < [Fe/H] \leq -0.2$, $[Fe/H] > -0.2$) of red clump giants.

- Middle subpopulation: $\alpha_{tilt} = (-0.62 \pm 0.18) \arctan(|z|/R_0)$
- Metal-rich subpopulation: $\alpha_{tilt} = (-0.70 \pm 0.10) \arctan(|z|/R_0)$

The subpopulations show different results for the velocity dispersions but the results for the tilt within the errors are in agreement for all the three subpopulations (Fig. 4.18). We can assume that the tilt of the velocity ellipsoid is zero close to the plane ($z < 300$ pc) and fit the data at $z > 300$ pc:

- Metal-poor subpopulation: $\alpha_{tilt} = (-0.67 \pm 0.19) \arctan(|z|/R_0)$
- Middle subpopulation: $\alpha_{tilt} = (-0.63 \pm 0.22) \arctan(|z|/R_0)$
- Metal-rich subpopulation: $\alpha_{tilt} = (-0.74 \pm 0.10) \arctan(|z|/R_0)$

Therefore, we can claim that the orientation of the velocity ellipsoid is the same for each subpopulation and the tilt angle is zero close to the plane.

4.6 Tilt close to the plane

The result found for the orientation of the velocity ellipsoid establishes that the radial and vertical motion are not decoupled. From the epicycle approximation theory we know, however, that close to the plane it is possible to separate the motion of the stars in the radial and vertical direction because the gravitational potential can be separated ($\Phi(R, z) = \Phi(R) + \Phi(z)$) (Binney & Tremaine 2008).

From our analysis of the red clump stars it is not possible to claim neither that the tilt of the velocity ellipsoid close to the plane is zero nor that it has the same inclination as at larger heights. We can only suggest that the velocity ellipsoid is parallel to the midplane close to the plane because otherwise the tilt angle for different subpopulations would be small. The results would be significantly smaller than the recent measurements. For understanding this point we want to use the second selection of stars which was described earlier, the cold dwarfs. The cold dwarfs lie in the first ~500 pc only, without a further extension in height. The estimation of the tilt at this height is not easy because the tilt angle corresponds to a value of ~2° at 500 pc for an alignment with the spherical coordinates. The number of dwarfs is, however, very large and we can estimate accurately the value for the tilt with errors less than 1°. We can divide the sample of 45774 stars in five bins of 100 pc each and the result for the least-square fit is (Fig. 4.19):

$$\alpha_{tilt} = (-0.71 \pm 0.05) \arctan(|z|/R_0)$$

The result for the tilt angle of the velocity ellipsoid is consistent with zero up to 300 pc. For distances larger than 300 pc the tilt angle is in agreement with the result found with the red clump analysis.

4.7 Discussion

The large number of observations and very high resolution of line-of-sight velocity make RAVE data good for the study of stellar kinematics in the extended solar neighbourhood. This survey observes in a cone in direction of both North and South Galactic Pole in infrared, therefore we have very small absorption. It is also complementary to the Sloan Digital Sky Survey (SDSS) because it observes at magnitudes between 9 and 13. This means that most stars are observed close to the plane and less at larger heights. They are also extended in a large radial range so that we can pursue studies beyond the classic solar neighbourhood region.

We selected two samples for our analysis, red clump giants and cold dwarfs. The giants are good to sample large distances from the Galactic plane, whereas the cold dwarfs are good for kinematical studies close to the plane. We performed a study of the extended solar neighbourhood considering only stars in a cylinder of 1 kpc radius ($7 \leq R \leq 9$ kpc) and in a height range $-2 \leq z \leq 2$ kpc.

The number of stars in the plane is very large and it decreases strongly with the height. For this reason it is not good to bin the data with the same number of stars per bin. We have binned in intervals of 100 pc and applied two methods for studying the shape and the orientation of the velocity ellipsoid in the meridional plane: a MCMC discrete likelihood fitting (Büdenbender et al. 2014) and a robust biweight function.

The MCMC method does not work well because the farther we go from the plane, the faster decreases the number of stars, sampling only a few hundred stars per bin though a greater number of data is required for it to work properly. Another reason is that the radial and vertical velocity distributions in the bins are not Gaussian, showing asymmetries in the tail or too sharp peaks. The biweight method produces better results. The vertical velocity dispersion for the giant sample is 15 km/s in the plane increasing up to 36 km/s at 2 kpc and the radial velocity dispersion results in 26 km/s in the plane increasing up to 61 km/s at 2 kpc.

Binney et al. (2014a) performed an analytic fit to the variation of the velocity ellipsoid within the meridional plane by a technique that avoids binning RAVE data. Their values are greater than ours: they found values for the $\sigma_z \sim 21$ km/s in the plane rising up to 55 km/s at 2 kpc and for $\sigma_R \sim 37$ km/s in the plane rising up to 82 km/s at $z = 2$ kpc. Despite the different results for the radial and vertical velocity dispersions, the result for the inclination of the velocity ellipsoid for both the giants and dwarfs sample is consistent with Binney et al. (2014a).

This result of the tilt is also consistent with past measurements, which found out that the longer axis of the velocity ellipsoid is pointing towards the Galactic centre with large errorbars (Siebert et al. 2008; Casetti-Dinescu et al. 2011; Smith et al. 2012; Pasetto et al. 2012a,b). The latest measurement was carried out by Büdenbender et al. (2014) who applyed a MCMC fitting to ~16000 G-dwarfs from the SDSS/SEGUE survey, studying first seven different subpopulations and then the full sample of stars at $z > 0$ and $z < 0$. They arrived to determine that the orientation of the velocity ellipsoid is consistent with Siebert et al. (2008) with errors for the tilt less than 4° in a height range between $0.4 \leq z \leq 2$ kpc ($\alpha_{tilt} = (-0.78 \pm 0.2) \arctan(|z|/R_{\odot})$). Fig. 4.20 shows the comparison between their results and ours.

The novelty of this work is that we split the RAVE sample of the red clump giants in three subpopulations of different metallicity ($[Fe/H] \leq -0.5$, $-0.5 < [Fe/H] \leq -0.2$, $[Fe/H] > -0.2$). Studying the kinematics (σ_R, σ_z and σ_{Rz}) we found different results for the radial and vertical velocity dispersions. The more metal-poor the subpopulation is, the larger their velocity dispersions in the meridional plane. The metallicity is a proxy of age, where more metal-poor stars correspond to older population. Therefore, they had time to be affected by dynamical heating mechanisms probably driven by the spiral structure or satellites accretion. Although the radial and velocity dispersions are different for different subpopulations, we found that the tilt is the same as for the full sample. Better results are given using a double fit, assuming that the velocity ellipsoid is parallel to the mid-plane up to 300 pc. This is because the stellar orbits can be separated in a radial and vertical motion, due to the separability of the gravitational potential (Binney & Tremaine 2008).

For the case of separable distribution functions and a Stäckel potential the velocity ellipsoid is oriented with the spheroidal coordinate system. In the last Chapter, we fixed the value of the focal point to $\Delta = 4$ kpc from observation of the velocity ellipsoid found by Binney et al. (2014a) based on RAVE data and we constructed a Stäckel model for the extended solar neighbourhood. We changed the parameter of the focal point for different values, between 1 and 10 kpc. We looked at the impact that different values of Δ produce on the different kinematical properties, like the radial density profile, the scale length and the vertical force. The conclusion was that the determination of the Δ is crucial in the construction of a dynamical model for the extended solar neighbourhood. In this Chapter, we have confirmed the results found by Binney et al. (2014a) and Büdenbender et al. (2014) for the orientation of the velocity ellipsoid in the meridional plane. This confirms our best choice for the focal point $\Delta = 4$ kpc. Since all the stars experience the same total gravitational potential, the value Δ has to be the same not only for all the stars but also for different subpopulations. This can be considered a test of 'stäckelness' and a confirmation of the Stäckel model we have constructed in the last Chapter. The same orientation of the velocity ellipsoid for different subpopulations means that this parameter has the same impact on the Jeans equations, i.e. on the gravitational force and asymmetric drift.

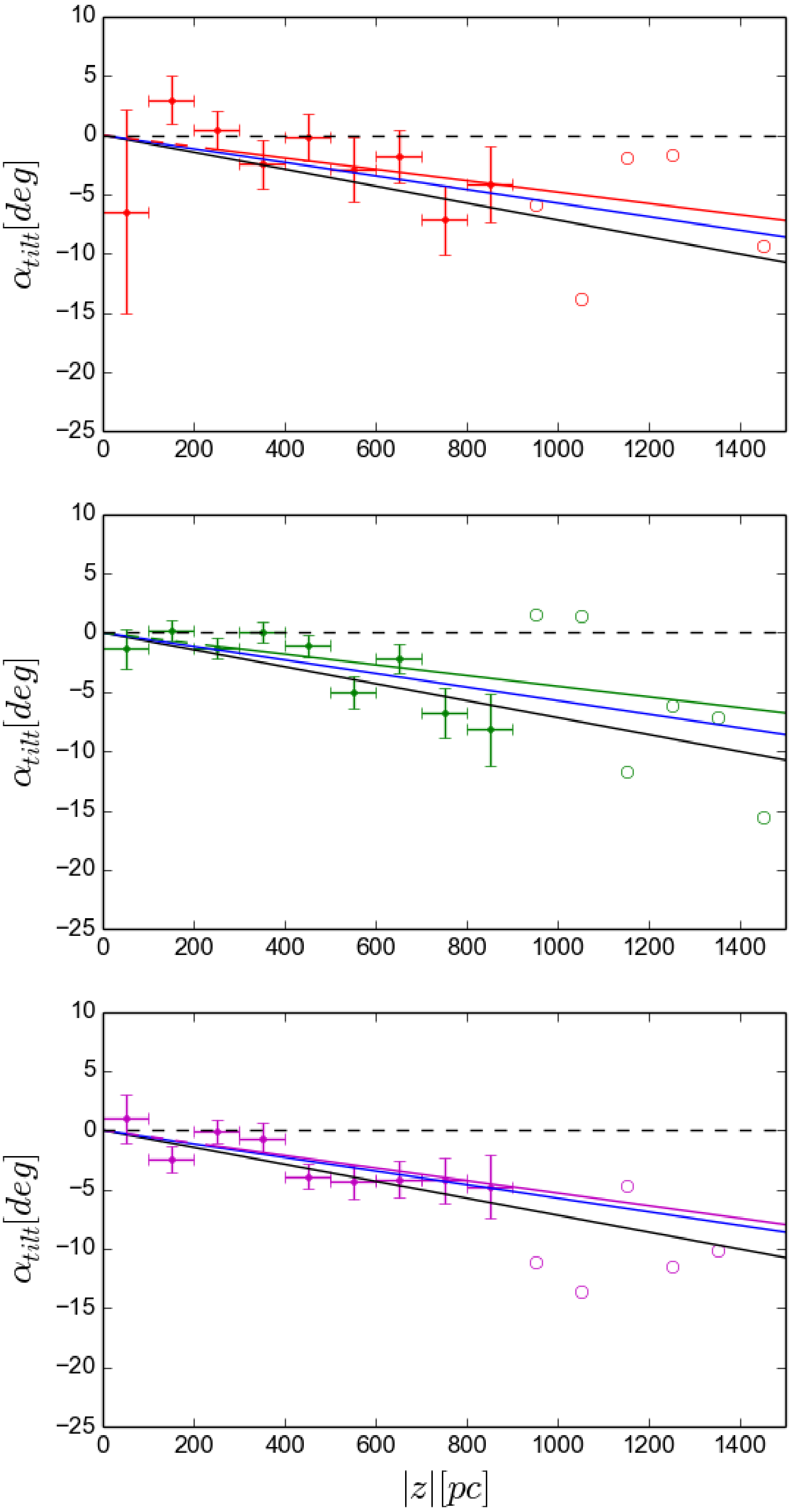

Figure 4.18: Tilt of the velocity dispersion for three subpopulations ($[Fe/H] \leq -0.5$, $-0.5 < [Fe/H] \leq -0.2$, $[Fe/H] > -0.2$) of red clump giants.

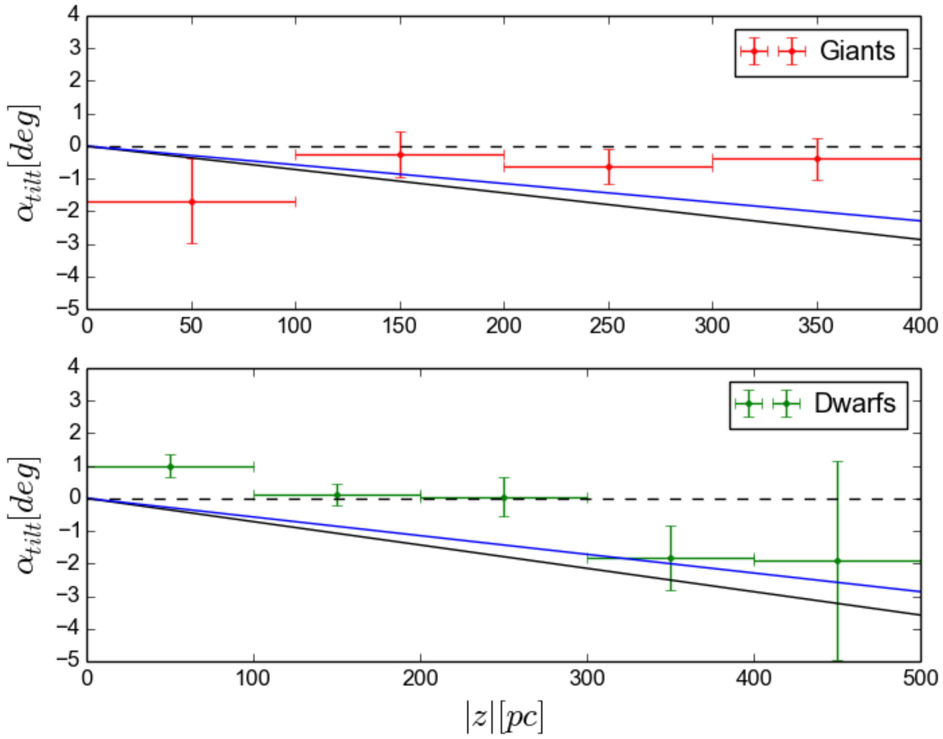

Figure 4.19: Tilt of the velocity ellipsoid for the red clump giant sample and the cold dwarf sample close to the plane ($-500 < z < 500$ kpc) using the biweight method.

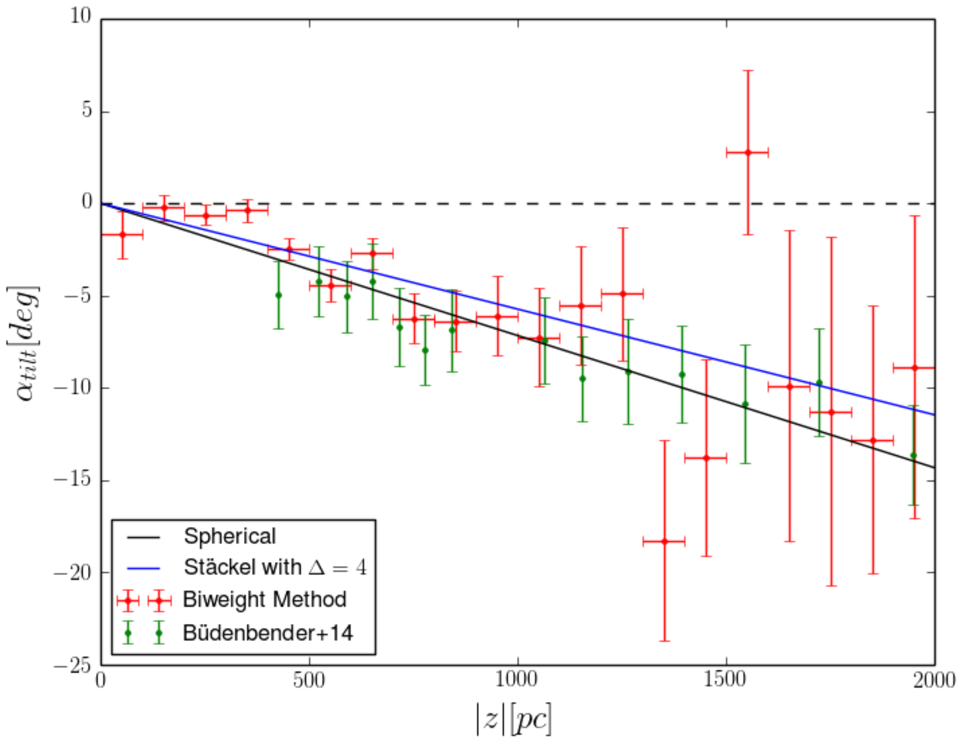

Figure 4.20: Comparison of the tilt of velocity ellipsoid for red clump giants using the biweight method and Büdenbender et al. (2014).

5

Future work

5.1 Two-component model

In Chapter 3 we used an Ansatz to derive the gravitational force from an expression for the ’vertical’ potential function $G(v)$, which is simple and representative for the total potential. In this Chapter we want to use a function $G(v)$, which corresponds to a more realistic one, composed of two components, namely an ’exponential’ approximation for the disc plus a cored isothermal profile for the dark matter halo. We choose the integration constant C_0, which enters in the ’radial’ potential function $F(u)$ to fix the gravitational potential in the plane to the given one by a Bessel potential for the disc and a cored isothermal profile for the dark matter halo. We set the values of the central surface density and the radial scale length for the Bessel disc, and the core radius for the dark matter halo with the values found by Golubov (2012). These two components generate a flat rotation curve at R_0. We select as ’radial’ function $F(u)$ the one corresponding to the logarithmic case.

The complete expression for the gravitational force in the spheroidal coordinates reads:

$$K_z = -\frac{\partial \Phi}{\partial z} = -\left(\frac{\partial \Phi}{\partial v}\frac{\partial v}{\partial z} + \frac{\partial \Phi}{\partial u}\frac{\partial u}{\partial z}\right) \tag{5.1}$$

The spheroidal coordinates lead to many terms when we study the situation away from the plane. The larger the value of the focal point Δ is, the smaller are the variations of the coordinate u with z. However, as we have seen in Section 3.8 the second term in the vertical force cannot be neglected.

We want to use an Ansatz for the $G(v)$ potential, splitting the contribution in baryonic and dark matter. We can choose an approximation for the vertical force due to the tracers of the form:

$$G(v)_{exp} = -v_{z,s}^2\left[z_0^2 \exp\left(-\frac{\Delta \cosh u_0 \cos v}{z_0}\right) + z_0 \Delta \cosh u_0 \cos v - z_0^2\right]$$

where $v_{z,s}$ is the ’vertical’ oscillation frequency already discussed in the radial density section and z_0 is the scale height of the disc. u_0 is the value of the coordinate u at the solar position $(R_0, 0)$. In this way, there is no dependence on the coordinate u in the function $G(v)$, as required by the special form of the Stäckel potential, and the ’vertical’ potential is a function of $\cos v$ only.

This ’vertical’ potential has been chosen assuming the approximation for the vertical potential, which leads to an exponential vertical density profile as in the case of cylindrical coordinates. Since we are in the solar neighbourhood the behaviour of the vertical potential is approximately that of $G(v)$, then we rewrite the approximation in spheroidal coordinates. We could also use an isothermal sheet which will reproduce a $sech^2(z/z_0)$ vertical density profile. The vertical profile is not exactly known but it seems to lie between these two cases. When we take the second derivative of the 'vertical' potential, the contribution to the radial density will in both cases be given by the value of the new oscillation frequency, which is constant in the plane:

$$\left(\frac{1}{\Delta^2 \cosh^2 u}\frac{\partial^2 \Phi_s}{\partial v^2}\right)_{v=\pi/2} = -\nu_{z,s}^2$$

If we choose for the potential the exponential approximation or the case of isothermal sheet, the result remains the same.

The first derivative of $G(v)$ is:

$$G'(v) = -\nu_{z,s}^2 \left[z_0 \exp\left(-\frac{\Delta \cosh u_0 \cos v}{z_0}\right)(\Delta \cosh u_0 \sin v) - z_0 \Delta \cosh u_0 \sin v \right]$$

Interesting is that the z-derivative of the coordinate v in the plane results $-1/(\Delta \cosh u_0)$ and this would eliminate the same value in the numerator. Although the term $G'(v)dv/dz$ is the dominant term in the vertical force, we need to assume the complete formula for the K_z-force (Eqs. 3.26 and 3.27). Moreover, it is necessary to consider the complete dependence of the coordinate v from z, i.e. the z-derivative of the v coordinate does not remain constant for every z. We want to add a second $G(v)$ function which should correspond to the dark matter profile.

5.1.1 Linear profile

We can use a constant contribution for the dark matter with height which is reproducible with a quadratic profile for the gravitational potential:

$$G_{dm}(v) = -2\pi G \rho_{0,dm} \Delta^2 \cosh^2 u_0 \cos^2 v$$

This profile for the dark matter leads to an increase in the vertical force with a slope different from the first one given by the baryonic matter. Our result is in agreement with the observables when choosing a value for the scale height $z_0 = 300$ pc (Fig. 5.1). The K_z-force increases always linearly for the value of $\Delta = 10$ kpc. For smaller values the vertical force curves towards lower values at larger heights. This is because for smaller values of Δ the coordinates u become more spherical.

We can estimate the value at 2 kpc, which is 103 $M_\odot/pc^2$ for $\Delta = 4$ kpc. This value is larger than the values found by Bienaymé et al. (2014). Their value for the focal point is smaller and we expect that the vertical force is smaller at large heights for smaller Δ. However, the K_z-force in our case remains approximately the same for all the different values of Δ up to 2 kpc.

Bienaymé et al. (2014) calculated the vertical force fitting a distribution function depending on the three isolating integrals of motion in a potential of the Stäckel form. Their result is 96.9 ± 2.2 $M_\odot/pc^2$.

5.1.2 Isothermal profile

A second possibility for the dark matter halo is to choose an isothermal profile with a core radius R_c and flattening parameter q. The 'vertical' isothermal profile can be written in the following way:

$$G_{dm}(v) = -4\pi G \rho_{0,dm} R_c^2 \log\left(\sqrt{\frac{\Delta^2 \sinh^2 u_0 + \Delta^2 \cosh^2 u_0 \cos^2 v + R_c^2}{\Delta^2 \sinh^2 u_0 + R_c^2}}\right)$$

We substitute the vertical potential depending on z with the transformation for the spheroidal coordinates. The potential is chosen in a way that it is zero in the plane ($G(v = \pi/2) = 0$) as requested during the

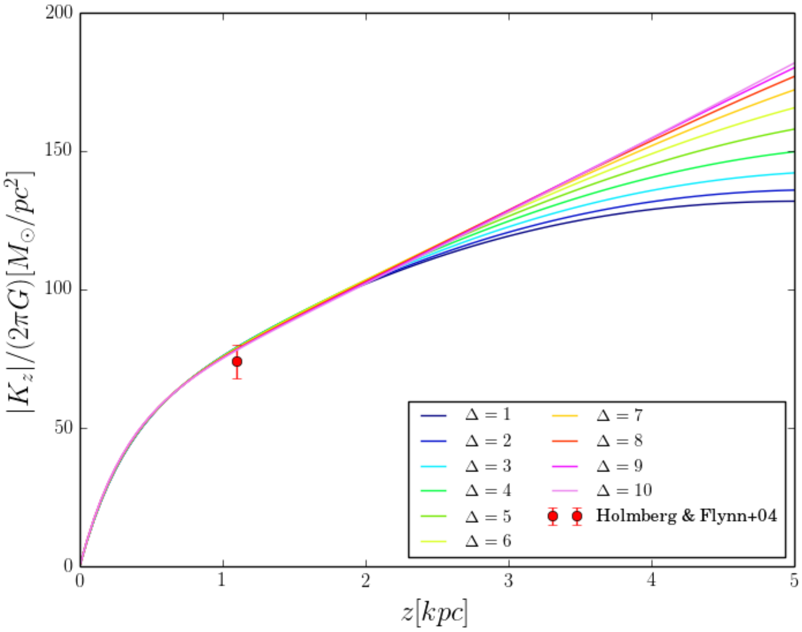

Figure 5.1: Local vertical force for a two-component model for the potential function $G(v)$ using a linear profile for the dark matter halo with scale height $z_0 = 300$ pc, for different values of Δ. The observational constrain is given by Holmberg & Flynn (2004).

study of the radial profile. We assume that the dark matter density is ~10% of the baryonic matter at R_0 and the core radius $R_c = 3.5$ kpc.

We obtain a linear behaviour as for the linear case away from the plane, but with a different slope. We consider only the case when the flattening parameter q is equal to one. This would mean that the dark matter halo is spherical. Values for q smaller than one reproduce an oblate (flattened) dark matter halo, while values greater than 1 produces a prolate halo. This parameter can be used to change the value and the slope of the rotation curve. A flattened dark matter profile leads to a larger dark matter density in the plane, with a consequently greater circular speed.

We obtain for the K_z-force the result shown by Fig. 5.2, which is in agreement with Holmberg & Flynn (2004). Although we are studying the vertical force in spheroidal coordinates, we can obtain the same profile for all the values of Δ up to heights of ~3 kpc. At larger height, the vertical force changes for different values of Δ. For $\Delta = 10$ kpc the force continues to increase linearly, while for smaller Δ it curves towards smaller values. This is because, for small values of Δ, the coordinate system becomes more spherical. We found a value for the K_z force at 2 kpc of 90 $M_\odot/pc^2$, and thus almost in perfect agreement with the result found by Bienaymé et al. (2014).

5.1.3 Surface density at 1.1 kpc ($K_{1.1}(R)$)

After having fixed all the free parameters we can predict how the vertical force behaves at different galactocentric radii in the extended solar neighbourhood by considering the value at $z = 1.1$ kpc. We can compare this value with the result found by Bovy & Rix (2013) where they determined the radial surface density at 1.1 kpc away from the plane in a radial range between $4 \leq R \leq 9$ kpc. Their result is that the radial surface density, and the radial dependence of the vertical force at 1.1 kpc, are well fitted by an exponential.

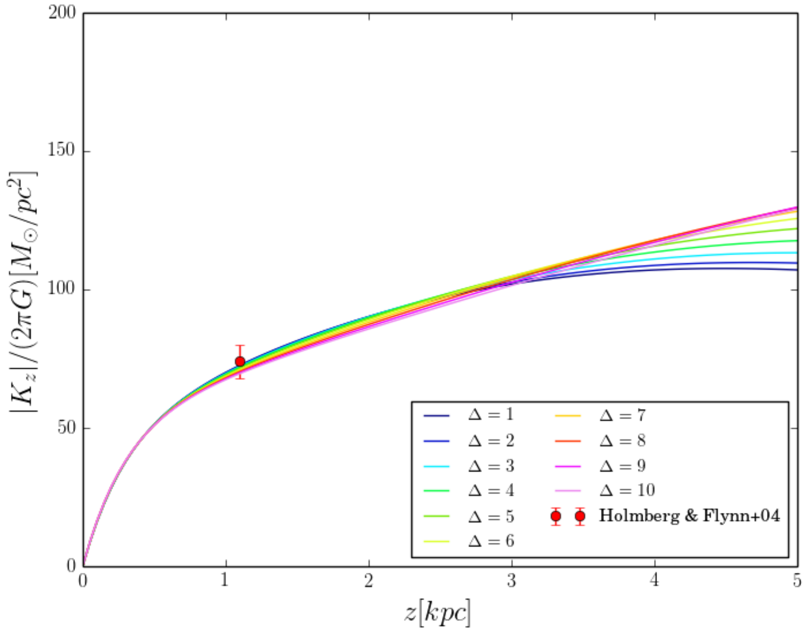

Figure 5.2: Local vertical force for a two-component model for the potential function $G(v)$ using a cored isothermal profile for the dark matter halo with scale height $z_0 = 300$ pc with a flattening $q = 1$, for different values of Δ. The observational constrain is given by Holmberg & Flynn (2004).

We consider Eq. 5.1, we fix $z = 1.1$ kpc and look at the behaviour at different radii. For small values of Δ the surface density results in larger values at small galactocentric radii and smaller values at larger radii. We can compare these results with a gravitational force declining exponentially with radius (Fig. 5.3):

$$\frac{|K_z(R, 1.1)|}{2\pi G} = \frac{|K_z(R_0, 1.1)|}{2\pi G} \exp(-(R - R_0)/R_d)$$

where $K_z(R_0, 1.1)$ is the value of the K_z-force at the solar position at $z = 1.1$ kpc and R_d is the value of the scale length for the logarithmic potential ($R_d = 2.55$ kpc). We chose an integration constant in a way to normalize the radial gravitational potential to that given by a Bessel disc plus a cored isothermal halo. This is valid for a local fit. However, if we want a global fit, we have to choose an integration constant equals to zero. The difference from an exponential density profile for $\Delta = 4$ kpc is approximately 10%. We are not able to reproduce an exponential declining vertical force with the galactocentric radii. This means that we are not able to reproduce a disc with constant thickness (Fig. 5.4).

5.2 Future work

We studied the Stäckel potential because it leads to the derivation of an analytic expression for the third integral of motion. This requires the knowledge of the gravitational potential. We constructed a model for the extended solar neighbourhood using four free parameters. First, we fixed the focal point of the spheroidal coordinate system, Δ. Second, we fixed the 'radial' and 'vertical' function of the Stäckel potential from observational constrains, as the rotation curve, the local volume density and the vertical surface density. After having fixed these parameters, we made predictions on the radial surface density at 1.1 kpc. We showed that it is not possible to reproduce three functions – the rotation curve, the shape of the gravitational potential and a constant disc thickness – at the same time using only two constrains.

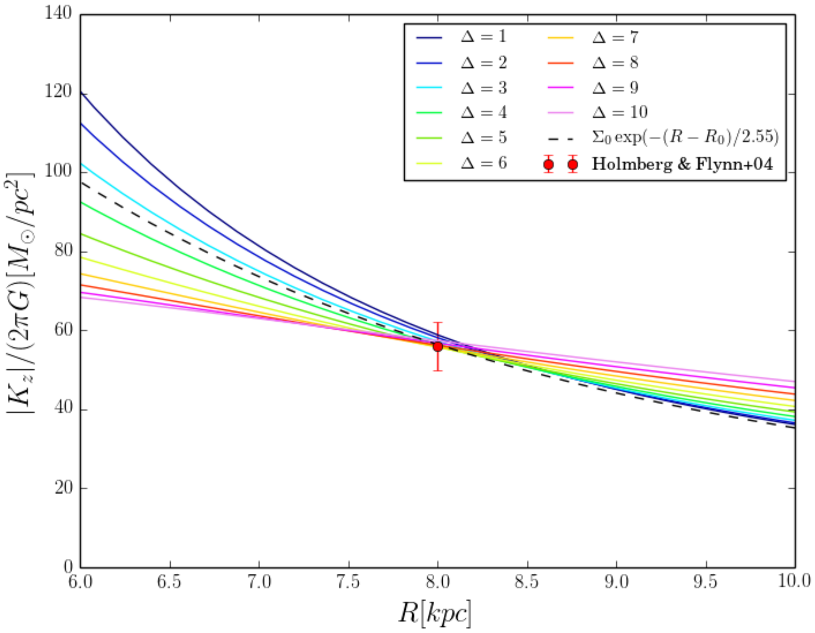

Figure 5.3: Radial surface density at $z = 1.1$ kpc for different values of Δ. The observational constrain is given by Holmberg & Flynn (2004). The dashed line corresponds to an exponential profile with scale length $R_d = 2.55$ kpc derived from the radial profile for the logarithmic case.

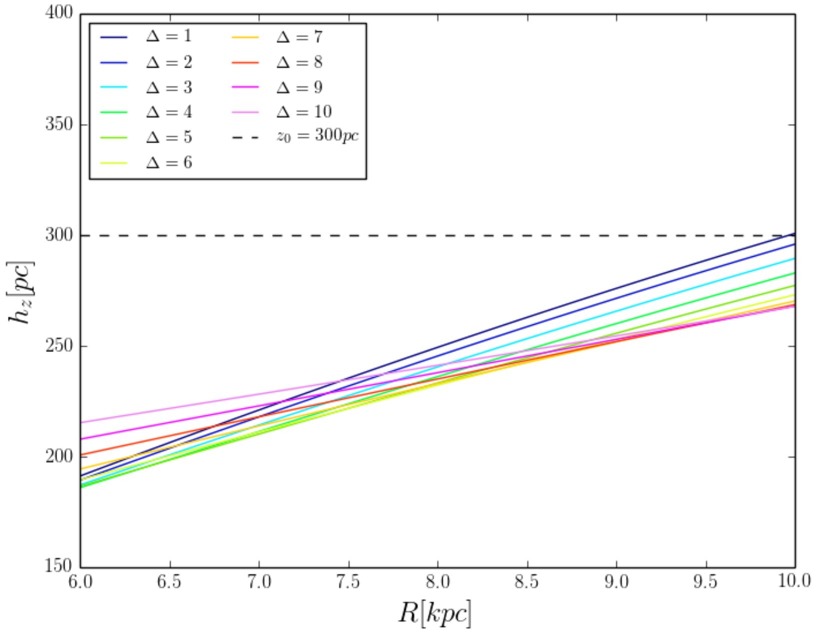

Figure 5.4: Dynamical estimation of the disc thickness using a two-component model for the potential function $G(v)$ for different values of Δ.

The result was that we cannot reproduce the constant disc thickness with radius and we obtained an increasing disc thickness with radius.

Since that we have fixed all the free parameters, we have an analytic approximation for the extended solar neighbourhood and we can derive the third integral of motion. The next step would be to look if the third integral of motion derived analytically remains constant during the stellar orbits. This integral of motion should recover the value of the vertical energy for stellar disc orbits near the plane and the total angular momentum for orbits far away from the plane, which belong to the halo. Between the plane and the halo the third integral should have a behaviour in between these two cases. The orbit integration can be carry out using a known gravitational potential or using the generated gravitation potential of the Stäckel form, as approximation for the true potential. If the third integral remains constant during the stellar orbital motions, we can confirm its isolating property and use it in the construction of a phase-space distribution function.

The construct of a phase-space distribution function is no easy task. Many scientists worked on it in the past, with many studies using the Stäckel potential. This function will be not unique, because it is a function of three quantities, and the spatial density that reproduces is a function of two coordinates only. How to construct this function is suggested by the Jeans theorem, which claims that we need to construct a function depending on integrals of motion. This function should be as realistic as possible: disc stars possess a large vertical component of angular momentum and small radial and vertical velocities; halo stars on the contrary a large radial velocity and a small vertical angular momentum. The first assumption would be to use exponential forms, as suggested by Shu et al. (1969) for the distribution function in the plane. For the vertical part we could follow Spitzer (1942) and Binney (2010) assuming that the populations behave quasi-isothermal with the height. Bienaymé (1999) and Bienaymé et al. (2014) constructed a distribution function depending on three integrals: the energy, the vertical component of the angular momentum and the third integral approximating the potential with one of the Stäckel form. The three-dimensional distribution function has to recover the Schwarzschild DF for the region of the solar neighbourhood. The constructed distribution function has to reproduce the triaxiality and the orientation of the velocity ellipsoid in the meridional plane.

Binney (2010, 2012a,b) suggested a way to construct the DF based principally on observations, using action-angle variables. Action-angle variables are a set of canonical coordinates which are used when the Hamilton-Jacobi equations are separable. These quantities remain invariants during the orbital motions. The drawback of this theory is that it requires the solution of a one-dimensional integral of the velocities over the conjugate coordinate to obtain the actions. When this integral is solved, the three actions are derived and these adiabatic invariants can be assigned as the three integrals of motion. However, it is only possible to find actions for few analytic potentials. The 'adiabatic' approximation used by Binney (2010) in modelling the solar neighbourhood (Schönrich & Binney 2009) is valid only close to the plane, because it requires the assumption that the gravitational potential can be separated along the radial and vertical motion. This approximation is not valid when we go far away from the plane. For this reason, Binney (2012a) developed a method to derive the actions using the Stäckel potential approximation. This new method produces more accurate results than the 'adiabatic' one.

From a constructed three-dimensional distribution function it is possible to derive the stellar kinematic properties. Integrations over the velocity space of the DF lead to the spatial density and to the second order velocity moments for the stars. The stellar spatial density and their velocity moments are related with the gravitational potential through the Jeans equations. Since for the Stäckel potential the velocity ellipsoid tensor is aligned with the spheroidal coordinate system, only three second order moments of the velocity distribution remain. The three variances of the velocity dispersion tensor together with the three Jeans equations form a closed system. The Jeans equations in spheroidal coordinates can be closed. From the Jeans equations it is possible to study the asymmetric drift and the vertical force, both quantities still a matter of debate. From the asymmetric drift it can be derived the value for the local standard of rest, while from the vertical Jeans equation we can predict the local vertical force and derive the amount of the local dark matter with the generated Stäckel model (as in Bienaymé et al. (2014)).

A
Stäckel potential

A.1 De Zeeuw coordinate system

There are two different descriptions of the confocal spheroidal coordinates: the first description is the one that we focus on during the thesis where we used a combination of trigonometric and hyperbolic functions for the conversion in cylindrical coordinates (Kent & de Zeeuw 1991; Binney 2012a). The second description is a mathematical relation which avoids the use of this kind of functions. It was used in the literature by de Zeeuw (1985) for studies of elliptical galaxies and it is applied now from Sanders (2012) for axisymmetric galaxies. We want also to understand the link between our description and the one used by de Zeeuw (1985) and Sanders (2012), looking at advantages and disadvantages and then it will be possible to convert from one description to the other one.

The 'de Zeeuw description' describes the spheroidal coordinate system as a triple (λ, ϕ, ν) where ϕ is the azimuthal angle in ordinary cylindrical coordinates and λ and ν are roots for τ:

$$\frac{R^2}{\tau + \alpha} + \frac{z^2}{\tau + \gamma} = 1 \tag{A.1}$$

where $\alpha = -a^2$ and $\gamma = -c^2$. a and c are constants, then α and γ are defined as negative constants, with $0 \leq \nu \leq \gamma$.

$$\frac{R^2}{\tau - a^2} + \frac{z^2}{\tau - c^2} = 1$$

A choice of the focal distance: $\Delta = (|\gamma - \alpha|)^{1/2} = |(a^2 - c^2)|^{1/2}$ fixes the spheroidal coordinate system. Coordinates with constant λ are spheroids and coordinates with constant ν are hyperboloids of revolution with the z-axis as rotation axis. Relations between the two coordinate systems are:

$$R^2 = \frac{(\lambda - a^2)(\nu - a^2)}{c^2 - a^2}$$

$$z^2 = \frac{(\lambda - c^2)(\nu - c^2)}{a^2 - c^2}$$

When $a > c$, so that $c^2 \leq \nu \leq a^2 \leq \lambda$, the spheroids of constant λ are prolate, while the hyperboloids of constant ν have two sheets. λ and ν are elliptic coordinates in each meridional plane, with focal points on the z-axis at $z = \pm\Delta$. When $a < c$, so that $a^2 \leq \nu \leq c^2 \leq \lambda$, the spheroids are oblate. The hyperboloids are one-sheet. λ and ν are again elliptic coordinates in each meridional plane, but now with focal points on the R-axis.

We can find the roots of Eq. A.1:

$$\tau = \lambda, \nu = \frac{1}{2}(R^2 + z^2 + a^2 + c^2) \pm \frac{1}{2}\sqrt{(R^2 + z^2 + a^2 + c^2)^2 - 4(a^2c^2 + c^2R^2 + a^2z^2)} =$$

$$= \frac{1}{2}(R^2 + z^2 + a^2 + c^2) \pm \frac{1}{2}\sqrt{(R^2 - z^2 + a^2 - c^2)^2 + 4R^2z^2} \tag{A.2}$$

It is possible to show that:

$$\lambda + \nu = R^2 + z^2 - \gamma + \alpha \quad , \quad \lambda\nu = \alpha\gamma - R^2\gamma - z^2\alpha$$

The line element of this curvilinear coordinate system is equal to $ds^2 = P^2du^2 + Q^2dv^2 + R^2d\phi^2$ with metric coefficients:

$$P^2 = \frac{(\lambda - \nu)}{4(\lambda - a^2)(\lambda - c^2)} \quad ; \quad R^2 = \frac{(\lambda - a^2)(\nu - a^2)}{c^2 - a^2} \quad ; \quad Q^2 = \frac{(\nu - \lambda)}{4(\nu - a^2)(\nu - c^2)}$$

R is the scale factor due to the azimuthal coordinate ϕ. In small regions around the Sun's position in the Galactic plane, λ is approximately equivalent to R and ν to z, but for larger ranges their curvilinear nature becomes more evident.

The 'de Zeeuw description' shows some problems. First, there is a sign problem because the transformation between the two coordinate systems enter in a quadratic term and we do not know in which quadrant we are. Second, the description requires two constants, two free parameters for the description if the system is prolate or oblate and these two constants together describe the value of the focal point. These two values give the rotation of the coordinate system.

The density distribution of the perfect ellipsoid (de Zeeuw 1985) is given by:

$$\rho = \frac{\rho_0}{(1 + m^2)^2}$$

where ρ_0 is the central density and $m^2 = R^2/a^2 + z^2/c^2$ the square of the spheroidal radius. A prolate coordinate system produces oblate density distribution whereas an oblate coordinate system produces a prolate density distribution. We are interested in oblate potentials and then the corresponding case is a prolate coordinate system. The λ surfaces are elongated contrary to the equipotentials (see Fig. A.1). Once we set the values for the constants a and c we can generate a prolate (if $a > c$) spheroidal coordinate system (Fig. A.2).

Furthermore, this description shows problems with the origin of the coordinate system. We can vary the parameter a and c to obtain the same focal points with different coordinates. The case when the constant c is equal to zero ($c = 0$) represents the case that we studied. In this case we remain with only one parameter that expresses the focal point ($a = \Delta$). The difference between the coordinate system with $a = 0$ and $a = 1$ kpc is plotted in Fig. A.3. If we choose the parameter a to be zero we have a problem at the origin of our coordinate system.

A.1.1 Transformations

The conversion between the 'de Zeeuw description' and our trigonometric/hyperbolic description is known when we set the relation between the two constants for the determination of the focal point ($\Delta^2 = a^2 - c^2$):

$$\lambda - c^2 = \Delta^2 \cosh^2 u$$

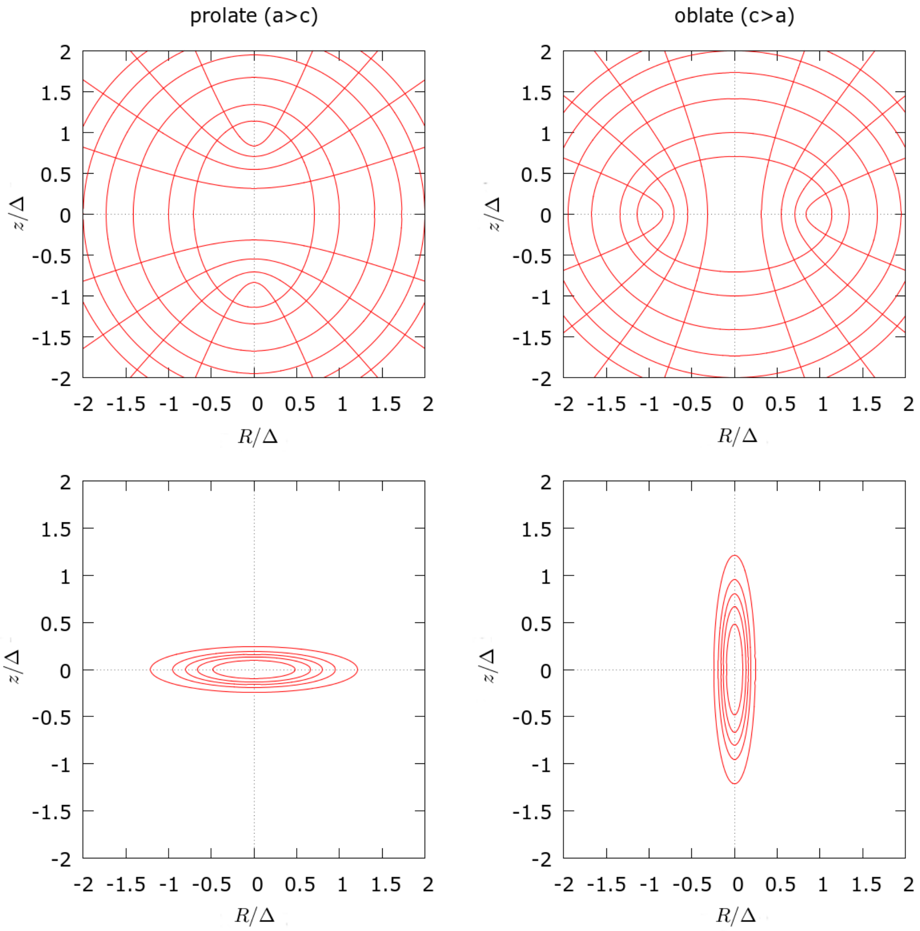

Figure A.1: Stäckel coordinates using the mathematical description of de Zeuuw. It is possible to obtain the prolate and oblate coordinate system considering $a > c$ or $a < c$. The prolate coordinate system generates an oblate density distribution, whereas the oblate coordinate system a prolate density distribution.

$$\lambda - a^2 = \Delta^2 \sinh^2 u$$

and

$$\nu - c^2 = \Delta^2 \cos^2 v$$

$$\nu - a^2 = -\Delta^2 \sin^2 v$$

A.2 Jacobian

Now, that we know the conversion between the coordinates, we can come back to our description and explain the mathematical derivations that were followed in Chapter 3. We have to calculate the Jacobian in order to know the right order of the triple of coordinates. The Jacobian has to be positive, otherwise two coordinates are inverted. We have to derive the Jacobian starting from the Cartesian coordinates to the spheroidal one, and not directly from cylindrical. The conversion between the Cartesian and spheroidal coordinates reads:

$$x = \Delta \sinh u \sin v \cos \phi$$

$$y = \Delta \sinh u \sin v \sin \phi$$

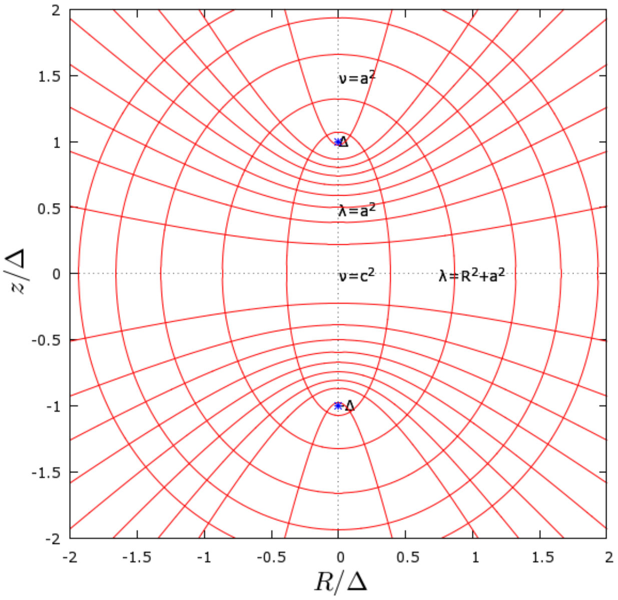
ν=a²
λ=a²
ν=c²
λ=R²+a²
Δ
Δ
2
1.5
1
0.5
0
-0.5
-1
-1.5
-2
-2
-1.5
-1
-0.5
0
0.5
1
1.5
2
z/Δ
R/Δ

Figure A.2: Prolate spheroidal coordinate system generated with the 'de Zeeuw description'.

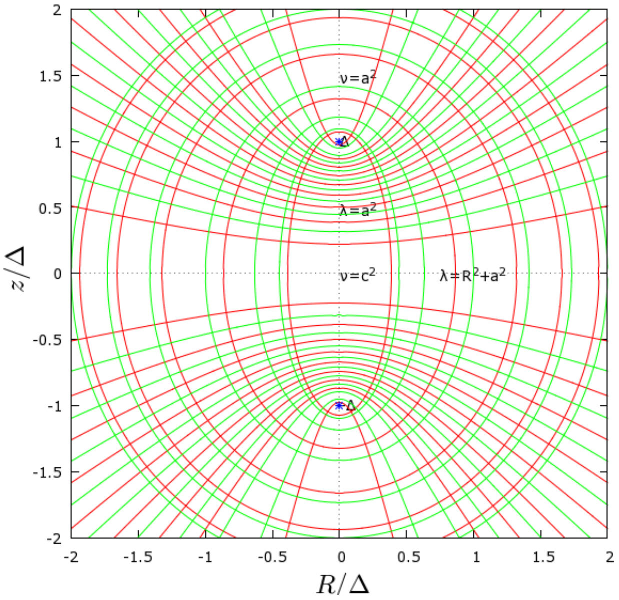
ν=a²
λ=a²
ν=c²
λ=R²+a²
Δ
Δ
2
1.5
1
0.5
0
-0.5
-1
-1.5
-2
-2
-1.5
-1
-0.5
0
0.5
1
1.5
2
z/Δ
R/Δ

Figure A.3: Prolate spheroidal coordinate system generated with the 'de Zeeuw description', assuming a value for the parameter $a = 1$ (red lines) and $a = 0$ (green lines).

$$z = \Delta \cosh u \cos v$$

We take the laplacian:

$$\begin{pmatrix} \frac{\partial x}{\partial u} & \frac{\partial x}{\partial v} & \frac{\partial x}{\partial \phi} \\ \frac{\partial y}{\partial u} & \frac{\partial y}{\partial v} & \frac{\partial y}{\partial \phi} \\ \frac{\partial z}{\partial u} & \frac{\partial z}{\partial v} & \frac{\partial z}{\partial \phi} \end{pmatrix} = \begin{pmatrix} \Delta \cosh u \sin v \cos \phi & \Delta \sinh u \cos v \cos \phi & -\Delta \sinh u \sin v \sin \phi \\ \Delta \cosh u \sin v \sin \phi & \Delta \sinh u \cos v \sin \phi & \Delta \sinh u \sin v \cos \phi \\ \Delta \sinh u \cos v & -\Delta \cosh u \sin v & 0 \end{pmatrix}$$

$$= \Delta \sinh u \sin v \Delta^2 (\sinh^2 u + \sin^2 v) = RP^2$$

The coordinate system has to be of the type (u, v, ϕ) so that the Jacobian is positive. If we choose (u, ϕ, v) for example, we would have a negative Jacobian and we would know that two coordinates are inverted.

A.3 Derivatives

A.3.1 Inverse transformation

The relations expressing the spheroidal coordinates u and v depending on the cylindrical coordinates are:

$$u = acosh\left[\sqrt{\frac{1}{2\Delta^2}[(R^2+z^2+\Delta^2) + \sqrt{(R^2+z^2+\Delta^2)^2 - 4\Delta^2 z^2}]}\right]$$

$$v = acos\left[\sqrt{\frac{1}{2\Delta^2}[(R^2+z^2+\Delta^2) - \sqrt{(R^2+z^2+\Delta^2)^2 - 4\Delta^2 z^2}]}\right]$$

A.3.2 First derivatives

We calculate in this section the first and second derivatives of the spheroidal coordinates with respect to R and z.

1. The derivative of u with respect to R:

$$\frac{\partial u}{\partial R} = \frac{\partial}{\partial R} acosh(\sqrt{x_+})$$

where we define

$$x_+ = \frac{1}{2\Delta^2}[(R^2+z^2+\Delta^2) + \sqrt{(R^2+z^2+\Delta^2)^2 - 4\Delta^2 z^2}]$$

We apply the chain rule:

$$\frac{\partial u}{\partial R} = \frac{1}{\sqrt{(\sqrt{x_+})^2 - 1}} \frac{1}{2\sqrt{x_+}} \frac{\partial x_+}{\partial R}$$

where

$$\frac{\partial x_+}{\partial R} = \frac{R}{\Delta^2}\left[1 + \frac{(R^2+z^2+\Delta^2)}{\sqrt{(R^2+z^2+\Delta^2)^2 - 4z^2\Delta^2}}\right]$$

The calculation at $z = 0$ results:

$$\left(\frac{\partial u}{\partial R}\right)_0 = \frac{1}{\sqrt{\frac{R^2+\Delta^2}{\Delta^2} - 1}} \frac{1}{2\sqrt{\frac{R^2+\Delta^2}{\Delta^2}}} \frac{2R}{\Delta^2} = \frac{1}{\sqrt{R^2+\Delta^2}}$$

2. The derivative of u with respect to z reads:

$$\frac{\partial u}{\partial z} = \frac{1}{\sqrt{(\sqrt{x_+})^2 - 1}} \frac{1}{2\sqrt{x_+}} \frac{\partial x_+}{\partial z}$$

where

$$\frac{\partial x_+}{\partial z} = \frac{z}{\Delta^2}\left[1 + \frac{(R^2+z^2+\Delta^2) - 2z\Delta^2}{\sqrt{(R^2+z^2+\Delta^2)^2 - 4z^2\Delta^2}}\right]$$

which is equal to zero in the plane, and it follows:

$$\left(\frac{\partial u}{\partial z}\right)_0 = 0$$

The z-derivative of the coordinates u results also zero in the plane and the coordinate u falls perpendicular to the plane.

3. The derivative of v with respect to R:

$$\frac{\partial v}{\partial R} = \frac{\partial}{\partial R} acos(\sqrt{x_-})$$

where we define:

$$x_- = \frac{1}{2\Delta^2}[(R^2 + z^2 + \Delta^2) - \sqrt{(R^2 + z^2 + \Delta^2)^2 - 4\Delta^2 z^2}]$$

We apply the chain rule

$$\frac{\partial v}{\partial R} = -\frac{1}{\sqrt{1 - (\sqrt{x_-})^2}} \frac{1}{2\sqrt{x_-}} \frac{\partial x_-}{\partial R}$$

We can see immediately that it the plane ($z = 0$):

$$(x_-)_0 = 0$$

and we have an infinite value for the derivative. It is possible to solve it, rearranging the terms before to substitute at $z = 0$:

$$\frac{\partial v}{\partial R} = -\frac{1}{\sin v} \frac{1}{\sqrt{2\Delta^2}} \frac{1}{\sqrt{2\Delta^2 \cos^2 v}} 2\Delta \sinh u \sin v \left(1 - \frac{R^2 + z^2 + \Delta^2}{\sqrt{(R^2 + z^2 + \Delta^2)^2 - 4\Delta^2 z^2}}\right)$$

$$= -\frac{\sinh u}{\cos v}\left(-\frac{2\Delta^2 \cos^2 v}{\sqrt{(R^2 + z^2 + \Delta^2)^2 - 4\Delta^2 z^2}}\right)$$

the R-derivative of the coordinate v at $z = 0$ results:

$$\left(\frac{\partial v}{\partial R}\right)_0 = 0$$

The coordinate v remains constant with the radius.

4. The last derivative is the z-derivative of the coordinate v, and it can be also managed in a way that we do not obtain an indefinite value:

$$\frac{\partial v}{\partial z} = -\frac{1}{\sqrt{1 - x_-}} \frac{1}{2} \frac{1}{\sqrt{x_-}} \frac{1}{2\Delta^2} \left[2z - \frac{1}{2} \frac{2(R^2 + z^2 + \Delta^2)2z - 4\Delta^2 2z}{\sqrt{(R^2 + z^2 + \Delta^2)^2 - 4\Delta^2 z^2}}\right]$$

$$\frac{\partial v}{\partial z} = -\frac{1}{\sin v} \frac{1}{\Delta^2} \frac{\Delta \cosh u \cos v}{\cos v} \left[1 - \frac{(R^2 + z^2 + \Delta^2) - 2\Delta^2}{\sqrt{(R^2 + z^2 + \Delta^2)^2 - 4\Delta^2 z^2}}\right]$$

it results in the plane ($z = 0$):

$$\left(\frac{\partial v}{\partial z}\right)_0 = -\frac{1}{2\Delta^2} \sqrt{R^2 + \Delta^2} \frac{2\Delta^2}{R^2 + \Delta^2} = -\frac{1}{\sqrt{R^2 + \Delta^2}}$$

the first derivatives are equal in pairs, differing with the sign:

$$\left.\frac{\partial u}{\partial R}\right|_0 = -\left.\frac{\partial v}{\partial z}\right|_0 = \pm\frac{1}{\sqrt{R^2+\Delta^2}}$$

$$\left.\frac{\partial u}{\partial z}\right|_0 = \left.\frac{\partial v}{\partial R}\right|_0 = 0$$

and this behaviour should be extendible also outside from the plane (Kent & de Zeeuw 1991; Amendt & Cuddeford 1991). These transformations are called conformal.

A.3.3 Second derivatives

1. We derive also the expressions for the second derivatives. The second derivative of the coordinate u with respect to R is:

$$\frac{\partial^2 u}{\partial R^2} = \frac{\partial}{\partial R}\left[\frac{1}{\sqrt{x_+-1}}\frac{1}{2\sqrt{x_+}}\frac{\partial x_+}{\partial R}\right]$$

$$= -\frac{1}{2(x_+-1)^{3/2}}\frac{1}{2\sqrt{x_+}}\left(\frac{\partial x_+}{\partial R}\right)^2 - \frac{1}{\sqrt{x_+-1}}\frac{1}{4(x_+)^{3/2}}\left(\frac{\partial x_+}{\partial R}\right)^2 + \frac{1}{\sqrt{x_+-1}}\frac{1}{2\sqrt{x_+}}\frac{\partial^2 x_+}{\partial R^2}$$

   where

$$\frac{\partial^2 x_+}{\partial R^2} = \frac{\partial}{\partial R}\left[\frac{1}{2\Delta^2}\left(2R + \frac{2R(R^2+z^2+\Delta^2)}{\sqrt{(R^2+z^2+\Delta^2)^2-4z^2\Delta^2}}\right)\right]$$

$$= \frac{1}{2\Delta^2}\left[2 + \frac{2(R^2+z^2+\Delta^2+2R^2)}{\sqrt{(R^2+z^2+\Delta^2)^2-4z^2\Delta^2}} - \frac{2R(R^2+z^2+\Delta^2)\frac{1}{2}\frac{2(R^2+z^2+\Delta^2)2R}{\sqrt{(R^2+z^2+\Delta^2)^2-4z^2\Delta^2}}}{(R^2+z^2+\Delta^2)^2-4z^2\Delta^2}\right]$$

   at $z = 0$ the calculation results:

$$\left.\frac{\partial^2 x_+}{\partial R^2}\right|_0 = \frac{1}{2\Delta^2}\left[2 + \frac{6R^2+\Delta^2}{R^2+\Delta^2} - \frac{4R^2}{R^2+\Delta^2}\right] = \frac{2}{\Delta^2}$$

   Calculating all the terms together at $z = 0$ the second R-derivative of u reads:

$$\left.\frac{\partial^2 u}{\partial R^2}\right|_0 = -\frac{1}{2}\left(\frac{\Delta^2}{R^2}\right)^{3/2}\frac{\Delta}{2\sqrt{R^2+\Delta^2}}\left(\frac{2R}{\Delta^2}\right)^2 - \frac{1}{4}\frac{\Delta}{R}\frac{\Delta^3}{(R^2+\Delta^2)^{3/2}}(\frac{2R}{\Delta^2})^2 + \frac{1}{2}\frac{\Delta}{R}\frac{\Delta}{\sqrt{R^2+\Delta^2}}\frac{2}{\Delta^2}$$

$$= -\frac{1}{R\sqrt{R^2+\Delta^2}} - \frac{R}{(R^2+\Delta^2)^{3/2}} + \frac{1}{R\sqrt{R^2+\Delta^2}} = -\frac{R}{(R^2+\Delta^2)^{3/2}}$$

$$\left.\frac{\partial^2 u}{\partial R^2}\right|_0 = -\frac{R}{(R^2+\Delta^2)^{3/2}}$$

2. Second z-derivative of u-coordinate. We can apply the same chain rule for the derivative respect to z:

$$\frac{\partial^2 u}{\partial z^2} = \frac{\partial}{\partial z}\left(\frac{1}{\sqrt{x_+-1}}\frac{1}{2\sqrt{x_+}}\frac{\partial x_+}{\partial z}\right)$$

   we need to study only the last term because the z-derivatives of the first two terms are equal to zero in the plane ($\partial x_+/\partial z|_0 = 0$):

$$\frac{\partial^2 x_+}{\partial z^2} = \frac{1}{2\Delta^2}\frac{\partial}{\partial z}\left[2z + \frac{2z(R^2+z^2+\Delta^2)-4z^2\Delta^2}{\sqrt{(R^2+z^2+\Delta^2)^2-4z^2\Delta^2}}\right]$$

$$= \frac{1}{2\Delta^2}\left[2 + \frac{2(R^2+z^2+\Delta^2)-4\Delta^2}{\sqrt{(R^2+z^2+\Delta^2)^2-4z^2\Delta^2}} - \frac{(1st)(2nd)'}{(2nd)^2}\right]$$

$(1st)$ is the numerator and $(2nd)$ the denominator. Since the denominator is proportional to z, this term goes to zero in the plane ($z = 0$). It remains:

$$\left.\frac{\partial^2 x_+}{\partial z^2}\right|_0 = \frac{1}{2\Delta^2}\left[2 + \frac{2(R^2-\Delta^2)}{R^2+\Delta^2}\right] = \frac{2R^2}{\Delta^2(R^2+\Delta^2)}$$

Putting all the terms together we obtain for the second derivative of u with respect to z in the plane:

$$\left.\frac{\partial^2 u}{\partial z^2}\right|_0 = \frac{\Delta}{R}\frac{1}{2}\frac{\Delta}{\sqrt{R^2+\Delta^2}}\frac{1}{\Delta^2}\frac{2R^2}{R^2+\Delta^2} = \frac{1}{R}\frac{R^2}{(R^2+\Delta^2)^{3/2}}$$

$$\left.\frac{\partial^2 u}{\partial z^2}\right|_0 = \frac{R}{(R^2+\Delta^2)^{3/2}} = -\left.\frac{\partial^2 u}{\partial R^2}\right|_0$$

3. The second mixed derivative of the u-coordinate can be calculated taking the first R-derivative of u and then deriving by z:

$$\frac{\partial^2 u}{\partial R \partial z} = \frac{\partial}{\partial z}\left(\frac{\partial u}{\partial R}\right)$$

For the calculation in the plane we need to know the result of $\partial^2 x_+/\partial R\partial z$ because $\partial x_+/\partial z$ is zero. This term is zero in the plane and it follows that the second mixed derivative of the u-coordinate is zero as well:

$$\left.\frac{\partial^2 u}{\partial R \partial z}\right|_0 = 0$$

A.4 Derivatives of Stäckel potentials

We remember that the expression for the Stäckel potential is:

$$\Phi_s(u,v) = \frac{U(u)-V(v)}{\sinh^2 u + \sin^2 v}$$

We can assume for the potential $U(u)$ and $V(v)$ the following form:

$$U(u) = \cosh^2 u F(u)$$

and

$$V(v) = (\sinh^2 u_0 + \sin^2 v)G(v)$$

where $\sinh^2 u_0$ represents the value of u at the solar position $(R_0, 0)$. Here we demonstrate all the steps for the results given during the thesis about the derivatives of the Stäckel potential.

A.4.1 u-derivatives

The first u-derivative of the Stäckel potential is:

$$\frac{\partial \Phi_s}{\partial u} = \frac{U'(u)}{\sinh^2 u + \sin^2 v} - \frac{(U(u)-V(v))2\sinh u\cosh u}{(\sinh^2 u + \sin^2 v)^2}$$

and the second u-derivative:

$$\frac{\partial^2\Phi_s}{\partial u^2} = \frac{U''(u)}{\sinh^2 u + \sin^2 v} - \frac{2U'(u)2\sinh u\cosh u}{(\sinh^2 u + \sin^2 v)^2} - \frac{(U(u) - V(v))2(\cosh^2 u + \sinh^2 u)}{(\sinh^2 u + \sin^2 v)^2}$$

$$+\frac{(U(u) - V(v))4\sinh^2 u\cosh^2 u2(\sinh^2 u + \sin^2 v)}{(\sinh^2 u + \sin^2 v)^4}$$

where $U'(u)$ is the first u-derivative of the potential $U(u)$ and $U''(u)$ is the second u-derivative of $U(u)$. Since the function $V(v)$ depends only on v, its derivative with respect to u is zero. The derivatives of $U(u)$ are:

$$\begin{cases} U(u) = \cosh^2 uF(u) \\ U'(u) = 2\cosh u\sinh uF(u) + \cosh^2 uF'(u) \\ U''(u) = 2(\cosh^2 u + \sinh^2 u)F(u) + 4\cosh u\sinh uF'(u) + \cosh^2 uF''(u) \end{cases}$$

where $F'(u)$ and $F''(u)$ are the first and second derivative of $F(u)$ with respect to u.

The first derivative of the Stäckel potential in the plane results:

$$\left.\frac{\partial\Phi_s}{\partial u}\right|_{v=\pi/2} = \frac{2\cosh u\sinh uF(u)}{\cosh^2 u} + F'(u) - \frac{2\cosh u\sinh u\cosh^2 F(u)}{\cosh^4 u} + \frac{2\sinh u\cosh uV_0}{\cosh^4 u}$$

$$= F'(u) + \frac{2\sinh u}{\cosh^3 u}V_0$$

where V_0 is the value of $V(v)$ on the plane, which is a constant value.

The second derivative results:

$$\left.\frac{\partial^2\Phi_s}{\partial u^2}\right|_{v=\pi/2} = \frac{2(\cosh^2 u + \sinh^2 u)F(u)}{\cosh^2 u} + \frac{4\cosh u\sinh uF'(u)}{\cosh^2 u} + F''(u) - \frac{8\sinh^2 u\cosh^2 uF(u)}{\cosh^4 u}$$

$$-\frac{4\sinh u\cosh^3 uF'(u)}{\cosh^4 u} - \frac{(\cosh^2 uF(u) - V_0)2(\cosh^2 u + \sinh^2 u)}{\cosh^4 u}$$

$$+\frac{(\cosh^2 uF(u) - V_0)8\sinh^2 u\cosh^2 u\cosh^2 u}{\cosh^8 u}$$

terms $F'(u)$ cancels

$$\left.\frac{\partial^2\Phi_s}{\partial u^2}\right|_{v=\pi/2} = 2F + 2F(u)\frac{\sinh^2 u}{\cosh^2 u} + F'' - 8F(u)\frac{\sinh^2 u}{\cosh^2 u} - 2F(u) - 2F(u)\frac{\sinh^2 u}{\cosh^2 u} +$$

$$+2V_0\left(\frac{1}{\cosh^2 u} + \frac{\sinh^2 u}{\cosh^4 u}\right) + 8F(u)\frac{\sinh^2 u}{\cosh^2 u} - 8V_0\frac{\sinh^2 u}{\cosh^4 u}$$

terms $F(u)$ cancel and it results:

$$\left.\frac{\partial^2\Phi_s}{\partial u^2}\right|_{v=\pi/2} = F''(u) + 2V_0\left(\frac{1}{\cosh^2 u} - 3\frac{\sinh^2 u}{\cosh^2 u}\right)$$

A.4.2 v-derivatives

The first v-derivative of the Stäckel potential is:

$$\frac{\partial \Phi_s}{\partial v} = -\frac{V'(v)}{\sinh^2 u + \sin^2 v} - \frac{(U(u) - V(v))2 \sin v \cos v}{(\sinh^2 u + \sin^2 v)^2}$$

The second derivative:

$$\frac{\partial^2 \Phi_s}{\partial v^2} = -\frac{V''(v)}{\sinh^2 u + \sin^2 v} + \frac{2V'(v)2 \sin v \cos v}{(\sinh^2 u + \sin^2 v)^2} - \frac{(U(u) - V(v))2(\cos^2 v - \sin^2 v)}{(\sinh^2 u + \sin^2 v)^2}$$

$$+ \frac{(U(u) - V(v))4 \sin^2 v \cos^2 v 2(\sinh^2 u + \sin^2 v)}{(\sinh^2 u + \sin^2 v)^4}$$

where $V'(v)$ is the first v-derivative of the potential $V(v)$ and $V''(v)$ is the second v-derivative of $V(v)$. Since the function $U(u)$ depends only on u its derivative respect to v is zero. We can see immediately that the second and the last terms are zero in the plane ($v = \pi/2$) because of the term $cosv$.

The derivatives of $V(v)$ are (the arrows mean the calculation in the plane):

$$\begin{cases} V(v) = (\sinh^2 u_0 + \sin^2 v)G(v) \rightarrow \cosh^2 u_0 G_0 \\ V'(v) = (\sinh^2 u_0 + \sin^2 v)G'(v) + 2G(v) \sin v \cos v \rightarrow \cosh^2 u_0 G_0' \\ V''(v) = (\sinh^2 u_0 + \sin^2 v)G''(v) + 4G'(v) \sin v \cos v + 2G(v)(\cos^2 v - \sin^2 v) \rightarrow \cosh^2 u_0 G_0'' - 2G_0 \end{cases}$$

where $G'(v)$ and $G''(v)$ are the first and second derivative of $G(v)$ with respect to v, and the subscript 0 corresponds to the value in the plane.

The first derivative in the plane:

$$\left.\frac{\partial \Phi_s}{\partial v}\right|_{v=\pi/2} = -\frac{V'(v)}{\cosh^2 u} = -\frac{\cosh^2 u_0}{\cosh^2 u} G_0'$$

but it is also true that:

$$\frac{\partial \Phi}{\partial z} = \frac{\partial \Phi}{\partial u}\frac{\partial u}{\partial z} + \frac{\partial \Phi}{\partial v}\frac{\partial v}{\partial z}$$

the z-derivative of the u-coordinate is zero in the plane and if we want to avoid a cusp in the plane we have to assume that $G'(v)$ is zero in the plane.

The second derivative in the plane is:

$$\left.\frac{\partial^2 \Phi_s}{\partial v^2}\right|_{v=\pi/2} = -\frac{\cosh^2 u_0}{\cosh^2 u} G_0'' + \frac{2G_0}{\cosh^2 u} + \frac{2F(u)}{\cosh^2 u} - 2G_0 \frac{\cosh^2 u_0}{\cosh^4 u}$$

If we are exactly at the solar neighborhood:

$$\left.\frac{\partial^2 \Phi}{\partial v^2}\right|_{v=\pi/2;u=u_0} = -G_0'' + \frac{2F_0}{\cosh^2 u_0}$$

If we are not in the solar neighbourhood as in the calculation that we have pursued we need to consider all four terms. Our assumptions are that the 'vertical' potential $G(v)$ is zero in the plane ($G_0 = 0$) because of the symmetry and because most of the mass is away from the centre. Also the first derivative of $G(v)$ is zero in the plane ($G_0' = 0$) because we want to avoid a cusp in the potential in the plane.

A.5 Hamiltonian-Jacobi equation

After we have chosen a coordinate system, it is possible to write the Hamiltonian as a function of the spheroidal coordinates u, v and their conjugate momenta p_u, p_v. The first step is to write the expression for the Lagrangian:

$$\mathscr{L} = \frac{1}{2}|\dot{\vec{x}}|^2 - V(\vec{v})$$

The Lagrangian can be calculated for the spheroidal coordinates as:

$$\mathscr{L} = \frac{1}{2}\Delta^2[(\cosh^2 u \sin^2 v\dot{u}^2 + \sinh^2 u \cos^2 \dot{v}^2)$$

$$+(\sinh^2 u \cos^2 v\dot{u}^2 + \cosh^2 u \sin^2 \dot{v}^2) + \sinh^2 u \sin^2 v\dot{\phi}^2] - \Phi(u, v)$$

which results:

$$\mathscr{L} = \frac{1}{2}\Delta^2[(\sinh^2 u + \sin^2 v)(\dot{u}^2 + \dot{v}^2) + \sinh^2 u \sin^2 v\dot{\phi}^2] - \Phi(u, v)$$

The momenta are given by the equation $p_i = \partial\mathscr{L}/\partial\dot{q}_i$:

$$p_u = \Delta^2(\sinh^2 u + \sin^2 v)\dot{u}$$

$$p_v = \Delta^2(\sinh^2 u + \sin^2 v)\dot{v}$$

$$p_\phi = \Delta^2 \sinh^2 u \sin^2 v\dot{\phi}$$

From the Lagrangian we can determine the Hamiltonian ($H = p\dot{q} - \mathscr{L}$):

$$H = \frac{1}{2}\left[\frac{p_u^2}{\Delta^2(\sinh^2 u + \sin^2 v)} + \frac{p_v^2}{\Delta^2(\sinh^2 u + \sin^2 v)} + \frac{p_\phi^2}{\Delta^2 \sinh^2 u \sin^2 v}\right] - \Phi(u, v)$$

According to Landau & Lifshitz (1976), we have to remember that when we do a coordinate transformation does not mean that the Hamiltonian of the system will be conserved. To guarantee that the Hamilton's equations are valid also in the new representation, the Principle of Least Action must hold. The most general condition that a coordinate transformation must satisfy is the following condition:

$$p\dot{q} - H(q, p; t) = P\dot{Q} - \hat{H}(Q, P; t) + \frac{\partial F}{\partial t}$$

Q, $\dot{Q}$, P, $\hat{H}$ are the coordinates, momenta and Hamiltonian in the new coordinate system, respectively, while F is an arbitrary function of an old, a new coordinate (or momentum) and of the time. The function F is called the generating function of the transformation and there are four types of canonical transformations. We assume as form for $F = F(q, P; t)$ the canonical transformation of second kind:

$$F = -QP + F_2(q, P; t)$$

This choice for the generating function leads to:

$$p\dot{q} - H(q, p; t) = P\dot{Q} - \hat{H}(Q, P; t) - \dot{Q}P - Q\dot{P} + \frac{\partial F_2}{\partial q}\dot{q} + \frac{\partial F_2}{\partial P}\dot{P} + \frac{\partial F_2}{\partial t}$$

$$\left[p - \frac{\partial F_2}{\partial q}\right]\dot{q} - H(q, p; t) = \dot{P}\left[-Q + \frac{\partial F_2}{\partial P}\right] - \hat{H}(Q, P; t) + \frac{\partial F_2}{\partial t}$$

To preserve the least action principle the following relations have to be satisfied:

$$p = \left(\frac{\partial F_2}{\partial q}\right) \qquad ; \qquad Q = \left(\frac{\partial F_2}{\partial P}\right) \qquad ; \qquad \hat{H}(Q,P;t) = H(q,p;t) + \frac{\partial F_2}{\partial t}$$

The generating function F establishes a bridge between the new and old representation.

If the Hamiltomian has no dependence on one of the phase-space variables, then the conjugate variable is conserved. The Hamilton-Jacobi theory is the formalism to find the special canonical transformations such that the Hamiltonian is constant. We now introduce the condition that the transformed Hamiltonian must not only be constant but we ask it to be zero:

$$H\left(\frac{\partial S}{\partial q}, q, t\right) + \frac{\partial S}{\partial t} = 0$$

where we have replaced p by $(\partial S/\partial q)$. This is the Hamilton-Jacobi equation (HJE), a first order, partial differential equation for S as a function of q and t. Since the function S enters the equation only through its derivative, one of this constant is additive (S_0), so that a complete integral of the HJE (see Landau & Lifshitz (1976)) is:

$$S = S(q, \alpha; t) + S_0$$

where α and S_0 are arbitrary constants.

If the Hamiltonian does not depend on time, we know it is a constant of motion, E_0. Taking a function S of the form:

$$S = W(q) - \alpha t$$

and substituting it in the HJE, we get:

$$H\left(\frac{\partial W}{\partial q}, q\right) = \alpha = E_0$$

This is a first order differential function for W as a function of q. W is known as Hamilton's characteristic function. So, solving for W (or S) is equivalent to solve the original problem.

We have seen that solving Hamilton's equation for a system with a time-independent Hamiltonian, is equivalent to solve the HJE in the form:

$$H\left(\frac{\partial W}{\partial q}, q\right) = \alpha = E_0$$

Now, let us assume that W can be separated:

$$W(q_1, ..., q_n) = \sum_{i=1}^{n} W_i(q_i)$$

and that the Hamiltonian can also be separated:

$$H(q_1, ..., q_n) = \sum_{i=1}^{n} H_i\left(\frac{\partial W_i}{\partial q_i} q_i\right)$$

Then, the HJE can be separated in n-equations:

$$H_i\left(\frac{\partial W_i}{\partial q_i}, q_i\right) = \alpha_i$$

where the n integrations constants satisfy:

$$\sum_i \alpha_i = E_0 = H$$

A.6 Third integral of motion

Then, we arrive to the expression of the Hamiltonian in spheroidal coordinates:

$$H = \frac{1}{2}\frac{1}{\Delta^2(\sinh^2 u + \sin^2 v)}\left[\left(\frac{\partial W}{\partial u}\right)^2 + \left(\frac{\partial W}{\partial v}\right)^2\right] + \frac{1}{2}\frac{1}{\Delta^2 \sinh^2 u \sin^2 v}\left(\frac{\partial W}{\partial \phi}\right)^2 + \Phi(u, v)$$

where $W = W(u) + W(v) + W(\phi)$ is the separable Hamilton characteristic function and $p_i = \partial W_i/\partial q_i$ is the relation with the momenta.

We consider a potential of this form:

$$\Phi(u, v) = \frac{U(u) - V(v)}{\sinh^2 u + \sin^2 v}$$

The denominator vanishes when $u = 0$, $v = 0$. However we may avoid an unphysical singularity in Φ at this point by choosing $U(u)$ and $V(v)$ such that $U(0) = V(0) = 0$. Since H has no explicit dependence on time, it is equal to some constant E. Since H is independent on the coordinate ϕ, the azimuthal momentum p_ϕ is constant at some value L_z. After writing $H = E$ we obtain:

$$2\Delta^2[E \sinh^2 u - U(u)] - p_u^2 - \frac{L_z^2}{\sinh^2 u} = \frac{L_z^2}{\sin^2 v} + p_v^2 - 2\Delta^2[E \sin^2 v + V(v)]$$

The left side is function of u and p_u only while the right side is function of v and p_v only. The left side does not depend on v, and the right side does not depend on u, so both sides must be equal to some constant $2\Delta^2 I_3$ (or just I_3) (Binney & Tremaine 2008).

We can obtain the momenta depending on the three integrals of motion:

$$p_u = \pm\sqrt{2\Delta^2[E \sinh^2 u - I_3 - U(u)] - \frac{L_z^2}{\sinh^2 u}} \tag{A.3}$$

$$p_v = \pm\sqrt{2\Delta^2[E \sin^2 v + I_3 + V(v)] - \frac{L_z^2}{\sin^2 v}} \tag{A.4}$$

We want to derive the third integral of motion I_3. Starting from Eq. A.3 and A.4 we isolate the constant E and then equating the two results we can derive I_3:

1. First equation
$$\frac{1}{2\Delta^2}\left(p_u^2 + \frac{p_\phi^2}{\sinh^2 u}\right) + I_3 + U(u) = E \sinh^2 u$$
2. Second equation
$$\frac{1}{2\Delta^2}\left(p_v^2 + \frac{p_\phi^2}{\sin^2 v}\right) - I_3 - V(v) = E \sin^2 v$$
3. Multiplying 1) by $\sin^2 v$ and 2) by $\sinh^2 u$ and equating the two equations:

$$\left[\sinh^2 u\left(\frac{p_v^2}{2\Delta^2} - V(v)\right) - \sin^2 v\left(\frac{p_u^2}{2\Delta^2} + U(u)\right)\right] + \frac{p_\phi^2}{2\Delta^2}\left(\frac{\sinh^2 u}{\sin^2 v} - \frac{\sin^2 v}{\sinh^2 u}\right) =$$

$$= I_3(\sinh^2 u + \sin^2 v)$$

where

$$\left(\frac{\sinh^2 u}{\sin^2 v} - \frac{\sin^2 v}{\sinh^2 u}\right) = \left(\frac{\sinh^4 u - \sin^4 v}{\sinh^2 u \sin^4 v}\right) = \frac{(\sinh^2 u + \sin^2 v)(\sinh^2 u - \sin^2 v)}{\sinh^2 u \sin^2 v}$$

$$= (\sinh^2 u + \sin^2 v)\left(\frac{1}{\sin^2 v} - \frac{1}{\sinh^2 u}\right)$$

The expression for the third integral of motion I_3 in the case of Stäckel potential reads:

$$I_3 = \frac{1}{\sinh^2 u + \sin^2 v}\left[\sinh^2 u\left(\frac{p_v^2}{2\Delta^2} - V(v)\right) - \sin^2 v\left(\frac{p_u^2}{2\Delta^2} + U(u)\right)\right] +$$

$$+\frac{p_\phi^2}{2\Delta^2}\left(\frac{1}{\sin^2 v} - \frac{1}{\sinh^2 u}\right)$$

B

Data analysis

In Fig. B.1 are shown the error distribution in proper motions for the PPMXL catalogue and the error distribution for the line-of-sight velocity. There are some systematics, which show some bumps in the error distribution. If we would like to consider this catalogue for the proper motion, we have to take care of these systematics.

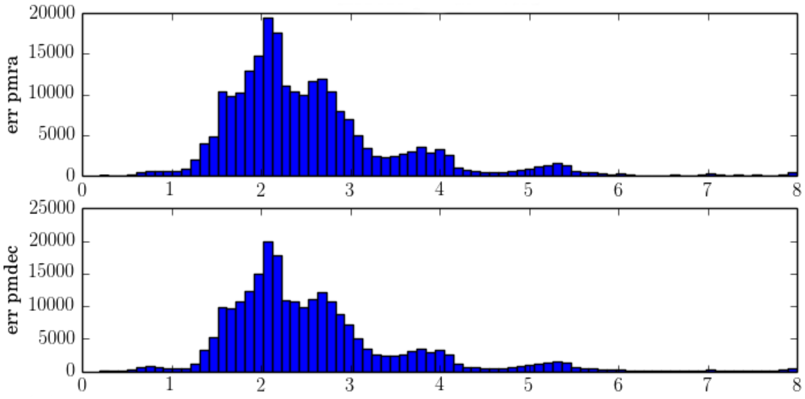

Figure B.1: Error distribution for the proper motion (pm rad and pm dec) for the PPMXL Catalogue.

We used for the data analysis the UCAC4 proper motion catalogue. In the error distribution there are no big effect due to systematics. In Fig. B.2 are plotted the error distribution in proper motion and radial velocity. Further, we plot also the log plot (Fig. B.3) and log-log plot (Fig. B.4). If the error distribution is perfectly log-normal, the result is a normal distribution in the log-plot and a quadratic behaviour in the log-log plot. We can see in Fig. B.4 that the error distribution in proper motions and line-of-sight velocity is log-normal. There are some deviations in the wings, but there are no strange bumps as in Fig. B.1.

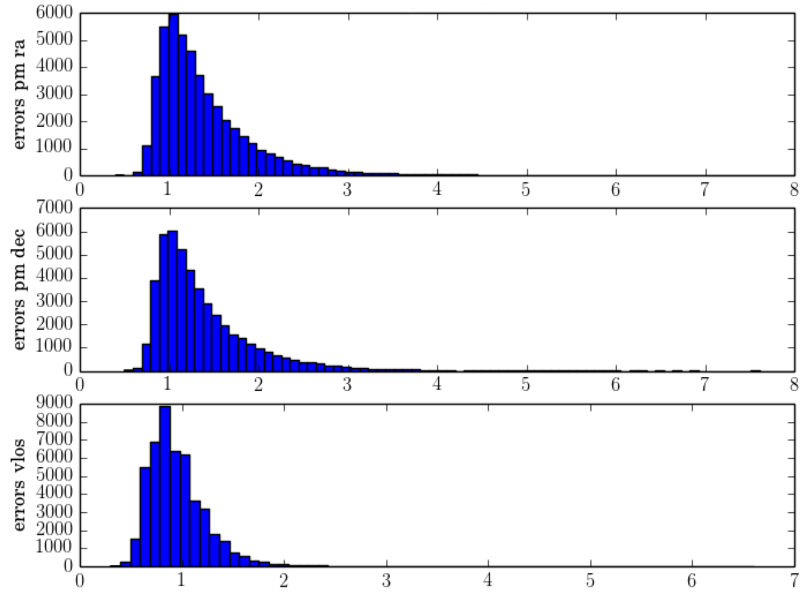

Figure B.2: Error distribution for the proper motions (pm rad and pm dec) for the UCAC Catalogue and the radial velocity distribution (vlos).

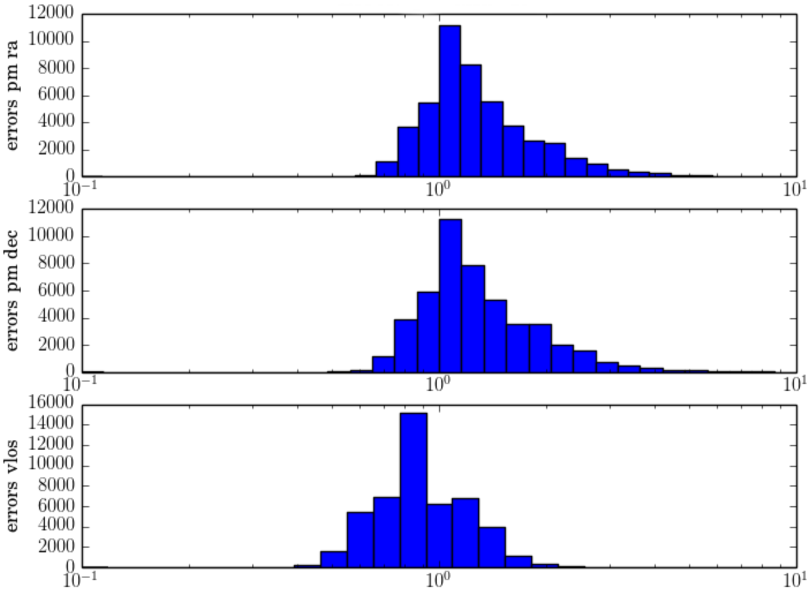

Figure B.3: Error distribution for the proper motions (pm rad and pm dec) and the radial velocity distribution (vlos) using log plot.

B.1 Overlapping bins

The first analysis that we explore in the calculation of the tilt of the velocity ellipsoid was to overlap bins. The idea was that, considering bins always with greater overlap region, the result for the tilt should show

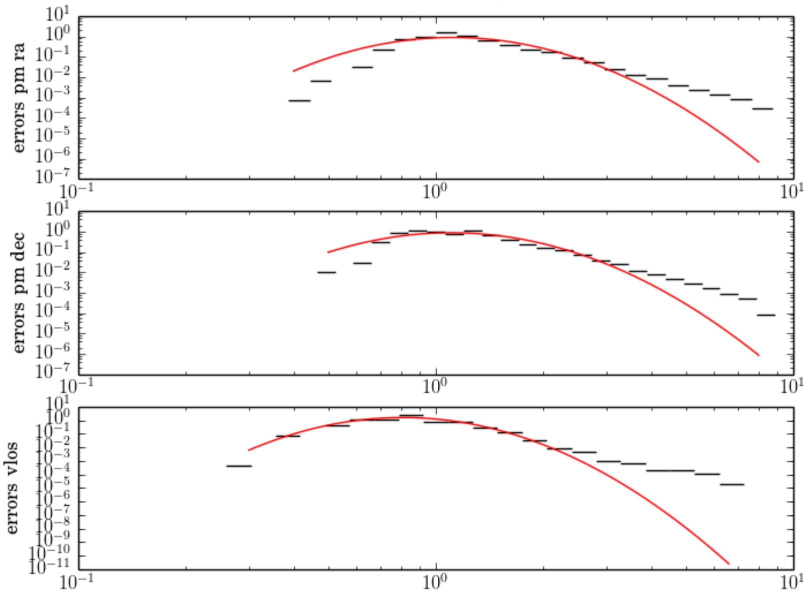

Figure B.4: Error distribution for the proper motion (pm rad and pm dec) and the radial velocity distribution (vlos) using log-log plot. The red line is a quadratic function which corresponds to a log-normal distribution in the normal plot.

some continuous behaviour. We obtain, instead, a random fluctuating result for the tilt as we can see in Fig. B.5.

B.2 Non-Axisymmetry effects

The MCMC method assumes that the bulk motion is zero and Büdenbender et al. (2014) showed that the effect of non-axisymmetry does not influece the tilt angle of the velocity ellipsoid. We can look at the biweight method and find that the deviation from axisymmetry is very small close to the midplane and at larger distances ($z > 1.5$ kpc) (Fig. B.6 and B.7). The deviations in the plane can be due to non-axisymmetry components like a bar or spiral arms. If the mean radial and vertical velocity are not zero, this brings a shift in the determination of the tilt of the velocity ellipsoid (Fig. B.8).

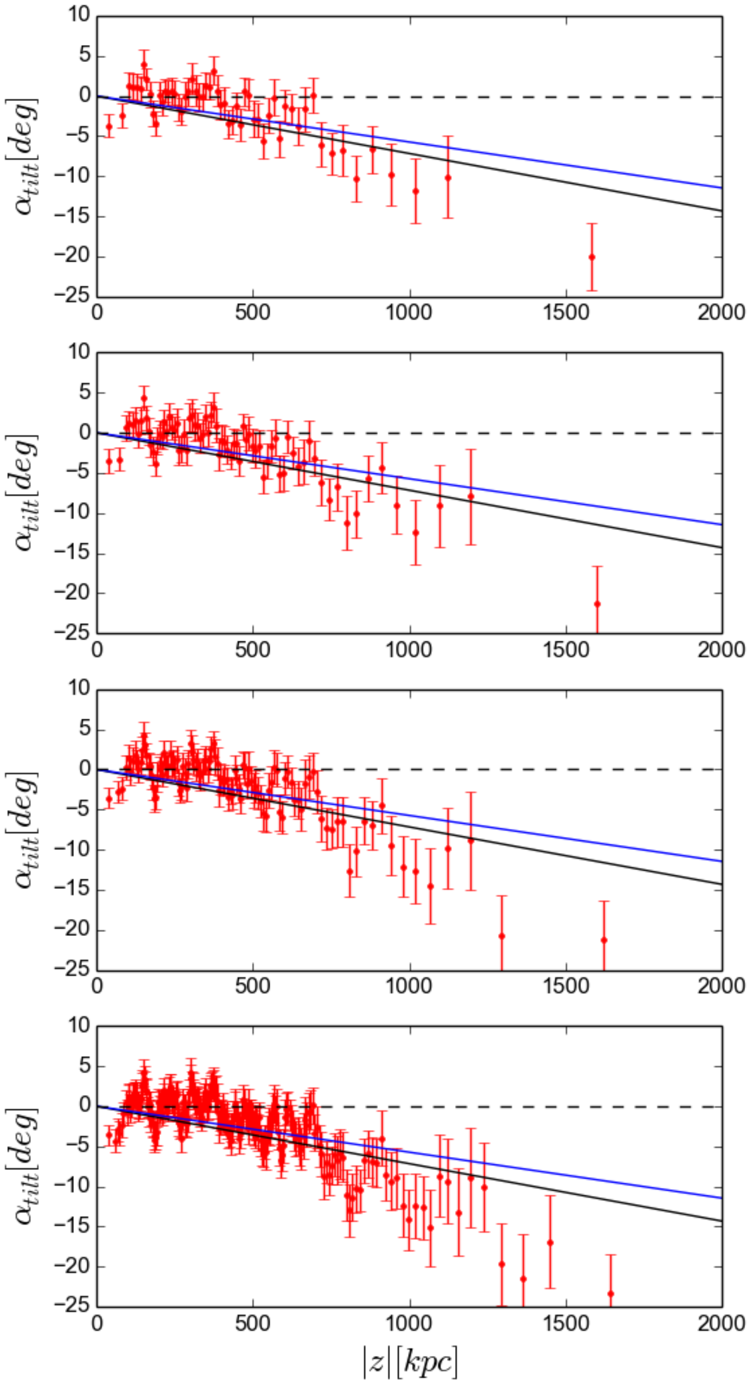

Figure B.5: Tilt of the velocity ellipsoid calculated using the MCMC method and using 1000 stars per bin for different overlaps. The overlaps are 200, 400, 600 and 800 stars between two following bins. The black line corresponds to an orientation of the velocity ellipsoid with the spherical coordinates and the blue line for the Stäckel model with $\Delta = 4$ kpc.

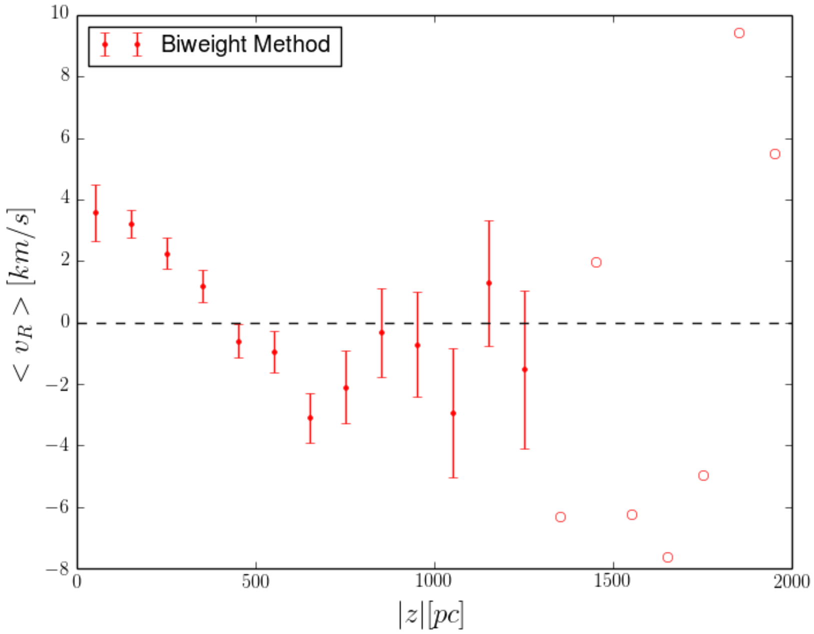

Figure B.6: Mean radial velocity $\overline{v_R}$ for the red clump giants using the biweight method.

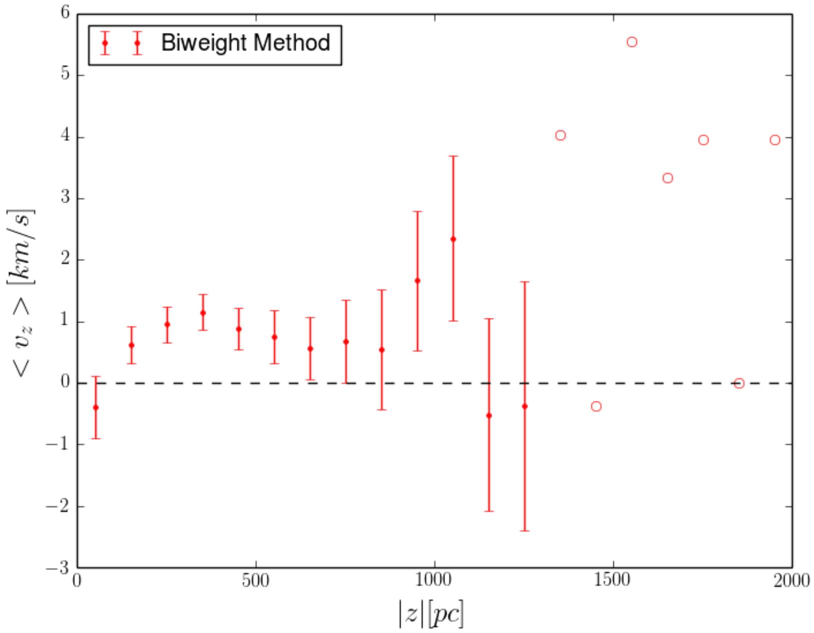

Figure B.7: Mean vertical velocity $\overline{v_z}$ for the red clump giants using the biweight method.

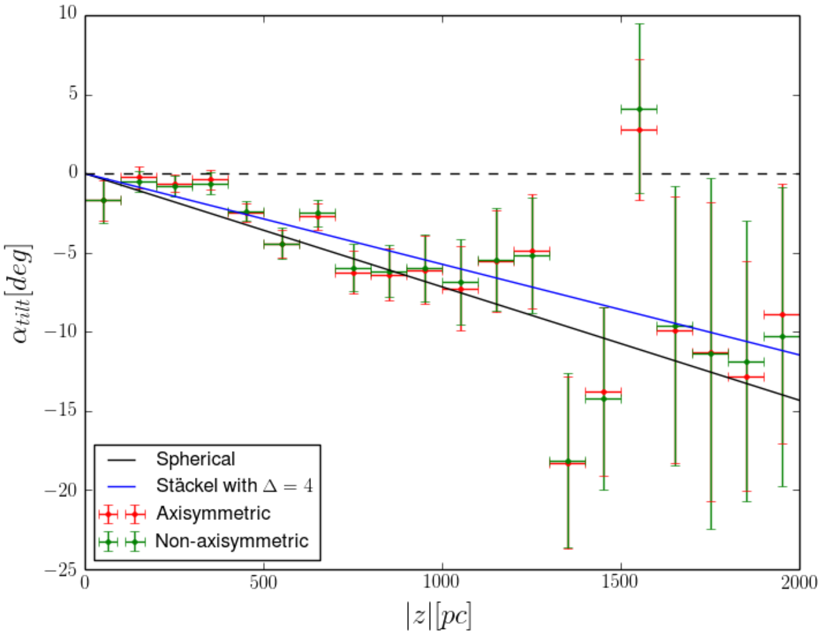

Figure B.8: Tilt of velocity ellipsoid for the red clump giants using the biweight method for the axisymmetric (red points) and non-axisymmetric case (green points).

Bibliography

Alves, D. R. 2000, ApJ, 539, 732

Amendt, P., & Cuddeford, P. 1991, ApJ, 368, 79

Aumer, M., & Binney, J. J. 2009, MNRAS, 397, 1286

Bahcall, J. N., Schmidt, M., & Soneira, R. M. 1982, ApJ, 258, L23

Batsleer, P., & Dejonghe, H. 1994, A&A, 287, 43

Beaulieu, S. F., Freeman, K. C., Kalnajs, A. J., Saha, P., & Zhao, H. 2000, AJ, 120, 855

Bienaymé, O. 1999, A&A, 341, 86

Bienaymé, O., Famaey, B., Siebert, A., et al. 2014, A&A, 571, AA92

Binney, J., & Merrifield, M. 1998, Galactic astronomy / James Binney and Michael Merrifield. Princeton, NJ : Princeton University Press, 1998. (Princeton series in astrophysics) QB857 .B522 1998

Binney, J., & Tremaine, S. 2008, Galactic Dynamics: Second Edition, by James Binney and Scott Tremaine. ISBN 978-0-691-13026-2 (HB). Published by Princeton University Press, Princeton, NJ USA, 2008

Binney, J. 2010, MNRAS, 401, 2318

Binney, J., & McMillan, P. 2011, MNRAS, 413, 1889

Binney, J. 2011, Pramana, 77, 39

Binney, J. 2012, MNRAS, 426, 1324

Binney, J. 2012, MNRAS, 426, 1328

Binney, J., Burnett, B., Kordopatis, G., et al. 2014, MNRAS, 439, 1231

Binney, J., Burnett, B., Kordopatis, G., et al. 2014, MNRAS, 437, 351

Boeche, C., Siebert, A., Williams, M., et al. 2011, AJ, 142, 193

Bovy, J., & Tremaine, S. 2012, ApJ, 756, 89

Bovy, J., Rix, H.-W., Hogg, D. W., et al. 2012, ApJ, 755, 115

Bovy, J., Allende Prieto, C., Beers, T. C., et al. 2012, ApJ, 759, 131

Bovy, J., & Rix, H.-W. 2013, ApJ, 779, 115

Breddels, M. A., Smith, M. C., Helmi, A., et al. 2010, A&A, 511, AA90

Büdenbender, A., van de Ven, G., & Watkins, L. L. 2014, arXiv:1407.4808

Burnett, B., Binney, J., Sharma, S., et al. 2011, A&A, 532, AA113

Carollo, D., Beers, T. C., Chiba, M., et al. 2010, ApJ, 712, 692

Casetti-Dinescu, D. I., Girard, T. M., Korchagin, V. I., & van Altena, W. F. 2011, ApJ, 728, 7

Clark, G. L. 1937, MNRAS, 97, 182

Clarkson, W., Sahu, K., Anderson, J., et al. 2008, ApJ, 684, 1110

Contopoulos, G. 1960, Zeitschrift für Astrophysik, 49, 273

Cropper, M., & Katz, D. 2011, EAS Publications Series, 45, 181

Cuddeford, P., & Amendt, P. 1991, MNRAS, 253, 427

De Bruyne, V., Leeuwin, F., & Dejonghe, H. 2000, MNRAS, 311, 297

Dehnen, W., & Binney, J. J. 1998, MNRAS, 298, 387

Dejonghe, H., & de Zeeuw, T. 1988, ApJ, 329, 720

Dekker, E. 1976, Physics Report, 24, 315

de Zeeuw, P. T. 1984, Ph.D. Thesis

de Zeeuw, T. 1985, MNRAS, 216, 273

Eddington, A. S. 1915, MNRAS, 76, 37

Ernst, A., Just, A., Berczik, P., & Olczak, C. 2011, A&A, 536, A64

Famaey, B., & Dejonghe, H. 2003, MNRAS, 340, 752

Ferrarese, L., & Merritt, D. 2000, ApJ, 539, L9

Flynn, C., Holmberg, J., Portinari, L., Fuchs, B., & Jahreiß, H. 2006, MNRAS, 372, 1149

Fuchs, B., Dettbarn, C., Rix, H.-W., et al. 2009, AJ, 137, 4149

Garbari, S., Read, J. I., & Lake, G. 2011, MNRAS, 416, 2318

Garbari, S., Liu, C., Read, J. I., & Lake, G. 2012, MNRAS, 425, 1445

Gillessen, S., Eisenhauer, F., Fritz, T. K., et al. 2009, ApJ, 707, L114

Gilmore, G., & Reid, N. 1983, MNRAS, 202, 1025

Girard, T. M., van Altena, W. F., Zacharias, N., et al. 2011, AJ, 142, 15

Goldstein, H., Poole, C., & Safko, J. 2008, Classical Mechanics: Third Edition

Golubov, O. 2012, Ph.D. Thesis,

Golubov, O., Just, A., Bienaymé, O., et al. 2013, A&A, 557, AA92

Henon, M., & Heiles, C. 1964, AJ, 69, 73

Holmberg, J., & Flynn, C. 2000, MNRAS, 313, 209

Holmberg, J., & Flynn, C. 2004, MNRAS, 352, 440

Hori, G. 1962, Publ. Astr. Soc. Japan, 15, 100

Ivezić, Ž., Sesar, B., Jurić, M., et al. 2008, ApJ, 684, 287

Jenkins, A. 1992, MNRAS, 257, 620

Johnson, D. R. H., & Soderblom, D. R. 1987, AJ, 93, 864

Jurić, M., Ivezić, Ž., Brooks, A., et al. 2008, ApJ, 673, 864

Just, A., Berczik, P., Petrov, M. I., & Ernst, A. 2009, MNRAS, 392, 969

Just, A., & Jahreiß, H. 2010, MNRAS, 402, 461

Kaasalainen, M., & Binney, J. 1994, MNRAS, 268, 1033

Kent, S. M., & de Zeeuw, T. 1991, AJ, 102, 1994

Kordopatis, G., Gilmore, G., Steinmetz, M., et al. 2013, AJ, 146, 134

Kordopatis, G., & RAVE collaboration 2014, arXiv:1410.4254

Kuijken, K., & Gilmore, G. 1989, MNRAS, 239, 571

Kuzmin, G. G. 1953, Publ. Tartu Astr. Obs., 32, 332

Landau, L. D., & Lifshitz, E. M. 1976, Mechanics, Volume 1 of course of theoretical physics

Lynden-Bell, D. 1962, MNRAS, 124, 95

Manabe, S. 1979, PASJ, 31, 369

McMillan, P. J., & Binney, J. J. 2008, MNRAS, 390, 429

McMillan, P. J. 2011, MNRAS, 414, 2446

Mihalas, D., & Binney, J. 1981, San Francisco, CA, W. H. Freeman and Co., 1981. 608 p.

Navarro, J. F., Frenk, C. S., & White, S. D. M. 1996, ApJ, 462, 563

Ollongren, A. 1962, BAN, 16, 241

Oort, J. H. 1960, BAN, 15, 45

Oort, J. H. 1932, BAN, 6, 249

Pasetto, S., Grebel, E. K., Zwitter, T., et al. 2012, A&A, 547, AA70

Pasetto, S., Grebel, E. K., Zwitter, T., et al. 2012, A&A, 547, AA71

Piffl, T., Binney, J., McMillan, P. J., et al. 2014, MNRAS, 445, 3133

Reid, M. J., Menten, K. M., Zheng, X. W., et al. 2009, ApJ, 700, 137

Rix, H.-W., & Bovy, J. 2013, A&A Rev., 21, 61

Roeser, S., Demleitner, M., & Schilbach, E. 2010, AJ, 139, 2440

Sanders, J. 2012, MNRAS, 426, 128

Sanders, J. L., & Binney, J. 2014, MNRAS, 441, 3284

Schönrich, R., & Binney, J. 2009, MNRAS, 396, 203

Schönrich, R., Binney, J., & Dehnen, W. 2010, MNRAS, 403, 1829

Schönrich, R., Asplund, M., & Casagrande, L. 2011, MNRAS, 415, 3807

Schwarzschild, K., & Villiger, W. 1907, Astronomische Nachrichten, 174, 133

Shu, F. H. 1969, ApJ, 158, 505

Siebert, A., Bienaymé, O., Binney, J., et al. 2008, MNRAS, 391, 793

Siebert, A., Bienaymé, O., & Soubiran, C. 2003, A&A, 399, 531

Siebert, A., Famaey, B., Binney, J., et al. 2012, MNRAS, 425, 2335

Smith, M. C., Wyn Evans, N., & An, J. H. 2009, ApJ, 698, 1110

Smith, M. C., Whiteoak, S. H., & Evans, N. W. 2012, ApJ, 746, 181

Sofue, Y., Honma, M., & Omodaka, T. 2009, PASJ, 61, 227

Sommer-Larsen, J., & Zhen, C. 1990, MNRAS, 242, 10

Spano, M., Marcelin, M., Amram, P., et al. 2008, MNRAS, 383, 297

Spitzer, L., Jr. 1942, ApJ, 95, 329

Stäckel, P. 1890, Math. Ann. , 35, 91

Statler, T. S. 1989, ApJ, 344, 217

Valera, F., Aguilar, L., & Schuster, W. 1994, Numerical Simulations in Astrophysics, 111

van Albada, G. 1952, Proc. Kon. Ned. Akad. Wetensch., Series B, 55, No. 5, 620

van de Ven, G., Hunter, C., Verolme, E. K., & de Zeeuw, P. T. 2003, MNRAS, 342, 1056

Villalobos, Á., & Helmi, A. 2008, MNRAS, 391, 1806

Xue, X. X., Rix, H. W., Zhao, G., et al. 2008, ApJ, 684, 1143

Wielen, R. 1977, A&A, 60, 263

Yurin, D., & Springel, V. 2014, MNRAS, 444, 62

Zacharias, N., Finch, C., Girard, T., et al. 2010, AJ, 139, 2184

Zacharias, N., Finch, C. T., Girard, T. M., et al. 2013, AJ, 145, 44

Zhang, L., Rix, H.-W., van de Ven, G., et al. 2013, ApJ, 772, 108

Zwicky, F. 1933, Helvetica Physica Acta, 6, 110

Zwitter, T., Matijevič, G., Breddels, M. A., et al. 2010, A&A, 522, AA54

Acknowledgements

I would like to thank my scientific advisor Andreas Just for the help and support in the realization of this thesis. I would also like to thank Hans-Walter Rix and Glenn van de Ven as part of the IMPRS thesis committee, which together with my advisor led me to reach this important step; Glenn was always available and very helpful with discussions and ideas during these years. I would like to acknowledge Eva Grebel and Luca Amendola to be part of my examination committee. I am also very grateful to Stefano Pasetto for the scientific advice and motivation he gave me during a difficult period of my thesis.

Many thanks to Alex Büdenbender for the help with the Monte Carlo Markov Chain simulation and discussions about our projects. A thanks to Corrado Boeche for giving me advice about RAVE data. Great thanks to Reza Moetazedian and Avon Huxor for the proof reading of my thesis, your advice was very helpful. To Hendrik Heinl and Avon Huxor for having supported me psychologically when I needed. A special thanks to Jan Rybizki because we arrived in Heidelberg at the same time and we went through together to the difficult periods of a PhD. You were always available for discussions and help, especially with Python.

I would like to thank past and present people at ARI, in particular John Vickers, Johannes Ludwig, Sonia Duffau, Matthias Frank, Oleksiy Golubov, Mohammed Abbas, Veronica Lora, Peter Zeidler and Clio Bertelli Motta, with whom I had nice conversations and shared good moments during the last years. A thanks go to Raoul Haschke, Robert Schmidt, Thorsten Lisker, Frederik Schönebeck, Jan Rybizki and Christoph Olczak besides astronomy for having taken part in the Mitarbeiter Turnier. ARI Supergiants are and will always be the best team. A special thanks to Stefan Schmeja not only for being a good officemate, but also for sharing scientific discussions and helping with advice not related to astronomy.

To my basketball team in Dossenheim for the good effort during the matches. To the friends that I met in Heidelberg, Giacomo, Claudia, Rafael, Stefano, Jan, Magali, Gin Es und Valentin, with whom I spent many good enjoyable moments in this beautiful city. To Chiara, Matteo, Alessandra, Mariairene, and especially Lucile, Franzi, Christofer and Luisa. It is always nice to meet you in Germany or when I come back home to Italy. To the old friends, Luca, Roberto and Francesca for your good friendship despite we do not see each other very often. To Francesca, Ilaria, Paola, Elda and Dino, because you are so close as family.

A very warm thanks go to my family who gave me the possibility to study what I wanted and for your support. I am very grateful to my sister Michela, her husband Jacopo, my cousin Sara and Moretto for sharing wonderful moments in my life.

A special thanks go to you, Lara, you were there during a complicated period of my life and you supported me and cheered me up. Your kindness, your great help and continuous encouragement in the last year and especially in the last weeks of my PhD were unbelievable. You were immediately willing to enter in the world of astronomy when we first met and do not get bored when I or other friends speak about it also outside the institute. You were even available to proof read again this thesis giving comments for improvements. This thesis was also possible because of you.

I acknowledge support by the Collaborative Research Centre 'The Milky Way System' (SFB 881, subproject A7), the Max Planck Institute for Astronomy and the Heidelberg Graduate School of Fundamental Physics.